UNIVERSITÀ DEGLI STUDI DI MILANO

DEPARTMENT OF PHYSICS "ALDO PONTREMOLI"

PHD SCHOOL IN
PHYSICS, ASTROPHYSICS AND APPLIED PHYSICS
CYCLE XXXV

Galaxy-halo connection and clustering in the presence of dynamical dark energy and massive neutrinos

Disciplinary Scientific Sector FIS/05

PhD Thesis of:
Elisabetta Carella

Supervisor: Dr Carmelita Carbone (INAF/UniMi, Milan)
Internal Tutor: Prof. Luigi Guzzo
Director of the School: Prof. Matteo Paris

A.Y. 2022-2023

Commission of the final examination:

External Referees:
Dr Fabio Fontanot (INAF - Osservatorio Astronomico di Trieste)
Dr Ginevra Favole (Istituto de Astrofisica de Canarias)

External Members:
Prof. Giulia Rodighiero (Università degli Studi di Padova)
Prof. Federico Marulli (Alma Mater Studiorum - Università di Bologna)

Internal Member:
Prof. Luigi Guzzo (Università degli Studi di Milano)

Final examination:

26 July 2023

Università degli Studi di Milano, Dipartimento di Fisica, Milano, Italy

List of Publications

Refereed publications

"DEMNUni: comparing nonlinear power spectra prescriptions in the presence of massive neutrinos and dynamical dark energy", G. Parimbelli, C. Carbone, J. Bel, B. Bose, M. Calabrese, E. Carella, M. Zennaro, JCAP11(2022)041

Publications in preparation

1. "DEMNUni: The galaxy-halo connection in the presence of dynamical dark energy and massive neutrinos", E. Carella et al., in prep. (lead author).
2. Euclid pre-launch Key-Project (KP) CL-3 paper-4 "Halo mass function and bias in non-standard models", E. Carella et al., in prep. (lead author).
3. Euclid pre-launch KP-TH-1 paper-6 "Impact of nonlinear clustering on beyond-LCDM constraints with Euclid", B. Bose et al., in prep. (co-author in the first group).
4. Euclid pre-launch KP-JC-6 paper-3 "Cosmological constraint on non-standard cosmologies from simulated Euclid probes", G. D'Amico et al., in prep. (co-author in the first group).
5. Euclid pre-launch KP-CMBX-2 paper-1 "Mock simulations for CMB cross-correlation", M. Calabrese, et al., in prep. (co-author in the first group)
6. "DEMNUni: nonlinear ISW–galaxy and CMB-Lensing cross-correlations in the presence of massive neutrinos", V. Cuozzo, C. Carbone, M. Calabrese, E. Carella, M. Migliaccio, in prep.
7. "The Astrophysical Gravitational Wave Background: primary nonlinear AGWB-LSS cross-correlations and lens-induced secondary anisotropies from the DEMNUni simulations", M. Gaijan, C. Carbone, M. Calabrese, E. Carella, V. Cuozzo, A. Jenkins, M. Sakellariadou, in prep.

Contents

List of Publications **iii**

Introduction **vi**
Motivation vii
Thesis overview viii

1 The cosmological framework **1**
1.1 The standard cosmological model 1
1.1.1 The Einstein's Equations 1
1.1.2 The Friedmann–Lemaître–Robertson–Walker metric 2
1.1.3 Dynamics of the Universe 2
1.2 Linear perturbation theory 6
1.3 Dark Energy 7
1.4 Massive neutrinos in cosmology 11
1.4.1 The cosmic neutrino background 11
1.4.2 Neutrino decoupling and non-relativistic transition 12
1.4.3 Matter perturbations in the presence of massive neutrinos 12
1.4.4 Effects of the neutrino mass on the matter power spectrum 13
1.4.5 Effect of the neutrino mass on the halo mass function 15
1.4.6 Current constraints on the neutrino mass 17

2 Large scale structures: theory and observations **21**
2.1 Galaxy clustering 21
2.2 Cosmological simulations 28

3 The connection between galaxies and dark matter haloes **31**
3.1 Subhalo abundance matching 34
3.2 Extended Subhalo abundance matching 38
3.3 Hydrodynamical simulations 39
3.4 Semi-analytical models 40
3.5 Halo occupation models and conditional luminosity function 41
3.6 The stellar-to-halo-mass relation 42

4 Synthetic and observed data for the analysis pipeline **45**
4.1 N-body simulations: the DEMNUni suite 45
4.2 Galaxy surveys: SDSS and COSMOS 46
4.3 Used software libraries 50

5 The galaxy-halo relation in the ΛCDM model **55**
5.1 The SHAM method for ΛCDM haloes 55
5.2 Redshift Evolution of the SHMR 58
5.3 Comparison with the literature 58
5.4 Testing the stellar-to-halo mass relation 62
5.5 Galaxy clustering in real and redshift space 62

6 The galaxy-halo relation in alternative cosmologies **65**
6.1 The SHAM method in massive neutrino scenarios 65
6.2 The SHAM method in dynamical dark energy scenarios 73
6.3 SHAM in massive neutrino and dynamical dark energy scenarios 81
6.4 Galaxy Clustering in $\nu w_0 w_a$CDM cosmologies 83

7 Halo mass functions, power spectra and bias **93**
7.1 The Halo Mass Function in $\nu w_0 w_a$CDM cosmologies 93
7.2 Halo auto-spectra and bias in $\nu w_0 w_a$CDM cosmologies 96
7.2.1 Halo auto power-spectra 97
7.2.2 The effective halo bias from auto-spectra 101
7.3 Halo-matter cross-spectra and bias in $\nu w_0 w_a$CDM cosmologies 103
7.3.1 Halo-matter cross-spectra 103
7.3.2 The effective halo bias from cross-spectra 107
7.4 The halo bias in $\nu w_0 w_a$CDM cosmologies: mass bin analysis 109

8 Halo power spectrum multipoles in redshift space **115**
8.1 Power spectrum multipoles from the full halo catalogue 115
8.2 Power spectrum multipoles for a selected halo mass bin 119

Conclusions and future outlook **123**

Bibliography **125**

Introduction

Motivation

The connection between dark matter structures and galaxies is important to generate accurate galaxy mock catalogs from N-body simulations and it has been studied in great detail in the last two decades thanks to two joint revolutions. The first one is the advent of cosmological numerical simulations able to resolve dark matter structures, the haloes, and their substructures, the subhaloes, over volumes large enough to measure their spatial clustering properties. The second one is the advent of large galaxy surveys which can identify large samples of galaxies in a wide redshift range and measure their spatial clustering properties. In particular, this field had a large step forward with the advent of the Two-degree Field Galaxy Survey (2dFGRS), the Sloan Digital Sky Survey (SDSS) and the Cosmic Evolution Survey (COSMOS). Yet, the next generation of galaxy surveys, such as Euclid, will provide improvements in our understanding of galaxy formation and cosmological observables.

In addition to precise observations, theoretical modelling is required in order to maximize cosmological information. The most popular cosmological model which received many confirmations in recent years is the so-called Λ Cold Dark Matter (ΛCDM) model. It establishes a Universe consisting of three different components: the ordinary baryon matter (4.9%), composed by baryons, i.e., normal atoms that make up stars, gas, and galaxies, the so-called cold dark matter (26.8%), cold and collisionless, and the so-called cosmological constant, Λ, (68.3%) (Planck Collaboration et al., 2018), as expected in the most general form of Einstein's equations of general relativity. The standard cosmological model describes the Universe as a flat and expanding space-time governed by the laws of General Relativity (GR), characterised by features in agreement with observations, such as Cosmic Microwave Background (CMB), Supernovae, and Baryon Acoustic Oscillation (BAO) data.

However, the two main components of the current standard model, the cold dark matter and the dark energy, are still unknown. In the framework of the ΛCDM model, the dark matter (DM) of the Universe is mainly distributed in virialised structures. DM is indirectly observed by, e.g., cluster lensing measurements, and, for the most part can be described by cold, massive particles, having no or very weak interactions with ordinary matter, apart from the gravitational one. As the Universe evolves, on small scales the CDM component, usually modelled as a pressureless fluid, forms larger and larger overdensities under the effect of gravity instability, and finally virialises in dark matter haloes. The associated potential wells become deeper and deeper, trapping the baryons

which eventually, through cooling and condensation, form stars and galaxies at the centers of halos and subhalos.

As a result, galaxy properties, such as luminosity or stellar mass, are closely connected to the depth of the halo potential and therefore to its mass. Understanding the relation of the stellar mass content of a galaxy to the mass of the DM halo associated to that galaxy is a powerful tool to understand and constrain the processes related to galaxy formation.

Moreover, dark energy is also little understood. It has been introduced to explain the accelerated expansion the Universe is recently undergoing, observed for the first time in 1998 using Type Ia supernovae as standard candles (Riess et al., 1998; Perlmutter et al., 1999). The standard cosmological model assumes this acceleration to be due to Λ, which is described as a fluid with negative pressure and equation of state $w = -1$. Since the profound nature of this mechanism is not clear there exist other alternatives and theoretical hypothesis. The simplest theories of dark energy propose the existence of a scalar field, the so-called quintessence, driving the accelerated expansion, with its energy contribution possibly evolving in time together with its equation of state.

A further unknown in our Universe concerns the mass of neutrinos. Till few years ago, the three active neutrinos of the standard model of particle physics were assumed to be massless. However, in 1998 the Super-Kamiokande collaboration reported evidence of neutrino oscillations, indicating that at least two neutrinos are massive. Moreover, the presence of massive neutrinos modifies the expansion rate of the Universe, changing the time when the radiation energy density becomes lower than the matter energy density. Moreover, having very small masses, they are characterised by large thermal velocities, so that they avoid clustering on small scales, causing a suppression of matter and galaxy clustering.

The importance of neutrinos in cosmology comes from the effects their masses have on cosmological observables, such as galaxy clustering and weak lensing. These effects are significant for two reasons: first, the absolute neutrino mass scale is still unknown, therefore the analysis of cosmological effects could play a key role in its determination, being gravity sensitive mainly to the total neutrino mass, $M_\nu \equiv \Sigma m_\nu$, and much less to their mass splitting; second, an accurate description of massive neutrino effects on the Large Scale Structure (LSS) of the Universe is required to avoid systematic errors in the determination of cosmological parameters, such as the dark energy density and its equation of state, whose measurements represent one of the main goals of current and future cosmological experiments.

This PhD project thesis is particularly focused on the creation and analysis of mock galaxy and galaxy-cluster catalogues in the presence of massive neutrinos and dynamical dark energy, useful to provide modelling and make predictions for future galaxy surveys, Euclid in particular, and also to test codes for the data analysis pipeline in view of upcoming cosmological datasets.

Thesis overview

This work is focused on the connection between dark matter subhaloes and galaxies, exploiting a large set of cosmological N-body simulations spanning several cosmological models with different neutrino masses and/or different equations of state of dynamical dark energy. To this aim, the candidate used a set of cosmological simulations, the so-called "Dark Energy and Massive Neutrino Universe" (DEMNUni) project (Carbone et al. 2016, Parimbelli et al. 2022), which is a set of 15 large N-body simulations with massive neutrino particles and a time dependent equation of state of dark energy follow-

ing the so-called Chevallier, Polarski & Linder (CPL) parametrisation. In particular, the baseline cosmology is assumed to agree with parameter constraints from Planck 2013, namely a flat ΛCDM model generalised to a $\nu w_0 w_a$CDM, by varying the sum of the neutrino masses over the values $M_\nu = 0, 0.16, 0.32$ eV (and consequently the corresponding values of the neutrino density Ω_ν and the cold dark matter density Ω_c parameters, while keeping fixed the total matter density parameter Ω_m and the amplitude of primordial curvature perturbations). In addition, besides the Λ case, the simulations account for different dark energy equations of state (EoS), consisting of four different combinations of the CPL parameters w_0 and w_a. The EoS parameters are set within the Planck-2015 constraints: $w_0 = -0.9, -1.1$ and $w_a = -0.3, 0.3$.

I have applied to these simulations the so-called subhalo abundance matching (SHAM) technique, which assumes a one-to-one relation between a physical property of a dark matter halo/subhalo and an observational property of the galaxy that it hosts.

In particular, in this work I consider the stellar mass as a galaxy property, because it is expected to be closely related to the dark matter content of the hosting DM halo. As a DM halo/subhalo property I use its mass, representing a measure of the depth of the associated potential well.

I adopt an empirical parameterisation of the stellar-to-halo-mass relation (SHMR) from Moster et al. (2010) that links the halo mass to the corresponding stellar mass of a galaxy hosted by the halo. Via a MCMC bayesian approach, I computed the best-fit parameters of the SHMR as a function of redshift in the presence of dark energy and massive neutrinos, considering the datasets from the Sloan Digital Sky Survey (SDSS) for redshifts $z < 0.2$, and the Cosmological Evolution Survey (COSMOS) observations for $0.2 < z < 2$.

Main results

Implementing such method, I have populated with galaxies the dark matter structures in the DEMNuni simulations finding the dependence of the SHMR on the total neutrino mass and the dark energy equation of state. The obtained galaxy mocks account both for central and satellite galaxies, spanning the redshift range $0 < z < 2$, which covers both the photometric and spectroscopic galaxy samples of the upcoming Euclid survey.

Furthermore, I have obtained fitting formulas for the SHMR parameters, which allow us to reconstruct the stellar mass as a function of the neutrino mass and the time-dependent dark energy equation of state. This procedure can be very useful for the realisation of galaxy mock catalogues in cosmologies which span the most important cosmological parameters the Euclid mission has been conceived to measure.

Finally, I have estimated the galaxy and galaxy-cluster properties from simulated mock catalogues, such as the halo-mass-function, the matter/halo/galaxy power spectra, the correlation function both in real and redshift space and the multipoles of the power spectrum in redshift space. Also, from these measurements I evaluated the galaxy bias of the produced mock galaxy catalogues.

Organisational note

This thesis is organised as follows.

In Chapter 1 I describe the main features of the standard cosmological model and introduce alternative cosmological scenarios with massive neutrinos and dynamical dark energy.

In Chapter 2 I describe the main features of the Large Scale Structures, comparing theory and observations of the galaxy clustering.

In Chapter 3 I introduce the method to connect galaxies to dark matter halos. In particular, I describe the subhalo abundance matching method (SHAM) used in this work. Then I review a variety of other empirical method in literature as the extended subhalo abundance matching and the halo occupation models, and also physical models as the semi-analytical models.

In Chapter 4 I describe the input data from the simulations and the observations that I used to perform the SHAM method. Moreover, the tools and the libraries used to perform this analysis are presented in details.

In Chapter 5 I describe the procedure used to populate halos with galaxies in the ΛCDM model, the performed analyses and the obtained results of the steller-to-halo-mass-relation (SHMR), the stellar mass function and the clustering properties.

In Chapter 6 I populate the dark matter subhalos with galaxies in models with massive neutrinos and dynamic dark energy, using the SHAM method described in the previous chapter.

In Chapter 7 I show the results of the halo power spectra, the cross halo/matter power spectra and the halo bias from the simulated halo catalogues, with two different mass-cut values and in many mass bins.

In Chapter 8 the measurements of the multipoles, i.e. monopole, quadrupole, hexadecapole, of the halo power spectra from halo catalogues in many spherical overdensity values and redshift values are presented.

Finally, in the Conclusions I briefly summarise the main results of this work, and discuss future possible directions of this research.

CHAPTER 1

The cosmological framework

Modern cosmology is based on the assumption of the Copernican Cosmological Principle, which states that the Universe is spatially homogeneous and isotropic on large scale, for fundamental observers who are stationary with respect to the expansion/contraction of the spatial geometry. This means that our position in the Universe is not privileged; if we were in another region of the Universe the basic characteristics of our Universe would be the same, i.e. the Universe is homogeneous. Furthermore, there is no reason not to assume that the Universe is isotropic, that is, such that no spatial direction is preferred.

This principle is confirmed by observations. Experimentally it is observed that the distribution of the galaxies is homogeneous and isotropic on scales larger than 150 Mpc/h [1]. Moreover, another empirical evidence of the cosmological principle is provided by the observations of the cosmic microwave background radiation (CMB), that is the radiation emitted when photons decoupled from baryons, which composed an ionized plasma in the primordial Universe, and started to travel freely. The temperature of the radiation is incredibly isotropic with very small anisotropies of the order of $\Delta T/T \simeq 10^{-5}$ [2], [3], [4], which are the imprint of the density perturbations present in the plasma formed by photons and baryons in the pre-decoupling era. The anisotropies are distributed consistently with the spectrum of fluctuations expected to be generated in the early phase, called inflation, a period in which the amplitude of the primeval density fluctuations is enhanced.

In this chapter, I will review the cosmological context and the perturbation theory useful to describe the Large Scale Structure of the Universe. Then, I will provide a brief illustration of the standard cosmological model and also the alternative model with massive neutrinos and dark energy, which I adopted to build the galaxy mock catalogues.

1.1 The standard cosmological model

In the early 20th century, Albert Einstein set the stage for modern cosmology formulating his theory of gravity, General Relativity. He published his theory in the paper "Cosmological Considerations of the General Theory of Relativity" (Einstein, 1917 [5]).

1.1.1 The Einstein's Equations

The theory is based on the Einstein's field equations, that show the connection between the distribution of matter and the geometry of the Universe. They have the follow form:

$$G_{\mu\nu} = \frac{8\pi G}{c^4} T_{\mu\nu} \ , \tag{1.1}$$

where $T_{\mu\nu}$ is the so-called stress-energy tensor that describes the total matter-energy content, while $G_{\mu\nu}$ is the Einstein tensor defined by

$$G_{\mu\nu} = R_{\mu\nu} - \frac{1}{2} R g_{\mu\nu} \ , \tag{1.2}$$

where $R_{\mu\nu}$ is the Ricci tensor, R the curvature scalar, accounting for the local space-time curvature of the Universe, and $g_{\mu\nu}$ is the four-dimensional metric. They are both obtained calculating the trace of the Riemann tensor $R_{\mu\nu\rho\sigma}$

$$R_{\mu\nu} = R^{\lambda}_{\ \mu\lambda\nu} \ , \tag{1.3}$$

$$R = R^{\nu}_{\ \nu} = g^{\mu\nu} R_{\mu\nu} \ . \tag{1.4}$$

In short, the whole content of general relativity can be summarised as follows: the space-time is a manifold on which we define a Lorentz four-dimensional metric $g_{\mu\nu}$, and the curvature of $g_{\mu\nu}$ is determined by the matter distribution as in Equation (1.1).

Einstein assumed the Universe to be spatially homogeneous and isotropic. The metric describing the space-time that satisfies these requirements is the FLRW metric, derived by Friedman, Lemaître, Robinson, Walker.

1.1.2 The Friedmann–Lemaître–Robertson–Walker metric

The metric adopted to describe the Universe must obey the cosmological principle, therefore must be invariant under rotations and translations. It must also be able to describe a expanding (or contracting) space-time. The Friedmann–Lemaître–Robertson–Walker (FLRW) metric satisfied these requirements. The line element of this metric, valid for a class of comoving observers, in hyperspherical coordinates can be written as

$$\begin{aligned} ds^2 &= -c^2 dt^2 + a^2(t) dl^2 \\ &= -c^2 dt^2 + a^2(t) \left[dx^2 + f_k^2(x) d\Omega^2 \right] \ , \end{aligned} \tag{1.5}$$

where $d\Omega$ is the solid angle element, $d\Omega = d\theta^2 + sin^2\theta d\phi^2$. The spatial term is modulated by the scale factor $a(t)$, which takes into account the expansion of the space-time. Its value is determined setting $a = 1$ at the present epoch t_0.

The angular distance depends on the radial function $f_k(x)$ that is either a trigonometric, hyperbolic or linear function of x depending on whether the curvature K is respectively positive, negative or zero, as follows

$$f_k(x) = \begin{cases} K^{-1/2} \sin(\sqrt{K} x) & K > 0 \\ x & K = 0 \\ (-K)^{-1/2} \sin(\sqrt{-K} x) & K < 0 \end{cases} \tag{1.6}$$

1.1.3 Dynamics of the Universe

In order to study the dynamics of the Universe, i.e. the time evolution of the scale factor, we have to solve the Einstein's equations, Equation (1.1). They can be written making some assumptions on the stress energy tensor $G_{\mu\nu}$ and calculating the space-time term, i.e. the $G_{\mu\nu}$ tensor, from the metric Equation (1.5).

If we consider either the contribution of matter and radiation we can assume $T_{\mu\nu}$ in the form of perfect fluid with pressure P and total mass-energy density ρ (i.e. the sum of the densities of all the species present in the Universe), as follows

$$T_{\mu\nu} = \rho u_\mu u_\nu + P(g_{\mu\nu} + u_\mu u_\nu) \,. \tag{1.7}$$

This is also the most general form of a tensor compatible with homogeneity and isotropy. The u_μ is the four-velocity of the comoving observers.

Then the Einstein's equations are reduced from 10 to only 2 independent equations (the first coming from the time-time component and the second coming from the space-space components):

$$\begin{aligned} G_{00} &= \frac{8\pi G}{c^4}\rho \,, \\ G_{ii} &= \frac{8\pi G}{c^4}P \,. \end{aligned} \tag{1.8}$$

Calculating the tensors G_{00} and G_{ii} using the FLRW metric Equation (1.5) we can get the following system of equations

$$\left(\frac{\dot{a}}{a}\right)^2 = \frac{8\pi G}{3}\rho - \frac{Kc^2}{a^2} \tag{1.9}$$

$$\frac{\ddot{a}}{a} = -\frac{4\pi G}{3}\left(\rho + \frac{3P}{c^2}\right) \tag{1.10}$$

known as Friedmann's equations. The first one describes the expansion rate of the Universe, while the second one describes the acceleration of the scale factor.

Combining Equations (1.9) and (1.10) together we can derive conservation laws

$$\dot{\rho} + 3\frac{\dot{a}}{a}(\rho + P) = 0 \,, \tag{1.11}$$

that is the first law in thermodynamics, i.e. the energy conservation, in the cosmological context.

For each non-interacting component of the Universe the pressure is linked to the mass-energy density through an equation of state of the form

$$P_i = \omega_i \rho_i c^2 \,. \tag{1.12}$$

Substituting Equation (1.12) into the Equation (1.11) we obtain for each component the following equation

$$\dot{\rho} + 3\frac{\dot{a}}{a}\rho(1 + \omega) = 0 \,. \tag{1.13}$$

When ω is a constant quantity the general solution has the following form

$$\rho(t) = \rho_0 a^{-3(\omega+1)} \,. \tag{1.14}$$

The content of matter of the Universe is composed of cold dark matter and baryonic matter that have $P \ll \rho c^2$ in good approximation. As a result, the matter is called pressureless dust that is assumed to have $\omega = 0$. On the other hand, the radiation, that

contains relativistic matter as photons and massless neutrinos, has a pressure contribution. Its equation of state is $P = \frac{\rho c^2}{3}$. Inserting these expressions into Equation (1.14) we get the evolution of the mass density ρ for both components

$$\rho(t) = \rho_0 \begin{cases} a^{-3}(t) & \text{for dust: } \omega = 0 \\ a^{-4}(t) & \text{for radiation: } \omega = 1/3 \end{cases} \tag{1.15}$$

Therefore, the energy density of the radiation drops more rapidly with time than for ordinary matter. In addition, their contributions are negligible in the present Universe, while they were dominant in the early Universe when $a \to 0$.

However, Einstein proposed a modification on his theory, as he believed in a static Universe. As a consequence, he introduced a constant quantity, the so-called cosmological constant Λ. In this case, Einstein's equations become

$$G_{\mu\nu} + \Lambda g_{\mu\nu} = \frac{8\pi G}{c^4} T_{\mu\nu} \, . \tag{1.16}$$

Using this formulation the Friedmann's equations have a new term, as follows

$$\left(\frac{\dot{a}}{a}\right)^2 = \frac{8\pi G}{3}\rho - \frac{Kc^2}{a^2} + \frac{\Lambda}{3} \tag{1.17}$$

$$\frac{\ddot{a}}{a} = -\frac{4\pi G}{3}\left(\rho + \frac{3P}{c^2}\right) + \frac{\Lambda}{3} \tag{1.18}$$

The presence of mass-energy, expressed by the term ρ, makes the expansion decelerate, eventually causing the Universe to contract. On the other hand, the cosmological constant Λ changes the dynamics of the Universe because it has opposite sign. So, if its value dominates on the other terms, it can make the Universe expand, with a positive acceleration of the scale factor.

If we introduce the Hubble parameter $H = \dot{a}/a$, that expresses the expansion rate of the Universe, we can write the first Friedmann's equation as

$$\left(\frac{\dot{a}}{a}\right)^2 = H^2(t) = \frac{8\pi G}{3}\left[\rho(t) - \frac{3}{8\pi G}\frac{Kc^2}{a^2} + \frac{\Lambda}{8\pi G}\right] . \tag{1.19}$$

If we substitute $\rho(t)$ with Equation (1.15), that takes into account the radiation and matter contribution, and if we define the spatial curvature term and the cosmological constant term respectively as follows

$$\rho_{K,0} = -\frac{3}{8\pi G} Kc^2 \tag{1.20}$$

$$\rho_\Lambda = \frac{\Lambda}{8\pi G} \tag{1.21}$$

the first Friedmann's equation becomes

$$\left(\frac{\dot{a}}{a}\right)^2 = H^2(t) = \frac{8\pi G}{3}\left[\rho_{r,0}a^{-4} + \rho_{m,0}a^{-3} + \rho_{K,0}a^{-2} + \rho_\Lambda\right] . \tag{1.22}$$

We can note that, unlike the other terms, the energy density of the cosmological constant behaves as an energy density that remains constant in time. Setting Equation (1.14) equal to a constant, this implies

$$-3(\omega_\Lambda + 1) = 0 \quad \Rightarrow \quad \omega_\Lambda = -1 \quad \Rightarrow \quad P_\Lambda = -\rho_\Lambda c^2 \tag{1.23}$$

As a result, the cosmological constant has a negative pressure. If this is the dominant term, inserting the pressure of Equation (1.23) in the acceleration Equation (1.18) we obtain an expanding and accelerating Universe.

In conclusion, when the scale factor was very small, the early Universe was dominated by the radiation component. Then it was dominated by matter until the curvature energy density became the leading term in the total energy budget. Finally the cosmological constant becomes important only at late times.

We can define the critical density

$$\rho_{cr} = \frac{3H^2}{8\pi G\rho} \tag{1.24}$$

as the total density needed for the Universe to have a flat geometry, with $K = 0$.

In a ΛCDM model the value of the Hubble parameter at the present epoch is $H_0 = 67.4\,\mathrm{km\,s^{-1}\,Mpc^{-1}}$, the so-called Hubble constant. Using this constant, the critical density today is equal to $\rho_{cr} \approx 1.25 \times 10^{11}\,\mathrm{M_\odot\ Mpc^{-3}}$. In addition, defining the density parameters for each component as

$$\Omega_i(t) \equiv \frac{\rho_i(t)}{\rho_{cr}} \tag{1.25}$$

leading to the fact that

$$\sum_i \Omega_i(t) + \Omega_K(t) = 1\ , \tag{1.26}$$

where the density parameters of the curvature and the cosmological density are respectively

$$\begin{aligned} \Omega_K(t) &= -\frac{K}{a^2(t)H^2(t)}\ , \\ \Omega_\Lambda(t) &= \frac{\Lambda}{3H_0^2}\ . \end{aligned} \tag{1.27}$$

Therefore the present total density parameter of the Universe is

$$\Omega_0 = \sum_i \Omega_{i,0}\ . \tag{1.28}$$

In term of these parameters the first Friedmann equation takes the form

$$H^2(t) = H_0^2[\Omega_{r,0}a^{-4} + \Omega_{m,0}a^{-3} + \Omega_{K,0}a^{-2} + \Omega_\Lambda]\ . \tag{1.29}$$

The expression of Hubble rate depends on the present value of all density parameters $\Omega_{i,0}$ and the present Hubble parameter H_0. H_0 and the $\Omega_{i,0}$ express the current state of the Universe and they can be considered as cosmological parameters, linked to the abundances of each species, that are determined fitting cosmological observations.

Cosmological observations in the last two decades have led to the establishment of the standard cosmological model, the so-called ΛCDM. The Universe is composed of radiation, ordinary matter (electrons, protons, neutrons, neutrinos), non-baryonic cold dark matter (CDM), and the cosmological costant Λ. The background evolution of the Universe is led by a cold dark matter component, i.e. non-baryonic collisionless massive particles, and by the cosmological constant Λ. The Universe is assumed to be flat,

with spatial curvature $K = 0$. This is consistent with observations, such as the measurements from WMAP and Planck (Planck Collaboration at al. 2015 [3], 2018 [6]). The constraints on the cosmological parameters, such as the Hubble constant H_0, the physical baryon density $\Omega_{b,0}$, the dark matter density $\Omega_{m,0}$, the curvature parameter $\Omega_{k,0}$, the radiation density parameter $\Omega_{r,0}$, are set by Planck measurements of the cosmic microwave background (CMB) anisotropies, combining information from the temperature and polarisation maps and the lensing reconstruction.

$$
\begin{gathered}
H_0 = (67.4 \pm 0.5)\mathrm{kms}^{-1}\mathrm{Mpc}^{-1} \\
\Omega_{m,0} = 0.315 \pm 0.007 \\
\Omega_{b,0}h^2 = 0.0224 \pm 0.0001 \\
\Omega_{\Lambda,0} = 0.6889 \pm 0.0056 \\
\Omega_{k,0} = 0.001 \pm 0.002
\end{gathered}
$$

Table 1.1: Parameters of ΛCDM model that best fits the data from the Planck measurements of the CMB [6].

1.2 Linear perturbation theory

According to the ΛCDM model, galaxies and large-scale structure have grown gravitationally from tiny, adiabatic gaussian fluctuations in a spatially flat Universe, homogeneous and isotropic on large scales.

We use a fluid description in order to model CDM and baryons as two fluids, whose perturbations expand as waves and obey the conservation of mass and momentum. Given a fluid with average background density $\langle\rho\rangle$, the density contrast is defined as

$$
\delta(\vec{x}) \equiv \frac{\rho(\vec{x})}{\langle\rho\rangle} - 1 \, . \tag{1.30}
$$

It describes the deviation from the mean matter density as a function of the point $\vec{x}$. In addition, the density contrast filtered on a scale R is defined as the mean density contrast within a sphere of a radius R, centred in $\vec{x}$. This quantity is useful because from observations we can only reconstruct the density contrast filtered on a scale R. We can study the statistical properties of fluctuation with the correlation function, that is defined as

$$
\xi = \left\langle \delta(\vec{x})\delta(\vec{x}+\vec{r}) \right\rangle \, , \tag{1.31}
$$

that is the covariance of the field of density fluctuations on a scale r.

Mathematically it is simpler to study density perturbations in Fourier space rather than in real space. For this reason, we use the power spectrum, that is the Fourier transformation of the correlation function. Doing this transformation, it results to be linked to the amplitude of the density contrast in Fourier space $\delta(\vec{k})$ as follows

$$
(2\pi)^3 P(k)\delta^3(\vec{k}+\vec{k'}) = \left\langle \delta(\vec{k})\delta(\vec{k'}) \right\rangle \, , \tag{1.32}
$$

where $\delta^3(\vec{k}+\vec{k'})$ is the three-dimensional Dirac delta. The initial power spectrum has a power-law form $P(k) \propto k^n$ with $n \simeq 1$. This form shows the characteristic distribution of primordial perturbations, generated by a mechanism called cosmological inflation, a

period of accelerated expansion in the early Universe. The inflation creates perturbations through the amplification of quantum fluctuations, that are stretched to astrophysical scales because of rapid expansion. Then, these perturbations undergo gravitational instability and lead to structure formation.

Initially, the perturbations are small and their evolution can be described by the linear theory of cosmological perturbations. The law of perturbation growth can be derived considering a Universe subject to the Friedmann's equations Equation (1.9) and (1.10). We consider two spheres containing equal amount of material, one is the Universe with the background density ρ with radius a and the other one has a radius a_p with a homogeneous overdensity ρ_p. For the conservation of total mass in the two spheres, the densities of the spheres are related to their radii as

$$\rho_p a_p^3 = \rho a^3 \quad \Rightarrow \quad \delta = \frac{\rho_p}{\rho} - 1 \, . \tag{1.33}$$

Therefore, from Equation (1.33) we can express a_p as a function of δ and a and expanding to the first order in δ we obtain

$$a_P = a(1 - \delta/3) \, . \tag{1.34}$$

The second Friedmann's equation for the background is

$$\frac{\ddot{a}}{a} = -\frac{H_0}{2}\Omega_{m,0} a^{-3} \, , \tag{1.35}$$

while for the spherical perturbations the equation is the same, replacing a with a_p and the matter density term $\Omega_{m,0}$ with Ω_m.

Substituting Equations (1.34) and (1.33) in Equation (1.35) and expanding to the first order in δ, we obtain

$$\ddot{\delta} + 2H\dot{\delta} = 4\pi G \rho_m \delta \, , \tag{1.36}$$

that is a differential equation that describes the time evolution of the linear growth of perturbations. This is the equation of a harmonic oscillator: the right-hand side (gravity) compresses the spring, while the term in H (the expansion of the Universe) contrasts the contraction.

1.3 Dark Energy

Type Ia supernovae were used as standard candles to measure the expansion of the Universe. They are a proof that the Universe is currently accelerating its expansion. These observations cannot be explained considering only ordinary matter and dark matter components, but seem to match a Universe dominated by the dominant contribution of a cosmological constant Λ. In other words, the dynamics of the Universe cannot be explained by General Relativity considering that it is filled only by baryons and cold dark matter, so there must be something else that governs its expansion.

The effect of accelerated expansion due to a so-called dark energy starts from $z \sim 1$, when the dark energy contribution in terms of energy density becomes dominant over all the other components.

Current observations, such as ground- and space-based sky surveys, have improved our knowledge about dark matter and dark energy over the past two decades, and have led to a consensus model that considers a Universe filled by $\sim 5\%$ energy density in baryonic matter, $\sim 25\%$ in cold (non-relativistic) dark matter (CDM), $\sim 70\%$ in dark

energy. The probes used to measure the content of different species include the cosmic microwave background (CMB), galaxy clustering including the location of the baryon acoustic oscillation (BAO) feature and the impact of redshift space distortions (RSD); distances of type Ia supernovae (SNe Ia), weak gravitational lensing (WL), given by tiny distortions in the shapes of galaxies due to the deflection of light by intervening large-scale structure, and the abundance of clusters of galaxies.

The simplest and best-known model for dark energy is the cosmological constant. Introducing Λ in the model and leaving it as a free parameter allows us to fit observational data with great precision (see, for example, the results obtained by the Planck collaboration [4] using CMB data, or using galaxy clustering data by the BOSS [7] and VIPERS [8] collaborations). However, a physical interpretation of this constant is not trivial. A sensible hypothesis would be interpret it as linked to the zero-point energy of the vacuum. In this case, the predicted value for the energy density would be $\rho_{vac} \approx 5 \times 10^{93} \mathrm{gm}^{-3}$, to be compared to the measured value of $\rho_{vac} \approx 5 \times 10^{-27} \mathrm{gm}^{-3}$. The two values show an outstanding disagreement of 120 orders of magnitude, which points strongly either in the direction of wrong assumption in the model, or yet-to-explore physical phenomena.

There are several hypothesis that attempt to explain the cosmological constant as an effective theory, and they can be divided in three categories. The first one is a class of theories that attempts to explain the cosmological constant as a quantum effect at large scales, and is related to string and quantum gravity theories. Another family tries to explain the accelerated expansion considering that General Relativity is an effective theory that fails on very large scales; this class studies alternative or more general theories of gravity. In this work we consider the dark energy model known as dynamical dark energy. The prominent candidate in this respect is some minimally coupled scalar field ϕ often called quintessence, slowly rolling down its potential such that it can have negative pressure [9]. Actually, if this candidate is the right one, then it is possible to reconstruct its potential $V(\phi)$ and the corresponding equation of state (EoS).

Dark energy with dynamically evolving energy density is characterised by a time-dependent EoS

$$P_{DE} = w(a) c^2 \rho_{DE} \, . \tag{1.37}$$

The cosmological constant model is just the simplest case of a broader class of models where the dark energy is a scalar field rolling down its potential. The limit of a totally flat potential corresponds to $\omega = -1$.

We adopt the Chevallier-Polarski-Linder (CPL) parametrisation of EoS [9], [10], that expresses the time variation of $\omega(a)$ expanded up to the first order in the scale factor

$$w(a) = w_0 + w_a(1 - a) \, . \tag{1.38}$$

This parameterisation incorporates dynamical aspects but does not require model dependent elements that interfere with comparison of predictions among models. The values of the EoS parameters of the dynamical dark energy, which are used in this work, are shown in Figure 1.1.

Nowadays, an active research in cosmology is to test for different extensions to the simplest dark energy model and to put constraints on the corresponding parameters of the models. The Dark Energy Survey (DES) has this goal. It is a photometric survey imaging the sky in five filters and it has catalogued 300 million galaxies in an area of roughly 5000 deg^2. DES uses four probes to measure the effects of dark energy on the expansion history of the Universe and on the growth of the structures: the observations of thousands of supernavae, the weak gravitational lensing, the galaxy clustering and the

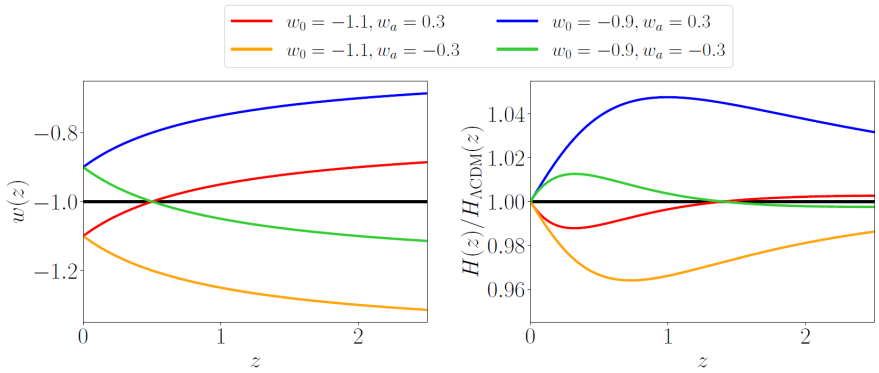

Figure 1.1: Evolution of the EoS parameters of dynamical dark energy (left) and its impact on the Hubble parameter (right) for the cosmological models used in this work. The black lines represent the ΛCDM model of reference; the coloured lines represent DDE models. [11]

distribution of galaxies across the cosmos through a technique called Baryon Acustic Oscillations (BAO). The constraints found by Dark Energy Survey (DES) for a time-varying equation-of-state, described by the parameters ω_0 and ω_a, are [12]:

$$\omega_0 = -0.69^{+0.30}_{-0.29}, \quad \omega_a = -0.57^{+0.93}_{-1.11} \quad \text{from DES alone,}$$

$$\omega_0 = -0.95^{+0.09}_{-0.08}, \quad \omega_a = -0.28^{+0.37}_{-0.48} \quad \text{from DES combined with external data.}$$

The constraint on the dynamical dark energy parameters are shown in Figure 1.2.

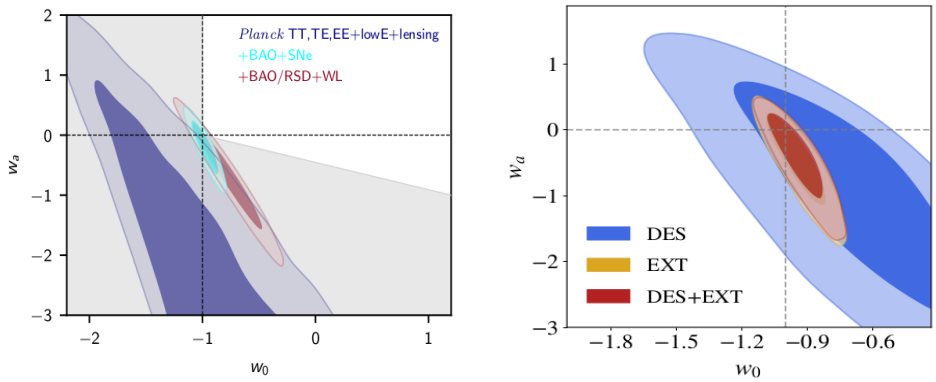

Figure 1.2: LEFT: Marginalised posterior distributions of the (w_0, w_a) parameters for various data combinations. The tightest constraints are found from the combination Planck TT, TE, EE+lowE+lensing+SNe+BAO and are compatible with ΛCDM. The dashed lines indicate the point corresponding to the ΛCDM model. [6]. RIGHT: Constraints on dark energy parameters (w_0, w_a). Blue contours show the 68% and 95% confidence regions from DES alone, yellow is external data alone, and red is the combination of the two. The intersection of the horizontal and vertical dashed lines shows the parameter values in the ΛCDM model [12].

The constraints from DES data, indicated in the right panel in Figure 1.2, are compatible with the cosmological-constant values of $(\omega_0, \omega_a) = (-1, 0)$, as a result they do not find evidence for the temporal variation of the equation of state.

Another constraint is found by Planck measurements of the CMB anisotropies, combined with Type 1a supernovae (SNe) data and baryonic acustic oscillation (BAO) measurements [6]. Assuming the (w_0, w_a) parameterization of $w(a)$ given in Equation 1.38, the constraints of dark energy equation of state parameters from Planck TT, TE, EE + lowE + lensing combined with SNe and BAO data are measured to be

$$\omega_0 = -0.957 \pm 0.080, \quad \omega_a = -0.29^{+0.32}_{-0.26}\,,$$

that are compatible with a cosmological constant. Moreover, considering the combination of Planck data with redshift space distortion (RSD) and weak lensing data the constraints are:

$$\omega_0 = -0.76 \pm 0.20, \quad \omega_a = -0.72^{+0.62}_{-0.54}\,.$$

The left panel in Figure 1.2 shows the marginalised contours of the posterior distribution for the dynamical dark energy parameters (w_0, w_a), found by Plank measurements in combination with other observational data. Using Planck data alone, a wide volume of dynamical dark energy parameter space is allowed, with contours cut off by our priors $(-3 < w_0 < 1, -5 < wa < 5)$. The left panel in Figure 1.2 also shows constraints adding BAO/RSD + WL and BAO + SNe to the Planck TT, TE, EE + lowE + lensing likelihood. The addition of external data sets narrows the constraints towards the ΛCDM values of $w_0 = -1, w_a = 0$. The tightest constraints are found for the data combination Planck TT, TE, EE + lowE + lensing + BAO + SNe. The difference in χ^2 between the best-fit DE and ΛCDM models for this data combination is only $\Delta\chi^2 = -1.4$.

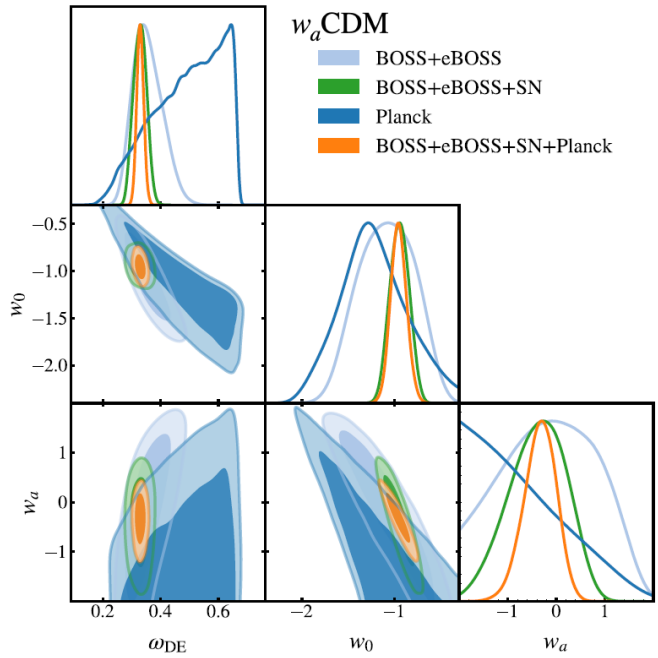

Figure 1.3: Marginalised posterior contours for dark energy parameters in w_aCDM, where the dark energy equation of state parameter w is allowed to evolve in time. We show constraints from the full-shape clustering analysis of BOSS DR12 galaxies in combination with eBOSS quasars (light blue), their combination with Pantheon SN Ia measurements (green), CMB constraints by Planck (in dark blue), and the combination of all four datasets (in orange) [13].

Figure 1.3 shows the constraints for the dark energy parameters, combining the clustering constraints from the galaxy sample of the Baryon Oscillation Spectroscopic Survey (BOSS) with SNe Ia measurements, which provide background constraints for the lowest redshifts and are, therefore, extremely useful for probing the evolution of dark energy [13]. All of the dataset combinations considered recover a value of w_0 that is consistent with -1. Planck does not constrain w_a on its own, but combining it with the clustering and supernovae data yields a value compatible with no evolution: BOSS+eBOSS+Planck+SN $w_a = -0.34^{+0.36}_{-0.30}$.

In observational cosmology, one of the main goals of several current and upcoming experiments, such as Euclid, is to reach an accuracy so high to measure a possible time evolution of the dark energy EoS $\omega(a)$. With its high-precision design, Euclid will investigate the properties of the dark energy by accurately measuring the acceleration as well as the variation of the acceleration at different ages of the Universe and it will test the validity of general relativity on cosmic scales.

1.4 Massive neutrinos in cosmology

Cosmological massive neutrinos have an important role in the evolution of the Universe and they modify several cosmological observables. In this section I will summarize the properties and evolution of neutrinos that fill the Universe and their effect on the growth of matter perturbations. I will describe the clustering features of Large-Scale Structure (LSS) in the presence of massive neutrinos. In particular, I will present the matter power spectrum and the halo mass function, employing a set of large-volume, high-resolution cosmological N-body simulations.

1.4.1 The cosmic neutrino background

The standard model of particle physics predicts the existence of three active massless neutrino species: electron (ν_e), muon (ν_μ) and tau (ν_τ) neutrinos. However, the recent discovery of neutrinos flavour oscillations implies that the neutrinos are massive particles. Experiments measuring neutrino oscillations, such as Kamiokande, SNO, Super-Kamiokande, have fixed the lower limit of the sum of neutrino masses to

$$M_\nu \equiv \sum m_\nu = m_{\nu_e} + m_{\nu_\mu} + m_{\nu_\tau} > 0.06 \text{ eV} . \tag{1.39}$$

In the early Universe neutrinos were produced at large temperatures by frequent weak interactions and neutrinos of different flavour, electronic ν_e, muonic ν_μ and tauonic ν_τ, were kept in equilibrium until these processes became ineffective in the course of the expansion of the early Universe. While coupled to the rest of the primeval plasma (relativistic particles such as electrons, positrons and photons) until the temperature of the Universe was of order 2-5 MeV, neutrinos were relativistic species (with kinetic energy larger than rest-mass energy) and they had a momentum distributed as a Fermi-Dirac distribution function [14]. For neutrinos of mass m_ν and momentum p, and temperature T_ν the distribution is

$$f_\nu(x, p, z) = \frac{1}{\exp \frac{pc}{K_B T_\nu} + 1} , \tag{1.40}$$

where $T_\nu(z)$ is the neutrino temperature at redshift z, c the speed of light and k_B the Boltzmann constant.

1.4.2 Neutrino decoupling and non-relativistic transition

As the Universe cools down, the weak interaction rate falls below the expansion rate and neutrinos decouple from the rest of the plasma. The neutrino interaction rate can be written as

$$\Gamma = n_\nu \langle v \sigma_v(E) \rangle \, , \tag{1.41}$$

where n_ν is the neutrino number density, v the velocity of the particle and $\sigma_v(E)$ the cross section that depends on the energy. Assuming that they only interact through weak force, their cross-section has the form

$$\sigma_\nu \approx \frac{G_F^2 (k_B T_{bg})^2}{\pi (\hbar c)^4} \tag{1.42}$$

where G_F is the Fermi coupling and T_{bg} is the background temperature. We obtain an estimate of the decoupling background temperature equating the interaction rate Γ with the expansion rate of the Universe, given by the Hubble parameter

$$H = \sqrt{\frac{8\pi\rho}{3M_P^2}} \, , \tag{1.43}$$

where $\rho \propto T^4$ is the total energy density dominated by radiation, and $M_P = 1/G^{1/2}$ is the Planck mass. If we approximate the numerical factors to unit, $\Gamma_\nu \approx G_F^2 T^5$ and $H \approx T^2/M_P$ we obtain the decoupling temperature that is around $T_{dec} \simeq 1 \; MeV$ [14]. This corresponds to a redshift

$$1 + z_{dec} \simeq 10^9 \, . \tag{1.44}$$

Because neutrinos cannot have masses much larger than 1 eV, they were ultra-relativistic at decoupling. As a consequence, we use Equation (1.40) to describe the distribution of neutrino momenta even after they become non-relativistic, because this phase-space distribution function remains frozen for all times after neutrino decoupling.

Shortly after neutrino decoupling the photon temperature drops below the electron mass, favouring $e^\pm$ annichilations that heat the photons. Assuming that this entropy transfer did not affect the neutrinos because they were already completely decoupled, the difference between the temperatures of relic photons and neutrinos is $T_\gamma / T_\nu = (11/4)^{1/3} \simeq 1.40102$ [15].

As the Universe expands and the background temperature drops down, the kinetic energy of neutrinos becomes lower than their rest-mass. The redshift when neutrinos become non-relativistic is found equating $m_\nu c^2 \simeq T_{\nu,0}(1+z)$, where the neutrino temperature today is $T_{\nu,0} = 1.95$ KeV and it corresponds to

$$1 + z_{nr} \simeq 1890 \left[\frac{m_\nu}{1 \text{ eV}} \right] . \tag{1.45}$$

1.4.3 Matter perturbations in the presence of massive neutrinos

After the non-relativistic transition, neutrinos contribute to the total energy density of the Universe, given by

$$\Omega_m = \Omega_{cdm} + \Omega_b + \Omega_\nu \tag{1.46}$$

where, in addition to the cold dark matter (CDM) and baryon component, we take into account the energy density Ω_ν associated to the massive neutrino component. We define

$\Omega_c \equiv \Omega_{cdm} + \Omega_b$ as the density corresponding to the sum of CDM and baryon densities. It can be shown that Ω_ν, in units of the critical value ρ_c^0, is proportional to the total neutrino mass as

$$\Omega_\nu = \frac{\rho_\nu}{\rho_c^0} = \frac{\sum m_\nu}{93.14\ h^2\ \mathrm{eV}}\ , \tag{1.47}$$

where the proportionality factor depends on the assumed photon temperature and neutrino to photon temperature ratio [15].

We use a fluid description in order to model CDM, baryons and neutrinos as fluids, whose perturbations expand as waves and obey the conservation of mass and momentum. Given a fluid with average background density $\bar{\rho}$, the density contrast is defined as

$$\delta(\vec{x}) \equiv \frac{\rho(\vec{x})}{\bar{\rho}} - 1\ . \tag{1.48}$$

It describes the deviation from the mean matter density as a function of the point $\vec{x}$.

At perturbation level massive neutrinos have a peculiar effect on matter density fluctuations. We can define the contrast density for neutrino and CDM respectively as $\delta_\nu = \delta\rho_\nu/\bar{\rho_\nu}$ and $\delta_c = \delta\rho_c/\bar{\rho_c}$. Also, considering the total mass density $\rho_m = \bar{\rho_m} + \delta\rho_c + \delta\rho_\nu$, where the total background matter density is $\bar{\rho_m} = \bar{\rho_c} + \bar{\rho_\nu}$ we can write

$$\delta_m = (1 - f_\nu)\delta_c + f_\nu\delta_\nu\ , \tag{1.49}$$

where f_ν is the neutrino fraction, that is defined as the ratio $f_\nu \equiv \Omega_\nu/\Omega_m$.

Neutrinos travel an average distance that depends on their thermal velocity and on their mass. This free-streaming length determines the scale below which neutrinos density perturbations are washed-out, that is

$$\lambda_{FS}(m_\nu, z) \simeq 8.1\frac{H_0(1+z)}{H(z)}\left(\frac{1\ \mathrm{eV}}{m_\nu}\right)\mathrm{h}^{-1}\mathrm{Mpc}\ . \tag{1.50}$$

The physical effect of free streaming is to suppress the growth of neutrino density fluctuations on scale smaller than the free-streaming length. In other words, the neutrinos cannot be confined into regions smaller than the free-streaming length, because their velocity is greater than the escape velocity from gravitational potential wells on those scales.

For particles becoming non-relativistic during matter domination, as it is usually the case for neutrinos, the comoving free streaming length, λ_{FS}/a is actually decreasing in time, and therefore assumes the largest value at the time of the non-relativistic transition [16]. This peculiar distance corresponds to the wave number

$$k_{nr} = k_{FS}(z_{nr}) \simeq 0.018\ \Omega_m^{1/2}\left(\frac{1\ \mathrm{eV}}{m_\nu}\right)^{1/2}\ \mathrm{h\ Mpc^{-1}}\ . \tag{1.51}$$

Free streaming effect damps small-scale neutrino density fluctuations at $k > k_{nr}$. Instead, on scales much larger than the free streaming scale $k < k_{nr}$, the neutrino velocity can be considered as vanishing, and after the non-relativistic transition the neutrino perturbations behave like CDM perturbations.

1.4.4 Effects of the neutrino mass on the matter power spectrum

The matter power spectrum probes the current Large Scale Structure of the Universe. It is defined as the two point correlation function of non-relativistic matter fluctuations in

Fourier space

$$P(k,z) = \langle |\delta_m^2| \rangle \ . \tag{1.52}$$

As a result, because the total matter power spectrum depends on δ_m, it can be written, substituting Equation 1.49 in Equation 1.52 as a sum of three contributions, that are the cold matter power spectrum P_{cc}, the neutrinos power spectrum $P_{\nu\nu}$ and the cross-power spectrum between cold matter and neutrinos $P_{c\nu} =< \delta_c \delta_\nu^* >$, that is

$$P_{mm} = (1-f_\nu)^2 P_{cc} + 2 f_\nu (1-f_\nu) P_{c\nu} + f_\nu^2 P_{\nu\nu} \ . \tag{1.53}$$

Equation (1.53) shows that the neutrino fraction has a direct impact on the total matter power spectrum.

The shape of the matter power spectrum is affected in a scale-dependent way by the free streaming caused by small neutrino masses, for this reason it is the key observable for constraining $\sum m_\nu$ with cosmological methods.

The small initial cosmological perturbations evolve within the linear regime at early times. During matter domination, the smallest cosmological scales start evolving non-linearily, leading to the formation of the structures we see today. In the recent Universe, the largest observable scales are still related to the linear evolution, while other scales can only be understood using non-linear N-body simulations. Below I will show the power spectrum in both linear and non-linear conditions.

The free-streaming effect is visible on the linear power spectrum, calculated solving numerically the evolution of the cosmological perturbations. Indeed, as it is shown in Figure 1.4, the small-scale matter power spectrum is reduced in presence of massive neutrinos at scale $k > k_{nr}$ and its suppression depends on the values of f_ν. In particular, the damping effect is greater for higher values of f_ν, that corresponds to higher values of Ω_ν.

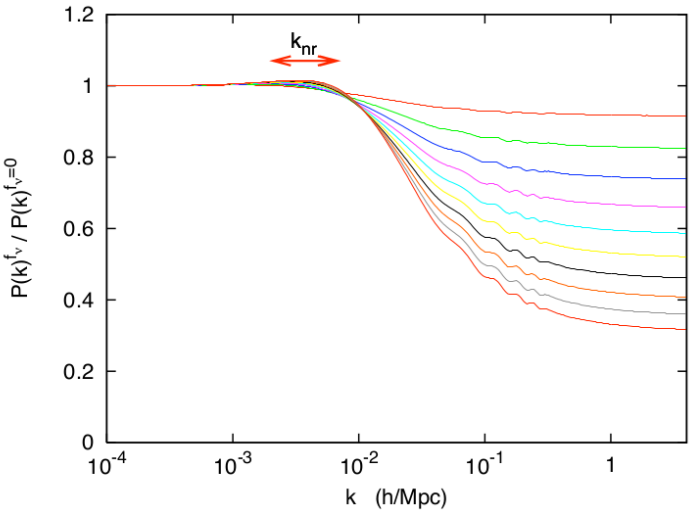

Figure 1.4: Ratio of the matter power spectrum including three degenerate massive neutrinos with density fraction f_ν to that with three massless neutrinos, calculated with CAMB code resolving numerically the evolution of the cosmological perturbations. From top to bottom the curves correspond to $f_\nu = 0.01, 0.02, 0.03, ..., 0.10$. The individual masses m_ν correspond to a range from 0.046 eV to 0.46 eV [16].

Moreover, the neutrino free streaming affects the non-linear matter power spectrum, that is calculated through N-body simulations accounting for a massive neutrino component. I show the results obtained from simulations in the Dark Energy and Massive Neutrino Universe (DEMNUni) project [17] and [18]. The DEMNUni simulations have been performed at the CINECA supercomputing centre, using the tree particle mesh-smoothed particle hydrodynamics (TreePM-SPH) code Gadget-3 [19]. This version of Gadget-3 follows the evolution of CDM and neutrino particles, treating them as two distinct sets of collisionless particles. The simulations are characterised by a comoving volume of $(2\,\mathrm{h}^{-1}\mathrm{Gpc})^3$ filled with 2048^3 dark matter particles with mass $M = 8 \times 10^{10} h^{-1} M_{\odot}$, and, when present, 2048^3 neutrino particles.

Figure 1.5 shows examples of measured power spectra from the DEMNUni simulations [11]. In particular, the upper panel in Figure 1.5 shows the total matter, CDM+b and neutrino power spectra, together with their linear predictions, at redshifts z = 0; 1; 2, in three cosmological scenarios: ΛCDM (massless neutrino case); $(w_0 = -1, w_a = 0)$ and $M_\nu = 0.16$ eV; $(w_0 = -1, w_a = 0)$ and $M_\nu = 0.32$ eV. On top of the suppression predicted in linear theory, the nonlinear power spectrum shows an additional excess of suppression in the power on scales $k \sim 1\ h\ Mpc^{-1}$, which is induced by the presence of neutrinos. On the other hand, the coloured diamonds in the bottom panel in Figure 1.5 show the measured responses, with respect to the ΛCDM case, of the matter power spectra in all the cosmological scenarios covered by the DEMNUni suite.

1.4.5 Effect of the neutrino mass on the halo mass function

The abundance of massive clusters as a function of redshift depends on the neutrino mass value. The DEMNUni simulations individuate locally overdense regions, known as halos, containing gravitationally bound dark matter. The halo mass function, i.e. the number density $n(M)$ of halos of mass between M and M+dM, is expressed as

$$n(M) = f(\sigma, z)\frac{\bar{\rho}_m}{M}\frac{d\ln\sigma^{-1}}{dM}dM\ . \tag{1.54}$$

where most of the cosmological information is encoded in the variance of the matter distribution in the linear regime σ.

In Equation (1.54), the number of halos at a given mass depends on the background density $\bar{\rho}_m$ of the Universe and on the variance σ of the matter density smoothed at a scale $R(M)$, corresponding to a lagrangian sphere containing a mass M with density $\bar{\rho}_m$

$$\sigma(M, z) \equiv \int P_{lin}(k, z)W(kR)k^2 dk\ , \tag{1.55}$$

where $P(k)$ is the linear matter power spectrum as a function of the wavenumber k, and W is the Fourier transform of the real-space top-hat window function with radius R. The function $f(\sigma; z)$ can be fitted to numerical simulations.

The massive neutrino free streaming affects the halo mass functions. Figure 1.6 shows the suppression due to this effect. In particular, the points show measurements from the DEMNUni simulations, at two redshifts $z = 0.5, 1$, in comparison with the theoretical predictions. The suppression is greater for higher values of neutrino total mass $\sum m_\nu$. Because more massive neutrinos become non-relativistic sooner, they suffer the free streaming for longer time from the transition redshift z_{nr}, Equation 1.45. Indeed, since neutrinos become non-relativistic, behaving like CDM, they can contribute to the growth of matter fluctuations. However, during non-relativistic period they cause a

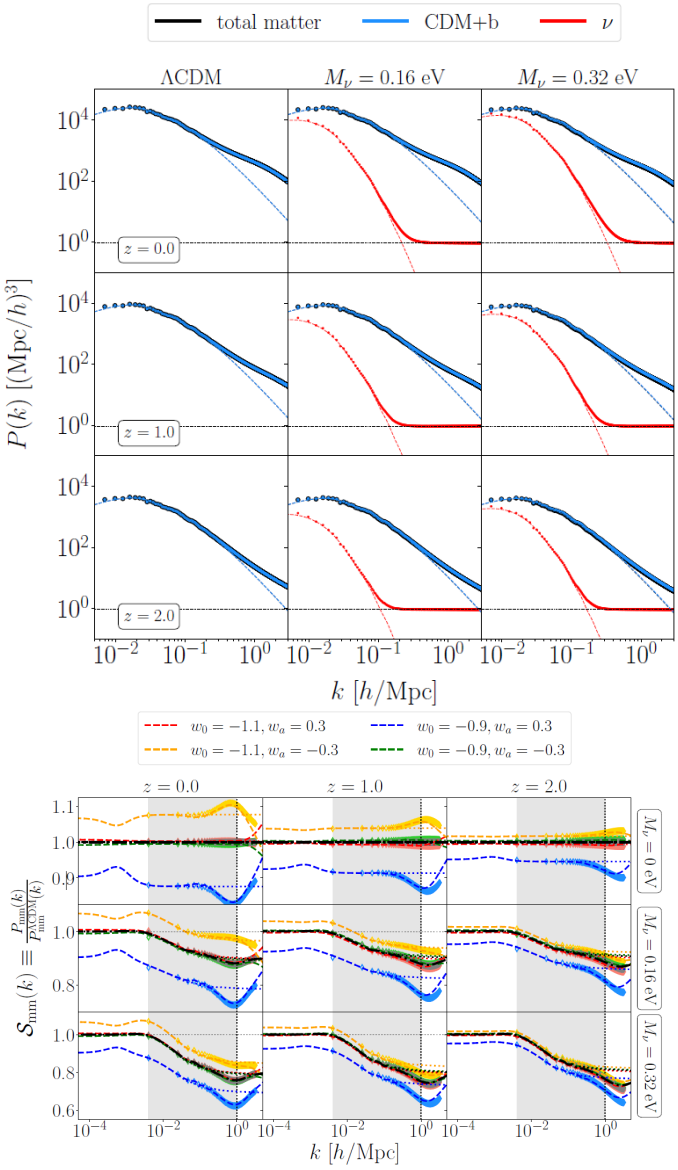

Figure 1.5: Upper panel: Power spectra measured from the DEMNUni simulations: ΛCDM (left column), ($w_0 = -1, w_a = 0$) and $M_\nu = 0.16$ eV (middle column), ($w_0 = -1, w_a = 0$) and $M_\nu = 0.32$ eV (right column). Different rows label redshift z = 0; 1; 2, respectively. Black, blue and red dots label measured total matter, CDM+baryons and neutrino power spectra, while dashed lines of the same colour refer to the corresponding linear spectra at the same redshift. The dotted horizontal line represents the Poisson shot noise for CDM+b and neutrinos [11]. Bottom panel: Response $S_{mm}(k)$ of $P_{mm}(k)$ to the introduction of massive neutrinos and dynamical dark energy at $z = 0$ (left), $z = 1$ (middle) and $z = 2$ (right). Each panel contains the prediction for five different cosmologies: the top row contains the simulations with vanishing neutrino mass, while the middle and bottom rows contain simulations with $M_\nu = 0.16, 0.32$ eV, respectively [11].

slight damping of the growth of fluctuations at small scale ($<< \lambda_{FS}$) due to their thermal speed.

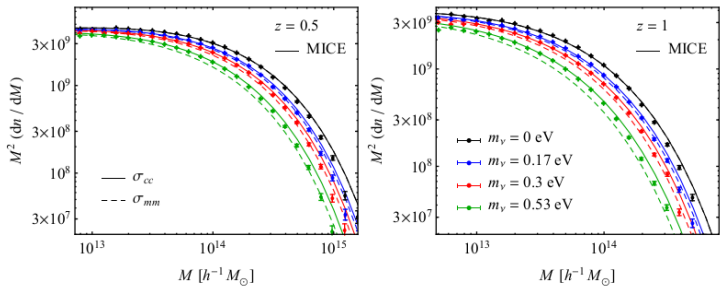

Figure 1.6: Massive neutrino effects on the mass function of dark matter halos. Data points show the mass function measured from the DEMNUni simulations for $\sum m_\nu = 0, 0.17, 0.3, 0.53$ eV. Errors are derived from the assumption of a Poisson distribution for each bin. Theoretical predictions are obtained as a function of $\sigma_{cc}(M)$ (continuous curves) and $\sigma_{mm}(M)$ (dashed curves). Different panels correspond to redshifts $z = 0.5, 1$ [17].

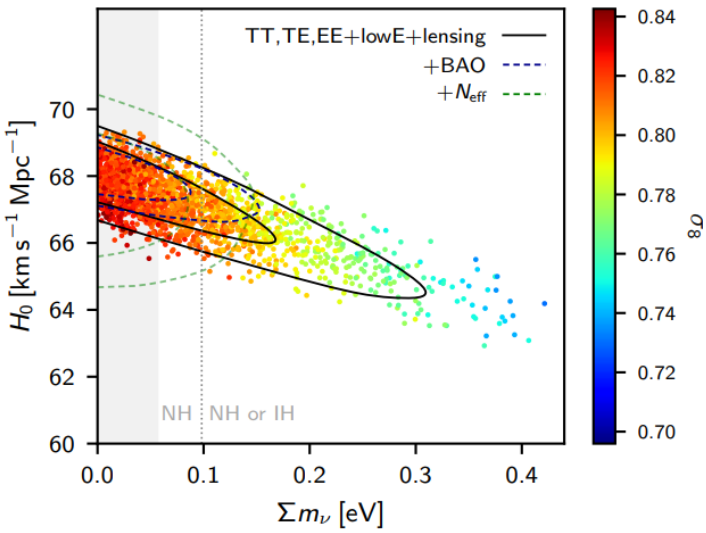

Figure 1.7: $\sum m_\nu - H_0$ plane with the constraints from Planck 2018 measurements of TT, TE, EE + lowE + lensing (solid black lines) and the joint constraint from Planck TT, TE, EE + lowE + lensing combined with BAO data (dashed black lines). Points show samples from Planck TT, TE, EE + lowE chains, colour-coded by σ_8 [4].

1.4.6 Current constraints on the neutrino mass

Recent constraints of the total mass of neutrinos are performed by the full-mission Planck measurements of the cosmic microwave background (CMB) anisotropies, combining information from the temperature and polarization maps and the lensing reconstruction.

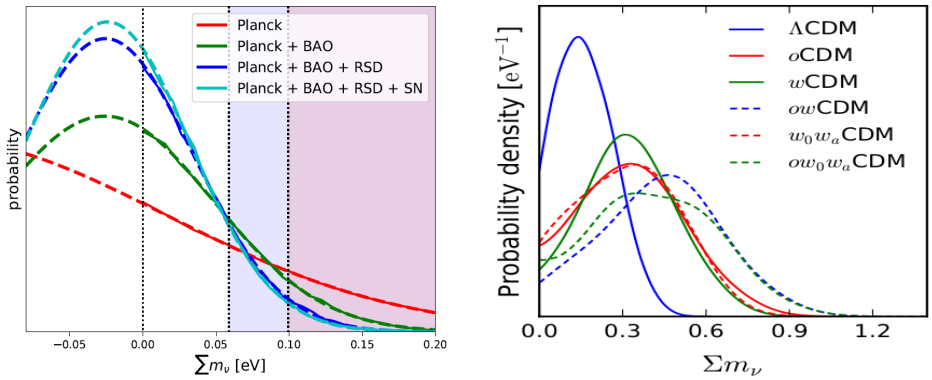

Figure 1.8: LEFT: Posterior for sum of neutrino masses for selected data with a νCDM cosmology, from the combination of Planck CMB measurements with BAO measurements from SDSS, SDSS-II, BOSS, and eBOSS. Dashed curves show the implied Gaussian fits. Shaded regions correspond to lower limits on normal and inverted hiearchies [20]. RIGHT: Probability density for neutrino total mass $\sum m_\nu$ from full-likelihood-analysis from the joint data set of Baryonic Acoustic Oscillation and CMB measurement, at different cosmological models [7].

The current constraint of neutrino mass, considering a neutrinos degenerate mass spectrum, from the CMB power spectra is limited by the geometrical degeneracy. Combining Barionic Acustic Oscillation (BAO) data to the Planck likelihood significantly tightens the neutrino mass constraints [6]. Without CMB lensing Planck 2018 constraints of neutrinos total mass are

$$\sum m_\nu < 0.16eV \quad \text{(95 \%, Planck TT+lowE+BAO)},$$

$$\sum m_\nu < 0.13eV \quad \text{(95 \%, Planck TT,TE,EE+lowE+BAO)},$$

and combining also the lensing measurements the limits further tighten to

$$\sum m_\nu < 0.13eV \quad \text{(95 \%, Planck TT+lowE+BAO)},$$

$$\sum m_\nu < 0.12eV \quad \text{(95 \%, Planck TT,TE,EE+lowE+BAO)}.$$

The constraints from Planck 2018 are indicated in Figure 1.7 in the $\sum m_\nu - H_0$ plane. Increasing the neutrino mass leads to lower values of H_0, and it aggravates the tension with the distance-ladder determination [21].

Moreover, the combination of data from the Sloan Digital Sky Survey (SDSS - SDSS-II), and Baryon Oscillation Spectroscopic Survey (BOSS - eBOSS), offers independent measurements of baryon acoustic oscillation (BAO) measurements. The results of SDSS BAO and RSD, Planck, Pantheon Type Ia supernovae (SNe Ia), and DES weak lensing give a constraint on the upper limit on the sum of neutrino masses at $M_\nu < 0.111$ eV (95% confidence) [20], derived from Markov chains, containing a prior $M_\nu > 0$. The posterior distributions for four selected data combinations are plotted in the left panel in Figure 1.8.

However, if we consider the combination of massive neutrinos with dynamical dark energy the maximum likelihood value is at higher neutrino mass values. The right panel in Figure 1.8 shows the constraint calculated from the joint data sets of Baryon Oscillation

Spectroscopic Survey (BOSS) galaxy sample and Planck cosmic microwave background (CMB) measurement [7]. Assuming a cosmological model with dynamical dark energy, i.e. a $w_0 w_a CDM$ model, the value of neutrino mass that maximises the likelihood distribution is $\sum m_\nu = 0.32^{+0.18}_{-0.20}$ eV.

CHAPTER 2

Large scale structures: theory and observations

The visible Universe is highly inhomogeneous, it is composed of bound structures on scales of isolated galaxies, while on larger scales it is filled by groups, clusters and superclusters of galaxies separated by giant voids. Such voids have number densities of galaxies so small that can be considered almost empty [22]. The galaxies represent the building blocks of the Universe which define its large-scale structure. Figure 2.1 illustrates the distribution of the local galaxies detected by the Sloan Digital Sky Survey (SDSS) [1].

The structures, which form from gravitational instability of early density perturbations at small scales, are modelled by the theory of structure formation. In particular, these density perturbations are created as a result of small quantum fluctuations present in the early Universe, according to the theory of inflation. During inflation, these small overdensities are stretched to scales larger than the radius of the horizon. As a results, the structure formations are driven by gravitational instabilities, which in turn conduct the evolution of the resulting density field. As soon as the baryonic component has completely decoupled from the radiation, it begins to fall into the overdensities of dark matter, which in the meantime have accumulated forming the initial skeleton of halos and voids. The large-scale structure of the Universe is evidence of these gravitational processes. Another proof is represented by the presence of baryonic structures such as galaxies and stars.

2.1 Galaxy clustering

The spatial distribution of the galaxies is described with statistical methods, assuming the galactic field as a stochastic process that takes place in a three-dimensional space. Statistical methods, which are used to measure the spatial correlations between the internal elements, allow to fully characterize this random field.

The clustering properties of galaxies on a wide range of scales are described with statistical methods. The simplest approach is to use two-point correlation functions (2PCF) in Equation 1.31, which is the autocovariance of the density field of a generic proxy for the matter density field, represented by matter particles, haloes, galaxies, clusters. The 2PCF represents the excess probability of finding pairs of galaxies in a given separation r with respect to a random distribution. In the latter case $\xi(r) = 0$ by definition. In Equation 1.31 the argument of the 2PCF is only the modulus r of the separation vector $\mathbf{r}$. This is due to the fact that the Universe is assumed to be a homogeneous and isotropic random field.

[1] Image from http://www.sdss3.org/science/

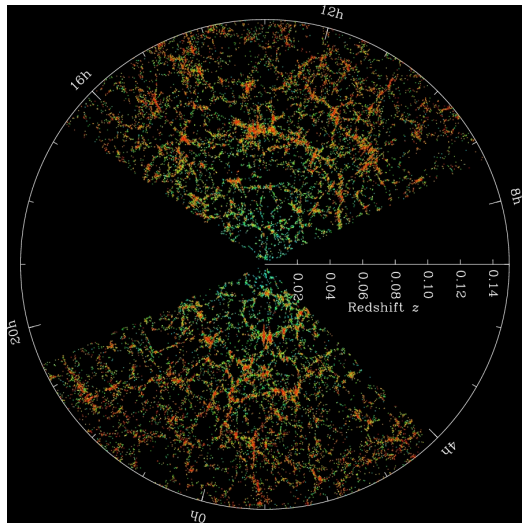

Figure 2.1: SDSS distribution of local galaxies

Many estimators have been implemented over the past years, in order to measure the correlation function from the present galaxy survey. The simplest method is the natural estimator, which it comes out directly from the definition of the correlation function. It expresses the 2PCF as

$$\xi_N(r) = \frac{GG(r)}{RR(r)} - 1 \,, \tag{2.1}$$

where GG(r) is the number of galaxy pairs separated by distance between $r - \Delta r$ and $r + \Delta r$. Instead, RR(r) is the expected number of pairs if galaxies were randomly distributed in space, therefore for a Poissonian distribution.

The most used estimators currently have greater accuracy and less dependence on the random samples used to calculate $\xi(r)$. Each of these estimators features the cross pairs $GR(r)$, thus reducing the dependency on the particular random sample used for the estimation of $\xi(r)$. One of the most used estimator is proposed by Landy-Szalay [23]:

$$\xi_{LS}(r) = \frac{GG(r) - 2GR(r) + RR(r)}{RR(r)} \tag{2.2}$$

It minimizes the variance of the recovered correlation function nearly to the Poisson limit.

The two-point correlation function shows the variation of the clustering amplitude of galaxies as a function of the comoving/physical scale. Therefore, higher values of $\xi(r)$ correspond to a greater probability of finding pairs and consequently to a greater intensity of the clustering. The correlation function is described with a power law on scales below $10\ h^{-1}$Mpc

$$\xi(r) = \left(\frac{r}{r_0}\right)^{-\gamma} \tag{2.3}$$

with spectral index $\gamma \sim 2$ and correlation length $r_0 \approx 5\ h^{-1}$Mpc.

However, we need to take into account how galaxies, which are the real observable, trace the matter density field. The density field of galaxies is a non-local, non-linear

and stochastic function of the underlying matter density. The galaxy bias is due to the effect of many physical processes, mainly including the physics of galaxy formation. For this reason, the baryon distribution is different from the dark matter one. Indeed, the galaxies are concentrated in the peaks of the matter distribution.

On large scale, the galaxy density contrast δ_g is assumed to be a linear function of the matter density contrast δ_m. Thus, the linear bias b is defined as

$$\delta_g(x) = b\delta_m(x) \ . \tag{2.4}$$

The galaxy bias strongly depends on the intrinsic characteristics of the sample (i.e. the luminosity, colour, morphology and age), because it represents how a particular galaxy sample is tracing the underlying matter distribution. Accordingly, taking into account Equation 1.31 the linear bias can be expressed as a function of the two-point statistics (both the correlation function and the power spectrum) as follows:

$$b = \left(\frac{\xi_g}{\xi_m}\right)^{1/2} = \left(\frac{P_g}{P_m}\right)^{1/2} \ , \tag{2.5}$$

where the subscripts g and m stand for galaxies and matter respectively.

Moreover, the bias can be directly measured on linear scales, where this ratio is approximately constant.

The measurement of redshifts of galaxies allows to reconstruct their spatial distribution, assuming Hubble's law. However, the radial distances inferred from the redshift differ from galaxy true positions, because of their peculiar velocities. The latter properties are generated from the gravitational interactions with the local environment where the galaxies are located. The effect of peculiar velocity to the measured redshift is a Doppler shift, which is added to the isotropic Hubble expansion [24]:

$$z_{obs} = z_{cosmo} + z_{pec} \tag{2.6}$$

This effect alters the distribution of galaxies along the line of sight. The displacement along the line of sight leads to redshift distortions in the pattern of clustering of galaxies in redshift-space, compared to real-space one, obtained using only the cosmological contribution z_{cosmo}.

The redshift-space distortions contain information about the dynamics of galaxies and as a results about the gravitational field, where they are embedded.

Indeed, the peculiar velocities are associated to the gravitational growth of inhomogeneities, which can be described by the logarithmic growth rate f of density perturbations δ:

$$f \equiv \frac{d\ln\delta}{d\ln a} \tag{2.7}$$

The growth rate can be well approximated, for many theories of gravity, by the following empirical relation

$$f(z) = [\Omega(z)]^{\gamma} \ , \tag{2.8}$$

derived from fluctuations in the linear regime and in the growing mode. For Einstein gravity, $\gamma = 0.55$.

The apparent position of galaxies is modified by the Doppler effect of their peculiar velocity v. For this reason, the redshift-space position s of galaxies located at r becomes

$$s = r + \frac{v_{\parallel}(r)\widehat{e_{\parallel}}}{aH(a)} \,, \tag{2.9}$$

where a is the scale factor, $H(a)$ the expansion rate and $v_{\parallel} = v \cdot \widehat{e_{\parallel}}$ the component of the galaxy peculiar velocity along the line of sight.

Assuming a plane-parallel approximation, therefore the redshift-space power spectrum can be written as [25]

$$P^s_{k,\mu} = \int \frac{d^2\mathbf{r}}{(2\pi)^3} e^{-ik\cdot r} \left\langle e^{-k\mu f \Delta u_{\parallel}} \times \left[\delta(\mathbf{x}) + f\partial_{\parallel} u_{\parallel}\right] \left[\delta(\,\mathbf{x'}\,) + f\partial_{\parallel} u_{\parallel}\right] \right\rangle \,, \tag{2.10}$$

with $\Delta u_{\parallel} = u_{\parallel}(x) - u_{\parallel}(x')$ and $r = x - x'$. Equation 2.10 expresses the anisotropies produced by peculiar velocities on the clustering of matter particles at each separation.

It is possible to identify two main regimes within which distortions occur. At large separations, matter mainly has coherent flow towards overdense regions, therefore velocities have the effect to enhance the clustering. In this linear regime, the density and velocity fields are strictly correlated. In particular, the velocity field is mainly irrotational, thus can be described by its divergence $\theta(x) = \nabla \cdot u(x)$ The resulting motions produce a systematic distortion of the large-scale distribution along the line of sight. This 'Kaiser effect' (Kaiser 1987) is basically produced by the terms inside the square brackets in Equation 2.10.

On the contrary, at typical scales of haloes, galaxy orbits across each other. Thus, random dispersion in velocities no preferred direction are generated at a given point. The resulting observed clustering amplitude is smaller than the true one on small scales, because structures appear stretched along the line of sight. This effect is the so-called 'Fingers of God' (Jackson 1972) and it is mainly generated by the exponential pre-factor in Equation 2.10 involving the moment generating function of the velocity field.

It is difficult to use Equation 2.10 in this form, because there is not an analytic formula to compute the ensemble average term inside the integral. To this aim, the approximate form, implemented by Kaiser 1987, can provide a way to estimate the redshift-space power spectrum from galaxy surveys. Considering the linear theory approximation in the kaiser model the exponential pre-factor is suppressed, because its impact on the largest scales is negligible and $\theta \propto \delta$. Moreover, if the bias relation between the galaxies and the matter is assumed to be linear, es Equation 2.4 it follows that

$$P^s(k,\mu) = \left(1 + \beta\mu^2\right)^2 b^2 P_{\delta\delta}(k) \tag{2.11}$$

where $P_{\delta\delta} = P$ is the linear real-space matter power spectrum and b is the linear galaxy bias.

Hamilton (1992) [24] has translated the Kaiser formalism in the linear regime from Fourier to configuration space. In this case, the redshift-space two-point correlation function can be written as

$$\xi^S(s,\mu) = \xi_0(s)\mathcal{L}_0(\mu) + \xi_2(s)\mathcal{L}_2(\mu) + \xi_4(s)\mathcal{L}_4(\mu) \tag{2.12}$$

where $\mu = \widehat{r} \cdot \widehat{z}$ is the cosine of the angle in real space between the pair separation $\vec{r}$ and the line of sight. Equation 2.12 is actually an expansion in spherical harmonics and each term represents the n-th Legendre polynomial $\mathcal{L}_n$, multiplied by the correspondent multipole moment ξ_n:

$$\xi_0^S(s,\mu) = \left(1 + \frac{2}{3}\beta + \frac{1}{5}\beta^2\right)\xi(r) \tag{2.13}$$

$$\xi_2^S(s,\mu) = \left(\frac{4}{3}\beta + \frac{4}{7}\beta^2\right)\left[\xi(s) - \frac{3J_3(s)}{s^3}\right] \tag{2.14}$$

$$\xi_4^S(s,\mu) = \frac{8}{35}\beta^2\left[\xi(s) + \frac{15}{2}\frac{J_3(s)}{s^3} - \frac{35}{2}\frac{J_5(s)}{s^5}\right], \tag{2.15}$$

where $\xi(s = r)$ is the real-space correlation function and J_l is defined as its integral functions:

$$J_l(x) = \int_0^x \xi(y) y^{l-1} dy\ . \tag{2.16}$$

Figure 2.2 shows the monopole and the quadrupole of the clustering measurements from the BOSS survey. The left panels represents the measurements of the power spectrum and the left side the results of the correlation functions. The sharp peak in the monopole of the correlation function $\xi_0(s)$ at scale $s \sim 100\ h^{-1}$ Mpc shows a turnaround, that corresponds to the horizon scale at the time of the equivalence between radiation and matter. At this epoch, matter begins to dominate the energetic content of the Universe, consequently baryons starts to fall within the potential wells created by the dark matter until that time. However, before this period, baryons are gravitationally attracted by dark matter, but simultaneously are electromagnetically coupled to photons, therefore they feel also the pressure created by photons. This combined effect causes baryonic matter to undergo oscillations, called baryons acoustic oscillations (BAO).

Figure 2.3 shows the measurement of the anisotropic correlation function $\xi(r_p;\pi)$ obtained from the VIPERS survey at $0.5 < z < 0.7$ and $0.7 < z < 1.2$ [27]. The VIPERS survey covers an overall area of 23.5 deg^2 over the W1 and W4 fields of the Canada-France-Hawaii Telescope Legacy Survey Wide (CFHTLS-Wide). These two different fields were covered using the VIMOS multiobject spectrograph with a mosaic of 288 pointings, 192 in W1 and 96 in W4 respectively. A bin size $\Delta_s = 0.5\ h^{-1}$ Mpc has been used in both parallel and orthogonal to the line of sight directions. The results coming from the two VIPERS fields W1 and W4 are combined by summing up the pair counts in each bin of separation and normalising for the total number of objects.

Furthermore, Figure 2.4 shows the measurements and best-fitting model of the monopole and quadrupole correlation functions, obtained in the two considered redshift bins [27]. A TNS model [28], with a Lorentzian damping and Gaussian error damping, is adopted to model the RSD analysis of the VIPERS data. This model is used because it is able to describe the RSD down to the quasi-linear regime. Indeed, it takes better into account the non-linear coupling between the density and the velocity field.

The redshift-space distortions are a useful tool for obtaining information about the dynamics of galaxies. Indeed, the measurements of linear RSD from galaxy redshift surveys constrain the linear redshift distortion parameter $\beta = f/b$, which is the b is an unknown linear galaxy bias parameter. Because of the linear bias is defined as the ratio $b = \sigma_8^{gal}/\sigma_8$, the measurements of $\beta\sigma_8^{gal}$ yield an estimate of a quantity that purely concerns dark matter: $f\sigma_8$, with σ_8 being the rms linear matter fluctuations within spheres of radius $8\ h^{-1}$ Mpc.

The measurements of the growth rate of structure times σ_8 obtained with the VIPERS survey at two different redshift values are

$$f\sigma_8(z = 0.6) = 0.55 \pm 0.12 \tag{2.17}$$

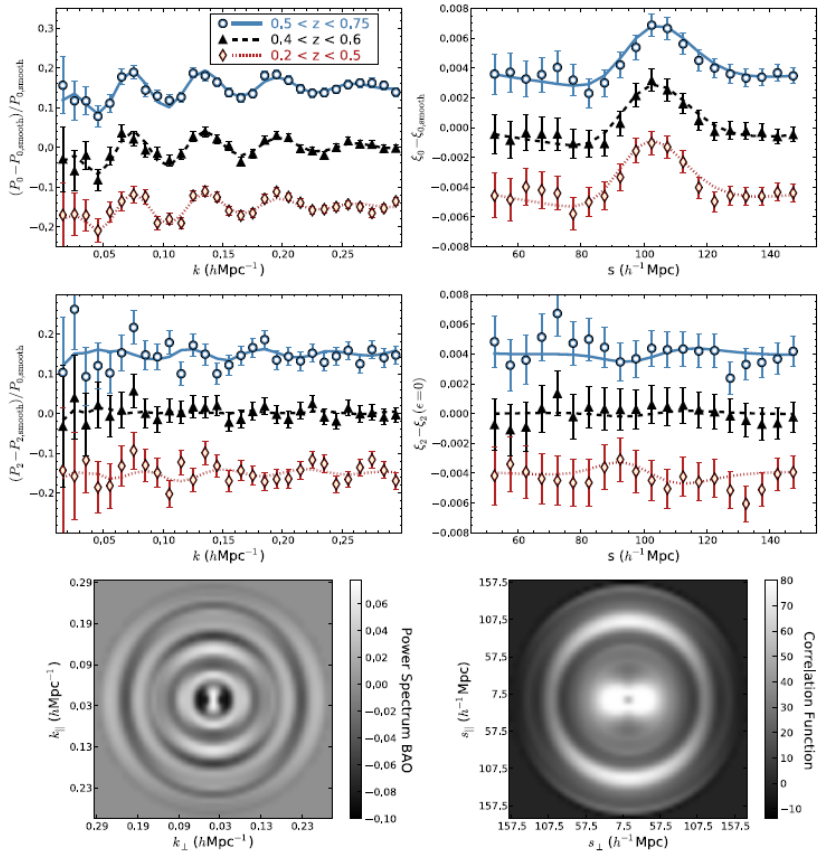

Figure 2.2: BAO signals in the measured post-reconstruction power spectrum (left panels) and correlation function (right panels) and predictions of the best-fit BAO models (curves) [26].

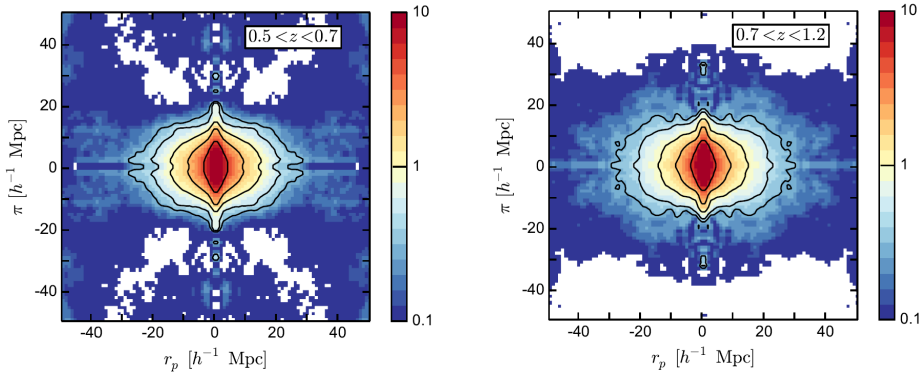

Figure 2.3: Final measurements of the anisotropic redshift-space correlation function, $\xi(r_p;\pi)$ from the final data of the VIPERS survey, within the two redshift ranges indicated by the labels. Solid contours correspond to iso-correlation levels of 0.3, 0.5, 1, 2, 5. [27]

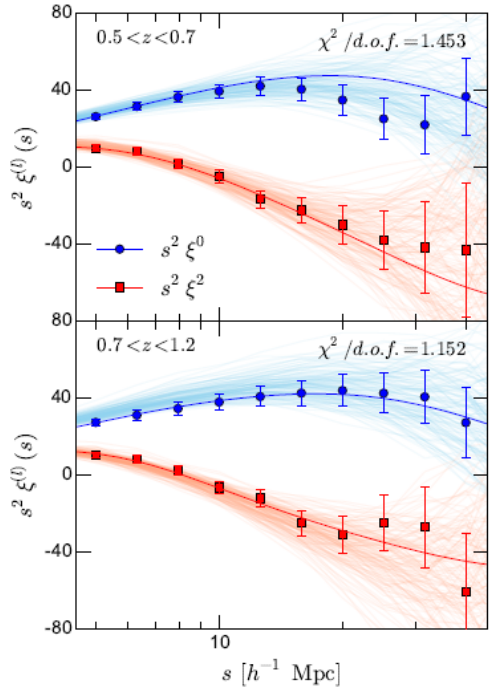

Figure 2.4: Monopole and quadrupole of $\xi(r_p;\pi)$ for the two redshift subsample of the final VIPERS dataset (solid points), together with the final best-fitting curves obtained using the TNS model. The likelihood computation has used data down to $s_{min} = 5h^{-1}$ Mpc, as indicated by the tests. Error bars are $1-\sigma$ deviations, and correspond to the dispersion of the mock measurements. Each of these is also shown as a faint background line. [27]

$$f\sigma_8(z = 0.86) = 0.40 \pm 0.11 \tag{2.18}$$

These values are compared in the left panel in Figure 2.5 with many measurements, including results from other surveys, the VIPERS earlier PDR-1 dataset, and parallel works which analyse using complementary techniques similar subsets of the VIPERS PDR-2 data-set. The latter results from PDR-2 data include measurements obtained from the combination of RSD with galaxy-galaxy lensing [29] or using the void-galaxy cross-correlation [30]. As shown in the left panel in Figure 2.5, the values measured by these different techniques on the same VIPERS data and also from other surveys at similar redshifts are all compatible within $1-\sigma$ error bars and agree with the predictions of a ΛCDM model governed by Einstein gravity, indicated with the shaded gray area.

The right panel in Figure 2.5 indicates the measurements of the growth factor, quantified by $f\sigma_8(z)$, from redshift-space distortions (RSD), using the anisotropic galaxy clustering data set of the pre-reconstruction density field from the Baryon Oscillation Spectroscopic Survey [26], part of the Sloan Digital Sky Survey III. The combined galaxy sample consists in 1.2 million massive galaxies over an effective area of 9329 deg^2 and volume of 18.7Gpc^3, divided into three partially overlapping redshift slices centred at effective redshifts 0.38, 0.51, and 0.61. The RSD measurements of $f\sigma_8$, at 6% precision, are consistent with the spatially flat cold dark matter model with a cosmological constant (ΛCDM). Also, the measurements from other surveys are consistent with those

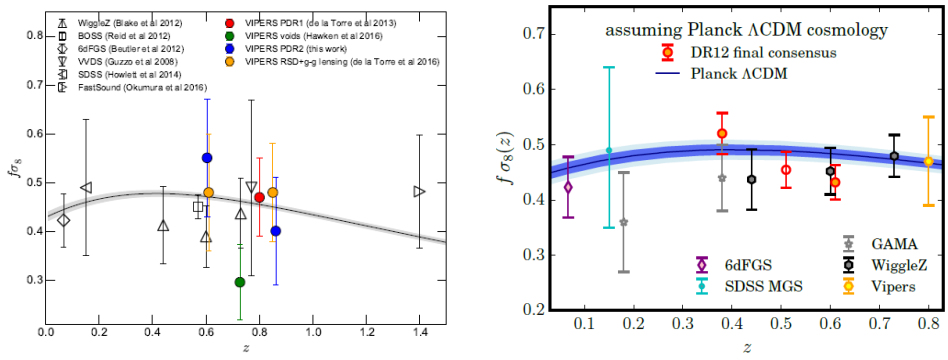

Figure 2.5: Comparison of $f\sigma 8$ as a function of redshift. LEFT: VIPERS results [27] together with many recent measurements. The previous results from 2dFGRS, 2SLAQ, VVDS, SDSS LRG, WiggleZ, BOSS, 6dFGS and FastSound surveys are shown with the different symbols. The solid curve and associated error correspond to the prediction for General Relativity in a ΛCDM model set to Planck 2015 cosmological parameters [3]. RIGHT: $f\sigma_8(z)$ results from the BOSS survey are compared with the measurements of the 2dfGRS and 6dFGS, the GAMA, the WiggleZ, the VVDS, and the VIPERS surveys, as well as the measurements from the SDSS-I and -II main galaxy sample and the SDSS-II LRG sample. The conditional constraints on $f\sigma_8$ are plotted assuming a Planck ΛCDM background cosmology. The growth rate measurements from BOSS is one of the best evidence of the validity of General Relativity in large scales [26].

from BOSS within their estimated errors.

2.2 Cosmological simulations

The evolution of dark matter, which drives the formation of galaxies, is described by the combination of the collisionless Boltzmann equation

$$\frac{df}{dt} = 0 \tag{2.19}$$

and the Poisson's equation

$$\nabla^2 \Phi = 4\pi G \int f dv \, . \tag{2.20}$$

The first Equation 2.19 shows the evolution of the distribution function $f = f(r, v, t)$ of the dark matter component under the gravitational effect of a potential Φ, with position r and velocity v of each DM particle at time t. The DM fluid feels its own self-gravitation through the Poisson's Equation 2.20.

These two equations have to be solved in an Universe with an expanding background described by the Friedmann equations, which are derived from the field equations of general relativity, as seen in Chapter 1. However, the equations cannot be solved with numerical methods that use standard methods for partial differential equations, because of the high dimensionality of the collisionless Boltzmann equation.

Thus, the growth of structure in a ΛCDM scenario has been studied and characterized especially by new numerical techniques, developed over the past decades. Indeed, the numerical simulations tackle the issue to make very detailed predictions of the density perturbations in the non-linear regime, which cannot be studied using analytical techniques.

The N-body method is the most popular numerical technique, which makes it possible to solve the Boltzmann and Poisson's equations. In particular, through N-body simulations the differential equations are integrated defining the particle motions in gravity. N-body simulations enable to solve the evolution of a given CDM distribution, due to gravity, up to very small scales, which can be up to 1 or a few h^{-1} Mpc ($k \simeq 1{-}5hMpc^{-1}$), depending on the resolution of the simulation.

The expanding Universe is represented as a cubic box, with a size at least equal to the scale at which the Universe becomes homogeneous, so as to represent the entire Universe with a fair sample. Indeed, the box contains a large amount of point masses of particles interacting through their mutual gravity. Usually the cube is treated with periodic boundary conditions in all directions, in order to sum the mutual N-body forces using computational techniques with Fourier methods. Also, the periodic boundary conditions allow to mimic the homogeneity and isotropy of the matter distribution of the Universe at large-scale, thus satisfying the cosmological principle.

There are currently numerous numerical techniques, differing primarily only in how the forces on each particle are calculated.

First, the simplest method consists in calculating the nonlinear evolution of a cosmological fluid, which is represented as a discrete set of particles. This method, called particle-particle calculations or PP, estimates the sum of the particle pairwise interactions with each other in order to calculate Newtonian forces. In particular, using a small time step, the estimation of the resulting acceleration is useful for updating the velocity and position of the particle. Therefore the interparticle forces are recalculated starting from the new positions and so on.

These techniques represent the particle configuration with a fluid approximation. Furthermore, since the Newtonian gravitational force between two particles grows as the particles get closer to each other, a very small time step must be chosen in order to resolve the large induced velocity changes. Since a very small time step would consume enormous CPU time resources and the formally divergent force terms when particles are arbitrarily close to each other cannot be handled by computers, each particle is treated as a body extended, rather than a point mass, in order to reduce computational resources.

Thus, in order to avoid infinite forces at zero separations, the Newtonian force between the particles is modified according the following Equation:

$$F_{ij} = \frac{Gm^2(x_j - x_i)}{(\epsilon^2 + |x_i - x_j|^2)^{3/2}} \,, \tag{2.21}$$

where the particles are at positions x_i and x_j and assuming that they all have the same mass m. The parameter ϵ in Equation 2.21, called softening length, has the function of suppressing the forces of two bodies on small scales. This is equivalent to replacing point masses with extended bodies having a dimension of the order ϵ.

Considering that the simulations contains N particles, the direct summation of all the $(N-1)$ interactions to compute the acceleration of each particle requires a total of $N(N-1)/2$ evaluations of Equation 2.21 at each time-step. For this reason, the main limitation of this method is the slowness of the computation, which requires a time scaling as N^2. As a consequence, the method of direct summation is practical to use for a maximum number of particles of order 10^4, a number not large enough to realistically simulate the formation of large-scale structure.

Moreover, a second method, called particle-mesh, is useful to improve the direct N-body summation in order to compute the forces between the particles. The latter quantities are evaluated by assigning mass points to a regular grid, on which the Poisson's

equation is solved. Basically, the density field is computed on the grid, then the potential is calculated by summing over the mesh. The PM method allow to compute the resulting forces at the grid points and the latter are interpolated to find forces on each particles.

In particular, considering a grid with periodic boundary conditions the Fast Fourier Transform (FFT) methods can be used to easily recover the potential, with the advantage of considerably speeding up the calculation of the forces between the particles. Indeed, an FFT is basically of order $N \log N$ in the number of grid points, as a results this can be a significant advantage for large N over the direct particle–particle summation method.

Furthermore, a hierarchical subdivision procedure, called 'tree-code', represents a useful method for increase the force resolution of a particle code, while keeping computational resources within a reasonable time limit.

This technique considers distant clumps of particles as a single massive pseudo-particles. A mesh is divided by the algorithm into many cells, so that each containing more than one particle is in turn divided into 2^3 sub-cells. As a next step, if the obtained subcells contain more than one particle they are subdivided again. The distant forces are simply treated using the coarse-grained distribution contained in the top level of the tree, while the short-grained forces radius consider the finer grid.

The fundamental disadvantage of these methods is the requirement of a huge memory resource, even if they have the advantage of requiring much less computational time than other particle-mesh techniques with the same resolution.

For this reason, the output data of N-body simulations are saved only for some predetermined timesteps, because of the huge amount of storage of the output data needed by simulations. The output data at a fixed time-step, or equivalently at a fixed redshift, is the so called snapshot. N-body simulations produce, as a first step, raw data of the positions of each CDM particle as a function of time. Next, it is necessary to map this raw data into real objects using data analysis tools, so that the simulations can mimic the structures of the real Universe.

Therefore, the tools, called 'halo-finder', have the aim of searching for the density field of dark matter within the simulations in order to identify very dense gravitationally bound systems, which are then labelled as dark matter haloes. One of the simplest methods, called 'friends-of-friends', allows to find gravitationally bonded particles within a defined bond length (Davis et al., 1985). Other more complex methods, implemented later, are for example SUBFIND [31], [32] and ROCKSTAR [33].

Moreover, when the collision particles as gas are taken into account the hydrodynamical simulations are implemented, as discussed in Section 3.3.

CHAPTER 3

The connection between galaxies and dark matter haloes

During inflation period, fluctuations in the density of matter increase, which once formed evolve with a decreasing amplitude in accordance with the expansion of the Universe. The gravitational collapse of a dark matter region, described by the density field $\delta(x)$, begins when the matter perturbation reaches an overdensity greater than the background density of the Universe. According to this model, called hierarchical structure formation scenario, the region contained within the excess density stops following the expansion of the Universe and begins to collapse forming a gravitationally self-bound structure [22]. The gravitational collapse of dark matter is described in the simplest hypothesis of a uniform sphere slightly denser than the background environment. Despite this, the collapsing structures are not spherically symmetrical, the collapse occurs when a condition of virial equilibrium is reached, in which the total kinetic energy of the system is linked to the gravitational potential energy according to the following equation:

$$\sum_{i=i}^{N} m_i \cdot \dot{r}_i^2 = -\sum_{i=1}^{N} F_i \cdot r_i \tag{3.1}$$

The right side of Equation 3.1 is the total potential energy for the system, which takes the form GM^2/r, in the case of a uniform sphere of radius r and $M = \sum_i m_i$, described by only the gravitational force, while the left side is twice the total kinetic energy of a system.

The equilibrium state of structures that become virial is described by the virial theorem. Gravity drives the formation and growth of structures, so dark matter dominates the gravitational potential. Haloes are the centers of dark matter overdensities [34]. Once haloes are formed, they grow by merging and accreting smaller systems to form larger and larger haloes, moving down with redshift.

In the standard cold dark matter paradigm, the formation and growth of galaxies is connected to the growth of the halo in which they form. Galaxies form by the cooling and condensation of gas in the centres of the potential wells of extended virialised dark matter haloes.

According to modern models of structure formation, a dark matter halo is the basic unit in which the matter collapses. It is a collapsed region that is decoupled from the Hubble expansion. It contains gravitationally bound matter. In numerical simulations the halo mass is defined in different ways. The "virial" mass of the halo M_{vir} is the mass defined by the virial theorem, Equation 3.1. Also, the halo mass can be defined specifying a given overdensity. M_Δ is the mass contained in R_Δ, which is the radius inside which the mean density ρ is Δ times the critical ρ_c or the background density ρ_b of the Universe:

$$M_\Delta = \frac{4\pi}{3} R_\Delta^3 \Delta \rho_c \, . \tag{3.2}$$

The value of Δ corresponds to the overdensity predicted for a virialised region that has undergone spherical collapse. The definition of Δ varies in the literature, in this work we consider $\Delta = 200b, 200c, 500c, 1000c, 2500c$.

A single dark matter halo may contain multiple virialised clumps of dark matter bound together by gravity, known as subhaloes. They are smaller than the host halo and they orbit within the gravitational potential of the host halo.

There are two basic approaches to connect galaxies to haloes. The first one is an empirical method, that uses data to constraint a specific set of parameters describing the connection as a function of time. These models connect observations from galaxy survey to the predictions of the properties and evolution of dark matter haloes in cosmological simulation. The predictions are made with gravity only N-body simulations and comprehend a number of subclasses of models (such as halo occupation distribution HOD, subhalo abundance matching SHAM, or even semi-analytic models SAM). The second method is a physical model, that directly simulates the physics of galaxy formation. For example, hydrodynamical simulations can simulate both dark matter haloes and the gas; physical processes involved in galaxy formation, such as star formation and various kinds of feedback, can therefore be implemented at the level of subgrid physics.

A schematic summary of these approaches to the galaxy–halo connection is given in Figure 3.1, which outlines the key elements of different methods. These modeling approaches can be summarized in a in a continuous pattern: starting from the left side and moving to the right side there are increasingly less physical models, that have flexibility to constrain the unknown aspects of the galaxy–halo connection directly with data, but the models become also less predictive and less directly connected to the physical prescriptions. Moreover, methods toward the right side also require significantly less computational resources than the more physical approaches [35].

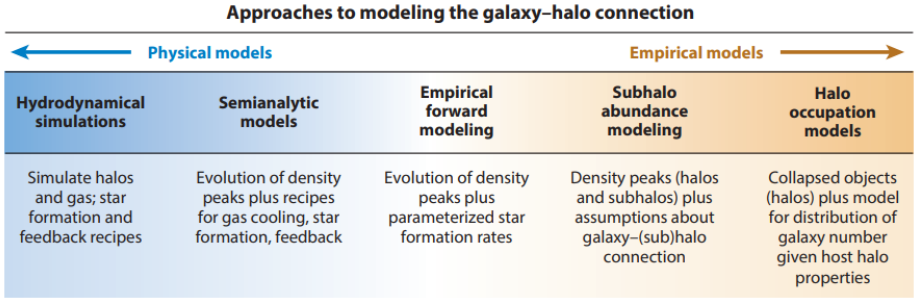

Figure 3.1: The gradient color scheme highlights the most significant assumptions of various method to modeling the galaxy–halo connection. The models are listed in a continuous list from left to right varying gradually from the most physical and predictive method, that makes more assumptions from direct simulations or physical prescriptions, to the most empirical one, which requires more flexible parameterizations, constrained directly from data. [35].

The totally physical method of galaxy-halo connection includes numerical simulations with both gas and dark matter, which assumes sub-grid processes, as the physical processes occurring on scales that are smaller than the resolution of the simulations. Another physical method consists in simulates the galaxy formations through hydrody-

namical simulations (e.g. Illustris simulations [36], Eagle simulations [37]), or semianalytic models (SAMs), e.g. [38], [39], [40].

However, the creation of large galaxy surveys in the last decades contributed to the development of totally empirical approaches to connect galaxies to haloes with a statistical technique, which solve the difficulty of the physical models to fully reproduce observed galaxies. One of the main methods is the halo occupation distribution formalism (HOD), which defines the probability distribution for a halo with mass M to host N galaxies with definite intrinsic properties, as luminosity, clustering properties, luminosity, types and colors. Moreover, the HOD method is extended with a more complex formulation, as the conditional luminosity function (CLF) formalism.

Nevertheless, the HOD and CL formalism are developed only at low redshift, due to unavailability of reliable galaxy clustering measurements at higher redshift. This issue can be avoided with the (sub)halo abundance matching (SHAM) method, which links galaxies and dark matter haloes with the assumption that a galaxy property, such as the stellar mass, or the galaxy luminosity, is monotonically related to an halo property, as the halo mass or the circular velocity of haloes. As a results, the connection between galaxies and dark matter haloes/subhaloes properties is carried out with a one-to-one association from the corresponding distributions, using only the stellar mass functions or luminosity function as observational input data.

In this chapter, first of all we focus on the abundance matching modeling that is a an empirical method that tackles the issues of connecting observed galaxies to simulated dark matter haloes and subhaloes using a correspondence between a property of the galaxies and a property of the haloes in which they live.

Figure 3.2 gives an example of dark matter distribution and the corresponding galaxy distribution, obtained with an abundance matching model, tuned to match galaxy clustering properties of an observed sample.

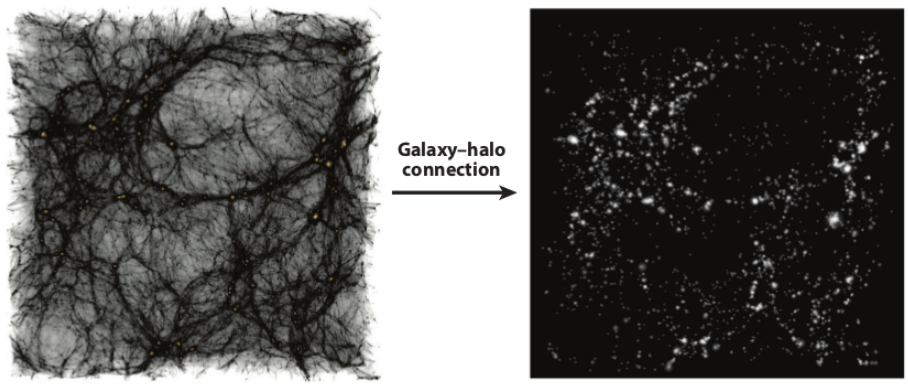

Figure 3.2: Dark matter distribution in a $90 \times 90 \times 30$ Mpc h^{-1} slice of a cosmological simulation (left) compared with the galaxy distribution using an abundance matching model (right) [35].

Secondly, we summarize the main features of the empirical method, Halo occupation model (HOD).

Finally, we describe the approaches to physical modeling of galaxy formation, including hydrodynamical simulations and semianalytic models (SAMs).

3.1 Subhalo abundance matching

The simplest assumption about the correspondence between galaxies and haloes is that the most massive galaxies form in the dark matter haloes characterised by the deepest potential wells. This basic method is generally known as abundance matching in the literature. Galaxies are linked to the corresponding dark matter structures using stellar mass or luminosity as galaxy property and a measure of halo mass or the circular velocity, as halo property (i.e. a proxy of the depth of the local potential well) [41], [42], [43], [44], [45], [46], [47], [48], [49].

One of the first approaches of subhalo abundance matching (SHAM) is to link the mass of a dark matter halo/subhalo and the luminosity of a galaxy hosted in it. Vale and Ostriker (2004) [43] find that the relation between these properties is a double power law. The mass-luminosity relation is obtained comparing the total mass function for haloes and their subhaloes to the galaxy luminosity function. The relation is asymptotic to $L \propto M^4$ at low mass, while at high mass the former follows $L \propto M^{0.28}$ and the latter $L \propto M^{0.9}$, as it is shown in Figure 3.3.

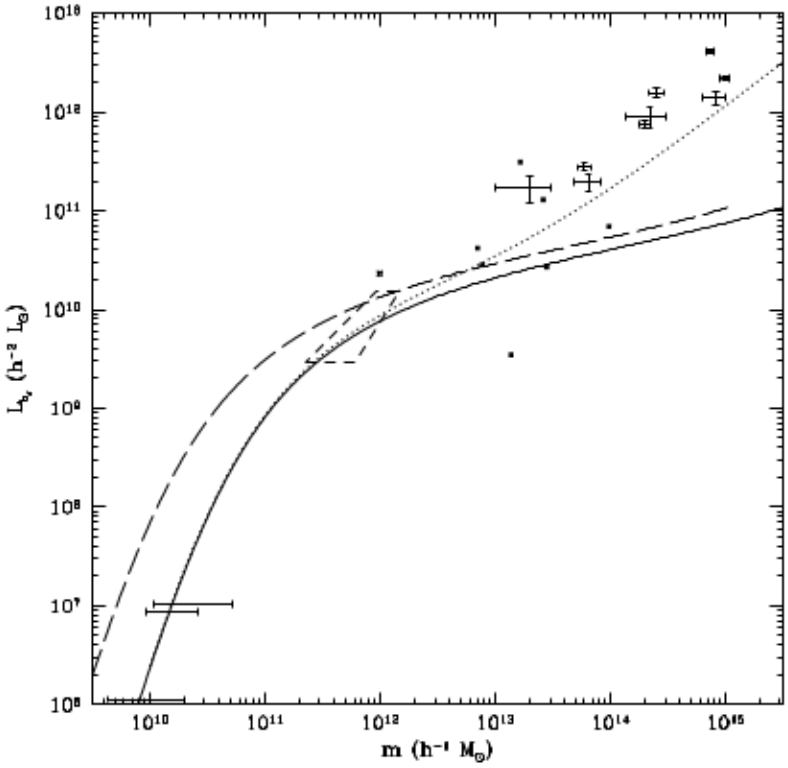

Figure 3.3: Relation between galaxy luminosity and the original mass of the dark matter halo which hosts it. The solid line is for each individual halo or subhalo, the dotted line shows the total group luminosity of the halo plus subhaloes system, in which case the x-axis m refers to the parent halo mass only [43].

A second approach is to determine the relationship between the stellar masses of galaxies and the masses of the dark matter haloes. Moster et al. (2010) [50] obtain a pa-

rameterised stellar-to-halo mass relation (SHMR) by populating haloes and subhaloes in N-body simulations with galaxies and requiring that the stellar mass function calculated from the galaxy catalog reproduces the observations. High-resolution dissipationless N-body simulations are used to identify distinct haloes and subhaloes which orbit within the potential of their host halo. Haloes and subhaloes are respectively populated with central and satellite galaxies using a parameterised SHMR relation.

The SHMR concerns central galaxies occupying the central regions of the dark matter haloes. Also, it is valid for satellite galaxies, which are hosted by smaller sub-haloes orbiting the potential well of the main halo.

For host haloes, the mass is given by the virial mass M_{vir} while for subhaloes they use the maximum mass of the halo over its history M_{max} since the stellar mass of the satellite galaxy is expected to be more tightly linked to this quantity. The ratio between stellar mass M_* and halo mass M_H is described by a function with four free parameters, a low-mass slope β, a characteristic mass M_A, a high-mass slope γ, and a normalisation A

$$\frac{M_*(M_H)}{M_H} = 2A\left[\left(\frac{M_H}{M_A}\right)^{-\beta} + \left(\frac{M_H}{M_A}\right)^{\gamma}\right]^{-1} . \tag{3.3}$$

A direct comparison of the halo mass function, calculated from simulations and the galaxy mass function, from observations of the Sloan Digital Sky Survey, is used to constrain the value of the parameters of the Stellar-to-Halo Mass function. As a result, the SHM function has a characteristic peak at $M_A \sim 10^{12} M_\odot$, declines steeply toward smaller mass ($\beta \sim 1$) and less steeply toward larger mass haloes ($\gamma \sim 0.6$), as it is shown in Figure 3.4.

The SHM relation is constrained at a given set of redshifts between $z = 0$ and $z = 4$, the resulting relations are shown in Figure 3.5. This allows to study how the four parameters of the SHM function depend on redshift. The evolution of each parameter is described with a redshift-dependent function. The characteristic mass increases with redshift, thus at high redshift, the peak efficiency of converting baryons into stars occurs in more massive haloes. On the other hand, the normalisation decreases with redshift, this indicates that there is less stellar content in haloes at higher redshifts. While at $z = 0$ the most efficient haloes have converted ~ 23 per cent of their baryons into stars, at $z = 4$ the peak efficiency is less than ~ 10 per cent.

Furthermore, the characteristics of the SHMR function describe the different growth rates of galaxies as a function of halo mass, accounting for various feedback processes acting at different mass scales. Behroozi et. al. (2010) [45] models the M_*-M_h relation with the following functional form:

$$\log(f^{-1}_{SHMR}(M_*)) = \log(M_h) = \log(M_1) + \beta \log \frac{M_*}{M_{*,0}} + \frac{\left(\frac{M_*}{M_{*,0}}\right)^{\delta}}{1 + \left(\frac{M_*}{M_{*,0}}\right)^{-\gamma}} + \frac{1}{2} . \tag{3.4}$$

The parameters of Equation 3.4 are the stellar mass scale $M_{*,0}$ and the characteristic mass of the halo M_1. In particular, the latter represents the normalization of M_h as a function of M_*, while the second parameter $M_{*,0}$ determines the position along the M_* axis. As a result, the two parameters describe the transition mass scale of the SHMR function between the small-scale and high-scale regimes. In particular, the small scale regime, i.e. with masses $M_* \lesssim 10^{10.5} M_\odot$, is represented with a power law function with the parameter β. Instead, at higher masses, $M_* \gtrsim 10^{10.5} M_\odot$, the SHMR is described with a sub-exponential law governed by the parameter δ. Finally, the γ parameter adjusts the transition zone.

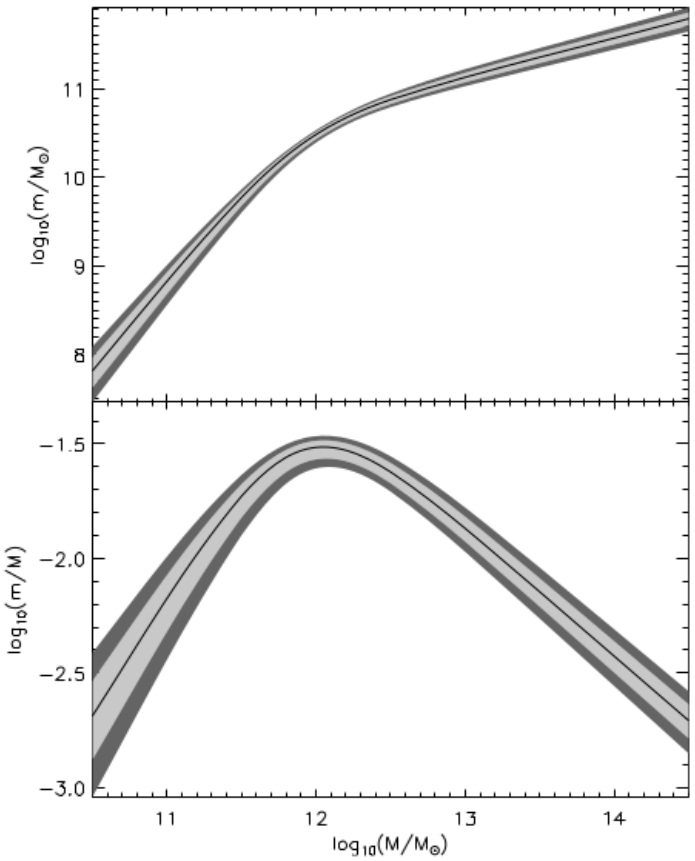

Figure 3.4: Relation between stellar mass m and halo mass M. The upper panel shows the SHM relation, while the lower panel shows the SHM ratio [50].

The ratio in Equation 3.4, i.e. the ratio M_*/M_h between the stellar mass and the mass of the halo, describes the efficiency of the galaxy formation process, taking into account all the processes that allow the conversion of baryons in stars, i.e. from gas cooling and star formation to stallar and AGN feedback. The baryon matter content of the haloes is equivalent to the universal baryon fraction $f_b = \Omega_b/\Omega_m \approx 0.16$, as a result the ratio M_*/M_h gives information on the fraction of baryons available in a dark matter halo which can be converted into stars. In particular, the M_*/M_h ratio provides the integrated baryon conversion efficiency during the lifetime of the halo at a fixed redshift value, taking into account the combination of all the different physical processes that regulate star formation during the life of the halo, such as mergers, gas accretion, feedbacks. The fact that the shape of the ratio M_h/M_* has a strong dependence on the halo mass indicates that star formation is regulated by various feedback mechanisms acting on different halo mass scales.

Finally, another approach is to use circular velocity as the halo property linked to the depth of its potential well. Galaxies are associates with the peak circular velocity of their haloes, that is the highest circular velocity a halo has had over its entire merger history [52]. This property is a measure of the potential wells of their dark matter haloes before

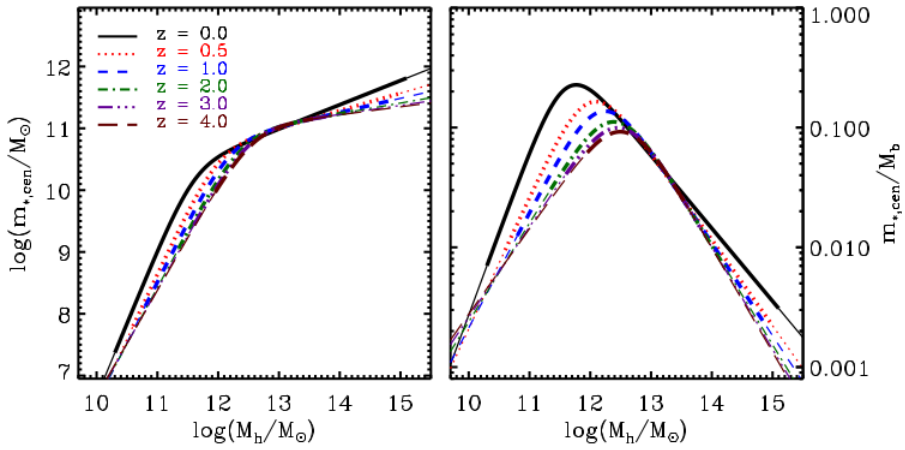

Figure 3.5: Stellar-to-halo mass relation for central galaxies as a function of redshift. Left panel: Evolution of the SHM relation. Right panel: Evolution of the stellar-to-halo ratio [51].

they are impacted by larger structures. Figure 3.6 shows the correlation between the circular velocity v_{peak} of haloes and the stellar mass of galaxies.

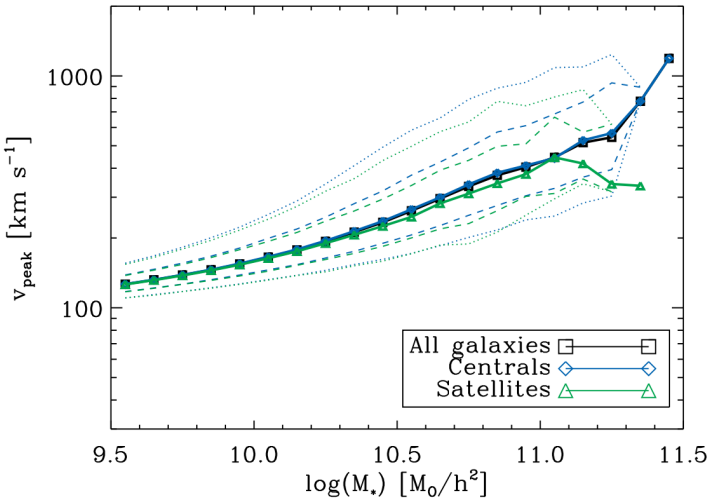

Figure 3.6: Relationship between halo circular velocity and galaxy mass. Blue indicates centrals galaxies, while green satellites. Solid black lines are the median of the total galaxies (satellites plus centrals). Solid lines are the median values of v_{peak} for bins in M_*, while dashed and dotted lines contain given the 68% and 95% bounds on galaxies in each bin, centred at the median [52].

Moreover, the validity of the subhalo-abundance-matching is studied by Chaves-Montero et al. (2016) [53]. Indeed, they examine the performance, implementation, and assumptions of SHAM using the hydrodynamical simulations EAGLE. They implement different "flavour" of SHAM, each using $V_{circ}(z)$, the maximum of the radial circular velocity of haloes, defined at a different time: V_{max} the maximum circular velocity of a subhalo at the present time, V_{peak} the maximum circular velocity that a subhalo has

reached, V_{infall} the maximum circular velocity at the last time a subhalo was identified as a central, V_{relax} the highest value of the circular velocity attained by a subhalo while it satisfies a relaxation criterion. They find that V_{relax} is the subhalo property that correlates most strongly with galaxy stellar mass M_*. The correlation is shown in Figure 3.7.

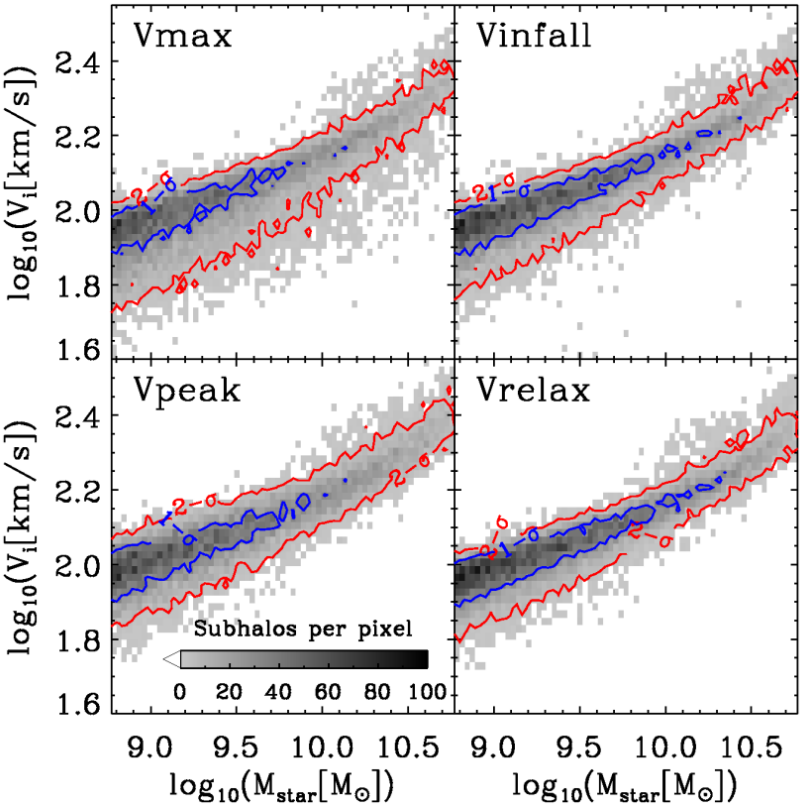

Figure 3.7: Relation between the M_{star} of galaxies from EAGLE simulations and different type of velocity of dark matter haloes. Blue and red contours mark the regions containing 68% and 95% of the distribution, respectively [53].

3.2 Extended Subhalo abundance matching

The basic SHAM method, used to populate the subhaloes, is generalized in the Extended Subhalo abundance matching (SHAMe) [54], [55], [56], in order to improve the predictions of galaxy clustering in both real and redshift space. This method, taking into account information about orphans galaxies, tidal disruption and a flexible number of galaxy assembly bias, can realistically and efficiently populate dark matter simulations, in order to constrain cosmological information from galaxy clustering.

The SHAMe model make improvements, as a small number of free parameters, and the precision with which it can reproduce the real and redshift space galaxy clustering, particularly on small scales. The first advance of a small number of free parameters can reduce the susceptibility to degeneracy with cosmological parameters. The second one

of the high accuracy on small scales is useful to constrain power of galaxy clustering in the non-linear regime.

The model starts by matching a subhalo property (as the peak velocity v_{peak}) to the expected luminosity function, where v_{peak} is defined as the maximum circular velocity ($v_{max} \equiv max\sqrt{GM(<r)/r}$) reached during the entire evolution of a halo/subhalo. Then, the model introduces orphan galaxies, that are satellite structures with known progenitors, expected to exist in the halo but not resolved in simulation.

A large amount of orphan galaxies is included by tracking the most bound particle of subhaloes with no known descendant. The orphan galaxy is assumed to merge with its central structure when the time since accretion t_{infall} becomes larger than a dynamical friction timescale $t_{infall} > t_{dyn}$ [54]. The latter dynamical friction time t_{dyn} corresponds to the moment in which the satellite subhalo becomes an orphan and it can be computed according the following Equation:

$$t_{dyn} = \frac{1.17 t_{merger} d_{host}^2 V_{host} (M_{host}/10^{13} h^{-1} M_\odot)^2}{G \ln(M_{host}/M_{sub} + 1) M_{sub}} \,, \tag{3.5}$$

where t_{merger} is a free dimensionless parameter that effectively regulates the number of orphan galaxies; d_{host} is the distance of the subhalo to the centre of its host halo; V_{host} is the virial velocity of the host halo; M_{host} is the virial mass of the host halo, and M_{sub} is the subhalo mass.

The SHAM method basically assumes that the relation between a subhalo property (as the mass or the peak velocity) and a galaxy property (as the stellar mass) is constant through time and it is the same for central and satellites. However, the v_{peak} - stellar mass relation is not identical for centrals and satellites. Indeed, the satellite galaxies can decrease their stellar mass to the point of disappearing into the intra-cluster medium, with the effect of removing some satellite galaxies of a given sample, mostly located near the centre of a halo. For this reason, the next step in the SHAMe method is to remove from the sample galaxies that became satellites a long time ago.

After a period of time, satellite galaxies begin to lose stellar mass, reducing their luminosity. Moreover, satellite galaxies can lose their cold gas content, which makes galaxies redder and as a result their brightness is reduced. The galaxy clustering predictions are improved excluding all galaxies with satellites for an extended period of time, i.e. $t_{infall} > \beta_{lum}$, with β_{lum} a free parameter.

Finally the SHAMe method is implemented to include additional galaxy assembly bias, which is the change in galaxy clustering caused by the propagation of halo assembly bias into the galaxies [57]. This propagation occurs because the occupation of galaxies depends on halo properties that cause halo assembly bias [58]. At fixed halo mass, the halo assembly bias quantifies the dependency of the clustering on the secondary halo properties, usually correlated with the assembly history of the dark matter halo.

3.3 Hydrodynamical simulations

Physical models, such as hydrodynamic simulations and semi-analytical models, aim to directly simulate or model the main physical processes that occur in the formation of galaxies.

Through hydrodynamic simulations the formation of galaxies is modelled by solving the gravitational and hydrodynamic equations in the cosmological context. Thus, star formation processes, such as gas cooling, winds driven by stellar feedback and feedback from black holes and supernovae, and in some cases magnetic fields and cosmic rays are

taken into account in the modelling. In this way, the properties of dark matter, gas and stars in certain resolution elements can be traced over time.

However, these simulations are unable to simulate galaxy formation across the full-scale range in a cosmological context. Therefore, they need to consider some parameterizations concerning sub-resolution scales, which are able to model the physics of the sub-grid. The physical parameterizations of the subgrid are constrained, either by testing them directly with the observations or by comparing them with the results of empirical model constraints which link the observations to dark matter halos.

Hydrodynamic simulations are categorized into two main groups.

The first is the Lagrangian or smoothed particle hydrodynamics (SPH) method, whose frame of reference is the particles and their properties, such as temperature, mass and metallicity. The particles are then uniformed by assigning them a weight depending on those nearby that fall within a fixed separation, i.e. the linking length.

The second group includes the Eulerian method, which assumes a Cartesian frame of reference, in which fluid particles are discretized in fixed cells where their physical properties are quantified. In order to achieve the higher resolution necessary for galaxy formation, this method can be extended to the Adaptive Mesh Refinement (AMR) procedure, which subdivides cells that meet certain criteria, such as temperature or density, into smaller sub-cells reaching a higher resolution.

However, since these methods have some difficulties, such as the inability of SPH to resolve shocks and the sensitivity of AMR results to bulk velocities, new sets of mesh models have been developed. They are a middle class between the Lagrangian and Euler methods, as they use Voronoi tessellation to subdivide the space around the particles, such that this mesh can continuously deform and reform as the particles move. The key advantage of this method is that it tracks both dark matter and gas particles simultaneously. However, the high computational cost required by these hydrodynamic simulations limits the physical volume that can be simulated. Furthermore, the physical parameter space that can be explored for a given mass resolution is also limited.

3.4 Semi-analytical models

Since hydrodynamic simulations require high computational resources, an alternative method to simulate the same basic processes of galaxy formation is provided by semianalytic models (SAMs) of galaxy formation, e. g. [59], [60], [61]. It approximates baryonic physical processes with analytic prescriptions, which are traced through the merging history of dark matter haloes on the top of N-body dark matter only simulations. These prescriptions, usually traced through the merger trees extracted from simulations, adopt a set of simplified flow equations, describing the physical processes, for bulk components, mapped into dark matter merger trees, and track through cosmic time the assembly of baryons and its corresponding host dark matter haloes. The SAMs have the advantage to be significantly less computationally expensive than hydrodynamical simulations, making it possible to simulate galaxies for larger volumes over a greater range of halo mass. However, they generally have a large number of parameters, from 10 to 30, depending on the degrees of complexity. Indeed, the SAMs can include many ingredients, as star formation, gas accretion, chemical/mechanical/radiative feedback and metal enrichment. Moreover, gas and metals can be modelled with a distribution following the density profile of dark matter, splitting the gas into cold or hot phases, with outflows carrying away metal enriched gas and reionization feedback. The resulting implemented models are able to generate average baryonic properties for a given halo. A recent improvements consist in using a Monte Carlo Markov chain techniques directly

constraining the SAMs parameter space with data, in order to find the best set of model parameters which fits input observations, as cold gas mass fractions or relation between black-hole and bulge mass, [62]. Due to the large parameter space and high computational resources, it remains difficult to fully constrain these models with clustering data and other spatial statistics.

3.5 Halo occupation models and conditional luminosity function

A further method used to describe the relationship between galaxies and haloes is through the halo occupation distribution (HOD). It differs from abundance matching because it is a statistical approach.

Indeed, it specifies the probability distribution for the number of galaxies meeting some criteria, for example a luminosity or stellar mass threshold, in a halo, generally conditioned on its mass, $P(N|M)$. Central and satellite galaxies give separate contributions to the probability $P(N|M)$ that a halo of virial mass M contains N galaxies of a particular class [63]. For the central galaxies $P(N|M)$ is assumed as a Bernoulli distribution, while for satellites it is a Poisson distribution. Therefore, under these hypothesis the standard HOD is totally characterized by its mean occupation number $\langle N|M\rangle$.

The connection between modern HOD methods and measurements of galaxy clustering is well constrained for a large amount of galaxy samples, thanks to many works in the early 2000s, e. g. [64], [65], [66], [63], [67]. The functional form of the HOD for galaxies selected according their mass or luminosity is usually expected to be similar to the one of dark matter subhaloes within their host haloes. Indeed, the HOD for a large number of selected subhaloes is well represented by a power law of subhaloes following the distribution $N \sim M$, adding a central galaxy, [41]. By setting a threshold on the stellar mass of galaxies, a central galaxy is usually found in haloes that are 10-30 times less massive than those hosting satellite galaxies for the same stellar mass. This analytical formula is valid for threshold-luminosity or stellar-mass-threshold galaxy samples. This type of HOD is typically modeled with three to five parameters for a fixed set of galaxies. Indeed, a common parameterization, e. g. [63], which describes the mean occupation function for central galaxies, can be well approximated by

$$\langle N_{cen}\rangle_M = \frac{1}{2}\left[1 + erf\left(\frac{\log M - \log M_{min}}{\sigma_{\log M}}\right)\right], \tag{3.6}$$

where $erf()$ is the error function. The free parameters are M_{min}, that is the characteristic minimum mass of haloes that can host such central galaxies, and $\sigma_{\log M}$, the characteristic transition width. This functional form corresponds to a Gaussian distribution of $\log M_{gal}$, at fixed halo mass M.

On the other hand, at low masses the mean occupation function for satellite galaxies is well represented by a power law in the following form

$$\langle N_{sat}\rangle_M = [(M - M_0)/M_1^{'}]^{\alpha}, \tag{3.7}$$

for $M > M_0$, where M_0 is the characteristic mass for satellite galaxies.

Moreover, the complete distribution of the galaxies, at a fixed halo mass, can be further characterized thanks to the conditional luminosity function (CLF) and the conditional stellar mass function (CSMF). The distribution is then described distinctly by the contribution of the brightness of the central galaxy, $P(L_c|M)$, and by that of the satellites, $\Phi(L_{sat}|M)$,according to what was found by the measurements of the groups and

clusters (e. g. [68], [69], [70]). In particular, central galaxies and satellites are distinguished by this parameterization. Indeed, the former follow a log-normal distribution of stellar masses or luminosities at a given fixed mass of the halo, while the latter follow a Schechter function, whose parameters depend on the mass of the halo.

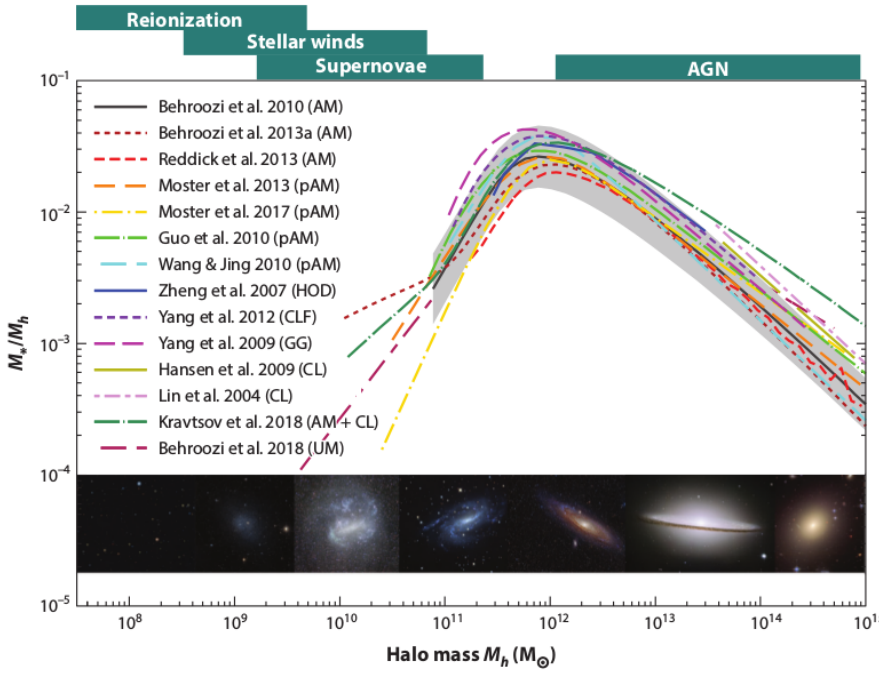

Figure 3.8: The galaxy stellar-to-halo mass ratio of central galaxies at $z = 0$. The figure shows constraints from a number of different methods: direct abundance matching (AM) ([45], [71], [52]); parameterised abundance matching (pAM), that use a parameterised relationship and the parameters are fit with the stellar mass function ([72], [51], [73], [74]); modeling the halo occupation distribution (HOD) ([67]) or the conditional luminosity function (CLF) ([69], [75]) and constraining it with two-point clustering; direct measurements of the central galaxies in galaxy groups and clusters (CL) ([68], [70], [69], [76]); and the Universe Machine (UM) [77], an empirical model that traces galaxies during their histories. Bottom panel shows galaxies that are hosted by haloes in the specified mass range, while the top panel indicates the key physical processes that may be responsible for ejecting or heating gas or suppressing star formation at those mass scales [35].

3.6 The stellar-to-halo-mass relation

The basic shape of the SHM relation derives from the mismatch between the halo mass function and the galaxy stellar mass function or luminosity function, which decreases rapidly below typical galaxies and has a slightly shallower slope than the halo mass function. The SHMR for central galaxies is shown in Figure 3.8, in the cases in which it is inferred by parameterised models, or measured directly, or predicted with models of galaxy formation. There are several characteristics of this relation, that are identified consistently using different methods to constrain it. First, the peak efficiency of galaxy formation is always quite low. Indeed, the SHMR peaks at just a few percent.

As a result, assuming that all haloes host the universal baryon fraction of 17%, just $20-30\%$ of baryons have turned into stars. This maximum galaxy-formation efficiency occurs around the mass of haloes hosting typical L_* galaxies like the Milky Way, around $10^{12}M_\odot$. At higher and lower masses, galaxy formation is even less efficient. Roughly, the stellar mass of central galaxies scales as $M_* \sim M_H^{2-3}$ at dwarf masses and $M_* \sim M_H^{1/3}$ at the high-mass end.

The reduction of the star formation efficiency is due to strong feedback processes from the formation of stars and black holes. There are a combination of a number of processes: at high mass, AGN (active galactic nuclei) feedback can heat halo gas and for this reason they limit future star formation; at low mass, feedback from massive stars is believed to be important in driving winds that eject gas or prevent it from coming into a galaxy; at even lower masses, galaxies can be too small to hold onto their gas during the reionisation period around $z \sim 6$.

Below some threshold halo mass, galaxies will no longer be able to form at all. The smallest known galaxies, ultrafaint dwarf galaxies, have measured dynamical masses in their inner regions larger than a few times $10^7 M_\odot$, which is most likely equivalent to halo virial masses of greater than $10^9 M_\odot$. The exact value of the minimum mass at which a halo can host a galaxy is still somewhat uncertain, as is the slope of and scatter in SHMR for haloes below $\sim 10^{11} M_\odot$.

CHAPTER 4

Synthetic and observed data for the analysis pipeline

In this Chapter I describe the data used to implement the SHAM method, needed to construct the mock galaxy catalogues.

First, we describe the characteristics of the dark matter N-body simulations and in particular the halo/subhalo catalogues, needed as input data to derive the halo mass functions for the SHAM technique.

Second, we focus on the observed data which are significantly important to compute the stellar mass functions, needed as input data and compared with the respective simulations using the SHAM method.

Finally, in the last section we summarize the computational tools, needed to construct the SHAM method. Moreover, the libraries, used to estimate the correlation functions from the galaxy catalogues and the halo power spectra from the halo catalogues both in real and redshift space, are presented.

4.1 N-body simulations: the DEMNUni suite

This work exploits the "Dark Energy and Massive Neutrino Universe" simulations (DEMNUni) [18, 17], performed at the CINECA supercomputing centre, using the tree particle mesh-smoothed particle hydrodynamics (TreePM-SPH) code GADGET-3 [78, 19]. This version of GADGET-3 follows the evolution of CDM and neutrino particles, treating them as two distinct sets of collisionless particles.

The DEMNUni project is a set of 16 large N-body simulations to study the evolution of large scale structures in the presence of massive neutrinos and dynamical dark-energy, with Equation of State (EoS) parametrised according to Chevallier, Polarski & Linder (CPL) [9, 10]. Each simulation is characterised by a softening length $\epsilon = 20\mathrm{kpc}/h$, a comoving volume of $8(h^{-1}\mathrm{Gpc})^3$, filled with 2048^3 cold dark matter particles with mass $M \sim 8 \times 10^{10} M_\odot$, and, when present, 2048^3 neutrino particles. Each run has an initial redshift $z_i = 99$, 63 different output times logarithmically equispaced in the scale factor $a = 1/(1+z)$ down to $z = 0$, 49 of which lay between $z = 0$ and $z = 10$. For each of the 63 output times, a particle snapshot composed by both CDM and neutrino particles has been dumped on the fly, and post-processed with the friends-of-friends (FoF) algorithm included in GADGET-3 [78, 32], setting to 32 the minimum number of particles, i.e. fixing the halo minimum mass to $M_{\mathrm{FoF}} \simeq 2.5 \times 10^{12}\, h^{-1} M_\odot$. Finally, the FoF catalogues have been processed via the SUBFIND algorithm (also included in GADGET-3) so that in each initial FoF parent halo multiple subhaloes are identified, with the result of an increase in the total number of identified objects and of a lower minimum mass limit. In this work we consider outputs in the range $0 < z < 2$, as we focus on the redshift range of upcoming galaxy surveys, such as Euclid.

The DEMNUni simulations have a baseline Planck 2013 [2] ΛCDM reference cosmology together with different cosmological models. In particular, in this work we consider the following cosmological scenarios:

- A flat *ΛCDM-cosmology* with $\Omega_{\rm m} = 0.32$, $\Omega_{\rm b} = 0.05$, $\sigma_8 = 0.83$ and $H_0 = 67$.
- Three flat *νΛCDM-cosmologies* where the sum of the neutrino masses runs over the values $\sum m_\nu = 0,\ 0.16,\ 0.32$ eV (here the density parameters Ω_ν and Ω_c are assumed to vary, while Ω_m and the amplitude of primordial curvature perturbations are kept fixed).
- Four flat $w_0 w_a$*ΛCDM-cosmologies* described by the CPL parametrisation of the DE EoS $w(a) = w_0 + (1-a)w_a$, with w_0 and w_a chosen within the 2015 Planck boundaries [3] and given by $w_0 = -0.9, -1.1$ and $w_a = -0.3, 0.3$.
- Four flat $\nu w_0 w_a$*ΛCDM-cosmologies* obtained by combining the four $w_0 w_a$ΛCDM-cosmologies with the three values of the total neutrino masses $\sum m_\nu = 0,\ 0.16,\ 0.32$ eV.

4.2 Galaxy surveys: SDSS and COSMOS

In order to associate galaxies to subhaloes, we have to compare simulations with observations. We consider the galaxy stellar mass function derived from Baldry et al. (2008) [79] for redshifts $z < 0.2$. This is determined using the New York University - Value Added Galaxy Catalog (NYU-VAGC) sample derived from the Sloan Digital Sky Survey (SDSS) observations. The Sloan Digital Sky Survey is a major multi-spectral imaging and spectroscopic galaxy redshift survey which exploits a dedicated 2.5 m wide-angle optical telescope at the Apache Point Observatory in New Mexico, United States.

The data from the NYU-VAGC low-z sample include 49968 galaxies. These data are matched to the stellar masses estimated by Kauffmann et al. (2003), Gallazzi et al. (2005), and Panter et al. (2007); with 49473, 32473 and 38526 matches, respectively. The stellar mass function is calculated dividing the galaxies into logarithmic stellar mass bins, for each set of stellar masses. For each bin, the galaxy stellar mass function (GSMF) is then given by

$$\phi_{\log M} = \frac{1}{\Delta \log M} \sum_i \frac{1}{V_{max,i}} \omega_i \ , \tag{4.1}$$

where $V_{max,i}$ is the comoving volume over which the *i*th galaxy was observed, and w_i is any weight applied to the galaxy. The stellar mass function is calculated assigning to each galaxy a weight ω_i that depends on the numerical density as a function of the redshift. In particular Baldry et al. (2008) set ω_i, for each galaxy, equal to $1/n(z)$ where n is the normalised number density at the galaxy redshift. Moreover, the mass used for each galaxy is the average of four $\log M$ estimates: Kauffmann et al. (2003), Gallazzi et al. (2005), Panter et al. (2007) and Baldry et al. (2008). The stellar mass function calculated with this method is represented by the points in Figure 4.1.

In addition, these data are fitted with a double Schechter function given by

$$\phi(M)dM = e^{-\frac{M}{M_*}} \left[\phi_1^* \left(\frac{M}{M_*} \right)^{\alpha_1} + \phi_2^* \left(\frac{M}{M_*} \right)^{\alpha_2} \right] \frac{dM}{M_*} \ , \tag{4.2}$$

where $\phi_M dM$ represents the number density of galaxies with mass between M and $M + dM$, M_* is the characteristic stellar mass, α_1 and α_2 are the slopes, and ϕ_1^* and ϕ_2^* correspond to the normalisations. The fitting function is shown in Figure 4.1.

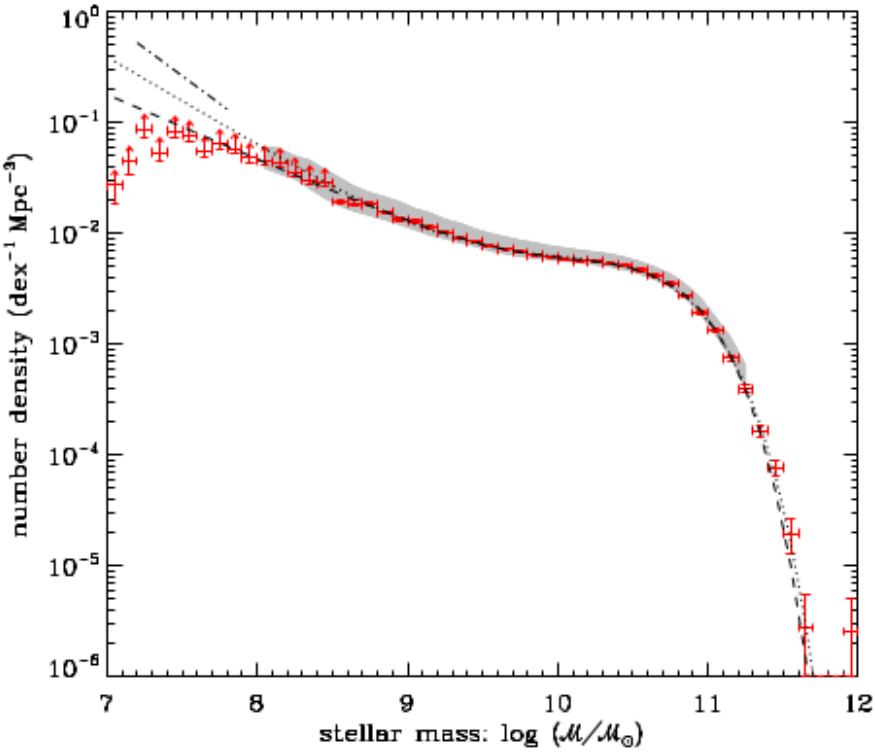

Figure 4.1: Galaxy stellar mass function, calculated from the Sloan Digital Sky Survey observations. The points represent the non-parametric GSMF with Poisson error bars. The dashed line represents a double-Schechter function extrapolated from a fit to the data points. The shaded region shows the range in the GSMF from varying the assumed stellar mass and changing the redshift range [79].

The uncertainties that affect the estimate of the stellar mass function of Baldry et al. (2008) are the poissonian errors on galaxy counts, the observational errors on the stellar mass measurements and on the spectroscopic redshifts of galaxies.

On the other hand, for higher redshifts in the range from 0.2 up to 2, we use Stellar Mass Function (SMF) derived by Weaver et al. (2022) [80] for galaxies in the NIR-selected catalogue of the Cosmological Evolution Survey (COSMOS).

COSMOS is a 2 deg^2 field with deep coverage from the UV to the IR bands, and it is able to collect robust statistics of distant, massive galaxies, thanks to its large area. The field has been observed with most of the major space-based (Hubble, Spitzer, GALEX, XMM, Chandra, Herschel, NuStar) and ground based telescopes (Keck, Subaru, Very Large Array (VLA), European Southern Observatory Very Large Telescope (ESO-VLT), United Kingdom Infrared Telescope (UKIRT), The National Optical Astronomical Observatory (NOAO) Badde and Blanco telescopes, the Canada France Hawaii Telescope (CFHT), and others). All these telescopes perform photometric observations with broad, intermediate and narrow band filters. In particular, the IR photometry is necessary to obtain precise stellar mass estimates over a large redshift range.

Weaver et al. (2022) constructs a large, deep sample of $\sim$ 1000000 galaxies selected using the latest UltraVISTA DR4 data release [81], which is an Ultra Deep, near-infrared

survey with the new VISTA surveys telescope of the European Southern Observatory (ESO). It represents currently the longest running near-infrared survey and in addition it complemented by deeper data in the optical band provided by Subaru's HyperSuprime-Cam instrument. The sample is constructed using the photometric catalogue of galaxies with photometric redshift z_{phot} between $z = 0.2$ and $z = 7.5$. Galaxies in COSMOS2020 are selected from a near-infrared izY JHKs CHI-MEAN co-added detection image (Szalay et al. 1999; Bertin 2010), which guarantees a mass-selected sample complete down to $10^9 M_\odot$ at $z \approx 3$. The deepest band is i, with a 3σ sensitivity limit at 27.0 mag, and the shallowest is K_s at 25.9 mag. The COSMOS2020 survey provides a deep and homogeneous near-infrared coverage of galaxy sources with a large effective area of $1.27 deg^2$. This increase results in an improvement in the sample statistics and in the estimation of spatial variations, i.e. cosmic variance, especially for rare and massive galaxies. Moreover, compared to previous studies, the increase in effective area pushes the observations to higher redshifts with greater confidence and mass completeness.

The galaxy stellar masses are estimated by fitting the galaxy spectral energy distribution (SED). Weaver at al. (2022) estimates the SMF in 12 bins of redshift in fixed bins of stellar mass $\Delta M = 0.25$ above the mass limit for that z-range, using the $1/V_{max}$ non-parametric method. Briefly, this method is used to statistically correct for selection incompleteness by weighting each detected object by the maximum comoving volume in which it can be observed, given the characteristics of the telescope survey. The volume V_{max} of each galaxy is estimated computing the maximum redshift z_{max} at which the best fit SED can no longer be observed due to the flow limit of the survey. Instead the minimum redshift z_{min} corresponds to the value at which the source would become too bright and would make the camera saturated, although in practice it is the lower bound of the redhsift bin in which the galaxy is located z_{low}. Thus, the maximum observable volume for the i-th galaxy in the bin $z_{low} < z < z_{high}$ is:

$$V_{max,i} = \frac{4\pi}{3} \frac{\Omega}{\Omega^{sky}} \left\{ D^3_{cov} \left[min(z_{max,i}, z_{high}) \right] - D^3_{cov} \left[max(z_{min,i}, z_{low}) \right] \right\} , \tag{4.3}$$

where Ω is the solid angle subtended by the sample, $\Omega^{sky} \equiv 41253$ deg^2 is the solid angle of a sphere, and $D_{cov}(z)$ is the co-moving distance at redshift z.

The statistical uncertainty on the number density of the SMF consists of the error contributions due to Poisson noise (σ_N), cosmic variance fluctuations (σ_{cv}), and the uncertainties on the estimation of the masses carried out with the SED fitting method (σ_{SED}). The total error budget on SMF consists of the quadrature addition of these three different sources of uncertainty: $\sigma_\Phi = \sigma^2_N + \sigma^2_{cv} + \sigma^2_{SED})^{1/2}$. The different uncertainty contributions of total SMF error budget is indicated in Figure 4.2 as a function of stellar mass in many redshift bins.

The process of measuring the abundance of discrete quantities, as galaxy counts, generates Poisson noise. In the SMF the Poisson error σ_N for each mass bin is estimated as $\sqrt{N}$ where N is the number of galaxies in each bin. In Figure 4.2 the error contribution of σ_N is increasing with mass and redshift and it reaches the maximum at $M > 10^{11.5} M_\odot$.

The properties of the galaxies are influenced by the environmental density, determining the clustering properties. Indeed, the mass density of galaxy clusters has the effect of increasing the overall normalization of the stellar mass function. In addition, they usually increase the high-mass end of the mass function since they contain the most massive systems. This phenomenon of environmental distortion is called cosmic variance. It is the uncertainty in observational estimates of the number density of galaxies in finite volume, arising from the underlying large-scale density fluctuations that exist

in a larger volume than the observed one [82]. This uncertainty increases with the mass since more massive galaxies are more biased than galaxies of lower mass. The cosmic variance is fundamental to accurately evaluate the uncertainties of the sample, during the procedure of inferring universal or intrinsic properties of galaxies. Figure 4.2 shows the error budget of σ_{CV}, which is the dominant error contribution for low-mass systems at all redshifts and becomes increasingly important at high masses as z increases.

In addition, uncertainties generated by the SED template-fitting procedure, i.e. the observational error on the stellar mass and on the photo-z, are taken into account. As shown in Figure 4.2, the contribution from σ_{SED} become dominant only at $M > 10^{11.5} M_{\odot}$, in some cases becoming larger than unity. The error contributions of σ_{SED} are comparable with the Poison noise across the entire mass range.

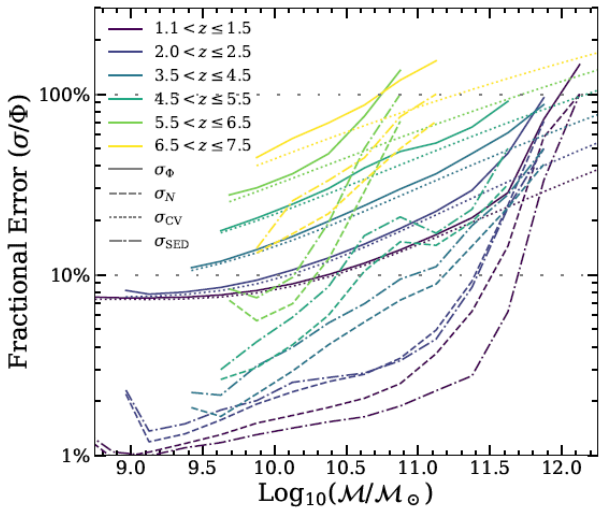

Figure 4.2: Estimates for the total uncertainty σ_{ϕ} (solid) as a function of stellar mass at many redshifts, indicated with different colors, for COSMOS 2020 mass complete samples. Contributions include uncertainties from Poisson noise σ_N (dashed), Cosmic Variance σ_{CV} (dotted), and SED fitting σ_{SED} (dash-dotted) [80].

The SMF for the total sample, containing both star-forming and quiescent galaxies, in 12 redshift bins from $z = 0.2$ to 7.5 in fixed bins of stellar mass $\Delta M = 0.25$ above the mass limit for each z-range. In Figure 4.3 the COSMOS 2020 SMF is indicated with the shape and normalization that changes considerably over the ~ 10 billion years corresponding to this redshift range [80].

In this work we use the Schechter function fit of Weaver (2022) [80] over the V_{max} non-parametric data. The form of the double Schechter function used to fit data is given by Equation (4.2), that expresses the number density of galaxies as a function of their stellar mass.

The uncertainties in the stellar mass could bias the estimate of the high-mass end. Indeed, errors in the stellar mass scatters more galaxies into the massive end than the reverse, because the galaxy density exponentially decreases towards massive galaxies. This effect is the Eddington bias, which is avoided in the fitting procedure. The stellar mass uncertainties are well characterised by the product of a Lorentzian distribution $L(x) = \tau/[(\tau/2)^2 + x^2]/(2\pi)$ with $\tau = 0.04(1 + z)$ and a Gaussian distribution G with

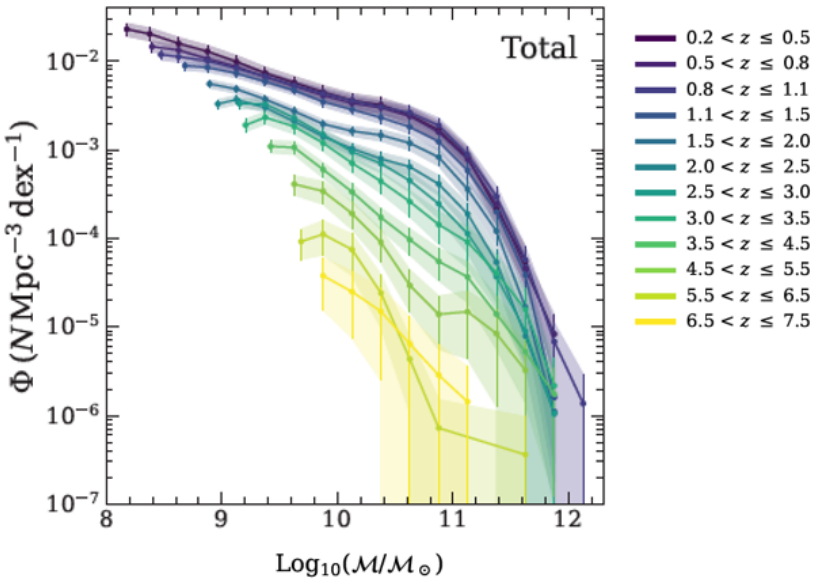

Figure 4.3: Evolution of the galaxy stellar mass function over 12 redshift bins ($0.2 < z < 7.5$) for the total sample [80].

$\sigma = 0.5$. The convolved SMF with the stellar mass uncertainties is fitted to the Vmax non-parametric data. Thus, the intrinsic mass function is recovered with the unconvolved Schechter fit with the best-fit parameters, which are deconvolved by the expected stellar mass uncertainties. As a results, the estimated intrinsic SMFs, used in this work, do not suffer from the Eddington bias.

The inferred intrinsic galaxy stellar mass functions derived by Weaver et al. (2022) are indicated in Figure 4.4. Each colored solid curve shows the SMF at different redshift bin. In this work we consider these intrinsic Schechter functions of SMFs up to $z = 2$.

Moreover, we compute the areas of SMF within the 68% confidence level regions from the entire Monte Carlo Markov chain for each redshift, in order to take into account the covariances between the parameters. In particular, we sample the five Schechter parameters of Equation 4.2 (M_*, α_1, α_2, ϕ_1^*, ϕ_2^*) from the Monte Carlo Markov chains and we evaluate the 84 and 16 percentile ranges, in order to obtain the $\pm 1 - \sigma$ envelopes of the SMFs.

4.3 Used software libraries

CosmoBolognaLib: In order to estimate the clustering properties of the galaxy mock catalogues, computed with the SHAM method, we use the CosmoBolognaLib, a large set of Open Source C++ and Python numerical libraries for cosmological calculations of the large scale structures of the Universe [83]. The main goal of this software is to analyze data from astronomical catalogues, both real and simulated, measuring one-point, two-point (2PCF) and three-point (3PCF) correlation functions in configuration space, exploiting a specifically designed parallel chain-mesh algorithm to count pairs and triplets.

The CBL creates catalogues from samples of astronomical objects, e.g. galaxies, clus-

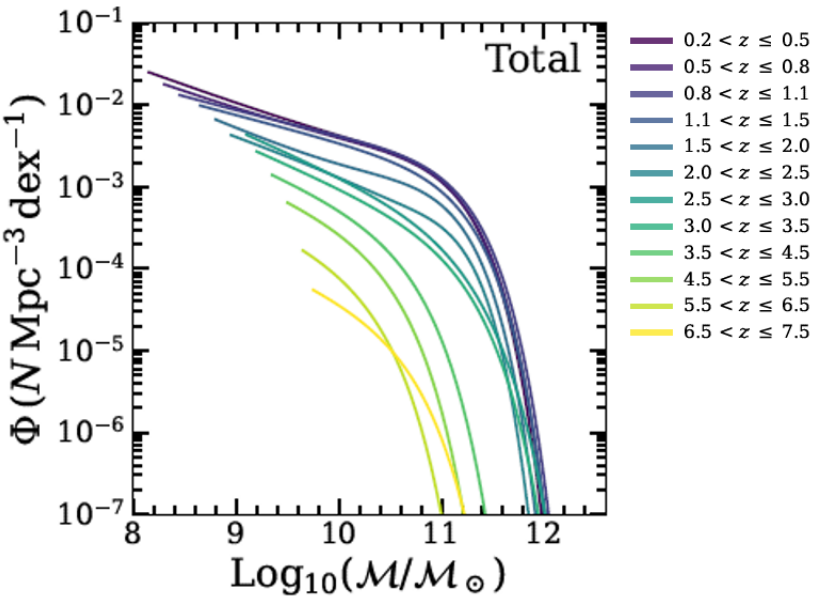

Figure 4.4: Inferred galaxy stellar mass function evolution. Best-fit parameters are estimated by a Markov Chain Monte Carlo fitting with a Schechter Function at fixed redshift convolved with a redshift dependent kernel from which the inferred intrinsic mass function is recovered with the unconvolved Schechter fit (colored solid curves) [80].

ters of galaxies, dark matter haloes and generic mock objects. Moreover, several operations can be performed from the catalogues, such as estimating the distribution of any property of the object members, dividing the catalogues in sub-samples, or creating a smoothed version of the original catalogue.

In this work we use the CBL libraries to measure and model the clustering properties of the galaxy mock catalogues, in particular the two-point correlation function (2PCF).

The 2PCF, $\xi(r)$, is defined as

$$dP_{12} = n^2[1 + \xi(r)]dV_1 dV_2 \,, \tag{4.4}$$

where n is the average number density, and dP_{12} is the probability of finding a pair with one object in the volume dV_1 and the other one in the volume dV_2, separated by a comoving distance r. The algorithm, implemented in the CBL, evaluates this function with the Landy and Szalay (1993) estimator [23]:

$$\xi(r) = \frac{DD(r) + RR(r) - 2DR(r)}{RR(r)} \tag{4.5}$$

where DD, RR and DR are the data-data, random-random and data-random normalised pair counts, respectively, for a separation bin $r \pm dr/2$.

Moreover, the errors of 2PCF measurements are estimated with specific functions in the CBL, which evaluate the covariance matrix defined as follows:

$$C_{ij} = F \sum_{k=1}^{N} (\xi_i^k - \widehat{\xi}_i)(\xi_j^k - \widehat{\xi}_j) \,, \tag{4.6}$$

where the indexes i and j run over the spatial bins of the 2PCF, the index k refers to the 2PCF of the k^{th} realisation, $\widehat{\xi}$ is the mean 2PCF over all the N realisations. Considering jackknife or boostrap errors, the factor F is respectively equal to either $(N-1)/N$ or $1/N$. By definition, the diagonal elements of this matrix represent the variance of the i-th spatial bin, indicated with σ_i^2.

In particular, the CBL provide functions to estimate errors in the covariance matrix with a jackknife method, by sub-sampling the data catalogue and measuring the 2PCF for all but one region, or through a bootstrap method for a random extraction of regions. The volume can be partitioned in cubic sub-regions. This procedure is useful when analysing simulation snapshots. In this work we use the bootstrap technique to estimate the errors on the 2PCF of the galaxy mock catalogues from DEMNUNI simulations.

DenHF: Furthermore, in Chapter 7 we identify haloes catalogues from the stored particle snapshot of DEMNUni simulations using the DenHF halo finder, which consists in a Spherical Overdensity (SO) algorithm ([84]). This method is slightly closer to physical models of halo formation and the Spherical Overdensity definition of halo mass is similar to how mass is defined in observational data.

First of all, the local dark matter density is estimated for each particle at the corresponding position, computing the distance $d_{i;10}$ to the tenth nearest neighbour. Therefore, it is possible to assign a local density $\rho_i \; d_{i;10}^{-3}$ to each particle.

As a second step, the particles are sorted according their density and the position of the densest particle is assigned as the the centre of the first halo. Around this centre a sphere start to grow and the process stops when the mean density within the sphere falls below a fixed critical value. Therefore, all the particles located inside the sphere are assigned to the newly identified halo and are removed from the global list of particles.

As a next step, the densest particle of those remaining is chosen as a centre of a new sphere and the previous points are repeated: a new sphere grows around this particle until the mean enclosed density falls below a fixed threshold. This process is repeated until none of the remaining particles has a local density large enough to be the centre of halo composed by 10 particles. The remaining particles which are not assigned to any halo are called 'field' or 'dust' particles.

In Chapter 7 we extract halo catalogues from the DEMNuni suite for six different values of the overdensity threshold: $\Delta = 2500\rho_c, 1000\rho_c, 500\rho_c, 200\rho_c, 200\rho_b, \Delta_{vir}$, where the comoving density of the background is:

$$\rho_{com} \equiv \rho_b = \rho_c(0)\Omega_m(0) = \rho_c(z)\Omega_m(z) \; , \tag{4.7}$$

and $\rho_c(0) \equiv 3H_0^2/8\pi G \simeq 2.775 \times 10^{11} h^{-1} M_\odot h^3 Mpc^{-3}$ is the critical density.

Expressed all in terms of the background density, ρ_b, the overdensity thresholds considered in this work read in the Planck-15 cosmology as:

$$\Delta_{vir}(z=0) \simeq 319\rho_b \; ,$$

$$200\rho_c(z=0) \simeq 625\rho_b \; ,$$

$$500\rho_c(z=0) \simeq 1562.5\rho_b \; ,$$

$$1000\rho_c(z=0) \simeq 3125\rho_b \; ,$$

$$2500\rho_c(z=0) \simeq 7812.5\rho_b \; .$$

Figure 4.5 shows a summary scheme of haloes identified with DenHF halo finder. All the catalogs contain the halo 1 in common, instead the halos, identified with the numbers 2 and 3, are present respectively only in the overdensity $1000\rho_c$ and virial mass catalogs. In fact, as can be seen in the plot on the right in Figure 4.5 of their density profiles, since halo 1 is dense enough to pass from the highest overdensity $2000\rho_c$ to the lowest overdensity $200\rho_b$, it is common to all catalogues. On the other hand, halos 2 and 3 only reach $1000\rho_c$ and virial overdensity, respectively, and consequently are only present in those catalogs.

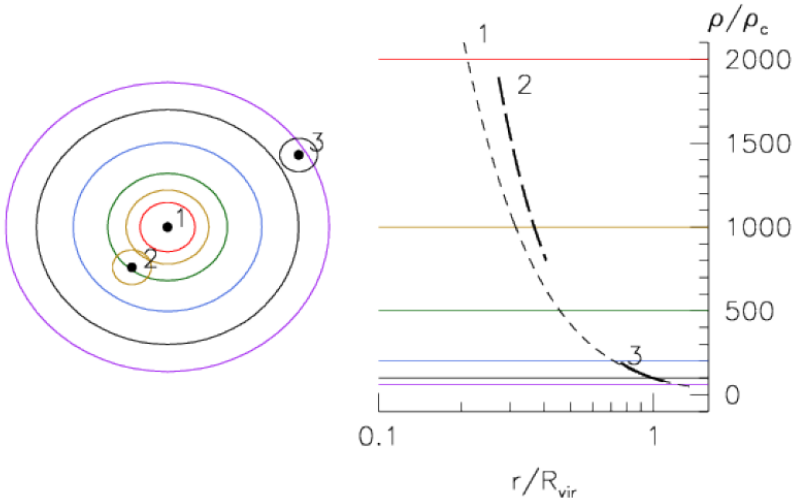

Figure 4.5: Schematic representation of the halo identified in the particle density distribution at z = 0, using the DenHF finder. The results at each overdensity values, from $2000\rho_c$ down to $200\rho_b$, are indicated with different colors. The panel on the right in the figure expresses the density profile of three halos (identified with number 1, 2, 3). The halo centered at 1 is common to all the catalogues, because the SO halo finder DenHF starts to grow the sphere starting from the densest particle. Instead, the ones at 2 and 3 belong only to $1000\rho_c$ and to the virial catalogue, respectively [84].

NbodyKit: Furthermore, in order to compute the power spectra from the halo catalogues from DEMNUni simulations I used the NbodyKit libraries [1]. Nbodykit is an open source project written in Python language. It implemented a large set of algorithms in order to analyse the cosmological datasets of large-scale structure, from N-body simulations and observational surveys. The available algorithms run using the Message Passing Interface (MPI) and they are mainly parallel.

In the NbodyKit libraries the FFTPower algorithm is included. It is fundamental to estimate the 1D power spectrum $P(k)$, the 2D power spectrum $P(k, \mu)$ and the multipoles $P_l(k)$. The algorithm can be used on data sets in periodic simulation boxes, because the power spectrum is computed through a single FFT of the density mesh.

In this work, I use these libraries to estimate the 1D power spectra of the matter distribution, the halo power spectra for many halo overdensity values $200\rho_c(z)$, $200\rho_b$, $500\rho_c(z)$, $1000\rho_c(z)$, $2500\rho_c(z)$ and virial value, and the cross power spectra between the matter distribution and the halo catalogues. All the estimates at five redshift values $z = 0, 0.5, 1, 1.5, 2$ are illustrated in Chapter 7.

[1] https://nbodykit.readthedocs.io/en/latest/index.html

These values of the overdensity thresholds are adopted because they are very close to the ones generally used in Cosmology. In fact, $200\rho_b$ and $200\rho_c$ are the common values used in Tinker et al. 2008 [85]. In particular, $200\rho_b$ is motivated by the spherical collapse model in an Einstein de-Sitter Universe and $200\rho_c$ is generally used to define galaxy cluster masses. Moreover, $500\rho_c$ and higher overdensity thresholds, such as $1000\rho_c$ and $2500\rho_c$, are used in X-ray analyses, and in general in observations that are able to resolve only the inner parts of haloes. Therefore, we consider the corresponding halo catalogues in Chapters 7 and 8, in order to compute the mass function and bias of clusters (not their substructures). Instead, the DEMNUni halo catalogues, identified via the SUBFIND algorithm, are used in Chapters 5 and 6 to populate them with galaxies using the SHAM method. To this aim the SUBFIND finder is preferable to spherical overdensity halo finders, such as DENHF, as it allows one to find also substructures, i.e. subhalos, and therefore to populate the simulations with satellite galaxies as well as the central ones.

CHAPTER 5

The galaxy-halo relation in the ΛCDM model

The goal of this work is to connect dark matter structures in N-body simulations with galaxies, using an abundance matching method. As a result, it is possible to build a mock catalogue of galaxies in different cosmological models. To this end we consider dark matter subhaloes in the "Dark Energy and Massive Neutrino Universe" simulations (DEMNUni), described in Chapther 4.

In this Chapter we focus on the connection between galaxies and subhaloes, considering simulations in the ΛCDM cosmological model. First, we describe the implemented method of abundance matching and the parameterised form of SHMR, needed to connect subhalo mass with galaxy mass; second, we use this procedure to populate simulations with galaxies. Third, we present and discuss the obtained results. Finally, we compare the clustering properties of these mock galaxy catalogues with the observations from the VIPERS survey.

5.1 The SHAM method for ΛCDM haloes

In order to connect the halo/subhalo mass to the mass of their central/satellite galaxy, we adopt an empirical parameterisation of the stellar-to-halo-mass relation (SHMR) as a function of the halo mass, which depends on four free parameters, used in Moster et al. (2010) [50]:

$$\frac{M_*(M_H)}{M_H} = 2A\left[\left(\frac{M_H}{M_A}\right)^{-\beta} + \left(\frac{M_H}{M_A}\right)^{\gamma}\right]^{-1} . \tag{5.1}$$

The ratio of the stellar-to-halo mass content peaks at a characteristic halo mass, and decreases at higher and lower halo masses. The four parameters describe the shape of the stellar-to-halo mass relation, in particular they determine its slope at high and low masses respectively, the normalisation of the SHMR, and the characteristic mass corresponding to the peak of the stellar-to-halo ratio. The stellar-to-halo mass relation has a redshift evolution, and, therefore, also its parameters are redshift dependent.

First, we find the fitting parameters characterising the SHMR, by matching the subhalo mass function (SHMF) of the DEMNuni simulations to the observed galaxy stellar mass function (SMF), obtained from galaxies samples of the Sloan Digital Sky Survey (SDSS) and the Cosmological Evolution Survey (COSMOS), over the redshift range $0 < z < 2$. In particular, we use the SDSS data at redshifts up to $z = 0.2$, and the COSMOS observations for higher redshifts up to $z = 2$.

We compute the SHMF considering the subhalo catalogue, in a range of mass from $3.7 \times 10^{12} M_\odot$ to $7.5 \times 10^{15} M_\odot$. Since we need information about the abundance of subhaloes with mass smaller than the minimum subhalo mass provided by the simulations (namely $3.7 \times 10^{12} M_\odot$), we fit to the simulated catalogues the theoretical subhalo mass

function at each redshift, and extend it by extrapolating its low-mass tail. Therefore, in order to compute the parameters characterising the stellar mass function, we do not use directly the subhalo catalogues from the simulations, but instead we exploit fits of a functional form of the subhalo mass function against the simulated subhalo catalogues. In other words, we implement a subhalo mass extrapolation, finding the best-fit parameters of the Angulo et al. (2013) [53], recovering the SHMF of the simulations at high masses, *i.e.* larger than $3.7 \times 10^{12} M_{\odot}$, but extending it down to low masses larger than $1.5 \times 10^{10} M_{\odot}$. The model of Angulo et al. (2013) [53] provides a functional form that describes the subhalo abundance in simulations according to the expression below:

$$\frac{dn}{d\ln M} = -\frac{1}{3}\frac{\bar{\rho}_{m,0}}{M} f(\sigma) \frac{d\ln\sigma}{d\ln R} \,. \tag{5.2}$$

In Equation (5.2), the number of subhaloes at a given mass depends on the mean mass density $\bar{\rho}_{m,0}$ of the Universe and on the variance σ of the matter density smoothed at a scale $R(M)$, corresponding to a lagrangian sphere containing a mass M with density $\bar{\rho}_m$

$$\sigma(M,z) \equiv \int P_{lin}(k,z) W(kR) k^2 dk \,, \tag{5.3}$$

where $P(k)$ is the linear matter power spectrum as a function of the wavenumber k, estimated using CAMB package, and W is the Fourier transform of the real-space top-hat window function with radius R. In addition, Equation (5.2) depends on the function $f(\sigma)$, which is expected to be universal in redshift and model cosmology, and it is parametrised in terms of

$$f(\sigma(M)) = A \left[\frac{b}{\sigma(M)} + 1\right]^a \exp\left[-\frac{c}{\sigma(M)^2}\right] , \tag{5.4}$$

with parameters (A, a, b, c) that we calibrated on DEMNUni simulations.

From the data of SMF and SHMF we calculate the corresponding cumulative mass function, shown in Figure 5.1. In particular, the galaxy cumulative number density N_* and the subhalo cumulative number density N_H above a certain mass are respectively given by

$$N_*(M_*) = \int_{M_*}^{+\infty} \phi_*(M) dM \,, \tag{5.5}$$

and

$$N_H(M_H) = \int_{M_H}^{+\infty} \phi_H(M) dM \,, \tag{5.6}$$

where ϕ_* and ϕ_H are respectively the stellar and the subhalo mass functions.

As a consequence, the stellar mass of a galaxy we can associate to a given subhalo mass is the one for which the number densities obtained by the corresponding cumulative mass functions (respectively the mass function for the simulated haloes/subhaloes, and the observed one for galaxies) are the same. In other words, we find the value of M_H corresponding to M_* such that

$$N_*(M_*) = N_H(M_H) \,. \tag{5.7}$$

Using this matching technique, we can calculate the ratio between the stellar mass for satellite galaxy and the subhalo mass as a function of the subhalo mass at different redshifts, corresponding to different outputs of the simulations. As a result, we compute the SHMR.

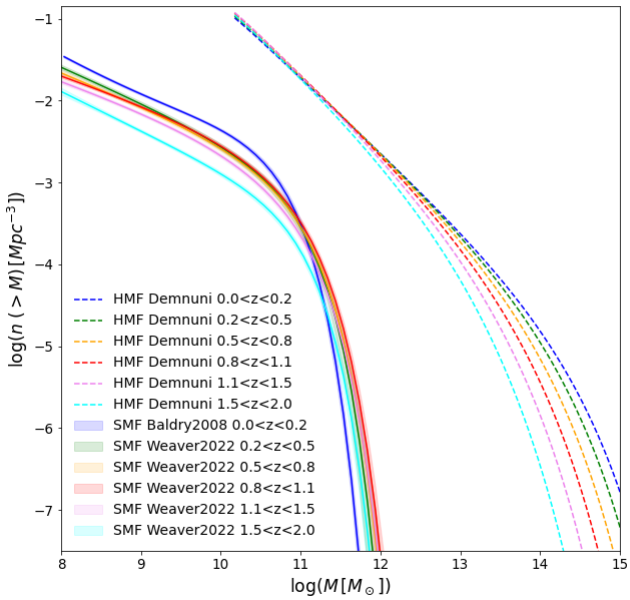

Figure 5.1: Comparison between the cumulative galaxy stellar mass functions and the cumulative halo mass functions. Solid lines represent the stellar mass functions from Baldry et al. (2008) [79] and Weaver et al. (2022) [80] with associated 1–σ uncertainty (shaded area). Dashed lines represent the subhalo mass funtions from the DEMNUni simulations in the ΛCDM scenario. Different colors indicate different redshift ranges.

After performing this matching, and using a Monte Carlo Markov Chain (MCMC) fitting procedure, we find the parameters A, M_A, β, γ of the Moster et al. (2010) [50] relation, Equation (5.1), that fit the SHMR computed for each redshift. To fit the model of SHMR to the obtained data, we minimise a chi-square random variable, defined as:

$$\chi^2 = \sum_i \left(\frac{\frac{M_*}{M_H}(M_{H,i})_{data} - \frac{M_*}{M_H}(M_{H,i})_{model}}{\sigma_i} \right)^2 \tag{5.8}$$

where σ_i is the uncertainty of the ratio between the galaxy stellar mass and subhalo mass in a given halo mass bin $M_{H,i}$, calculated propagating the observational error of the SMF. For each of the redshift bins in the range $0 < z < 2$, we minimise Equation (5.8) using a MCMC algorithm[1]. This algorithm allows to sample the parameter space in order to derive the posterior distribution for the four free parameters considered. We use flat conservative priors on the parameters together with 100 walkers for 1000 steps, each with a different starting point randomly selected in a Gaussian distribution around the original starting point, fixed at the parameter values of the SHMR found by Moster et al. (2010) [50].

[1] we use the software package emcee, i.e. a purely python implementation of the Monte Carlo Markov chain (MCMC) [86]

Also, we use the Gelman-Rubin (GR) diagnostic method to check the MCMC convergence [87]. The sampling is stopped when the GR statistic (denoted with R) satisfies the condition $R < 1 + \delta$, with the threshold $\delta = 0.05$.

We show in Table 5.1 the best fit values for the four free parameters, as well as their 68% confidence interval in each redshift bins.

redshift	A	β	γ	$\log(M_A/M_\odot)$
$0.0 < z < 0.2$	$0.0266^{+0.0007}_{-0.0007}$	$1.116^{+0.030}_{-0.031}$	$0.687^{+0.008}_{-0.008}$	$12.004^{+0.024}_{-0.024}$
$0.2 < z < 0.5$	$0.0172^{+0.0008}_{-0.0008}$	$1.017^{+0.045}_{-0.047}$	$0.590^{+0.023}_{-0.024}$	$12.232^{+0.050}_{-0.050}$
$0.5 < z < 0.8$	$0.0172^{+0.0006}_{-0.0006}$	$1.048^{+0.062}_{-0.067}$	$0.564^{+0.018}_{-0.018}$	$12.285^{+0.048}_{-0.049}$
$0.8 < z < 1.1$	$0.0206^{+0.0007}_{-0.0007}$	$1.164^{+0.068}_{-0.070}$	$0.534^{+0.016}_{-0.016}$	$12.227^{+0.041}_{-0.043}$
$1.1 < z < 1.5$	$0.0176^{+0.0005}_{-0.0005}$	$1.149^{+0.058}_{-0.062}$	$0.499^{+0.016}_{-0.017}$	$12.303^{+0.039}_{-0.040}$
$1.5 < z < 2.0$	$0.0161^{+0.0005}_{-0.0005}$	$1.266^{+0.061}_{-0.063}$	$0.520^{+0.017}_{-0.016}$	$12.458^{+0.037}_{-0.038}$
$2.0 < z < 2.5$	$0.0130^{+0.0007}_{-0.0007}$	$1.174^{+0.071}_{-0.074}$	$0.506^{+0.033}_{-0.034}$	$12.619^{+0.057}_{-0.061}$

Table 5.1: Best-fit values of the parameters $\{M_A,\, A,\, \beta,\, \gamma\}$ modelling the SHMR (see Equation (5.1)) together with their 1–σ uncertainties, obtained from the DEMNUni simulations in the ΛCDM massless neutrino case, for the redshift bins of the considered galaxy surveys.

5.2 Redshift Evolution of the SHMR

In Figure 5.2 we show the values of the best-fit parameters at different redshifts. The error bars indicate the 1–σ uncertainties of the parameters. In addition, following Girelli et al. (2020) [88] for each SHMR parameter we use a redshift evolution according the following equations:

$$\log M_A(z) = \big(\log M_A(z)\big)_{z=0} + \mu\, z = M_0 + \mu\, z\,, \tag{5.9}$$

$$A(z) = \left(\frac{M_*}{M_H}\right)(z) = \left(\frac{M_*}{M_H}\right)_{z=0} (1+z)^\nu = A_0(1+z)^\nu\,, \tag{5.10}$$

$$\beta(z) = \beta_0 + B\, z\,, \tag{5.11}$$

$$\gamma(z) = \gamma_0(1+z)^\eta\,. \tag{5.12}$$

In Figure 5.2 we show the resulting fitting curves, which describe the redshift evolution of the SHMR parameters according Equations (5.12), (5.11), (5.10), (5.9), together with the corresponding shaded areas at 1–σ and 2–σ confidence level, calculated by propagating the errors of the parameters estimated with the MCMC method. In Table 5.2 we report the best-fit values of the eight parameters and its 1–σ uncertainties.

Using the fitting functions, the stellar mass of a central/satellite galaxy is then given as a function of the virial mass of its dark matter halo/subhalo M_{vir} and redshift z. As a result, we obtain a SHM relation $m(M, z)$ depending on the virial mass of the main halo/subhalo and the redshift of the corresponding central/satellite galaxy.

5.3 Comparison with the literature

We compare our assumed model for the SHMR with other works in literature. In Figure 5.3 we show this comparison at $z \sim 0.1$, $z \sim 1$ and $z \sim 1.8$, respectively. The blue

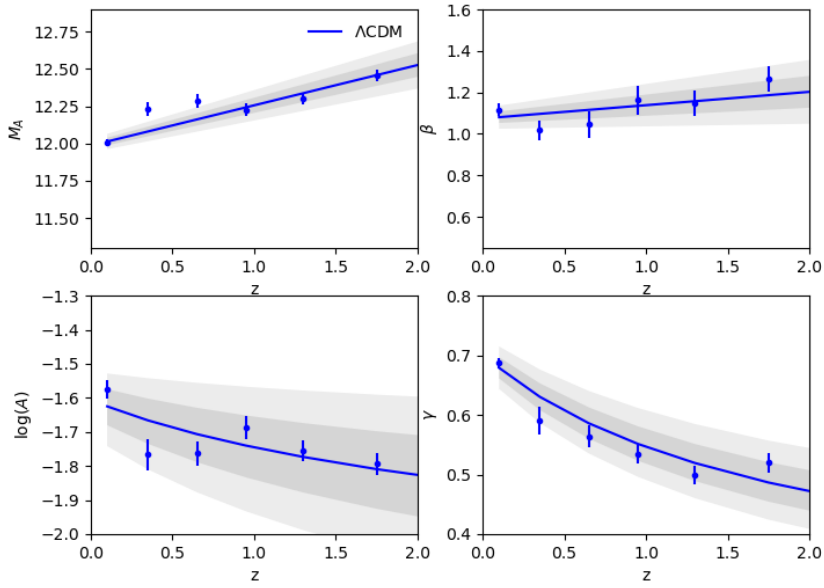

Figure 5.2: Redshift evolution of the four SHMR parameters $\{M_A,\ A,\ \beta,\ \gamma\}$. The points represent the best-fit values of the SHMR parameters computed applying the SHAM technique to the DEMNUni subhalo catalogues in the ΛCDM massless neutrino scenario, for the redshift bins reported in Table 5.1. The error bars show the associated 1–σ uncertainties obtained via the MCMC method. Solid lines indicate the best-fit model describing their redshift evolution (see Equations (5.9)-(5.12)), and shaded areas represent the associated 1–σ and 2–σ uncertainties.

$\log(M_A)$	$M_0 = 11.99 \pm 0.02$	$\mu = 0.27 \pm 0.03$
A	$A_0 = 0.025 \pm 0.003$	$\nu = -0.46 \pm 0.15$
β	$\beta_0 = 1.07 \pm 0.03$	$B = 0.06 \pm 0.03$
γ	$\gamma_0 = 0.703 \pm 0.015$	$\eta = -0.36 \pm 0.05$

Table 5.2: Best-fit values of the parameters modelling the redshift evolution of the SHMR parameters $\{M_A,\ A,\ \beta,\ \gamma\}$ (see Equations (5.9)-(5.12)) together with their 1–σ uncertainties. The reported results have been obtained from the DEMNUni simulations in the ΛCDM massless neutrino case.

line shows the redshift-dependent SHM relation computed in the previous section. The shaded area represent the 1–σ and 2–σ region. The error on the SHMR model is calculated propagating the error of the parameters in Table 5.2, obtained with the MCMC method.

Among other works in the literature adopting the abundance matching technique, we consider for comparison with our results the ones from Moster et al. (2010) [50], that uses our same parametrisation for the SHMR, Equation (5.1), but with a different redshift-evolution of the parameters. Yet, Moster et al. (2013) [51] use a self-consistent

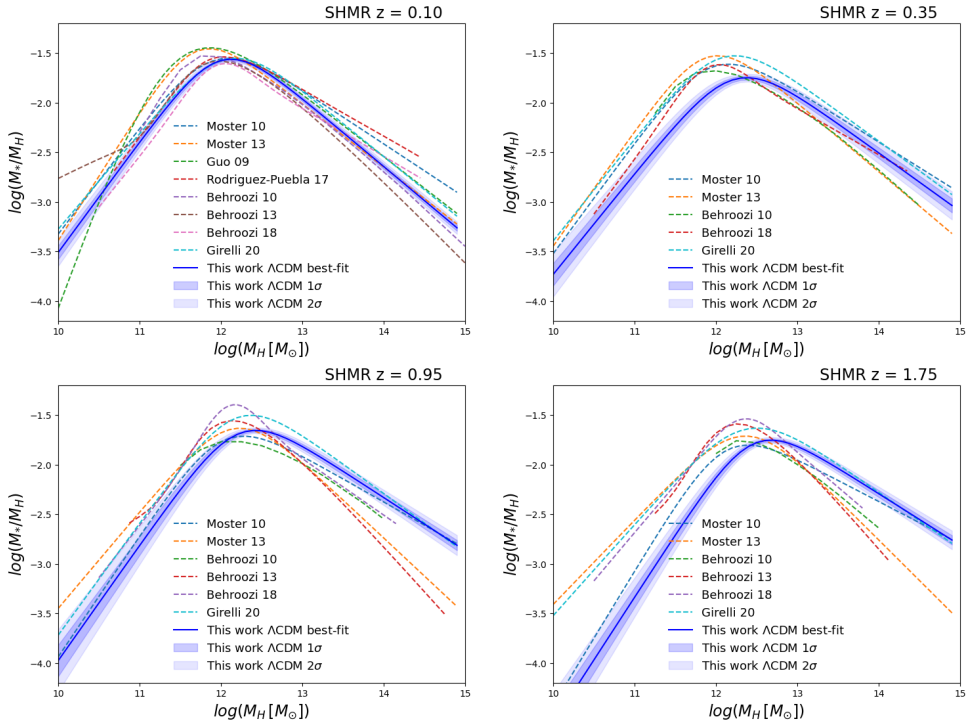

Figure 5.3: Comparison of the obtained SHMR against previous works in literature at $z = 0.1, 0.3, 1.0, 1.8$. In each panel the solid blue line shows the results of this work together with the corresponding 1–σ and 2–σ uncertainties represented by the shaded area. Dashed lines show the abundance matching results from Moster at al. 2010, 2013 [50, 51], Behroozi et al. 2010, 2013 2018 [89, 90, 91], Guo et al. 2009 [92], Rodriguez-Puebla et al. 2017 [93] and Girelli et al. 2020 [88].

multi-epoch abundance matching model. They adopt a redshift-dependent parameterisation of the stellar-to-halo mass relation to populate haloes and subhaloes in the Millennium simulations with galaxies, and constrain the parameters requiring that the observed stellar mass functions are reproduced simultaneously at different redshifts.

Moreover, in Figure 5.3 the results of Behroozi et al. [89, 90, 91] are also presented. They first provide a parameterisation of the intrinsic SHMR, then, using a MCMC method they determine the allowed parameter space for $M_*(M_H, z)$ by comparing, in a wide redshift range, the implied galaxy star formation rates and stellar mass abundances to observations.

Also, we consider the results of Guo et al. [92] for a further comparison. They connect the dark halo mass to the stellar mass of the central galaxy by assuming a one-to-one and monotonic relationship between the two. To derive the relation between M_H and M_* they combine the halo mass function with an equally precise observed stellar mass function for galaxies. They adopt a double power-law to approximate their SHMR function and find the corresponding best-fit parameters to their results.

Another comparison is the work from Rodriguez-Puebla et al. [93]. They determine the stellar-to-halo- mass relation that matches the evolution of the galaxy stellar mass function, the relation between the star formation rate and the stellar mass and the cosmic star formation rate.

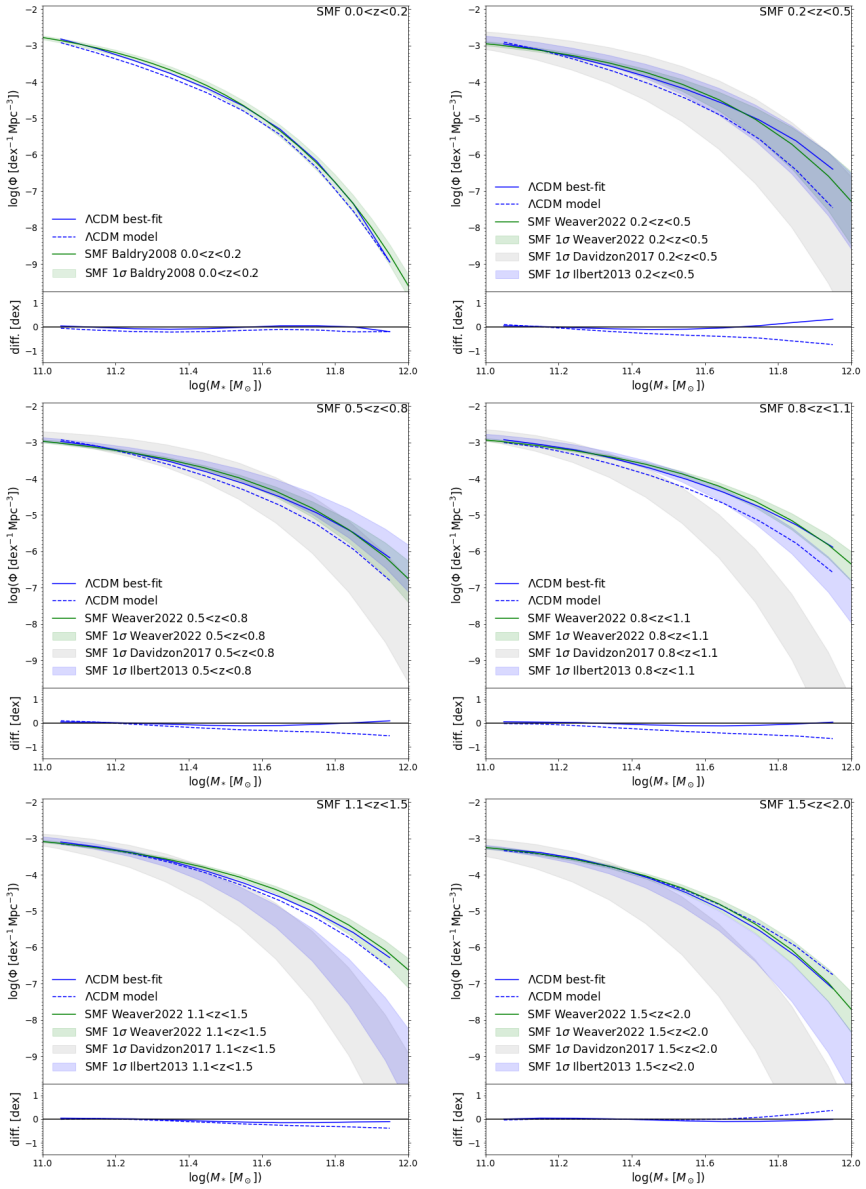

Figure 5.4: Stellar mass functions obtained from the galaxy mock catalogues of the DEMNUni simulations in the ΛCDM massless neutrino scenario at the different redshift bins in Table 5.1. In each plot the upper panels show the SMF calculated using the best-fit SHMR parameters in Table 5.1 (solid blue line) extracted at each redshift bin, or using the z-dependent SHMR model in Table 5.2 (dashed blue line). These results are compared to the observed SMFs of Baldry et al. (2008) [79] and Weaver et al. (2022) [80], with shaded green area representing the associated 1–σ uncertainty, as reported in the legenda. The lower panels show the logarithmic differences between the SMFs obtained from the simulations and the observed ones.

The model is consistent with other works, as Figure 5.3 shows. However we can

appreciate some differences due to different assumptions made by other works on the cosmological model and the definition of the halo mass. In particular, different halo finders, including the friends-of-friends (FOF), spherical-overdensity (SO) and phase-space based algorithms, produce difference up to 10% in halo mass, that increase with the redshift [94]. In addition, other works in the literature make use of different observed data, such as different stellar mass functions and measurements of stellar mass, in order to calibrate the SHMR model.

5.4 Testing the stellar-to-halo mass relation

After we have found the relation that links M_H to M_*, we can assign to each dark matter subhalo with virial mass M_{vir} the corresponding stellar mass of its satellite galaxy using two different methods.

The first one is to calculate the stellar mass from the double power-law Equation (5.1), using the corresponding best-fit parameters reported in Table 5.1.

The second method assigns the stellar mass M_* to each subhalo using our model for the z-dependence of SHMR (Equations (5.12)-(5.9)), with the obtained best-fit parameters in Table (5.2).

In addition, for both methods the spatial position assigned to each galaxy corresponds to the centre of the dark matter subhalo in which they reside.

In order to test the validity of our model to populate dark matter haloes/subhaloes of virial mass, we calculate the galaxy stellar mass function of the galaxy mock catalogues obtained from the simulations.

For each redshift output in the range $0 < z < 2$, we calculate the galaxy counts N_g in logarithmic bin of stellar mass with amplitude 0.1 in the range $11 < \log_{10} M_*[M_\odot] < 12$. Then, we divide the counts by the simulation volume $V = 8(\mathrm{Gpc}/h)^3$, and of the logarithmic mass bin $\log_{10} M_*[M_\odot] = 0.1$. Then, we compute the stellar mass function as the galaxy number density: $\phi = dN_g/(dV d\log M_*)$. We compare the stellar mass function from simulations to the corresponding observed data. We use the same stellar mass function data used to constraint the parameters of SHMR: Baldry et al. (2008) [79] SMF for $0 < z < 0.2$ and Weaver et al. (2022) [80] for $0.2 < z < 2$.

The simulated SMFs from cosmological boxes for each redshift interval are consistent with the observed data as expected by construction. Indeed the relative differences from observations for the simulated SMFs with the best-fit parameters and those obtained from the z-dependent model are respectively within 0.3 dex and 1 dex.

5.5 Galaxy clustering in real and redshift space

In this Section we check that the clustering of mock galaxy catalogues is correctly reproduced with the SHAM method described before, calculating its two-point correlation function (2PCF) and comparing it with the corresponding observations. We consider the galaxy mock catalogues on simulated boxes obtained with the best-fit SHMR parameters and we construct the redshift-space catalogues choosing z-direction as the line-of-sight direction. Assuming cartesian coordinates (r_x, r_y, r_z) we modify the r_z coordinate of the catalogue with the following approximation:

$$r_z^S = r_z + \frac{v_z(1+z_{box})}{H(z_{box})} \,, \tag{5.13}$$

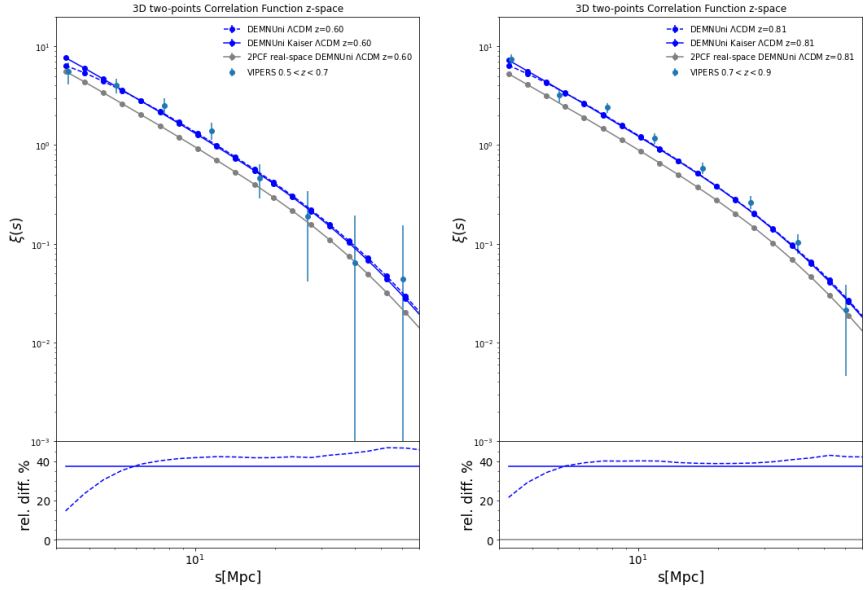

Figure 5.5: Galaxy 2-pt correlation functions (2PCFs) at $z_c = 0.6$ (right) and $z_c = 0.8$ (left). The upper panel shows the $\xi(s)$ measured from the ΛCDM DEMNUni galaxy mock catalogues with the redshift space distortions (blue dashed line) and the $\xi(s)$ predicted with Kaiser effect (blue solid line). Gray line shows the real-space 2PCF $\xi(r)$ measured from the simulations. Blue points with error bars indicates the galaxy 2PCF measured from the VIPERS data. The lower panel shows the relative percentage difference between $\xi(s)$ and $\xi(r)$, with $\xi(s)$ measured from the DEMNUni galaxy mocks (dashed line) and predicted with the Kaiser effect (solid line).

where v_z is the z component of the subhalo peculiar velocity and z_{box} the cosmological redshift of the snapshot.

We perform the measurements of the 2PCF on redshift space catalogues for galaxies with mass $M_* > 10^{11} M_\odot$, according the resolution of simulations, with the CosmoBolognaLib package [83], which directly computes it using the the Landy & Szalay estimator [23] given by

$$\xi_{LS}(r) = \frac{DD(r) - 2DR(r) + RR(r)}{RR(r)} \,, \tag{5.14}$$

where DD is the normalized pair counts of data (galaxies) in the sample, RR is that expected from a random distribution with the same mean density and geometry and DR are the normalized data-random pair counts.

The measurements of the correlation functions from the galaxy mock catalogues of DEMNUni simulations in the ΛCDM model are shown in Figure 5.5: the blue dashed line and the gray line are the 2PCFs in redshift and real space respectively at $z = 0.6 - 0.8$, compared with the 2PCF of galaxies observed (loght-blue points) in the VIPERS survey, at $0.5 < z < 0.7$ and $0.7 < z < 0.9$ respectively, as in Girelli et al. 2020 [88]. In addition, we estimate the theoretical correlation function in redshift space $\xi(s)$ from that in real space $\xi(r)$ according the Kaiser model computing analytically the linear RSD distortion parameter β

$$\xi(s) = \left(1 + \frac{2\beta}{3} + \frac{\beta^2}{5}\right)\xi(r) \tag{5.15}$$

$$\beta = \frac{f(z)}{b(z)} \simeq \frac{\Omega_m^{0.545(z)}}{b(z)} \,. \tag{5.16}$$

The linear bias $b(z)$ is calculated as the square root of the ratio between the real-space galaxy correlation function and the matter correlation function, that is the Fourier transform of the non-linear matter power spectrum evaluated with CAMB package. The bias is computed as the mean at large scales $r > 30\,\mathrm{Mpc}$ at which non-linear effects can be neglected. The theoretical prediction of the redshift space correlation function from DEMNUni simulations are shown in Figure 5.5 with the blue solid line, and the relative percentage difference between the measured and predicted 2PCFs in redshift space versus the real-space 2PCF are indicated in the lower panel in Figure 5.5.

CHAPTER 6

The galaxy-halo relation in alternative cosmologies

In this Chapter we connect galaxies to dark matter subhaloes in the DEMNUni simulations, considering cosmological models which take into account the presence of massive neutrinos and dark energy with a dynamical equation of state (EoS).

To this purpose, we exploit the abundance matching technique implemented in the Chapter 5. In particular, we analyse simulations with a total neutrino mass that varies over the values $\sum m_\nu = 0.16, 0.32$ eV. In addition, the dynamical dark energy has an equation of state with four different combination of the CPL parameters: $w_0 = -0.9, -1.1$ and $w_a = -0.3, 0.3$.

First, we analyse the case with massive neutrinos of different total mass, fixing the dark energy to a cosmological constant, *i.e.* dark energy EoS with $w_0 = -1$ and $w_a = 0$.

Second, we study the dynamical dark energy case, assuming the massless neutrino case.

Third, we analyse the galaxy-halo connection in simulations that accounts for the combination of massive neutrinos and dynamical dark energy. For each cosmological model we compute the SHMR comparing the observations with the corresponding subhalo mass function. Figure 6.1 shows the obtained subhalo mass functions. As in the previous section, at low-mass ($M_H < 2.5 \times 10^{12} M_\odot$) we implemented an extrapolation using Angulo et al. (2016) [95] model. In particular we compute the parameters of $f(\sigma)$ in Eq (5.4) that fit the DEMNUni SHMFs, evaluating the variance of the linear density field $\sigma(M)$ in Eq (5.3) with the linear power spectrum at each different alternative model using the CAMB package.

6.1 The SHAM method in massive neutrino scenarios

As expected in the left panel of Figure 6.1 the subhalo mass function in the presence of massive neutrinos differs from the the ΛCDM one. In particular, massive neutrinos affect the subhalo mass function and suppress it due to the neutrino free-streaming effect. Moreover, the suppression is higher for higher value of neutrino masses. Indeed, the relative difference to the massless case for the highest mass $M_\nu = 0.32$ eV is greater than the lower mass value $M_\nu = 0.16$ eV. The percent differences to the ΛCDM, at the largest subhalo masses, are more than 50% for $M_\nu = 0.16$ eV, and about 100% for $M_\nu = 0.32$ eV, as it is shown in the section below the upper panel in Figure 6.1.

Performing the abundance matching method described in the previous section, we find the four parameters of the Moster et (2010) relation [50], Equation (3.3), which fits the SHMR computed for each redshift bin of observations and for the two neutrino mass values, using an MCMC fitting procedure. The obtained parameters, *i.e.* the normalization A, the characteristic mass M_A, the high-mass slope γ, and the low-mass slope

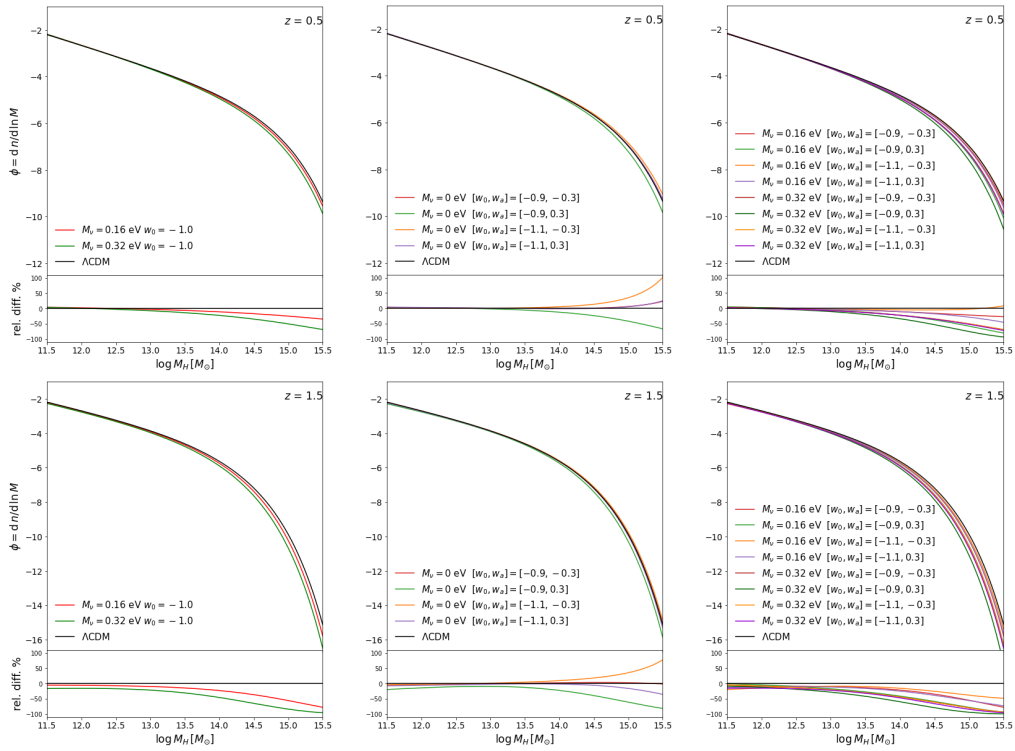

Figure 6.1: Subhalo mass functions from the DEMNUni simulations at $z = 0.5$ (upper panels) and $z = 1.5$ (lower panels). Left: SHMF in the cosmological constant scenario with total neutrino masses $M_\nu = 0.16, 0.32$ eV (here the black solid line represents the ΛCDM massless neutrino case). Middle: SHMF in the presence of dynamical dark energy with different EoS parameters (as reported in the legenda) and massless neutrinos. Right: SHMF in the presence of dynamical dark energy with different EoS parameters and massive neutrinos with $M_\nu = 0.16, 0.32$ eV. The relative percent differences between each model and the ΛCDM case are shown in the corresponding subpanels.

β, are represented respectively by the points with error bars in the redshift-M_ν plane in Figure 6.2.

Moreover, we study the evolution of the SHMR parameters with the redshift and the neutrino mass. Considering fixed redshift values, the trend of these parameters as a function of increasing neutrino mass is linear. In particular at high redshfit it is slightly linearly increasing for A and β, slightly linearly decreasing for M_A and constant for γ. For this reason, we consider the trend with a polynomial function at the first order of neutrino total mass M_ν, corresponding to the first lines in the each system of equations (6.1), (6.2), (6.3), (6.4). As we analysed in Section 5.1 the parameters evolve with redshift according a power-law for M_A and A and a linear function for β and γ. Therefore we consider redshift-dependent fitting functions according second and third lines in Equations (6.1), (6.2), (6.3), (6.4). Using the latter systems of equations we find the corresponding best-fit surfaces as a function of redshift and neutrino mass. The resulting surfaces are shown in Figure 6.2 and the best-fit parameter values of slope m_i^ν and intercept q_i^ν for each SHMR parameter $i = M_A, A, \beta, \gamma$ are listed in Table 6.1 with its 68%

confidence intervals.

$$\begin{cases} \log(M_A) = m^{\nu}_{M_A} M_\nu + q^{\nu}_{M_A} \\ m^{\nu}_{M_A} = A^{m}_{M_A}\, z + B^{m}_{M_A} \\ q^{\nu}_{M_A} = A^{q}_{M_A}\, z + B^{q}_{M_A} \end{cases} \tag{6.1}$$

$$\begin{cases} A = m^{\nu}_{A} M_\nu + q^{\nu}_{A} \\ m^{\nu}_{A} = A^{m}_{A}\, z^2 + B^{m}_{A}\, z + C^{m}_{A} \\ q^{\nu}_{A} = A^{q}_{A}\, z^2 + B^{q}_{A}\, z + C^{q}_{A} \end{cases} \tag{6.2}$$

$$\begin{cases} \beta = m^{\nu}_{\beta} M_\nu + q^{\nu}_{\beta} \\ m^{\nu}_{\beta} = A^{m}_{\beta}\, z + B^{m}_{\beta} \\ q^{\nu}_{\beta} = A^{q}_{\beta}\, z + B^{q}_{\beta} \end{cases} \tag{6.3}$$

$$\begin{cases} \gamma = m^{\nu}_{\gamma} M_\nu + q^{\nu}_{\gamma} \\ m^{\nu}_{\gamma} = A^{m}_{\gamma}\, z^2 + B^{m}_{\gamma}\, z + C^{m}_{\gamma} \\ q^{\nu}_{\gamma} = A^{q}_{\gamma}\, z^2 + B^{q}_{\gamma}\, z + C^{q}_{\gamma} \end{cases} \tag{6.4}$$

$\log(M_A)$	
$m^{\nu}_{M_A}$	$A^{m}_{M_A} = -0.116 \pm 0.062 \quad B^{m}_{M_A} = 0.020 \pm 0.010$
$q^{\nu}_{M_A}$	$A^{q}_{M_A} = 0.272 \pm 0.013 \quad B^{q}_{M_A} = 11.989 \pm 0.008$
A	
m^{ν}_{A}	$A^{m}_{A} = -0.0012 \pm 0.0010 \quad B^{m}_{A} = 0.0074 \pm 0.0096 \quad C^{m}_{A} = 0.0004 \pm 0.0003$
q^{ν}_{A}	$A^{q}_{A} = 0.0009 \pm 0.0012 \quad B^{q}_{A} = -0.0063 \pm 0.0052 \quad C^{q}_{A} = 0.0235 \pm 0.0027$
β	
m^{ν}_{β}	$A^{m}_{\beta} = -0.008 \pm 0.010 \quad B^{m}_{\beta} = 0.077 \pm 0.068$
q^{ν}_{β}	$A^{q}_{\beta} = 0.072 \pm 0.030 \quad B^{q}_{\beta} = 1.074 \pm 0.032$
γ	
m^{ν}_{γ}	$A^{m}_{\gamma} = 0.001 \pm 0.001 \quad B^{m}_{\gamma} = 0.008 \pm 0.002 \quad C^{m}_{\gamma} = -0.018 \pm 0.010$
q^{ν}_{γ}	$A^{q}_{\gamma} = 0.088 \pm 0.014 \quad B^{q}_{\gamma} = -0.272 \pm 0.026 \quad C^{q}_{\gamma} = 0.710 \pm 0.009$

Table 6.1: Best-fit values of the parameters entering the functions which model the redshift dependence of the slopes, m^{ν}, and the intercepts, q^{ν}, in the SHMR parameters $\{M_A,\, A,\, \beta,\, \gamma\}$ (see Equations (6.1)-(6.4)), for the cosmological constant scenario with massive neutrinos.

In order to test the redshift-M_ν dependence of our model, we compute the SHMR parameters using Equations (6.1)-(6.4) at fixed value of $M_\nu = 0,\, 0.16,\, 0.32$ eV and we compare the results in Figure 6.3 with solid lines as a function of the redshift. With

respect to the ΛCDM massless case, the differences of the parameter values for the neutrino mass $M_\nu = 0.32$ eV are about twice than for the case with $M_\nu = 0.16$ eV. Moreover, for both case the percent relative differences increase with the redshift. This effect is especially relevant for the normalization parameter A, as it is shown in the lower left panel in Figure 6.3.

The trend of the parameters with the variation of the neutrino mass is in agreement with the expected one. The reason of this trend is that the simulated SHMFs differ monotonically from the massless case, with increasing neutrino mass, as visible in the upper panel of Figure 6.1, due to the free streaming of neutrinos. As a result, the parameters of the SHMR calibrated on these halo mass functions are affected by this effect.

Furthermore, using the values of the parameters obtained with the abundance matching method, we calculate the model of SHMR, corresponding to Equation (3.3), at different values of the neutrino mass. We compare the resulting SHMR models, with the ΛCDM massless case, obtained in Section 5.1. Figure 6.4 shows the SHMR models, obtained for the two values $M_\nu = 0.16, 0.32$ eV, at central values of the SMFs redshift intervals. In each figure, the upper panel shows the SHMR ratio, while the lower panel shows the corresponding percent differences of both models versus the ΛCDM case.

The trend of the parameters with the variation of the neutrino mass is reflected in the SHMR model. Indeed, the differences are greater for higher values of the neutrino mass, and increase proportionally with the redshift for both models. In other words, the SHMR model for $M_\nu = 0.32$ eV differs from the ΛCDM massless case much more than for $M_\nu = 0.16$ eV. In particular, the differences of the SHMR with $M_\nu = 0.32$ eV are about twice larger than for $M_\nu = 0.16$ eV. The SHMR ratio is shifted to higher values with increasing neutrino mass. This effect is in agreement with the trend of the halo mass functions: it is necessary to compensate the damping of the mass functions due to the free-streaming effect of neutrinos in order to reproduce the same observations.

Finally, we populate the DEMNUni simulations with galaxies, assigning to every dark matter subhalo the corresponding stellar mass of its galaxy, using two different methods.

The first one is to use the double power-law Equation (3.3) together with the corresponding best-fit parameters obtained at different redshifs. The second method is to use our model for the redshift evolution of the SHMR (see Equations (6.1), (6.2), (6.3), (6.4)), with the obtained parameters.

In order to test the validity of our model used to populate dark matter subhaloes in the presence of massive neutrinos, we calculate the galaxy SMFs from the simulated galaxy mock catalogues.

We compare the stellar mass function from simulations with the corresponding observational data. We use the same stellar mass function data used to constraint the parameters of the SHMR: Baldry et al.(2008) SMF for $0 < z < 0.2$, and Weaver et al. (2022) for $0.2 < z < 2$. Figure 6.5 show the comparisons between the SMFs from simulations and the SMFs from observations.

We conclude that the models obtained for different values of the neutrino mass, *i.e.* $M_\nu = 0.16$ eV and $M_\nu = 0.32$ eV, are in agreement with the observations, and can be degenerate with the ΛCDM massless case. Indeed, with respect to the latter, the percent relative differences for both the models reproducing the observations are up to 0.1 dex.

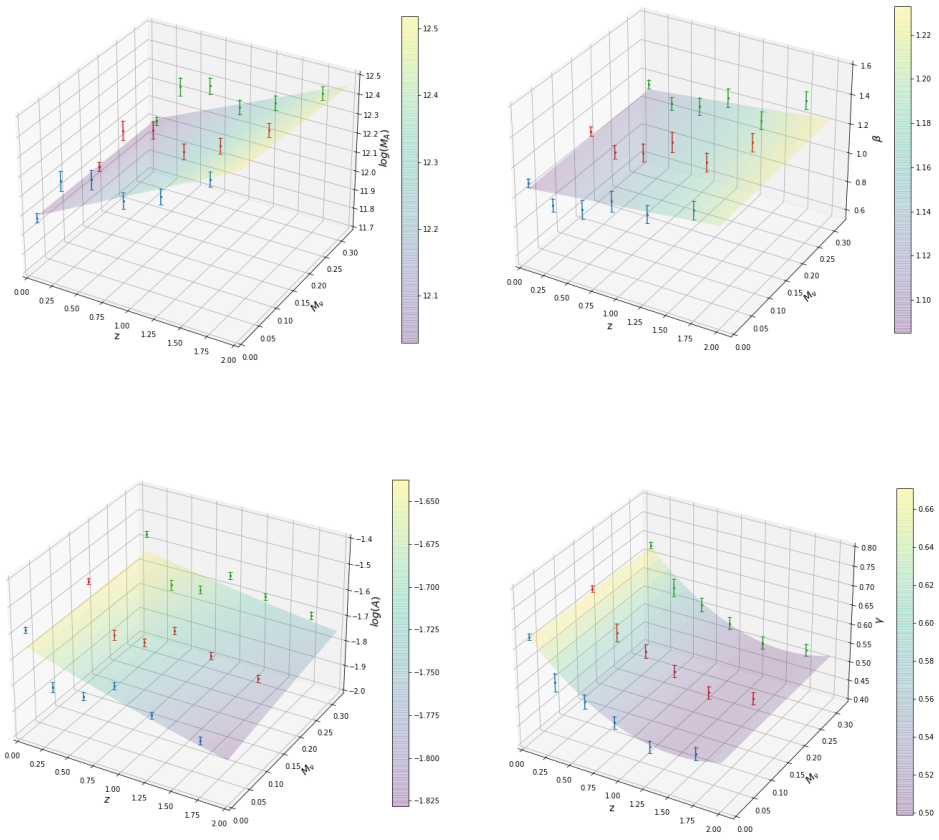

Figure 6.2: Joint redshift- and M_ν-dependence of the four SHMR parameters $\{M_A,\, A,\, \beta,\, \gamma\}$. The points indicate the best-fit values of the SHMR parameters obtained via the SHAM procedure applied to the DEMNUni subhalo catalogues in the redshift bins of Table5.1, for the cosmological constant scenarios with $M_\nu = 0$ eV (blue), $M_\nu = 0.16$ eV (red), $M_\nu = 0.32$ eV (green). The error bars show the associated 1–σ uncertainties obtained via the MCMC method. The colored surfaces represent the best-fit model obtained from Equations (6.1)-(6.4), with the corresponding parameter values as reported in Table 6.1.

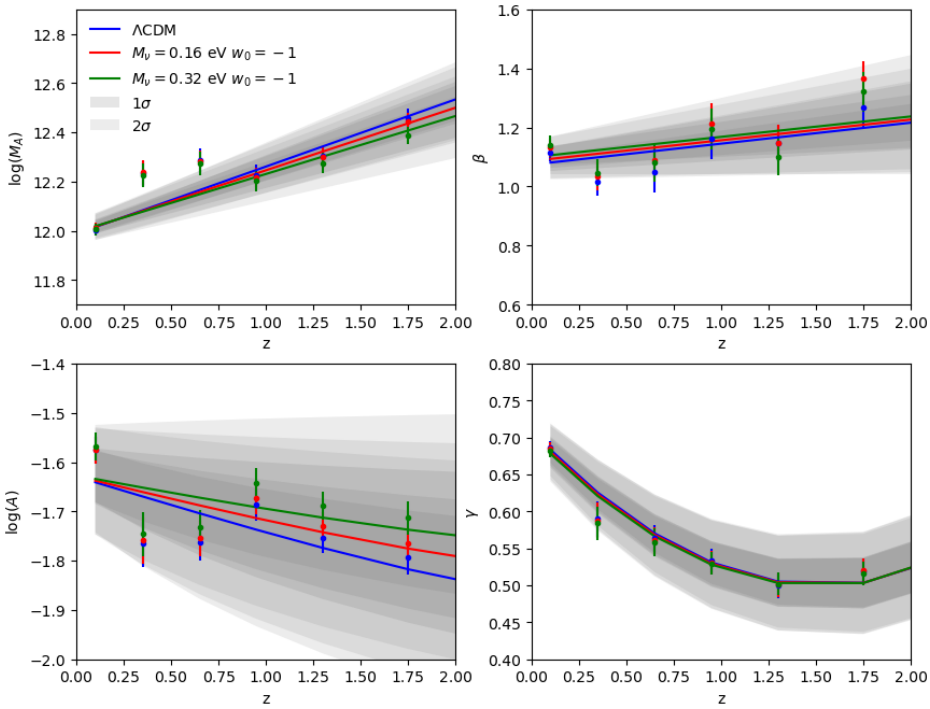

Figure 6.3: Redshift evolution of the four SHMR parameters $\{M_A, A, \beta, \gamma\}$ in the cosmological constant scenario with massive neutrinos. The points indicate the best-fit values of the SHMR parameters computed applying the SHAM technique to the DEMNUni subhalo catalogues in the redshift bins in Table 5.1, for the cosmological constant scenarios with neutrino masses $M_\nu = 0.16, 0.32$ eV. Solid lines indicate the best-fit model describing their redshift evolution for different neutrino masses (see Equations (6.1)-(6.4)). The corresponding best-fit parameter values are reported in Table 6.1. Dark and light shaded area show the 1–σ and 2–σ uncertainty regions for each best-fit curve. The error bars show the 1–σ uncertainties on the best-fit parameter values obtained with the MCMC method.

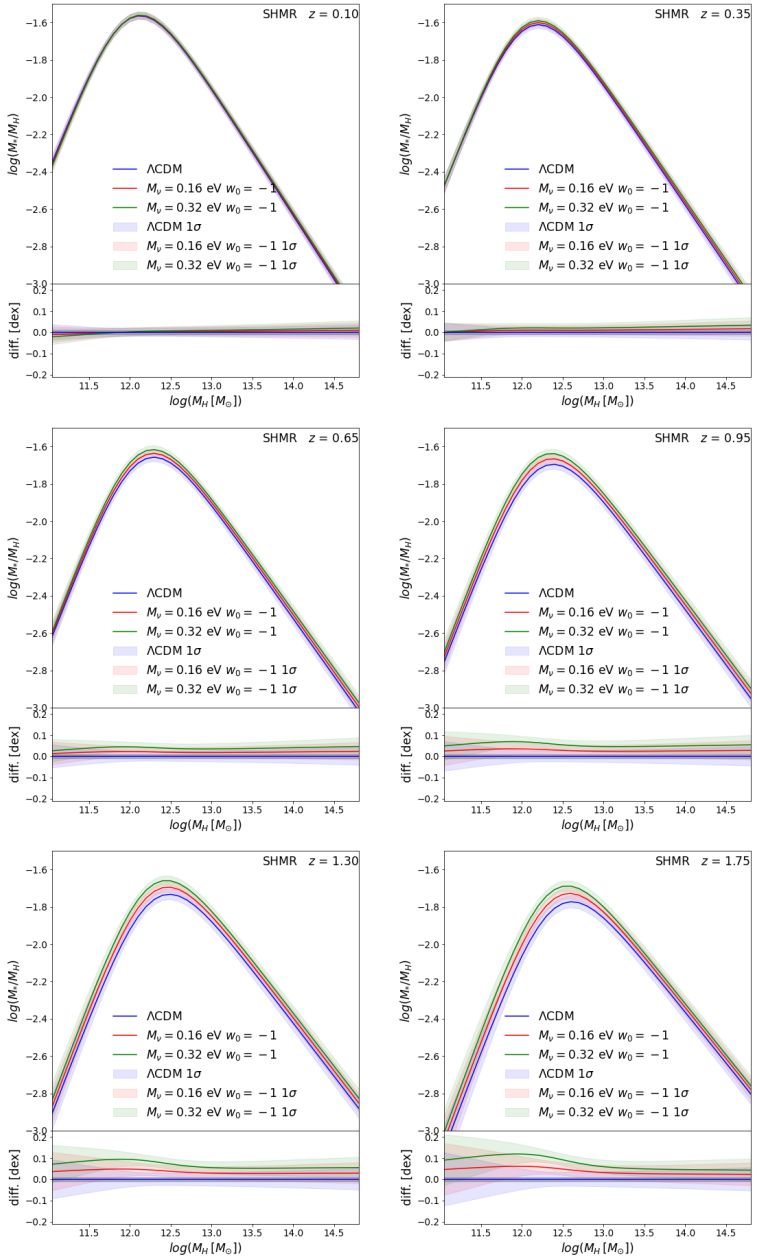

Figure 6.4: Best-fit SHMR models for the cosmological constant scenario with massive neutrinos. Results are shown for the redshift bins in Table 5.1, obtained inserting the best-fit values of Table 6.1 in Equations (6.1)-(6.4) and Equation (3.3). In each plot the upper panel shows the SHMR model in the case of a cosmological constant scenario with neutrino masses $M_\nu = 0.16, 0.32$ eV (red and green solid lines), compared to the ΛCDM massless neutrino case (blue solid line). The lower panels show the SHMR logarithmic difference between the massive neutrino and the ΛCDM cases, with the corresponding shaded areas representing the 1–σ error. The grey shaded areas within 0.01 dex (*i.e.* $\sim 2\%$ error) represent the case of better precision from forthcoming galaxy surveys.

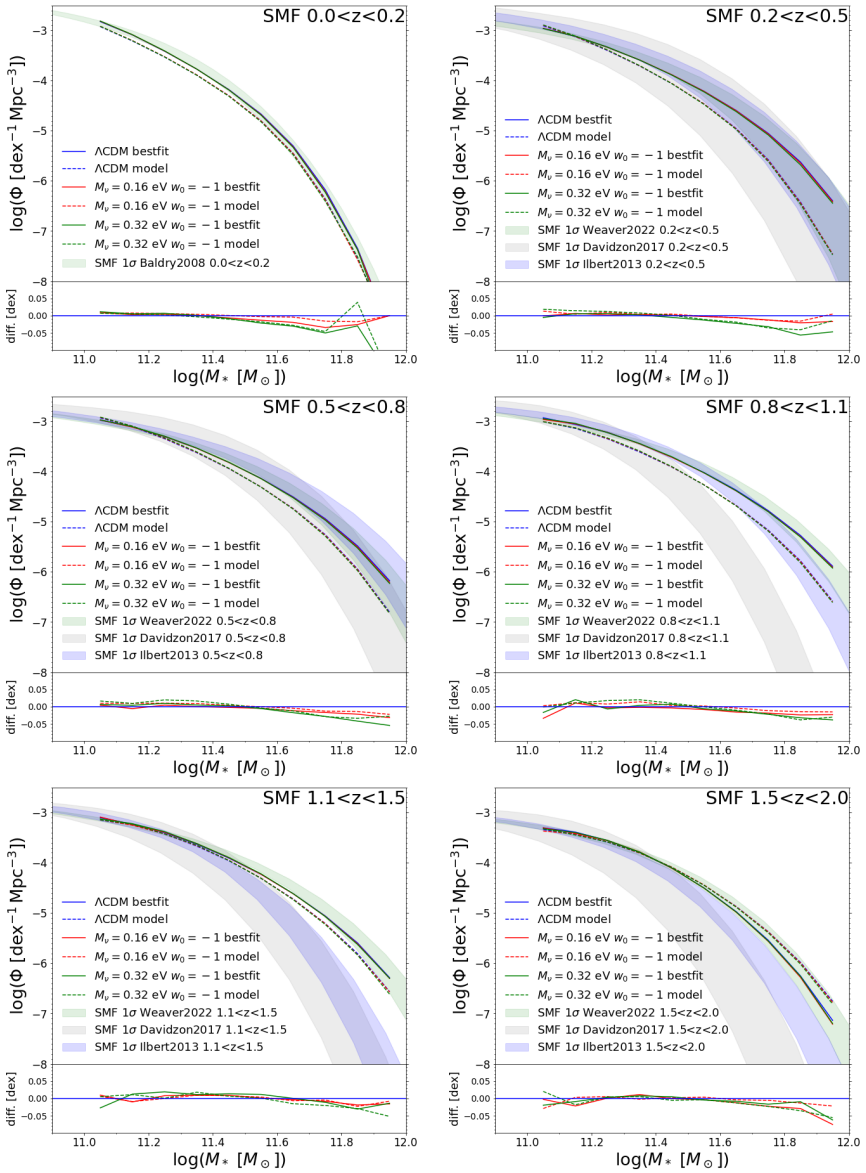

Figure 6.5: Stellar mass functions obtained from the galaxy mock catalogues of the DEMNUni simulations with massive neutrinos at the different redshift bins in Table 5.1. In each plot the upper panels show the SMF calculated using the best-fit SHMR parameters (solid lines) extracted at each redshift bin, or using the SHMR model dependent on z and M_ν (dashed lines). These results are compared to the observed SMFs of Baldry et al. (2008) [79] and Weaver et al. (2022) [80], with shaded area representing the associated 1–σ uncertainty, as reported in the legenda. The lower panels show the logarithmic differences between the SMFs obtained from the simulations with massive neutrinos and the ΛCDM case.

6.2 The SHAM method in dynamical dark energy scenarios

In this Section we analyse the galaxy-halo connection in DEMNUni simulations with the presence of dynamical dark energy, with a time-dependent EoS parameterized with the CPL model (Equation (1.38)). We analyse four different combinations of CPL parameters implemented in the DEMNUni simulations:

$$\begin{aligned} w_0 &= -0.9, -1.1 \\ w_a &= -0.3, +0.3 \end{aligned} \tag{6.5}$$

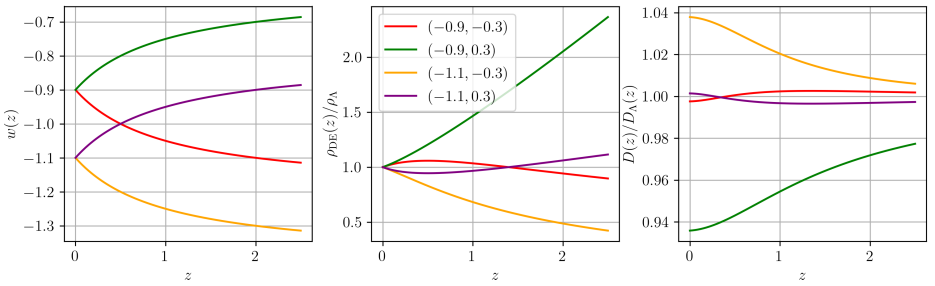

Figure 6.6: Redshift evolution of the dark energy equation of state, as Equation (1.38), with CPL parameters w_0, w_a in (6.5) [96].

I measure the SHMFs at different redshifts in the range $0 < z < 2$ for each model of dark energy EoS. The central panel in Figure 6.1 shows how the SHMF varies as the EoS parameters change, and the comparison to the ΛCDM model. There are two models that are degenerate, that is, that differ little from the ΛCDM model. Indeed, the percent relative differences of these models to the ΛCDM case are almost zero. These model are respectively characterised by $[w_0, w_a] = [-0.9, -0.3]$ and $[w_0, w_a] = [-1.1, +0.3]$. On the other hand, the other two models differ significantly to the ΛCDM. In particular, the model characterised by $[w_0, w_a] = [-1.1, -0.3]$ has differences more than 100%, while the model characterised by $[w_0, w_a] = [-0.9, +0.3]$ differs up to 100%, as it is shown in the lower central panel in Figure 6.1.

As in the non-degenerate w_0waCDM scenarios the luminosity distance (D) differs significantly from the ΛCDM, we convert the the stellar masses (M_*) and the volumes (V) in the observed SMFs according the following Equations:

$$\begin{aligned} \log(M_*)_2 &= \log(M_*)_1 + 2\log(D_2/D_1)\,, \\ V_2 &= V_1 \left(\frac{D_2}{D_1}\right)^3\,, \end{aligned} \tag{6.6}$$

where $\log(M_*)_1$, V_1, D_1 are the values in the cosmological model of the observations and $\log(M_*)_2$, V_2, D_2 are the new values in the w_0w_aCDM scenarios. The luminosity distance as a function of the redshidt and its variation with the cosmological parameters w_0, w_a is shown in the left panel in Figure 6.7. In addition, the rescaled SMFs are plotted in the right panel of Figure 6.7.

Using the abundance matching technique implemented in Section 5.1 we calculate the best-fit SHMR parameters with a MCMC method. Therefore, the results are calibrated on observations, which are scaled with the luminosity distance for each

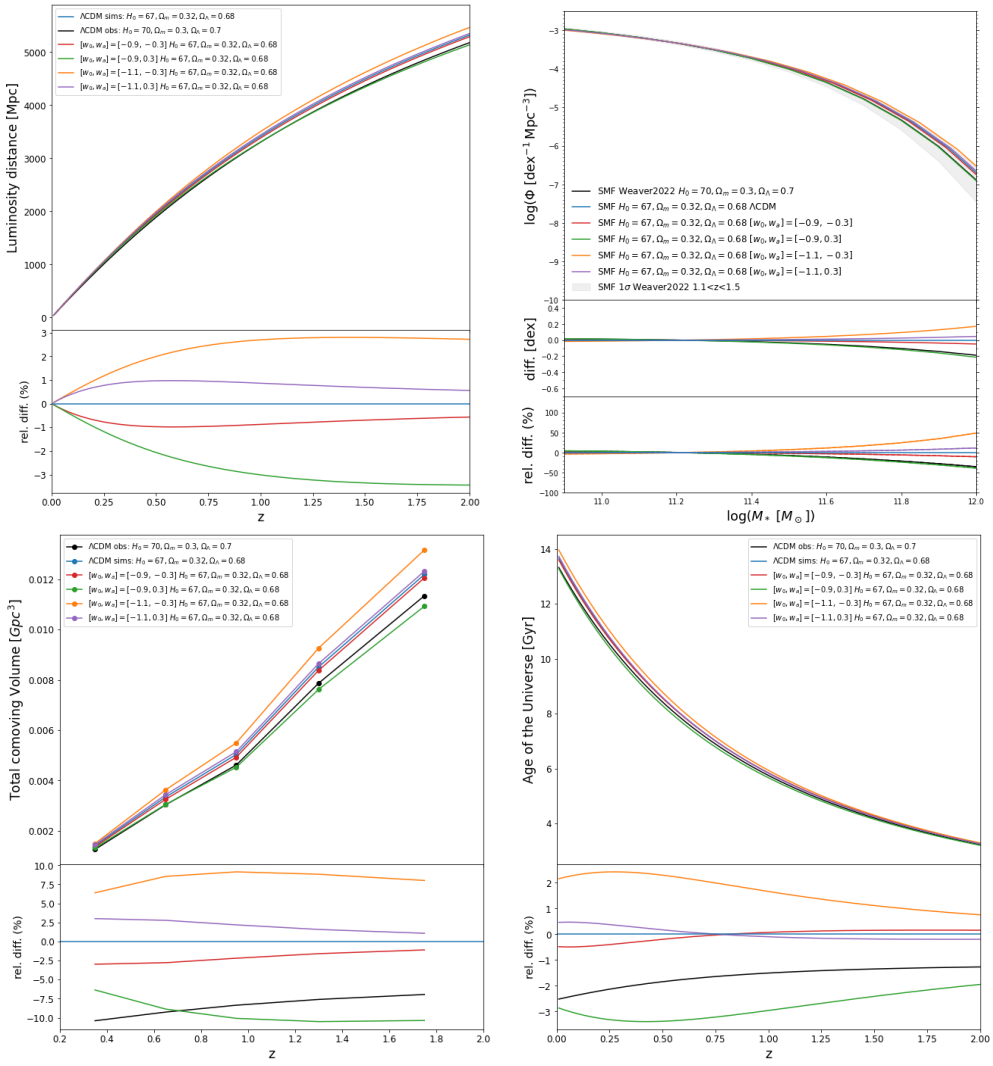

Figure 6.7: Top Left: The luminosity distance as a function of the redshift in the w_0w_aCDM scenarios compared with the ΛCDM luminosity distance. The lower panel shows the relative percent difference between each (w_0, w_a) case and the ΛCDM model. Top right: SMFs at $1.1 < z < 1.5$ computed rescaling the volume and the stellar mass according the luminosity distance in Equation (6.6) for each combination of EoS parameters (w_0, w_a). The lower panel shows the relative percent differences between each SMF in alternative scenarios and the ΛCDM case. Bottom left: Total comoving volume covering the COSMOS solid angle $2\,deg^2$ as a function of the redshift in the w_0w_aCDM scenarios, compared to the ΛCDM model of simulations. Bottom right: Age of the Universe as a function of the redshift in the w_0w_aCDM scenarios, compared to the ΛCDM model of simulations.

w_0w_aCDM model. The results are the points with 1–σ error bar in the $z - w_{tot}$ plane indicated in Figure 6.8.

Moreover, we construct a model dependent on the redshift and on w_{tot} according Equations (6.7), (6.8), (6.9), (6.10). The dependence on w_{tot} is linear, as in the the first

lines in each system of equations, while the evolution with the redshift is expressed in the slope m_i and intercept q_i for each SHMR parameter $i = M_A, A, \beta, \gamma$, as the second and third lines in the corresponding system of equations. In particular, we consider a first-order polynomial function for M_A, A and a second-order polynomial function for β, γ.

$$\begin{cases} \log(M_A) = m^w_{M_A}\, w + q^w_{M_A} \\ m^w_{M_A} = A^m_{M_A}\, z + B^m_{M_A} \\ q^w_{M_A} = A^q_{M_A}\, z + B^q_{M_A} \end{cases} \tag{6.7}$$

$$\begin{cases} \log(A) = m^w_A\, w + q^w_A \\ m^w_A = A^m_A\, z^2 + B^m_A\, z + C^m_A \\ q^w_A = A^q_A\, z^2 + B^q_A\, z + C^q_A \end{cases} \tag{6.8}$$

$$\begin{cases} \beta = m^w_\beta\, w + q^w_\beta \\ m^w_\beta = A^m_\beta\, z + B^m_\beta \\ q^w_\beta = A^q_\beta\, z + B^q_\beta \end{cases} \tag{6.9}$$

$$\begin{cases} \gamma = m^w_\gamma\, w + q^w_\gamma \\ m^w_\gamma = A^m_\gamma\, z^2 + B^m_\gamma\, z + C^m_\gamma \\ q^w_\gamma = A^q_\gamma\, z^2 + B^q_\gamma\, z + C^q_\gamma \end{cases} \tag{6.10}$$

Using our $z - w_{tot}$ dependent model we perfom a two-dimensional fit over the SHMR parameter values obtaining the best-fit surfaces, indicated in Figure 6.8. The corresponding best-fit parameter values of Equations (6.7), (6.8), (6.9), (6.10) are listed in Table 6.2 with its 1–σ uncertainties.

Furthermore, in order to check the validity of our $z - w_{tot}$ dependent model we compute the parameters with the previous Equations (6.7)-(6.10) in all four different combination of CPL EoS parameters of Equation (6.5). The results are indicated in Figure 6.9 with solid lines. We compare these functions with the initial best-fit values obtained with the abundance matching method, shown with points in Figure 6.9.

The dark energy models characterised by $[w_0, w_a] = [-0.9, +0.3]$ and $[w_0, w_a] = [-1.1, -0.3]$ have parameters that differ most from the ΛCDM model, *e.g.* the normalisation A differs respectively by up 7% and 2.2%. The remaining two models, corresponding to $[w_0, w_a] = [-0.9, -0.3]$ and $[w_0, w_a] = [-1.1, +0.3]$, have parameters with very small differences from the ΛCDM parameters, less than 1%. This is due to the fact that these models are characterised by degenerate halo mass functions, as visible in Figure 6.1. As a result, the corresponding SHMR parameters, calibrated on halo mass functions, are consequently affected by the same degeneracy.

Using the $z - w_{tot}$ model, we calculate the stellar-to-halo-mass ratio, as dark energy EoS parameters vary. Figure 6.10 shows the trend of the SHMR, at four different dark energy EoS parameters. In each figure the lower panel indicates for all four different models the relative percent differences to the ΛCDM case, which is significantly increasing at higher redshift values. As expected, the two degenerate models, corresponding respectively to $[w_0, w_a] = [-0.9, -0.3]$ and $[w_0, w_a] = [-1.1, 0.3]$, are characterised by small percent relative differences, less than 1%. On the other hand, the models with $[w_0, w_a] = [-0.9, 0.3]$ and $[w_0, w_a] = [-1.1, -0.3]$ differ from the ΛCDM model up to 3%. This effect is in agreement with the trend of the halo mass function, used to calibrate the SHMR parameters. Indeed, both of these models differ significantly from the ΛCDM one.

$\log(M_A)$	
$m^w_{M_A}$	$A^m_{M_A} = -0.063 \pm 0.037 \quad B^m_{M_A} = -0.0123 \pm 0.007$
$q^w_{M_A}$	$A^q_{M_A} = 0.200 \pm 0.085 \quad B^q_{M_A} = 11.979 \pm 0.094$
$\log(A)$	
m^w_A	$A^m_A = -0.012 \pm 0.016 \quad B^m_A = 0.056 \pm 0.041 \quad C^m_A = 0.008 \pm 0.021$
q^w_A	$A^q_A = 0.013 \pm 0.016 \quad B^q_A = -0.093 \pm 0.041 \quad C^q_A = -1.610 \pm 0.023$
β	
m^w_β	$A^m_\beta = -0.102 \pm 0.092 \quad B^m_\beta = 0.072 \pm 0.071$
q^w_β	$A^q_\beta = -0.060 \pm 0.093 \quad B^q_\beta = 1.154 \pm 0.123$
γ	
m^w_γ	$A^m_\gamma = -0.015 \pm 0.010 \quad B^m_\gamma = 0.054 \pm 0.043 \quad C^m_\gamma = -0.037 \pm 0.036$
q^w_γ	$A^q_\gamma = 0.072 \pm 0.040 \quad B^q_\gamma = -0.216 \pm 0.086 \quad C^q_\gamma = 0.672 \pm 0.039$

Table 6.2: Best-fit parameter values of functions that show the dependence of slope m^w and intercept q^w varying with the redshift, according second and third equations in systems Equations (6.7), (6.8), (6.9), (6.10)

We populate dark matter subhaloes with galaxies, assigning them the corresponding galaxy stellar mass. The latter is calculated using the SHMR (Equation (3.3)) with the best-fit parameters for each dark matter model. From the galaxy mock catalogues we calculate the SMF that we compare with the observed one, in order to verify the validity of the SHMR model. The upper panels in Figure 6.11 show the obtained SMF from the DEMNUni simulations with dynamical dark energy at different EoS parameters, as compared to the ΛCDM SMF and the observations of Baldry et al. (2008) [79] or Weaver et al. (2022) [80], depending on the redshift range. All the estimates are consistent with the observed SMF. Indeed, as it is evident from the central sub-panels in Figure 6.11, the percent relative differences of SMF estimates with dynamical dark energy to the corresponding ΛCDM SMF, that reproduces the observations, are within 0.07 dex for the degenerate models $[w_0, w_a] = [-0.9, -0.3]$ and $[w_0, w_a] = [-1.1, 0.3]$, while they are up to 0.25 dex for the non-degenerate models $[w_0, w_a] = [-0.9, 0.3]$ and $[w_0, w_a] = [-1.1, -0.3]$. Finally, in the lower sub-plots in Figure 6.11 we calculate the percent relative differences between each $w_0 w_a$CDM scenarios versus the corresponding observed SMFs corrected with its luminosity distance. As in Section 5.1 the differences are within 1 dex for all redshift bins.

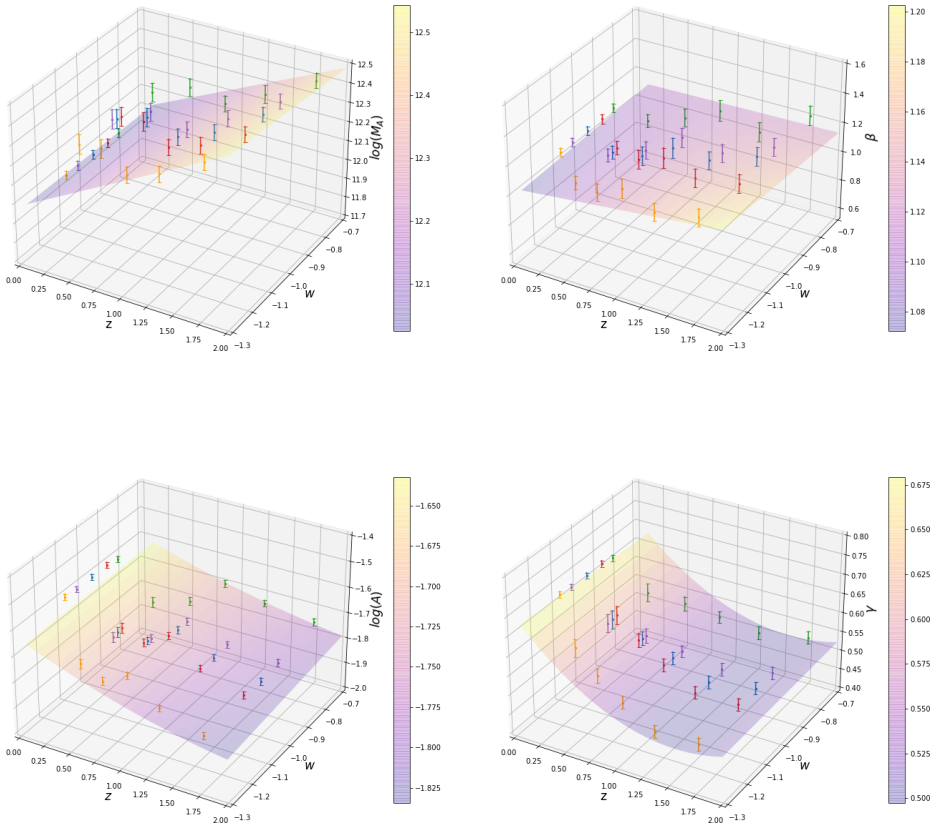

Figure 6.8: Joint redshift- and w_{tot}-dependence of the four SHMR parameters $\{M_A,\ A,\ \beta,\ \gamma\}$. The points indicate the best-fit values of the SHMR parameters obtained via the SHAM procedure applied to the DEMNUni subhalo catalogues in the redshift bins of Table 5.1, for the w_0w_aCDM scenarios with $[w_0, w_a] = [-1, 0]$ (blue), $[w_0, w_a] = [-0.9, -0.3]$ (red), $[w_0, w_a] = [-0.9, +0.3]$ (green), $[w_0, w_a] = [-1.1, -0.3]$ (orange), $[w_0, w_a] = [-1.1, -0.3]$ (purple). The colored surfaces represent the best-fit model obtained from Equations (6.7)-(6.10). The corresponding best-fit parameter values are reported in Table 6.2. The error bars show the 1–σ uncertainties on the best-fit parameter values obtained with the MCMC method.

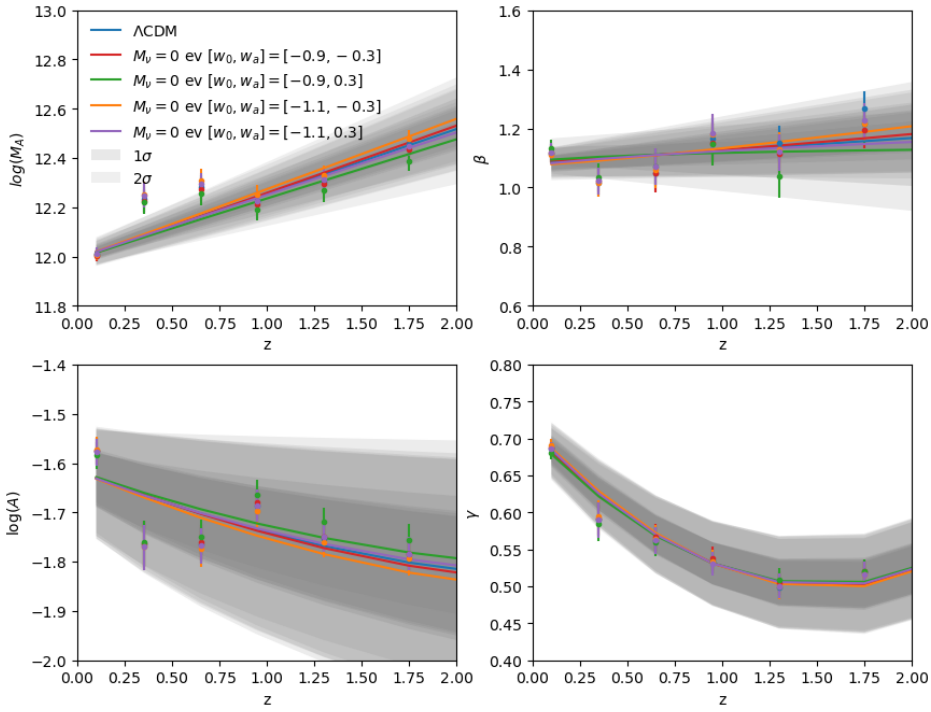

Figure 6.9: Redshift evolution of the four SHMR parameters $\{M_A,\ A,\ \beta,\ \gamma\}$, at different dark energy EoS parameters with massless neutrinos. The points indicate the best-fit values of the SHMR parameters computed applying the SHAM technique to the DEMNUni subhalo catalogues in different redshift bins. Solid lines indicate the best-fit model describing their redshift evolution for different $(w_0,\ w_a)$ parameters (see Equations (6.7)-(6.10)). The corresponding best-fit parameter values are reported in Table 6.2. Dark and light shaded area show the 1–σ and 2–σ uncertainty regions for each best-fit curve. The error bars show the 1–σ uncertainties on the best-fit parameter values obtained with the MCMC method.

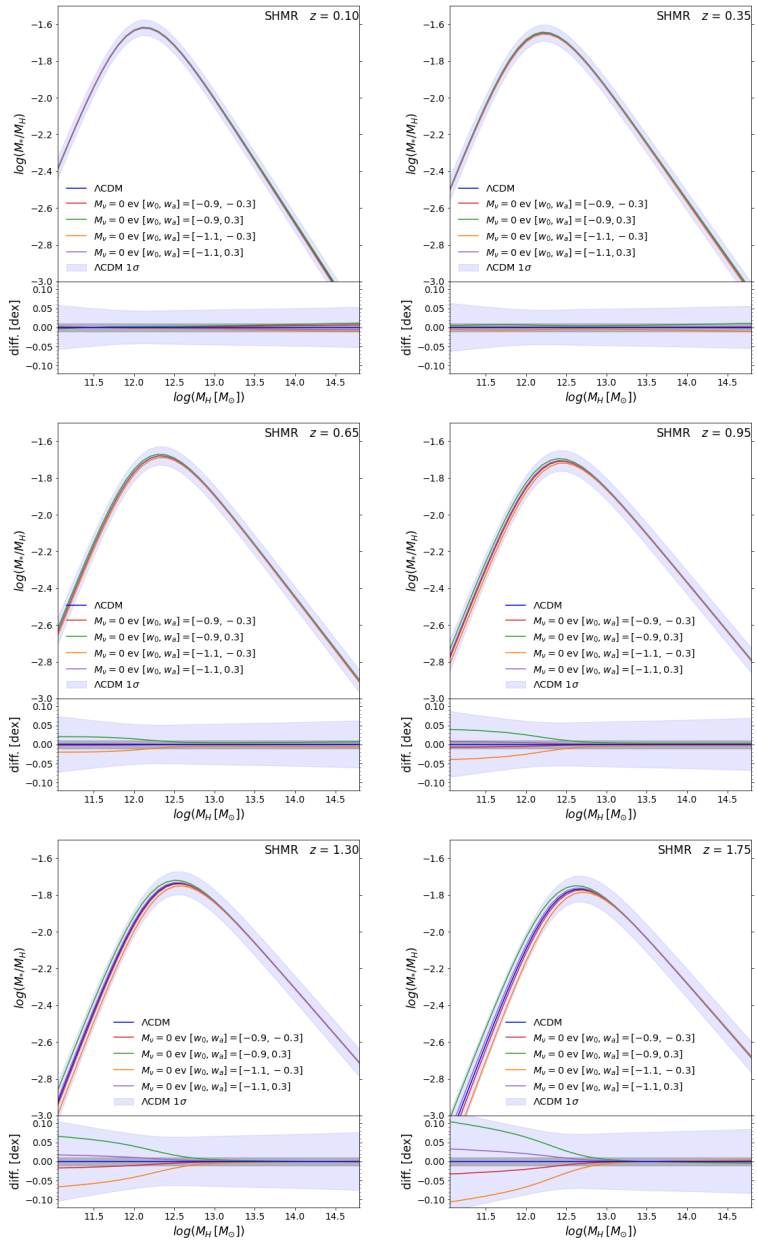

Figure 6.10: Best-fit SHMR models for the dynamical dark energy scenario with massless neutrinos. Results are shown for the redshift bins in Table 5.1, obtained inserting the best-fit values of Table 6.2 in Equations (6.7)-(6.10) and Equation (3.3). In each plot the upper panel shows the SHMR model in the case of dynamical dark energy with massless neutrinos (red, green, orange and purple solid lines), compared to the ΛCDM massless neutrino case (blue solid line). The lower panels show the SHMR logarithmic difference between the dynamical $w_0 w_a$CDM and the ΛCDM cases, with the corresponding shaded areas representing the 1–σ error. The grey shaded areas within 0.01 dex (*i.e.* $\sim 2\%$ error) represent the case of better precision from forthcoming galaxy surveys.

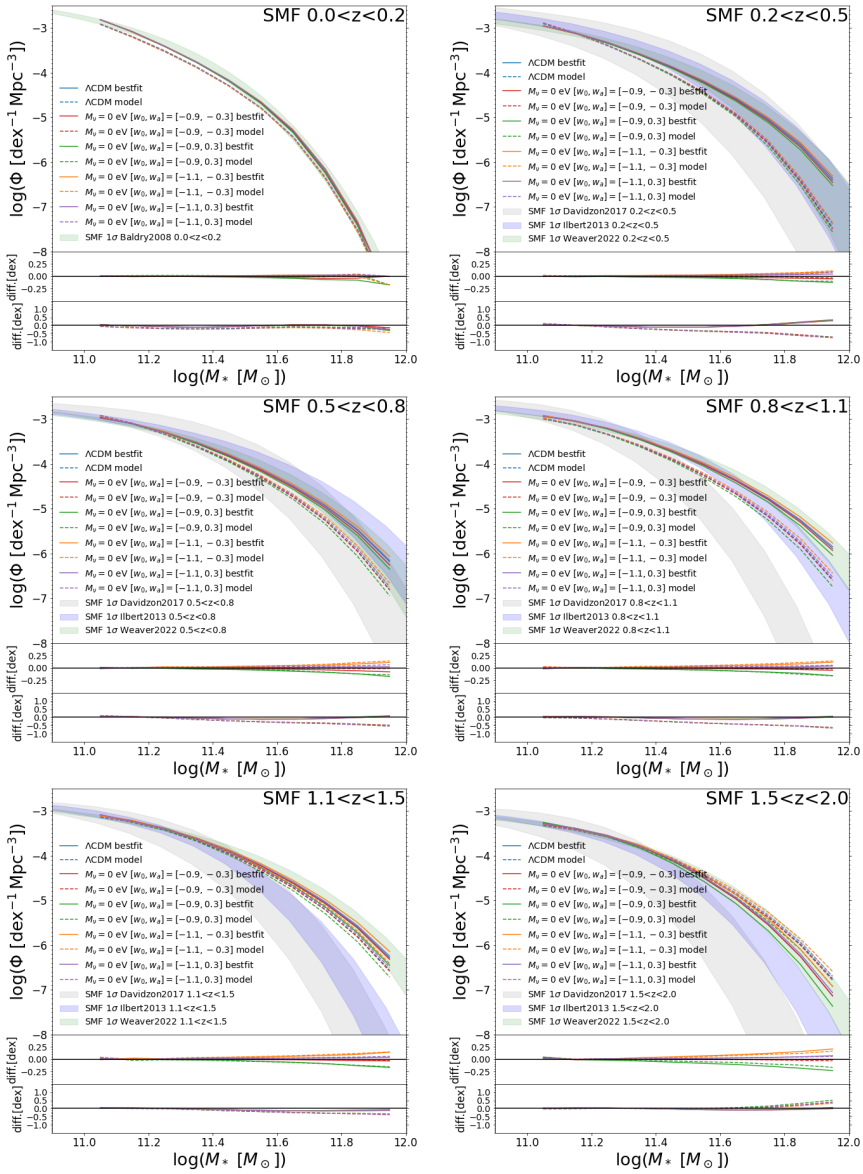

Figure 6.11: Stellar mass functions obtained from the galaxy mock catalogues of the DEMNUni simulations with dynamical dark energy and massless neutrinos at different redshift bins in Table 5.1. In each plot the upper panels show the SMF calculated using the best-fit SHMR parameters (solid lines) extracted at each redshift bin, or using the SHMR model dependent on z and (w_0, w_a) (dashed lines). These results are compared to the observed SMFs of Baldry et al. (2008) [79] and Weaver et al. (2022) [80], with shaded area representing the associated 1–σ uncertainty, as reported in the legenda. The middle sub-panels show the logarithmic differences between the SMF obtained from simulations with dynamical dark energy and the ΛCDM case. The lowest sub-panels show the logarithmic differences between the SMFs obtained from the simulations and the corresponding observed ones rescaled according the dependence of the luminosity distance on the parameters w_0 and w_a.

6.3 SHAM in massive neutrino and dynamical dark energy scenarios

In this Section we analyse the simulations with the combination of massive neutrinos with $M_\nu = 0.16, 0.32$ eV and the presence of dynamical dark energy with four different combination of the CPL EoS parameters in Equation (6.5). We compute an abundance matching method over the simulated SHMFs and the observed SMFs, which are corrected according the luminosity distance as in the previous Section 6.2, due to the effect of the dynamical dark energy.

The results for each SHMR parameter are the points with 1σ error bars, estimated from MCMC analysis, in the plane $(w - M_\nu)$ in Figure 6.12 at many redshift values individuated by different colors.

In order to model the simultaneous variation of these parameters with M_ν, w_{tot} and also with the deshift we perform a fitting procedure in two steps. First, we fit all SHMR points at the same fixed redshift using a bilinear function according Equations (6.11), (6.12), (6.13), (6.15), finding the corresponding best-fit parameters $A_i, M_{Ai}, \Gamma_i, B_i; \quad i = 0, 1, 2$. The resulting surfaces at every redshift interval are shown in Figure 6.12 with its color. Second, using these parameter values we fit for each of them the redshift variation with a polynomial function as Equation (6.15) obtaining the parameter values listed in Table 6.3, along with its 68% confidence level uncertainties.

$$\log(A) = A_0 w_{tot} + A_1 M_\nu + A_2 \tag{6.11}$$

$$\log(M_A) = M_{A_0} w_{tot} + M_{A_1} M_\nu + M_{A_2} \tag{6.12}$$

$$\gamma = \Gamma_0 w_{tot} + \Gamma_1 M_\nu + \Gamma_2 \tag{6.13}$$

$$\beta = B_0 w_{tot} + B_1 M_\nu + B_2 \tag{6.14}$$

$$\Sigma_i = D_{\Sigma_i} z^2 + E_{\Sigma_i} z + F_{\Sigma_i} \quad \Sigma_i = A_i, M_{A_i}, \Gamma_i, B_i \tag{6.15}$$

Moreover, using using our model dependent on $M_\nu - w - z$ we compute the SHMR parameters for $M_\nu = 0,\ 0.16,\ 0.32$ eV and w_0, w_a values in Equation(6.5) as a function of the redshift, plotted with solid lines in Figure 6.13. Each color shows different combinations of M_ν and w_0, w_a values. To perform a proper comparison we show in the same plot the best-fit values obtained with the abundance matching method with the points with error bars.

Using the z-M_ν-w_{tot} model, I calculate the stellar-to-halo-mass ratio, as the dark energy EoS parameters and the neutrino total mass vary. Figure 6.14 illustrates the trend of the SHMR, at eight different models, with two different neutrino masses and four combinations of the dark energy EoS parameters, together with the ΛCDM case. In each panel the subpanel indicates, for all eight different models, the relative differences in logarithmic scale to the ΛCDM case. We note that such differences increase with increasing redshift. Indeed, for the model with $M_\nu = 0.32$ eV and $[w_0, w_a] = [-0.9, 0.3]$, which differs most from the ΛCDM, the relative differences are within the 1-σ error bars of the ΛCDM measurements for redshift lower than $z = 0.65$. Then, for higher redshifts, $z > 0.95$, it exceeds the 1-σ error band, with increasing difference around the mass peak $M_h \sim 10^{11.8} M_\odot/h$ up to $\mathrm{diff} = 0.08, 0.12, 0.16\,\mathrm{dex}$, at $z = 0.95, 1.30, 1.75$, respectively.

We populate dark matter subhaloes with galaxies, assigning them the corresponding galaxy stellar mass. The latter is calculated using the SHMR (Equations (6.11)-(6.15) and Equation (3.3)) with the best-fit parameters for each dark energy and massive neutrinos model. In order to check the consistency of the SHMR model, I compute the SMF and compare the results with the observed one. The upper panels in Figure 6.15 show the

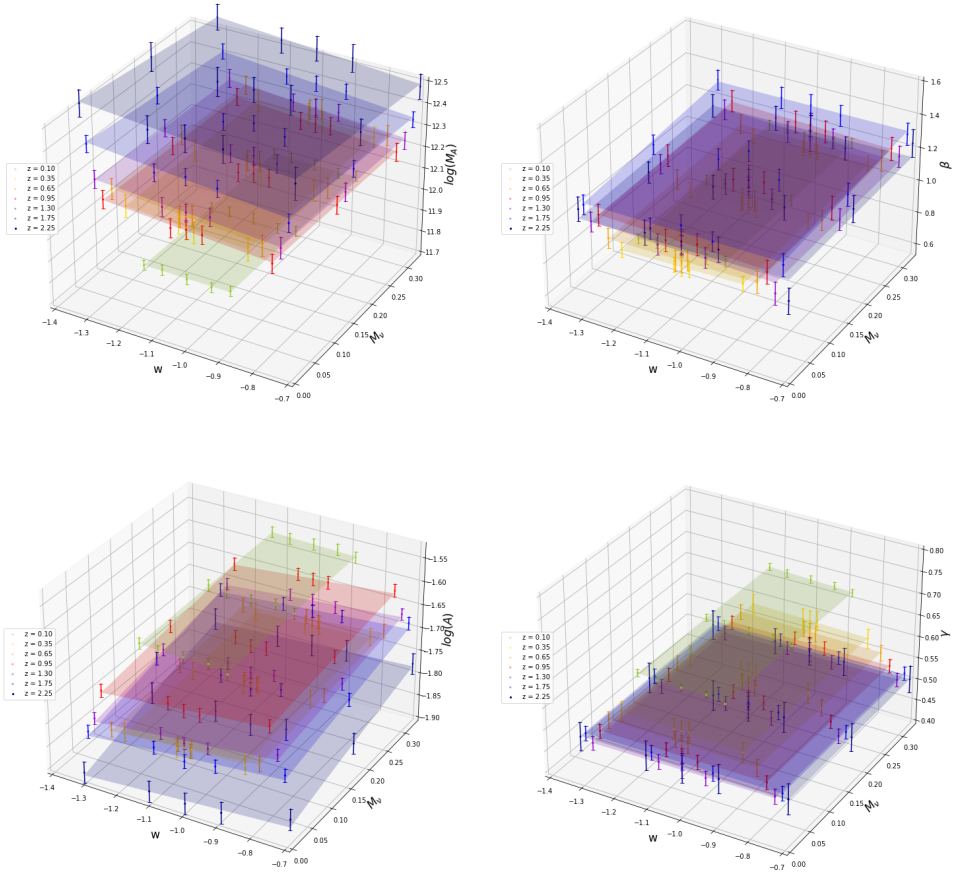

Figure 6.12: Joint M_ν- and w_{tot}-dependence of the four SHMR parameters $\{M_A,\, A,\, \beta,\, \gamma\}$. The points indicate the best-fit values of the SHMR parameters obtained via the SHAM procedure applied to the DEMNUni subhalo catalogues in the redshift bins of Table5.1, for the $\nu w_0 w_a$CDM scenarios. The colored surfaces represent the best-fit model obtained from Equations (6.11)-(6.15). The error bars show the 1–σ uncertainties on the best-fit parameter values obtained with the MCMC method.

obtained SMF from the DEMNUni simulations with dynamical dark energy and massive neutrinos at different EoS parameters, as compared to the ΛCDM SMF and the observations of Baldry et al. (2008) [79] or Weaver et al. (2022) [80], depending on the redshift range. As it is evident from the central sub-panels in Figure 6.15, the estimates are consistent with the observed SMF. Indeed, the percent relative differences of SMF estimates that reproduces the observations for $M_\nu = 0.32$ eV, are within $0.05\,\mathrm{dex}$ for the two mostly degenerate dark energy models, $[w_0, w_a] = [-1.1, +0.3]$ and $[w_0, w_a] = [-0.9, -0.3]$, $0.17\,\mathrm{dex}$ for $[w_0, w_a] = [-1.1, -0.3]$, and up to $-0.35\,\mathrm{dex}$ for $[w_0, w_a] = [-0.9, +0.3]$. The lower sub-panels in Figure 6.15 show the relative differences in logarithmic scale between each $\nu w_0 w_a$CDM scenarios versus the corresponding observed SMFs corrected with its luminosity distance. The differences are within $0.65\,\mathrm{dex}$ for the results obtained

$\log(M_A)$	
M_{A_0}	$D_{M_{A_0}} = 0.008 \pm 0.002 \quad E_{M_{A_0}} = -0.082 \pm 0.003 \quad F_{M_{A_0}} = -0.01 \pm 0.001$
M_{A_1}	$D_{M_{A_1}} = -0.097 \pm 0.001 \quad E_{M_{A_1}} = 0.007 \pm 0.001$
M_{A_2}	$D_{M_{A_2}} = 0.198 \pm 0.003 \quad E_{M_{A_2}} = 11.976 \pm 0.002$
$\log(A)$	
A_0	$D_{A_0} = -0.008 \pm 0.001 \quad E_{A_0} = 0.041 \pm 0.003 \quad F_{A_0} = -0.019 \pm 0.001$
A_1	$D_{A_1} = -0.033 \pm 0.003 \quad E_{A_1} = 0.190 \pm 0.007 \quad F_{A_1} = 0.004 \pm 0.002$
A_2	$D_{A_2} = 0.016 \pm 0.001 \quad E_{A_2} = -0.109 \pm 0.003 \quad F_{A_2} = -1.598 \pm 0.001$
β	
B_0	$D_{B_0} = 0.007 \pm 0.003 \quad E_{B_0} = -0.045 \pm 0.006 \quad F_{B_0} = 0.047 \pm 0.002$
B_1	$D_{B_1} = 0.050 \pm 0.001 \quad E_{B_1} = 0.061 \pm 0.001$
B_2	$D_{B_2} = 0.007 \pm 0.003 \quad E_{B_2} = -0.005 \pm 0.006 \quad F_{B_2} = 1.131 \pm 0.002$
γ	
Γ_0	$D_{\Gamma_0} = -0.013 \pm 0.003 \quad E_{\Gamma_0} = 0.046 \pm 0.007 \quad F_{\Gamma_0} = -0.032 \pm 0.004$
Γ_1	$D_{\Gamma_1} = -0.004 \pm 0.001 \quad E_{\Gamma_1} = 0.021 \pm 0.001 \quad F_{\Gamma_1} = -0.022 \pm 0.001$
Γ_2	$D_{\Gamma_2} = 0.018 \pm 0.001 \quad E_{\Gamma_2} = -0.122 \pm 0.003 \quad F_{\Gamma_2} = 0.653 \pm 0.001$

Table 6.3: Best-fit values of the parameters of Equations (6.11), (6.12), (6.14), (6.13), (6.15), that show the dependence of the SHMR parameters on the combination of M_ν, w_{tot} and z.

with the SHMR model, and $0.35\,\mathrm{dex}$ for the results using the best-fit values of SHMR.

6.4 Galaxy Clustering in $\nu w_0 w_a$CDM cosmologies

In this section we extend the analysis of the correlation functions to alternative models with massive neutrinos and dynamical dark energy.

We use the same procedure described before for the ΛCDM in section 5.5 as Equations (5.15)-(5.16) and we make the following modifications on the estimate of the linear growth factor in Equation (5.16) which is necessary to compute the theoretical redshift-space 2PCF in the alternative models. Indeed, for a model with a dark energy component the analytical approximation of the linear growth factor is $f = \Omega_m^\alpha(z)$ with [97]:

$$\alpha = \alpha_0 + \alpha_1[1 - \Omega_m(z)], \quad \alpha_0 = \frac{3}{5 - \frac{w}{1-w}}, \quad \alpha_1 = \frac{3}{125}\frac{(1-w)(1-3w/2)}{(1-6w/5)^3} \tag{6.16}$$

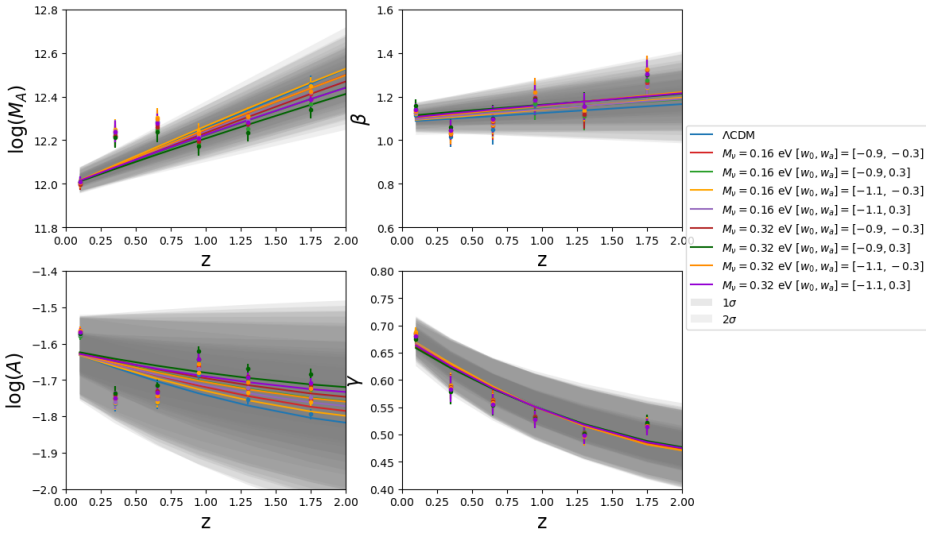

Figure 6.13: Redshift evolution of the four SHMR parameters $\{M_A,\, A,\, \beta,\, \gamma\}$, at different dark energy EoS parameters with neutrinos of mass $M_\nu = 0.16 - 0.32$ eV. The points indicate the best-fit values of the SHMR parameters computed applying the SHAM technique to the DEMNUni subhalo catalogues in different redshift bins. Solid lines indicate the best-fit model describing their redshift evolution for different $(w_0,\, w_a)$ and M_ν values (see Equations (6.11), (6.12), (6.13),(6.14), (6.15)). The corresponding best-fit parameter values are reported in Table 6.3. Dark and light shaded area show the 1–σ and 2–σ uncertainty regions for each best-fit curve. The error bars show the 1–σ uncertainties on the best-fit parameter values obtained with the MCMC method.

where w is the total dark energy EoS parameter in Equation (1.38). On the other hand, in the presence with massive neutrinos the approximation for the linear growth factor is $f = \mu \Omega_m^\alpha(z)$ with [97]

$$\mu = (1 - f_\nu)^\alpha, \quad f_\nu = \frac{\Omega_\nu}{\Omega_m}\,, \tag{6.17}$$

where f_ν is the fractional contribution of neutrinos to the total mass density in the Universe, with $\alpha = 0.545$ in the ΛCDM+massive neutrinos and α in Equation (6.16) in the $\nu w_0 w_a$CDM scenarios.

The obtained linear bias $b(z)$, computed as the square root of the ratio between the real-space galaxy correlation function and the matter correlation function, is indicated in Figure 6.16 for the ΛCDM model with and without massive neutrinos (upper panels), for the $w_0 w_a$CDM (central panels) and $\nu w_0 w_a$CDM scenarios (lower panels), the error bars are computed propagating the uncertainty of $\xi(r)$, estimated with the Bootstrap method. These computed values of bias $b(z)$ are needed to estimate β in Equation 5.16

In addition, in order to compare properly the measured 2PCF from simulations in the alternative cosmologies (with dynamical dark energy) with the observed VIPERS data in the ΛCDM model, we convert the measured 2PCF from the alternative models to the fiducial ΛCDM model. In particular, we correct the scale s performing the scaling with the Alcock-Paczynski (AP) factor α [98]:

$$\alpha_\parallel = \frac{H^{fid}(z) r_s^{fid}(z)}{H(z) r_s(z)}, \quad \alpha_\perp = \frac{D_A(z) r_s^{fid}(z)}{D_A^{fid}(z) r_s(z)}, \quad \alpha = \alpha_\parallel^{1/3} \alpha_\perp^{2/3}\,, \tag{6.18}$$

where $H(z)$ is the Hubble expansion rate, $D_A(z)$ the angular diameter distance and $r_s(z)$ the sound horizon for the fiducial and model cosmologies. The results of the measured resdhift-space 2PCF and its theoretical prediction using the Kaiser model are indicated in Figure 6.17, for the ΛCDM with massive neutrinos case, in 6.18 for the w_0w_aCDM scenarios and in Figure 6.19 for the combination of massive neutrinos and dynamical dark energy. We show the comparisons between the 2PCFs obtained from mock galaxy catalogues at stellar masses $M_* > 10^{11}M_\odot$, due to the resolution of the simulations, and the 2PCFs calculated from the subhalo catalogues of simulations using the same procedure.

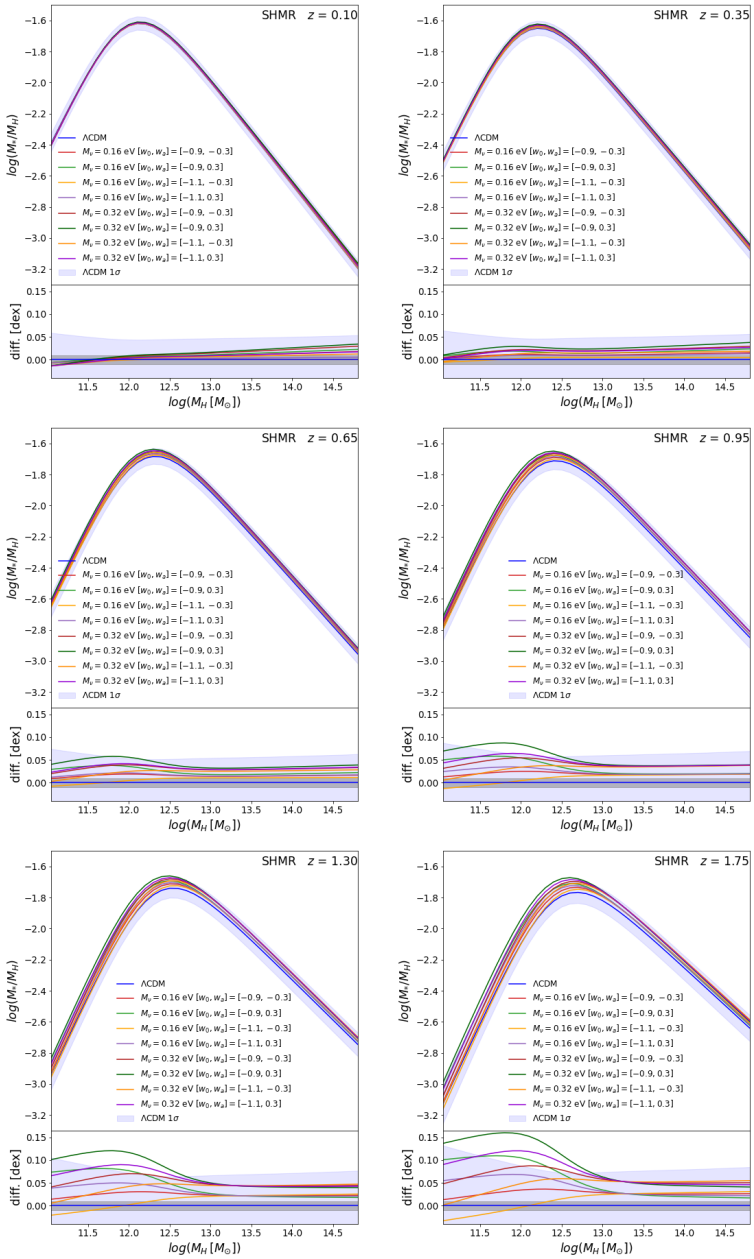

Figure 6.14: Best-fit SHMR models with dynamical dark energy and massive neutrinos ($M_\nu = 0.16 - 0.32$ eV). Results are shown for the redshift bins in Table 5.1, obtained inserting the best-fit values of Table 6.3 in Equations (6.11)-(6.15) and Equation (3.3). In each plot the upper panel shows the SHMR model in the case of dynamical dark energy with massive neutrinos, compared to the ΛCDM massless neutrino case (blue solid line). The lower panels show the SHMR logarithmic differences between the $\nu w_0 w_a$CDM and the ΛCDM cases, with the corresponding shaded areas representing the 1–σ error. The grey shaded areas within 0.01 dex (*i.e.* $\sim 2\%$ error) represent the case of better precision from forthcoming galaxy surveys.

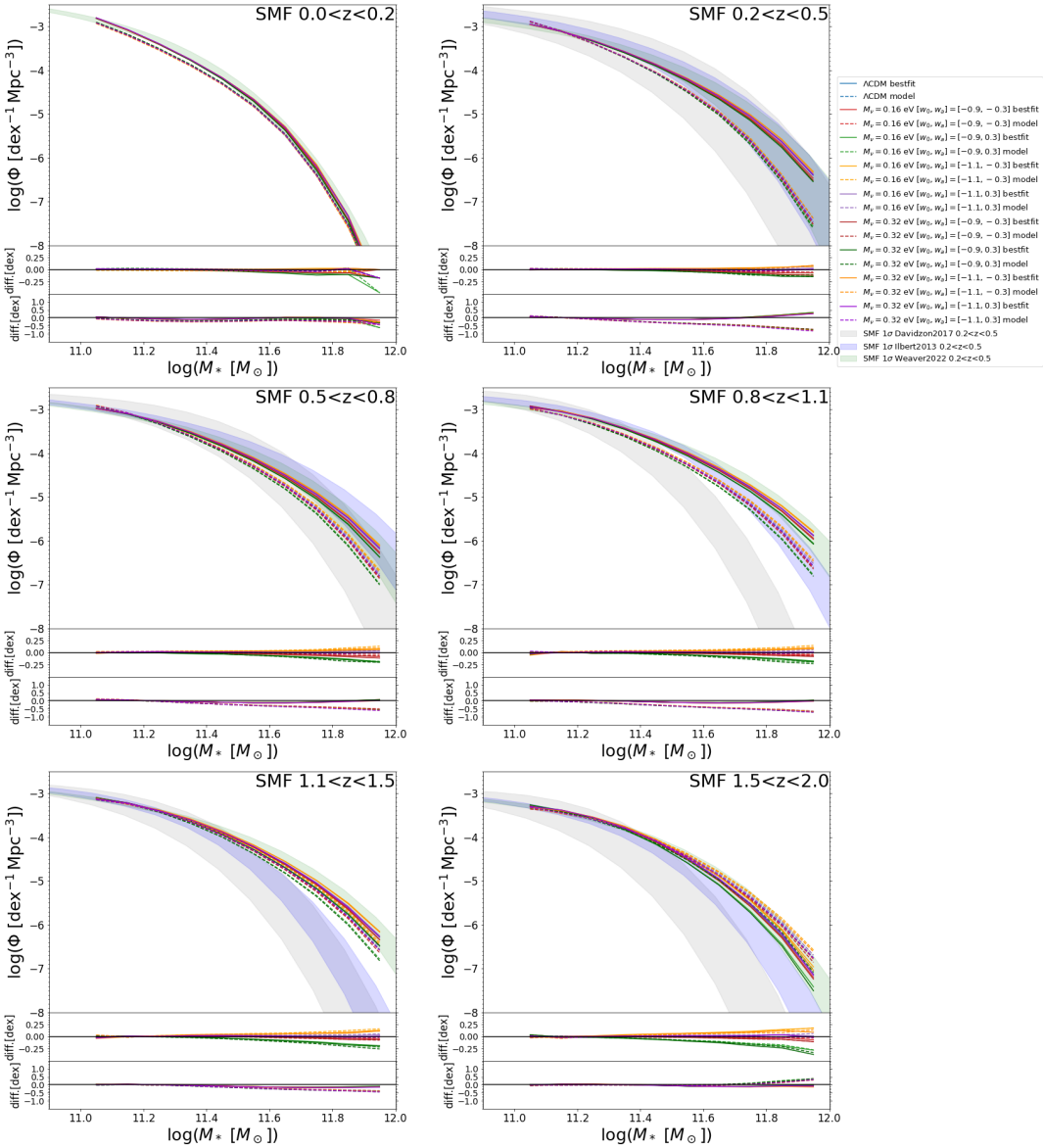

Figure 6.15: Stellar mass functions obtained from the galaxy mock catalogues of the DEMNUni simulations with dynamical dark energy and massive neutrinos ($M_\nu = 0.16, 0.32$ eV) at different redshift bins in Table 5.1. In each plot the upper panels show the SMF calculated using the best-fit SHMR parameters (solid lines) extracted at each redshift bin, or using the SHMR model dependent on z, $M_\nu$and (w_0, w_a) (dashed lines). These results are compared to the observed SMFs of Baldry et al. (2008) [79] and Weaver et al. (2022) [80], with shaded area representing the associated 1–σ uncertainty, as reported in the legenda. Green shaded area represents the Baldry 2008 SMF and the other coloured shaded areas the Weaver 2022 SMFs. The middle sub-panels show the logarithmic differences between the SMF obtained from simulations in the $\nu w_0 w_a$CDM scenarios and the ΛCDM case. The lowest sub-panels show the logarithmic differences between the SMFs obtained from the simulations and the corresponding observed ones rescaled according the dependence of the luminosity distance on the parameters w_0 and w_a.

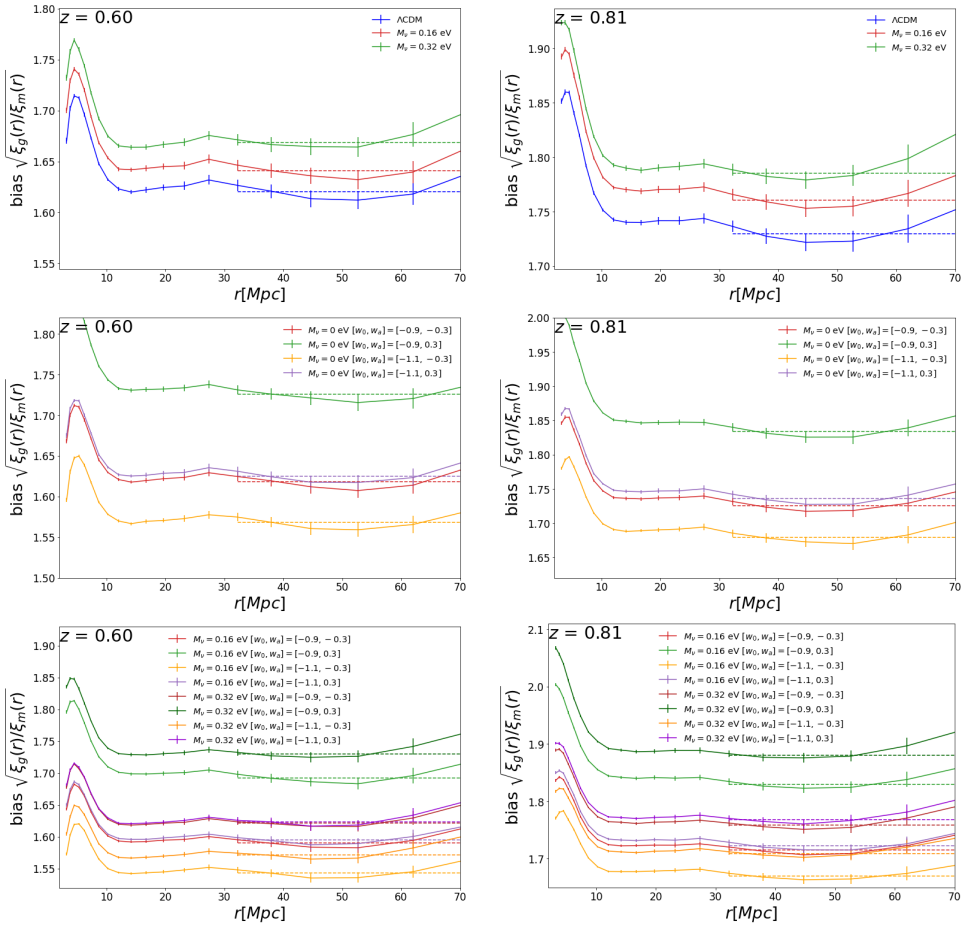

Figure 6.16: Bias obtained from the ratio between the real-space galaxy correlation function $\xi_g(r)$ and the matter correlation function $\xi_m(r)$ at $z = 0.60$ (left) and $z = 0.81$ (right). Upper panels show the results for the ΛCDM case and alternative models with massive neutrinos, the central panels for the dynamical dark energy and massless neutrinos while the lower panels for the combination of dynamical dark energy and massive neutrinos. Solid lines with different colors represent each cosmological model, while the dashed lines are the corresponding mean values of the bias calculated in the linear range 30 Mpc $< r <$ Mpc.

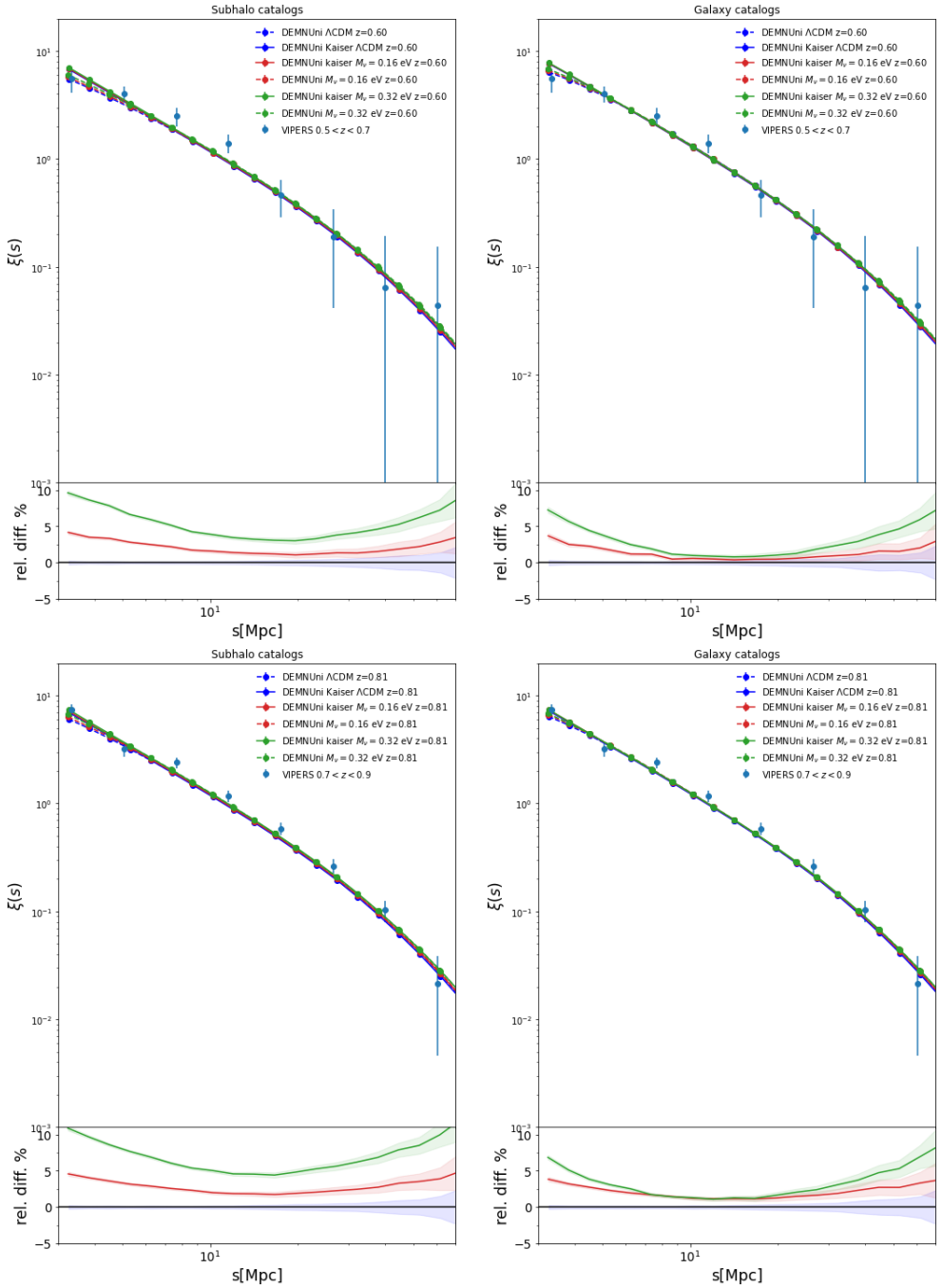

Figure 6.17: 2PCFs at $z_c = 0.6$ (top) and $z_c = 0.8$ (bottom) from subhalo catalogues (left) and galaxy catalogues (right) with the presence of massive neutrinos of $M_\nu = 0.16, 0.32$ eV. The upper panel shows the $\xi(s)$ measured from DEMNUni subhalo and galaxy mock catalogues with massive neutrinos with the redshift space distortions (dashed lines) and the $\xi(s)$ predicted with Kaiser effect (solid lines). Blue points with error bars indicates the galaxy 2PCF measured from the VIPERS data. The lower panel shows the relative percent difference between the $\xi(s)$ with massive neutrinos and the ΛCDM one. Each color represents different cosmological models.

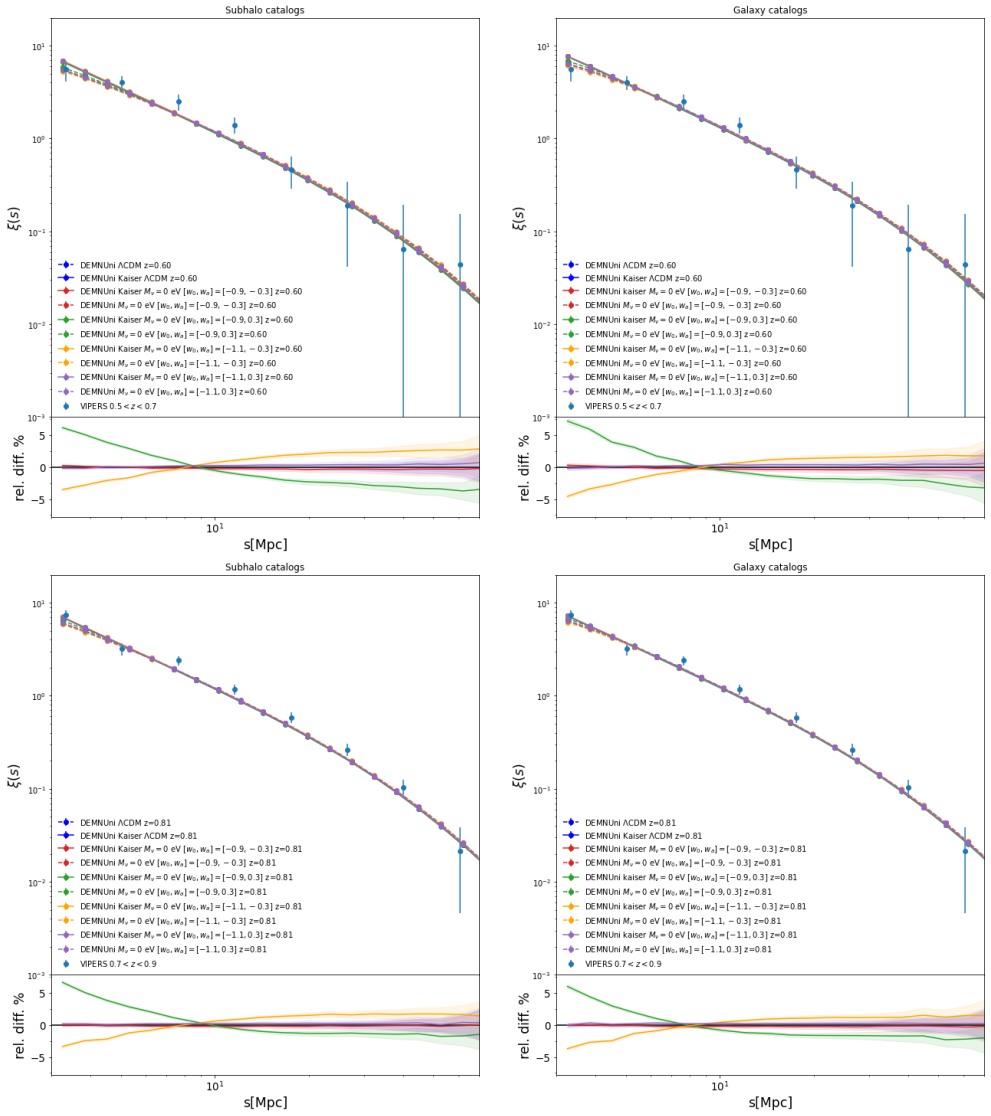

Figure 6.18: 2PCFs at $z_c = 0.6$ (right) and $z_c = 0.8$ (left) with the presence of dynamical dark energy and massless neutrinos. Lines and symbols are the same as in Figure 6.17.

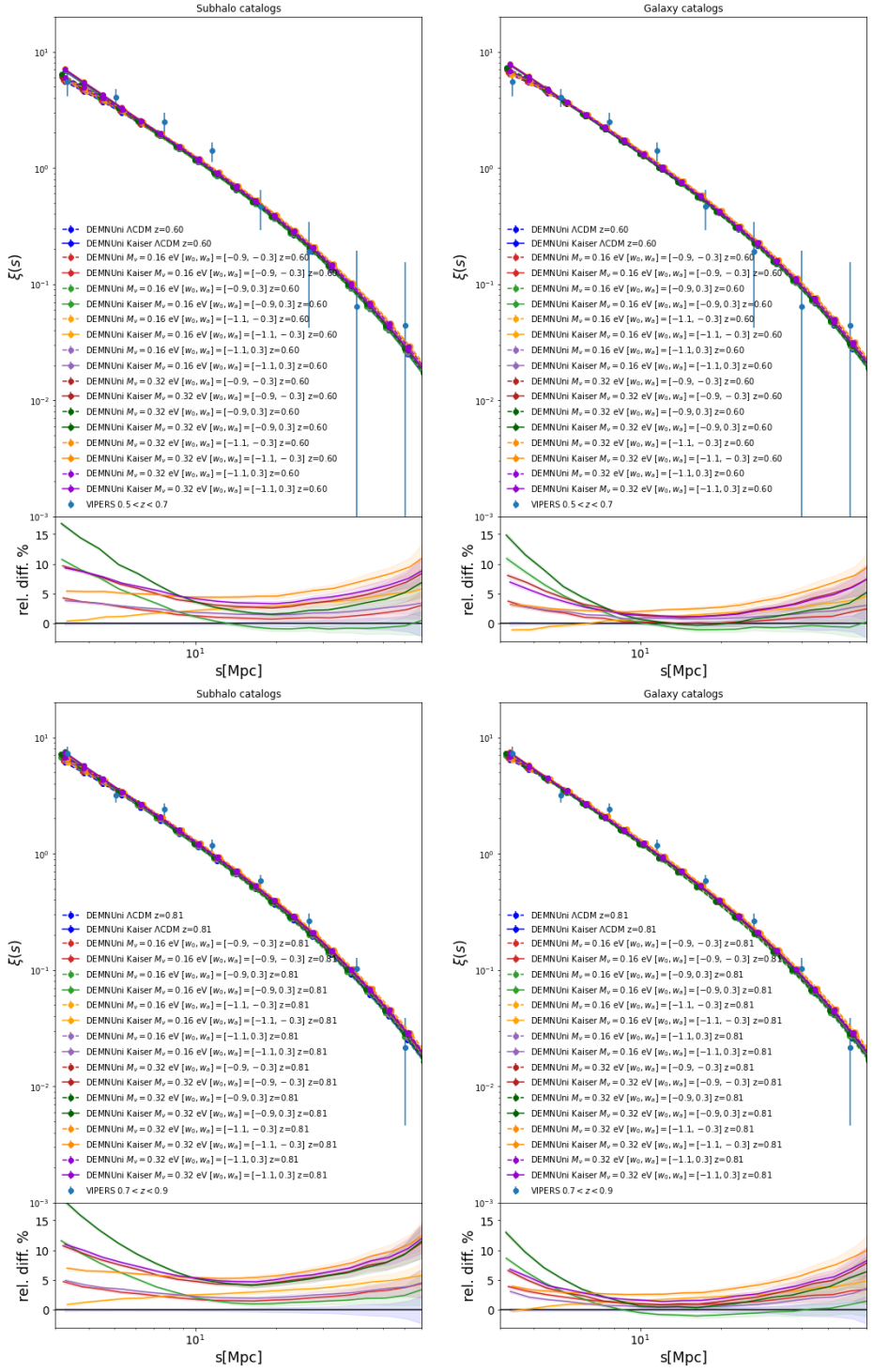

Figure 6.19: 2PCFs at $z_c = 0.6$ (right) and $z_c = 0.8$ (left) with the combination of dynamical dark energy and massive neutrinos. Lines and symbols are the same as in Figure 6.17.

CHAPTER 7

Halo mass functions, power spectra and bias

In this Chapter I show the measurements of the Halo Mass Function, Halo Power spectra and Halo Bias from the catalogs obtained with the DenHF code from the DEMNUni simulations.

This work is useful to improve the modelling of the cluster mass function and bias in cosmological scenarios with different neutrino masses and dark energy equations of state, as well as useful to provide a first estimate of the ability of disentangling between the analysed cosmological models using galaxy cluster data from the Euclid satellite.

Results at different overdensity values are presented in this Chapter. Since different overdensities represent different objects, or clusters selected in different ways, this study can be useful to understand which populations of objects (i.e. mass, detection method, eg Xray-SZ) is more sensitive to the cosmological parameters considered.

I wrote an automatic pipeline to run DenHF for various spherical overdensity thresholds and redshfit values of the comoving snapshots. In particular, I set the parameter file specifying these following characteristics:

- 100000 maximum number of particles per virialized halo
- consider only virialized haloes with a minimum number of particles $n_{vir} >= 10$
- gravitational softening 20 kpc/h
- 1000 minimum number of halo particles of which save the mass and density profiles.

Each snapshot is analysed with DenHF dividing the comoving volume in 64 sub-boxes.

7.1 The Halo Mass Function in $\nu w_0 w_a$CDM cosmologies

From the Halo catalogues obtained with the DenHF Halo Finder I compute the HMF with 20 logarithmic mass bins with the same width, starting from the minimum mass up to the maximum mass value of the catalogue. The measurements are obtained as $dn/d\ln(M)$, where n is the number density in each mass bins and $d\ln(M)$ is the bin width in logarithmic scale.

Figure 7.1 shows the HMF measurements in the ΛCDM model. Various overdensity values corresponding to $\Delta = 200_b, \Delta_{vir}, 200_c, 500_c$ are indicated with different line cross-spectra. The columns represent the measurements at redshifts $z = 0, 1, 1.5$.

At fixed redshift, as the spherical overdensity threshold increases, the HMF is more suppressed with respect to the case of the minimum threshold $\Delta = 200_b$ (line blue in Figure 7.1). Moreover, at $z = 0$ the rate of the damping effect increases at higher halo

mass values up to $M_h = 10^{15} M_\odot/h$, exceeding 50% relative difference for masses greater than $M_h > 10^{14} M_\odot/h$. This does not happen at higher redshifts, $z = 1, 1.5$, because massive haloes are rarer at those redshifts. Indeed, the difference with respect to the HMF for $\Delta = 200_b$ becomes increasingly significant as the redshift decreases: at $z = 0$ the difference between the HMF for $\Delta = 500_c$ (green line) and the one for 200_b (blue line) reaches the maximum value of almost 100% at $M_h = 10^{15} M_\odot/h$.

Furthermore, due to the decrease in the number of objects as the redshift increases, the HMF is increasingly damped as the redshift increases, as can be seen in the panels of Figure 7.1 moving from the left to the right side.

Finally, a significant effect is that for small overdensity thresholds $\Delta = 200_b, \Delta_{vir}, 200_c$ the different HMF are more distinguishable at low redshifts, as it can be observed in the left panel of Figure 7.1. Instead, as the redshift increases, the corresponding lines mostly overlap. This can be considered as an effect of structure formation that becomes more nonlinear as the redshift decreases, making the HMF more sensitive to small mass differences.

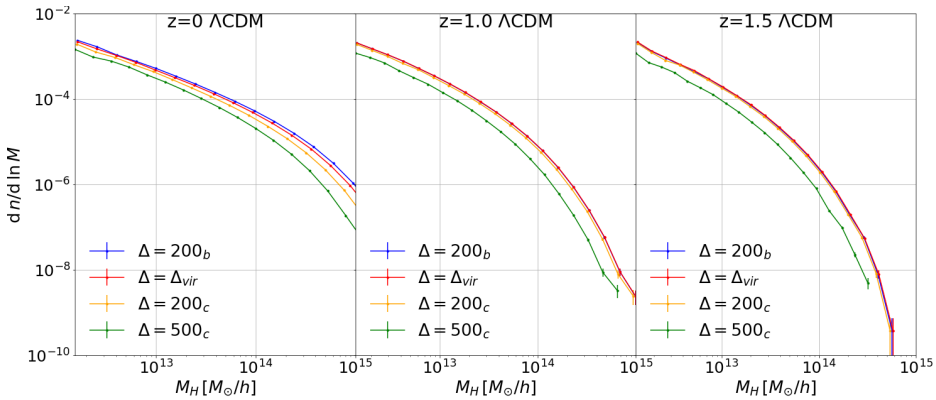

Figure 7.1: The halo mass-function in the ΛCDM model of Halo catalogs obtained with DenHF from DEMNUni simulations. Different colours show HMF at various overdensity values: 200_b, Δ_{vir}, 200_c, 500_c. Each column represents the measurements at different redshift values $z = 0, 1, 1.5$.

Furthermore, I estimate the HMF in cosmological models with massive neutrinos and dynamical dark energy, following the same method described above. Figure 7.2 shows the percent relative differences between measurements in $\nu w_0 w_a$CDM cosmologies with respect the ΛCDM one. First of all, the upper table of twelve panels shows such differences in the presence of massive neutrinos for two values of the total neutrino mass $M_\nu = 0.16, 0.32$ eV. Second, the middle table shows these differences for the case of dynamical dark energy and massless neutrinos, i.e. for $M_\nu = 0$ eV and four different combinations of the CPL parameters $w_0 = -0.9, -1.1$ and $w_a = -0.3, +0.3$. Third, the lower table represents the relative differences in models which combine the presence of massive neutrinos with dynamical dark energy for the (w_0, w_a) values aforementioned, for a total of eight different models. Moreover, moving from the left to right sides in each panel column measurements are indicated in increasing order of overdensity: $\Delta = 200_b, \Delta_{vir}, 200_c, 500_c$. Finally, each table is divided into three rows of panel for 3 different redshifts $z = 0, 1, 1.5$, in ascending order from top to bottom.

$\nu\Lambda$CDM scenarios: The effect of massive neutrinos is to suppress the HMF as their total mass increases. Indeed, the relative difference for models with massive neutrinos with respect to the standard (massless neutrino) ΛCDM case is increasingly negative and greater in absolute value as M_ν increases, starting from a few percent at small halo masses around $5\times10^{12}M_\odot/h$, until it reaches about 75% at the maximum halo mass value of $5\times10^{15}M_\odot/h$, as visible in the upper panels in Figure 7.2 in the case of $M_\nu = 0.32$ eV . The damping rate turns out to be higher for the cosmology with higher total neutrino mass value of $M_\nu = 0.32$ eV than for the one with the halved value of $M_\nu = 0.16$ eV. In fact, for example at $z = 0$, for a halo mass of $10^{15}M_\odot/h$, the difference for $M_\nu = 0.16$ eV (red line) is about 25%, while for $M_\nu = 0.32$ eV (green line) it doubles in absolute value up to 50%. In this case, the differences with respect to the ΛCDM case do not appear to be sensitive to the different overdensities. Instead, for the same overdensity and for the same halo mass, the differences increase as the redshift increases. We stress here that the mass resolution of the DEMNUni simulations does not allow to observe the trend of the HMF for halo masses $M_h < 5\times10^{12}M_\odot/h$. It is known that for small halo masses neutrino masses produce an inverted trend, i.e. for M_h the HMF increases as M_ν increases.

w_0w_aCDM scenarios: Moreover, as visible in the middle panels of Figure 7.2, in the case of dynamical dark energy and massless neutrinos, the HMF differ significantly from the ΛCDM case for the models with $[w_0, w_a] = [-1.1, -0.3]$ (orange line) and $[w_0, w_a] = [-0.9, +0.3]$ (green line), reaching at $M_h = 3\times10^{15}M_\odot/h$ a maximum difference of 40% and -70% respectively. Instead, in the other two cases (indicated with red and purple lines) the differences are only a few percent. This behaviour can be explained by the trend of the growth factor, $D(z)$, which affects structure formation, for the corresponding cosmologies, as shown in the right panel of Figure 6.6. In fact, one can notice that, in the case of $[w_0, w_a] = [-0.9, +0.3]$, $D(z)$ is suppressed with respect to the ΛCDM case, while, in the case of $[w_0, w_a] = [-1.1, -0.3]$, it is increased. For the other two DE models, $[w_0, w_a] = [-1.1, +0.3]$ (purple line) and $[w_0, w_a] = [-0.9, -0.3]$ (red line), the difference in $D(z)$ is at the sub-percent level, and this propagates to the behaviour of the HMFs, which, in this latter cases, are degenerate with the ΛCDM one. The relative differences are approximately similar with the variation of the overdensity while they vary considerably with redshift. Indeed, while at the minimum redshift the non-degenerate model (orange line) is significantly distinguishable from the ΛCDM, as the redshift increases it is increasingly suppressed until it becomes almost similar to the ΛCDM one at $z = 1.5$. On the contrary, this does not happen for the other non-degenerate model (green line) which is always distinguishable from the ΛCDM case.

νw_0w_aCDM scenarios: Finally, in cosmologies with the combination of neutrino mass and dynamical dark energy, we can observe that at $z = 0$ models with $M_\nu = 0.16$ eV and $[w_0, w_a] = [-1.1, -0.3]$ (solid yellow line) are completely degenerate with the ΛCDM case, because the suppression due to neutrino free streaming is compensated from the increase of the growth factor for these specific parameters of the dark energy equation of state. In general, for such DE parameters, the neutrino suppression of the HMF is always mitigated with respect to $\nu\Lambda$CDM scenarios (upper panel), independently of the redshift. On the contrary, DE models with $[w_0, w_a] = [-0.9, +0.3]$ (green light), always enhance the HMF suppression in the presence of neutrinos with respect to $\nu\Lambda$CDM scenarios. For the DE models degenerate with ΛCDM, i.e. $[w_0, w_a] = [-1.1, +0.3]$ and $[w_0, w_a] = [-0.9, -0.3]$, we recover mostly the trends shown in the upper panel. It is im-

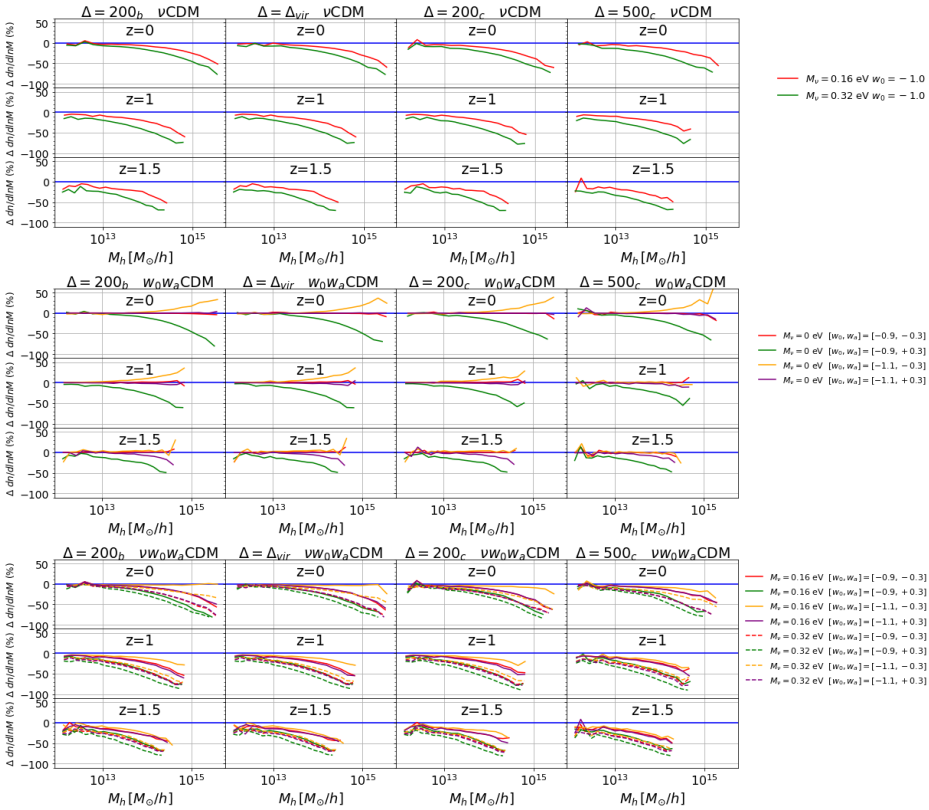

Figure 7.2: Percent difference with respect to the ΛCDM model of halo mass functions in $\nu w_0 w_a$CDM cosmologies. Upper panels: HMF in the presence of massive neutrinos with two values of total mass $M_\nu = 0.16, 0.32$ eV. Middle panels: HMF in the presence of dynamical dark energy. Lower panels: HMF in the presence of both massive neutrinos and dynamical dark energy. The columns and the rows in each panel represent the measurements for different overdensity values and redshift values respectively.

portant to notice that, by virtue of the dynamical dark energy effect on the growth factor, models with different neutrino masses may become mutually degenerate at different redshifts and different overdensity thresholds, as concern HMF measurements. Concerning differences with respect to the ΛCDM case, at a fixed halo mass they grow for all the eight different models as the redshift increases. In particular, for $M_h = 10^{14} M_\odot/h$, the relative differences grow in absolute values, starting from 30% at z=0, and reaching $60\% - 70\%$ at $z = 1, 1.5$, respectively.

7.2 Halo auto-spectra and bias in $\nu w_0 w_a$CDM cosmologies

As a next step, I process the halo catalogues, found via DenHF as described in the previous section , in order to calculate the power spectra, both auto and cross halo-matter. This analysis is useful to estimate the Halo Bias for different overdensities and redshifts as the cosmology varies.

I estimate the power spectra using the NbodyKit package. First of all, I read the

DenHF output catalogues using the Gadget-3 format libraries and extract the information of the halo masses and the 3D comoving Cartesian coordinates of the halo centers of mass (CM). Second, I construct the mesh from halo CM positions with the following specifications:

- number of meshes: $N_{mesh} = 2048$,
- size of the box: $L_{box} = 8\ \mathrm{Gpc}/h$,
- TSC resampler: method with interlaced and compensated specifications in order to correct the aliasing effects for low-resolution mesh measurements.

Then, the halo power spectra are computed with the FFTPower algorithm, specifying the 1D mode. Moreover, as we are implicitly assuming that measurements of the power spectra are uncorrelated under the Gaussian assumption, the minimal value for Δk should be the effective fundamental frequency defined as $k_{\mathrm{f}}^{\mathrm{eff}} \equiv 2\pi/V^{1/3}$, V being the volume sample. A value of Δk smaller than $k_{\mathrm{f}}^{\mathrm{eff}}$ would result in correlated bins even under the Gaussian assumption since $k_{\mathrm{f}}^{\mathrm{eff}}$ is the smallest difference in k one can resolve. That is:

$$\Delta k = \frac{2\pi}{L_{box}} \tag{7.1}$$

Also, the maximum scale in k [h/Mpc] unit, at which each power spectrum is computed, corresponds to

$$k_{max} = \frac{\pi N_{mesh}}{L_{box}} + \frac{\Delta k}{2} \tag{7.2}$$

7.2.1 Halo auto power-spectra

In this section, I analyse the measurements of the halo auto power spectra, computed selecting the halo catalogues with two different minimum masses: $M_{h,min} = 3 \times 10^{13} h^{-1} M_{\odot}$ and $M_{h,min} = 8 \times 10^{13} h^{-1} M_{\odot}$.

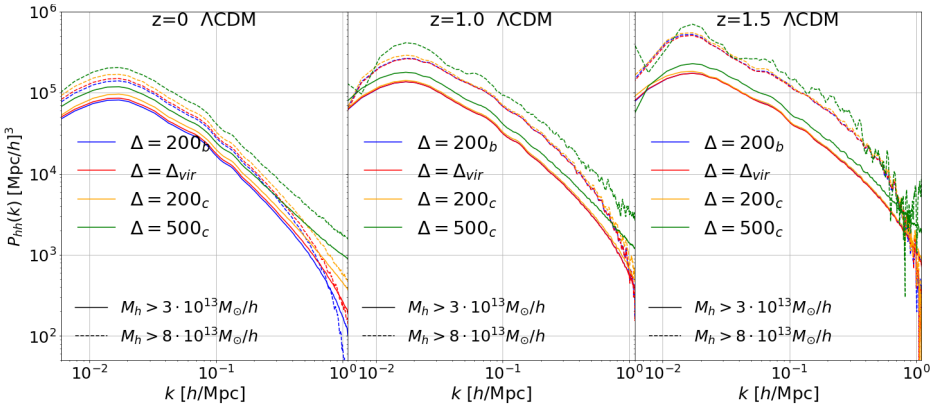

Figure 7.3: Halo auto-spectra in the ΛCDM model. Different colours show Power-Spectra at various overdensity values: 200_b, Δ_{vir}, 200_c, 500_c. Each column represent measurements at different redshift values $z = 0, 1, 1.5$. Moreover, solid lines indicate measurements with the minimum halo mass $M_{h,min} = 3 \times 10^{13} h^{-1} M_{\odot}$, while the dashed lines show those at $M_h > 8 \times 10^{13} h^{-1} M_{\odot}$.

Figure 7.3 shows the measurements of the halo power spectra in the ΛCDM model after shot-noise subtraction. The different overdensity values, corresponding to $\Delta = 200_b, \Delta_{vir}, 200_c, 500_c$, are indicated with different line cross-spectra, while the two mass thresholds, $M_{h,min} = 3 \times 10^{13} h^{-1} M_\odot$ and $M_{h,min} = 8 \times 10^{13} h^{-1} M_\odot$, are indicated with solid and dashed lines, respectively. The columns represent the measurements for different redshifts: $z = 0, 1, 1.5$. An increase of the power spectrum amplitude is detected as the overdensity increases: in fact, as the overdensity threshold increases, the corresponding HMF decreases, i.e. the halo number density decreases; this means that haloes become rarer objects for larger overdensity thresholds, and rarer objects are more clustered, i.e. have larger halo bias. For the same reason, there is a significant increase of signal (which becomes noiser) as the redshift increases, as observable looking from the left to the right in Figure 7.3. Similarly, the set of measurements made with the largest mass threshold ($8 \times 10^{13} h^{-1} M_\odot$) are systematically shifted to higher values with respect to the the smallest mass-cutoff ($3 \times 10^{13} h^{-1} M_\odot$), due to the decrease in the number of less massive objects, and therefore an increase of their bias, as we will show in the following sections.

Figure 7.4 and 7.5 show the percent relative differences between the shot-noise subtracted measurements of the halo auto-spectra in the $\nu w_0 w_a$CDM cosmologies with respect to the ΛCDM ones, at the two halo mass-cutoffs $M_{h,min} = 3 \times 10^{13} h^{-1} M_\odot$ and $M_{h,min} = 8 \times 10^{13} h^{-1} M_\odot$, respectively. First of all, the upper table of twelve panels shows the measurements for the $\nu\Lambda$CDM scenarios with $M_\nu = 0.16, 0.32$ eV. Second, the middle table represents the measurements in the $w_0 w_a$CDM cosmologies, i.e. for $M_\nu = 0$ eV and four different combinations of the CPL parameters $w_0 = -0.9, -1.1$ and $w_a = -0.3, +0.3$. Third, the lower table illustrates the relative differences in $\nu w_0 w_a$CDM cosmologies, i.e. for the combination of two neutrino masses, $M_\nu = 0.16, 0.32$ eV, and the four dynamical dark energy equations of state, for a total of eight different models. Moreover, looking from the left to the right side, each column of the multi-panel tables shows the measurements for increasing value of the overdensity threshold: $\Delta = 200_b, \Delta_{vir}, 200_c, 500_c$. The rows of the multi-panel tables shows three different redshifts $z = 0, 1, 1.5$, in ascending order from top to bottom.

$\nu\Lambda$CDM scenarios: As illustrated in the upper table of Figure 7.4, the halo auto-spectra with massive neutrinos are always characterised by a positive shift in amplitude. Also, the relative differences grow as both the redshift and neutrino mass increase. Indeed for $M_\nu = 0.16$ eV, at a fixed scale $k = 1\ h^{-1}$Mpc, the percent relative differences reach the level of $\Delta(\%) = 10\%, 15\%, 20\%$ for increasing redshifts $z = 0, 1, 1.5$, respectively. Furthermore, for the largest neutrino mass, $M_\nu = 0.32$ eV, the relative differences in the amplitude of the halo auto-spectra are more than doubled with respect to $M_\nu = 0.16$ eV, as they are $\Delta(\%) = 20\%, 40\%, 50\%$, respectively. On the other hand, relative differences do not depend from variations in the overdensity thresholds, as can be observed comparing the different columns of the upper table.

$w_0 w_a$CDM scenarios: As shown in the middle multi-panel table of Figure 7.4, in the presence of dynamical dark energy the relative difference of the halo auto-spectra with respect to the ΛCDM case is significant for the model with $[w_0, w_a] = [-0.9, +0.3]$, being up to $\Delta(\%) = 20\%$ at $z = 0$ and increasing up to $\Delta(\%) = 30\%, 35\%$ at larger redshifts $z = 1, 1.5$. The other model $[w_0, w_a] = [-1.1, -0.3]$ deviates slightly from ΛCDM with differences up to -5%. Instead, the other two remaining models are mostly degenerate with the ΛCDM case of $[w_0 = 1, w_a = 0]$. This again can be explained by looking at the

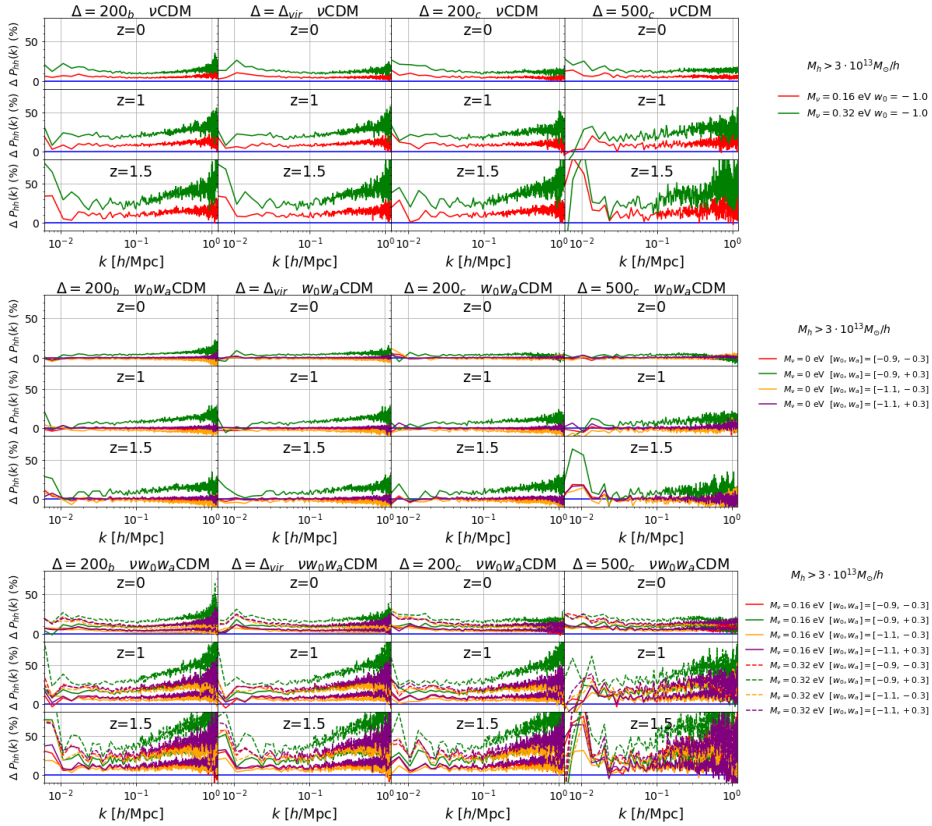

Figure 7.4: Percent difference with respect to the ΛCDM model of halo auto-spectra in $\nu w_0 w_a$CDM cosmologies. Minimum halo mass $M_{h,min} = 3 \times 10^{13} h^{-1} M_\odot$, relative difference to the ΛCDM model. Upper panels: Halo power spectra in the presence of massive neutrinos with two values of total mass $M_\nu = 0.16, 0.32$ eV. Middle panels: Halo power spectra in the presence of dynamical dark energy. Lower panels: Halo power spectra in the presence of both massive neutrinos and dynamical dark energy. The columns and the rows in each panel represent the measurements for different overdensity and redshift values respectively.

right panel of Figure 6.6. In fact, the growth factor is largely suppressed with respect to the ΛCDM model for $[w_0, w_a] = [-0.9, +0.3]$ (green line), and increased for $[w_0, w_a] = [-1.1, -0.3]$ (yellow line), implying that structure formation is suppressed in the first case and enhanced in the second case, therefore, at a fixed mass-cut, in the Universe there are fewer (more biased) haloes and more (less biased) haloes, respectively. Differences are instead negligible for the other two mostly degenerate dark energy models $[w_0, w_a] = [-1.1, +0.3]$ and $[w_0, w_a] = [-0.9, -0.3]$.

$\nu w_0 w_a$CDM scenarios: Finally, the lower multi-panel table in Figure 7.4 shows the measurements for the combination of massive neutrinos and dynamical dark energy. In this case, the differences are larger with respect to the $w_0 w_a$CDM models, due to the impact of a non-vanishing neutrino mass. In particular, the case with the highest neutrino mass, $M_\nu = 0.32$ eV, and $[w_0, w_a] = [-0.9, +0.3]$ deviates the most from the ΛCDM case, with increasing differences with $z = 0, 1, 1.5$ at $k > 0.05\,h/\mathrm{Mpc}$ up

to $\Delta(\%) = 60\%, 80\%, 100\%$, respectively. This is expected as, for this model, the combined effect of free-streaming massive neutrinos and dark energy growth suppression is maximised.

As shown in Figure 7.5, the measurements with the higher mass-cutoff have differences relative to the ΛCDM case with characteristics simlar to the lower cutoff in Figure 7.4. However, in this case we are selecting haloes with larger minimum mass, which are rarer than haloes with a lower mass-cutoff. Therefore, the relative differences are slightly enhanced due to the larger effective bias, as shonw in the following sections. In addition, especially at high redshifts $z = 1, 1.5$, and large overdensity thresholds, the signal turns out to be very noisy as the contribution of the shot noise dominates.

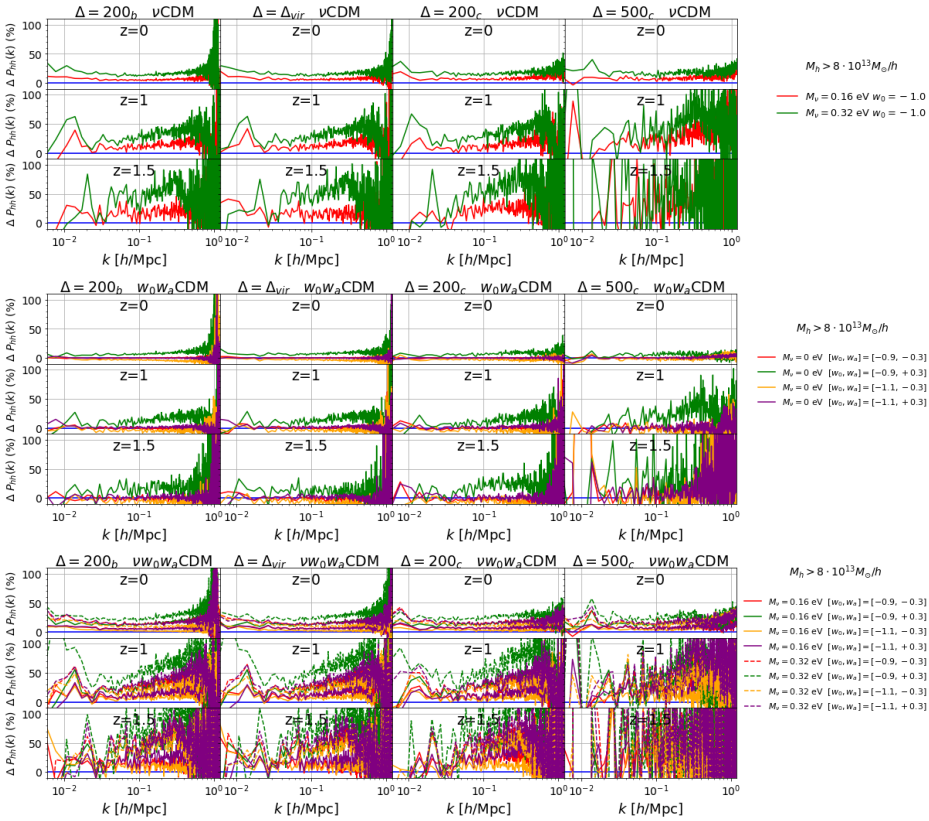

Figure 7.5: Percent difference with respect to the ΛCDM model of halo auto-spectra in $\nu w_0 w_a$CDM cosmologies. Minimum halo mass $M_{h,min} = 8 \times 10^{13} h^{-1} M_\odot$, relative difference to the ΛCDM model. Upper panels: Halo power spectra in the presence of massive neutrinos with two values of total mass $M_\nu = 0.16, 0.32$ eV. Middle panels: Halo power spectra in the presence of dynamical dark energy. Lower panels: Halo power spectra in the presence of both massive neutrinos and dynamical dark energy. The columns and the rows in each panel represent the measurements for several overdensity and redshift values respectively. Note the different scale along the y-axis with respect to Figure 7.4 due to the halo bias increase with the mass-cutoff.

7.2.2 The effective halo bias from auto-spectra

In this section I analyse the halo bias defined as the square root of the ratio between the halo auto power-spectrum P_{hh} and the matter power spectrum P_{mm}

$$b_{hh}(k) = \sqrt{\frac{P_{hh}(k)}{P_{mm}(k)}}. \tag{7.3}$$

In particular, the matter power spectrum is estimated reading the snapshot of the simulation and saving the positions of the cold dark matter particles. As a next step, a mesh is created with the same characteristics as the mesh for the density associated to the halo centres of mass. As a result, with the FFT algorithm in Nbobykit I compute the 1D auto-spectrum from the matter mesh. Figure 7.6 and 7.7 indicate the halo bias calculated from the measured halo and matter auto-spectra, for two different mass-cutoff, $M_{h,min} = 3 \times 10^{13} h^{-1} M_{\odot}$ and $M_{h,min} = 8 \times 10^{13} h^{-1} M_{\odot}$, respectively.

First of all, the upper multi-panel table shows the measurements of the halo bias in $\nu\Lambda$CDM scenarios with $M_{\nu} = 0.16, 0.32$ eV. Second, the middle table represents bias measurements in $w_0 w_a$CDM scenarios, for four different combinations of the CPL parameters $w_0 = -0.9, -1.1$ and $w_a = -0.3, +0.3$. Third, the lower table illustrates the relative differences in $\nu w_0 w_a$CDM scenarios.

As a common trend, for all the three distinct cosmological scenarios, as expected the halo bias grows significantly as the redshift increases. Furthermore, it has a constant value up to $k = 0.1\,h$/Mpc (linear bias), while for larger k it has an increasing trend, until it reaches the maximum at $k = 0.5$ h/Mpc. On the other hand, the value of the bias remains almost invariant for the different overdensity thresholds, except for $\Delta = 500_c$, when the bias is slightly larger if compared to the lower thresholds.

$\nu\Lambda$CDM scenarios: In particular, for cosmologies with massive neutrinos and cosmological constant, the bias increases with the total neutrino mass and with the redshift. Indeed, as shown in the upper panels of Figure 7.6, for $M_h > 3\ h^{-1} M_{\odot}$ at $z = 0$ the bias is up to 2, then at $z = 1$ goes up to 5 and 6 for $M_{\nu} = 0.16$ eV and 0.32 eV, respectively, and at $z = 1.5$ reaches values of 9 and 10. This is in agreement with the behaviour of the auto-spectra, as described in the previous section. Moreover, by comparison with the ΛCDM trend (blue line), we can observe a larger scale dependence with increasing M_{ν}, as expected from neutrino free streaming. Such an effect is enhanced as the redshift, and therefore the halo bias, increases.

$w_0 w_a$CDM scenarios: In the case of cosmologies with massless neutrinos and dynamical dark energy, as indicated in the middle table of Figure 7.6, the effective bias differs sensibly from the ΛCDM model only for $[w_0, w_a] = [-0.9, +0.3]$ (green lines). In this case, the halo bias at high redshift, $z = 1.5$, reaches values up to 7.5, with an increase of 15% with respect to the ΛCDM case. On the other hand, the other three remaining DE models are very similar to the ΛCDM one, but it is interesting to notice that, for all the different redshifts and overdensity threshods, the bias corresponding to $[w_0, w_a] = [-1.1, -0.3]$ (yellow lines) is alway slightly smaller than in the ΛCDM case. Also for these models, we are in agreement with the measurements of the halo auto-spectra.

$\nu w_0 w_a$CDM scenarios: Finally, for the combination of massive neutrinos and dynamical dark energy, as shown in the lower table in Figure 7.6, the halo bias is always larger than the corresponding value in the ΛCDM, with an increase of 47% at most, for $z = 1.5$,

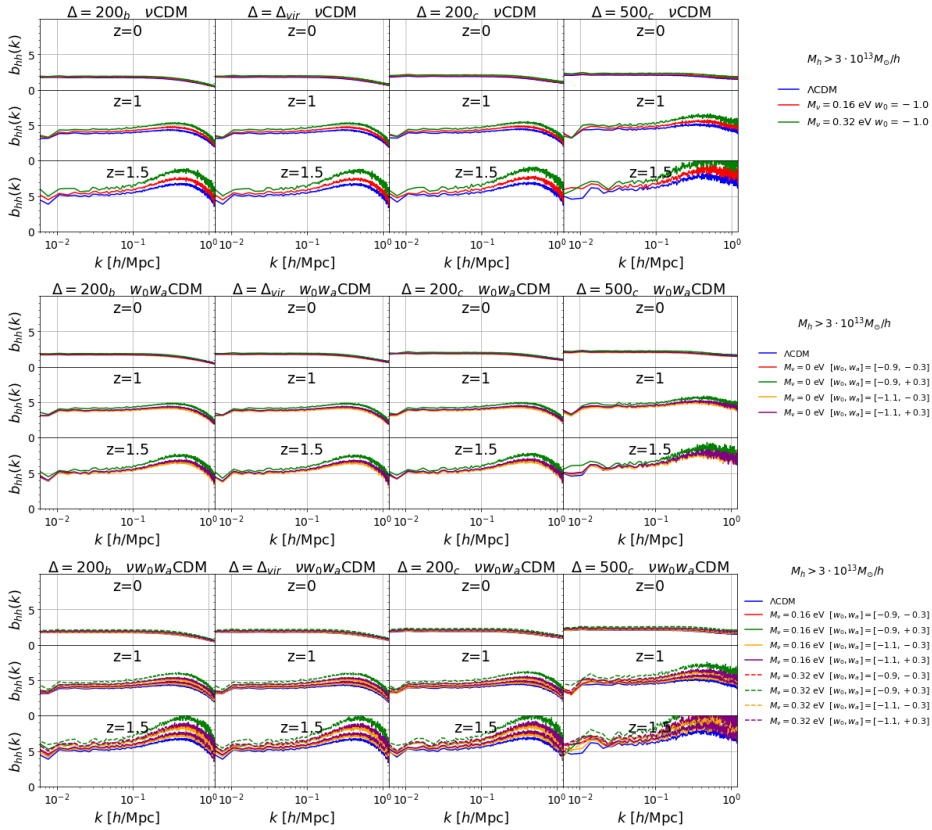

Figure 7.6: Effective halo bias from auto-spectra in $\nu w_0 w_a$CDM cosmologies. Minimum halo mass $M_{h,min} = 3 \times 10^{13} h^{-1} M_\odot$. Upper panels: Halo Bias in the presence of massive neutrinos with two values of total mass $M_\nu = 0.16, 0.32$ eV. Middle panels: Halo Bias in the presence of dynamical dark energy. Lower panels: Halo Bias in the presence of both massive neutrinos and dynamical dark energy. The columns and the rows in each panel represent the measurements for different overdensity and redshift values respectively.

$M_\nu = 0.32$ eV, $[w_0, w_a] = [-0.9, +0.3]$, and $\Delta = 200_b$. As for the auto-spectra, different DE equations of state can produce degeneracy between different neutrino masses, and in some cases, as for $[w_0, w_a] = [-1.1, -0.3]$ (yellow lines), they can decrease the halo bias with respect to $\nu\Lambda$CDM scenarios, due to the increase of growth factor and therefore structure formation, so that more smaller haloes are formed producing a lower total effective bias. On the other hand, the DE model with $[w_0, w_a] = [-0.9, +0.3]$ (green lines), increases the bias by suppressing structure formation, and, e.g., at $z = 1$ the bias reaches a value of about 12, for $M_\nu = 0.32$ eV and $[w_0, w_a] = [-0.9, +0.3]$.

Similarly, in Figure 7.7, the bias values at higher mass-cutoff, $8 \times 10^{13} h^{-1} M_\odot$, have the same characteristics as in Figure 7.6. However, in this case measurements are all shifted to larger values, due to the presence of fewer objects with small mass due to the higher mass-cutoff. For the same reason, especially at high redshifts, the bias signal is very noisy.

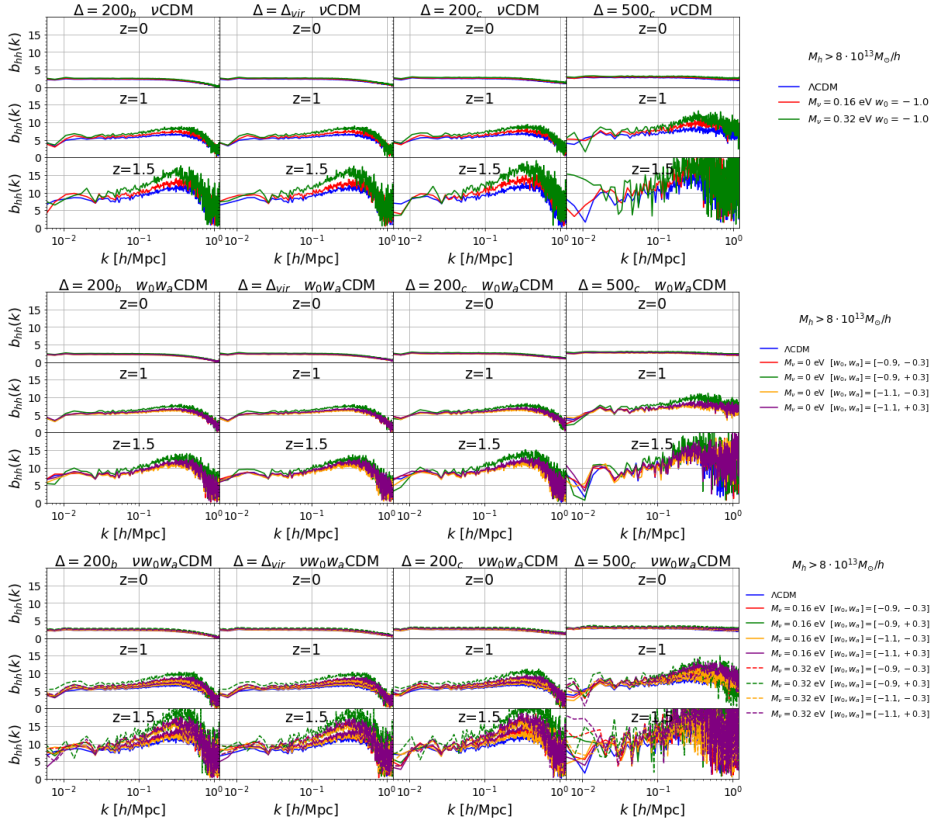

Figure 7.7: Effective halo bias from auto-spectra in $\nu w_0 w_a$CDM cosmologies. Minimum halo mass $M_{h,min} = 8 \times 10^{13} h^{-1} M_\odot$. Upper panels: Halo Bias in the presence of massive neutrinos with two values of total mass $M_\nu = 0.16, 0.32$ eV. Middle panels: Halo Bias in the presence of dynamical dark energy. Lower panels: Halo Bias in the presence of both massive neutrinos and dynamical dark energy. The columns and the rows in each panel represent the measurements for different overdensity and redshift values respectively. Note the different scale along the y-axis with respect to Figure 7.6 due to the halo bias increase with the mass-cutoff.

7.3 Halo-matter cross-spectra and bias in $\nu w_0 w_a$CDM cosmologies

In this section I analyse the cross-spectra between the halo catalogues and the matter distribution. I create two distinct meshes, one for matter and the other for haloes, with the same size $L_{box} = 2$ Gpc/h and number of meshes $N_{mesh} = 2048$. As a next step, I compute the 1D cross-spectra, passing the two meshes as two different arguments in the function FFTPower, implemented in Nbodykit.

7.3.1 Halo-matter cross-spectra

In Figure 7.8 I show the halo-matter cross-spectra in the ΛCDM model. Various overdensity thresholds, corresponding to $\Delta = 200_b, \Delta_{vir}, 200_c, 500_c$, are indicated with different colours, while the two different mass thresholds of $M_{h,min} = 3 \times 10^{13} h^{-1} M_\odot$ and $M_{h,min} = 8 \times 10^{13} h^{-1} M_\odot$ are indicated with solid and dashed lines, respectively. The

columns represent the measurements at different redshift values $z = 0, 1, 1.5$.

The set of measurements made with the largest mass-cutoff ($8 \times 10^{13} h^{-1} M_\odot$) have larger amplitude than the ones with the smallest mass-cutoff ($3 \times 10^{13} h^{-1} M_\odot$), due to the smaller number of less massive objects in the halo distribution. Such a difference increases with the redshift. For the same reason, when the overdensity threshold increases, the cross signal is greater in amplitude, due to the decrease in the number of haloes at high spherical overdensities. At low redshift, nonlinear structure formation make such a difference smaller.

Comparing Figure 7.8 with Figure 7.3 we can notice an important difference: the cross-spectra have a smaller amplitude with respect to the auto-spectra and moreover their amplitude decreases with increasing redshifts. This is due to the fact that in this case the decrease with z of the amplitude of matter perturbations dominates the increase of the halo bias, which in the cross-spectra enters linearly (while in the auto-spectra enters quadratically), as I will show in the following sections.

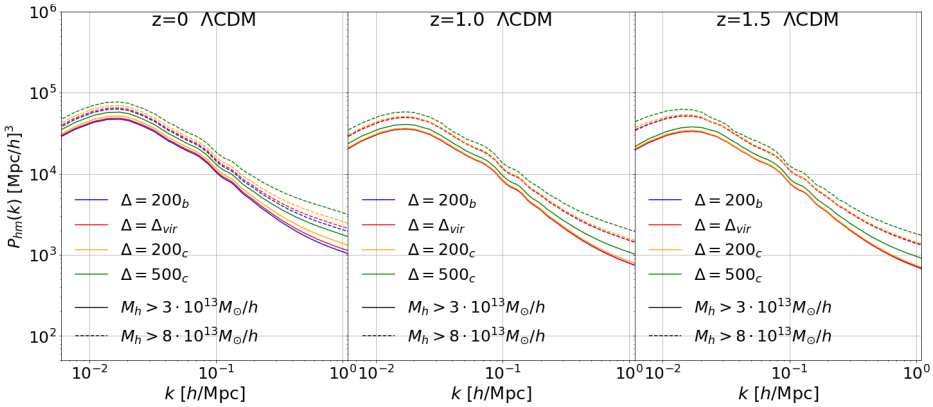

Figure 7.8: Halo-matter cross-spectra in the ΛCDM model. different colours show cross-spectra at various overdensity values: 200_b, Δ_{vir}, 200_c, 500_c. Each column represent the measurements at different redshift values $z = 0, 1, 1.5$.

Figures 7.9–7.10 show the percent relative differences between the measurements of the halo-matter cross-spectra in $\nu w_0 w_a$CDM cosmologies with respect the ΛCDM ones, at the halo mass-cutoffs $M_{h,min} = 3 \times 10^{13} h^{-1} M_\odot$ and $M_{h,min} = 8 \times 10^{13} h^{-1} M_\odot$, respectively. In general, the relative differences of $P_{hm}(k)$ for the various cosmological models with respect to the ΛCDM case at all redshifts and overdensities are quite small with respect to the auto-spectra, only a few percent within 5%, except at very large scales $k < 0.05$ h/Mpc, where the difference raises up to 15%. This is due to the fact that the bias enters linearly and not quadratically in P_{hm}, consequently this makes this measurements not very sensitive to the variation of the cosmological model. Furthermore, the halo-matter cross-spectrum is not an observational measure, because dark matter is not observable. However, $P_{hm}(k)$ measurements are mainly used to estimate the bias b_{hm}, because the latter could be measured from the cross between WL which is the integral of $P_{mm}(k)$ with the halo/galaxy distributions. For this and more reasons, it is useful to comment on the features of cross-spectra in $\nu w_0 w_a$CDM scenarios.

Cosmological model comparison: First we observe a very different trend between the case with massive neutrinos and the masseless one. In fact, the middle multi-panel ta-

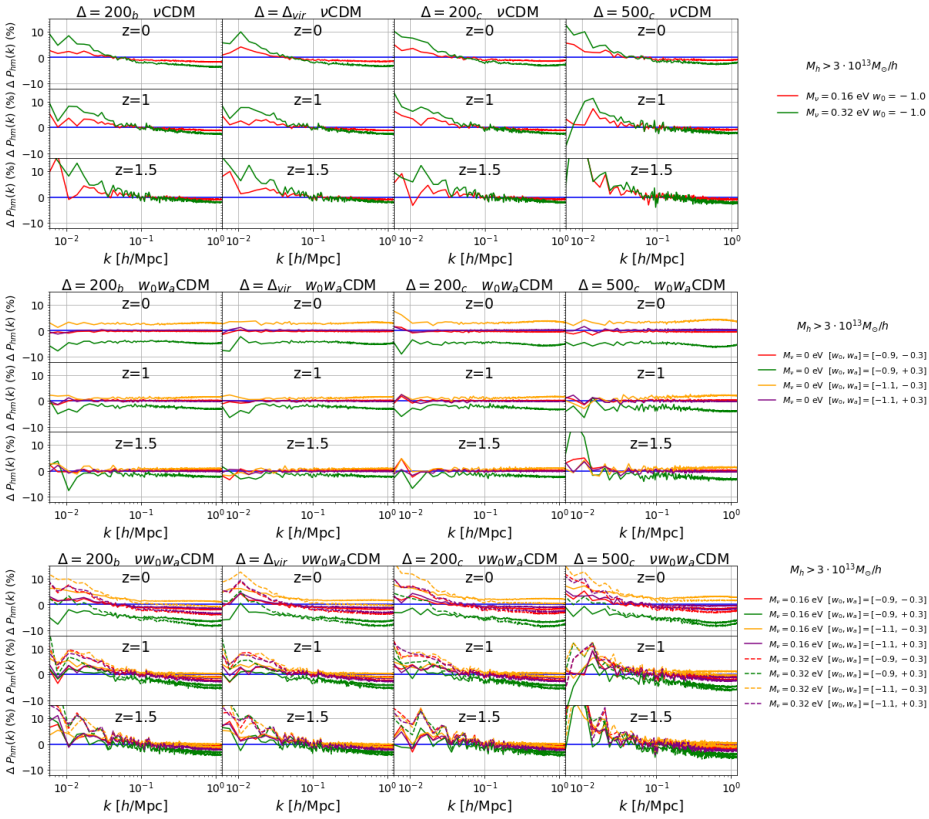

Figure 7.9: Percent difference with respect to the ΛCDM model of halo-matter cross-spectra in $\nu w_0 w_a$CDM cosmologies. Minimum halo mass $M_{h,min} = 3 \times 10^{13} h^{-1} M_\odot$, relative difference to the ΛCDM model. Upper panels: cross-spectra in the presence of massive neutrinos with two values of total mass $M_\nu = 0.16, 0.32$ eV. Middle panels: cross-spectra in the presence of dynamical dark energy. Lower panels: cross-spectra in the presence of both massive neutrinos and dynamical dark energy. The columns and the rows in each panel represent the measurements for different overdensity and redshift values respectively. Note the different scale from the auto-spectra in Figure 7.4, as cross-spectra are less sensitive to cosmological model variation.

ble in Figure 7.9 shows a mostly scale-independent trend, except for very large scales at high redshits (which are affected by cosmic variance). This is different from massive neutrino scenarios, both with cosmological constant and dynamical dark energy (upper and bottom panels in the same figure), where we can observe a scale-dependent trend in the relative differences. Such a scale-dependence is due to neutrino free streaming producing a scale-dependent suppression of the matter power spectrum, which at small scales dominates the bias increase. At large scales, the increase in amplitude, in the presence of massive neutrinos, could be due to the fact that at those scales neutrino do not free-stream, but do cluster as cold dark matter, while they anyway enhance the halo bias, as both the neutrino mass and redshift increase. In fact, larger the neutrino mass is, larger the amplitude is at large scales and the suppression at small scales, with respect to the ΛCDM case. Moreover, comparing the upper and bottom panels, we can see that the suppression at small scales may transform in an increase of power for

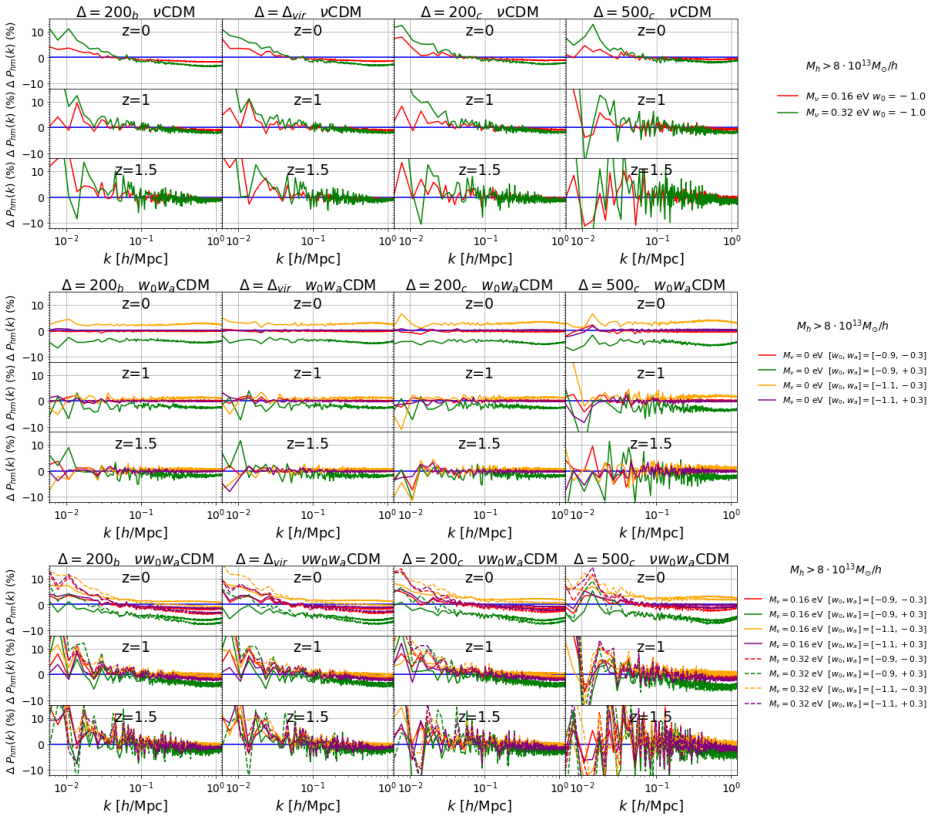

Figure 7.10: Percent difference with respect to the ΛCDM model of halo-matter cross-spectra in $\nu w_0 w_a$CDM cosmologies. Minimum halo mass $M_{h,min} = 8 \times 10^{13} h^{-1} M_\odot$, relative difference to the ΛCDM model. Upper panels: cross-spectra in the presence of massive neutrinos with two values of total mass $M_\nu = 0.16, 0.32$ eV. Middle panels: cross-spectra in the presence of dynamical dark energy. Lower panels: cross-spectra in the presence of both massive neutrinos and dynamical dark energy. The columns and the rows in each panel represent the measurements for different overdensity and redshift values respectively. Note the different scale from the auto-spectra in Figure 7.5, as cross-spectra are less sensitive to cosmological model variation.

$[w_0, w_a] = [-1.1, -0.3]$ (yellow lines), at least for small redshifts and large overdensity thresholds. This means that the excess of growth, with respect to the ΛCDM case, in the matter density perturbations (see Figure 6.6) dominates over neutrino free streaming and structure formation suppression. The opposite trend occurs for $[w_0, w_a] = [-0.9, +0.3]$ (green lines), where the cross-spectra suppression enhances the effect of neutrinos, as expected. Indeed, the latter DE model is able to cause the suppression of the cross-spectra amplitude even at large scales, for small neutrino masses and redshifts. The other two DE models, $[w_0, w_a] = [-1.1, +0.3]$ and $[w_0, w_a] = [-0.9, -0.3]$, being degenerate with the ΛCDM one, do not produce observable differences with respect to the $\nu\Lambda$CDM case.

Comparison between auto- and cross-spectra: Looking at the top panels of Figures 7.4 and 7.9, we can observe that, in the case of auto-spectra, the increase of the bias (entering quadratically the auto-spectra) due to neutrino suppression of structure forma-

tion, which makes objects of the same mass rarer than in the ΛCDM case, always dominates over the suppression of matter perturbations in the presence of massive neutrinos. Therefore, the differences with respect to the ΛCDM case, stay always positive and mostly scale independent at least at small redshifts, contrary to what happens to the cross-spectra. We can observe similar differences also comparing the bottom panels of Figures 7.4 and 7.9, where massive neutrinos are combined with dynamical dark energy models: for auto-spectra the bias increase always dominates over the change in the evolution of matter density perturbations in $\nu w_0 w_a$CDM cosmologies. Therefore, again the differences with respect to the ΛCDM case stay always positive, and mostly scale independent at low z. In particular, contrary to what happens for cross-spectra, for $[w_0, w_a] = [-1.1, -0.3]$ (yellow lines), the increase in the number density of small mass haloes, due to an excess in the growth factor (see Figure 6.6), produces a decrease of the effective halo bias with respect to the $\nu\Lambda$CDM case, and therefore a larger degeneracy with the massless neutrino ΛCDM case. Finally, comparing the middle panels of Figures 7.4 and 7.9, we can observe a completely opposite difference in the two cases: for auto-spectra the green (yellow) curves represent positive (negative) differences with respect to the ΛCDM case model, while for cross-spectra such differences are inverted in sign. Again, this happens because, for halo cross-spectra the increase (decrease) of the growth factor and amplitude of matter perturbations dominates the decrease (increase) of the halo effective bias.

Finally, Figure 7.10 show the measurements for the largest mass cutoff, $M_{h,min} = 8 \times 10^{13} h^{-1} M_\odot$. We can observe the same features as in Figure 7.9, but much noisier, especially at larger redshifts and overdensity thresholds, due to the increased shot-noise.

7.3.2 The effective halo bias from cross-spectra

I estimate the effective halo bias as the ratio between the cross power spectrum and the matter power spectrum, as:

$$b_{hm}(k) = \frac{P_{hm}(k)}{P_{mm}(k)} \tag{7.4}$$

Figures 7.11 and 7.12 show effective halo bias measurements from halo-matter cross-spectra for two different halo mass-cutoffs: $M_{h,min} = 3 \times 10^{13} h^{-1} M_\odot$ and $M_{h,min} = 8 \times 10^{13} h^{-1} M_\odot$, respectively.

As it is easily to observe, comparing Figure 7.11 with Figure 7.6, and Figures 7.12 and Figure 7.6, the halo bias from the cross-spectra is more non-linear and scale-dependent than the corresponding measurements from auto-spectra. Indeed, unlike b_{hh} at large k values, and more precisely in the non-linear regime at $k > 0.1\,h$/Mpc, the bias b_{hm} is increases rapidly. On the other hand, at $k < 0.1\,h$/Mpc the scale-dependence and amplitude of the bias b_{hm} is similar to the b_{hh} one, as it takes on a constant and similar value in that scale range.

$\nu\Lambda$CDM scenarios: In particular in the cosmologies with massive neutrinos and cosmological constant, b_{hm} increases with the total neutrino mass and the redshift. Indeed, at large scales, $k < 0.1\,h$/Mpc, for the 500_c overdensity, as shown in the upper panels of Figure 7.11, at $z = 0$ the bias for $M_h > 3\,h^{-1} M_\odot$ is up to 2, then at $z = 1$ is up to 5 and 5.5 for $M_\nu = 0.16$ eV and 0.32 eV respectively, until reaching 6.5 and 7 at $z = 1.5$. In particular, at small scales, $k > 0.1\,h$/Mpc, the increment of bias with the scale is more and more considerable as redshift increases. Due to this effect, the b_{hm} bias at different neutrino

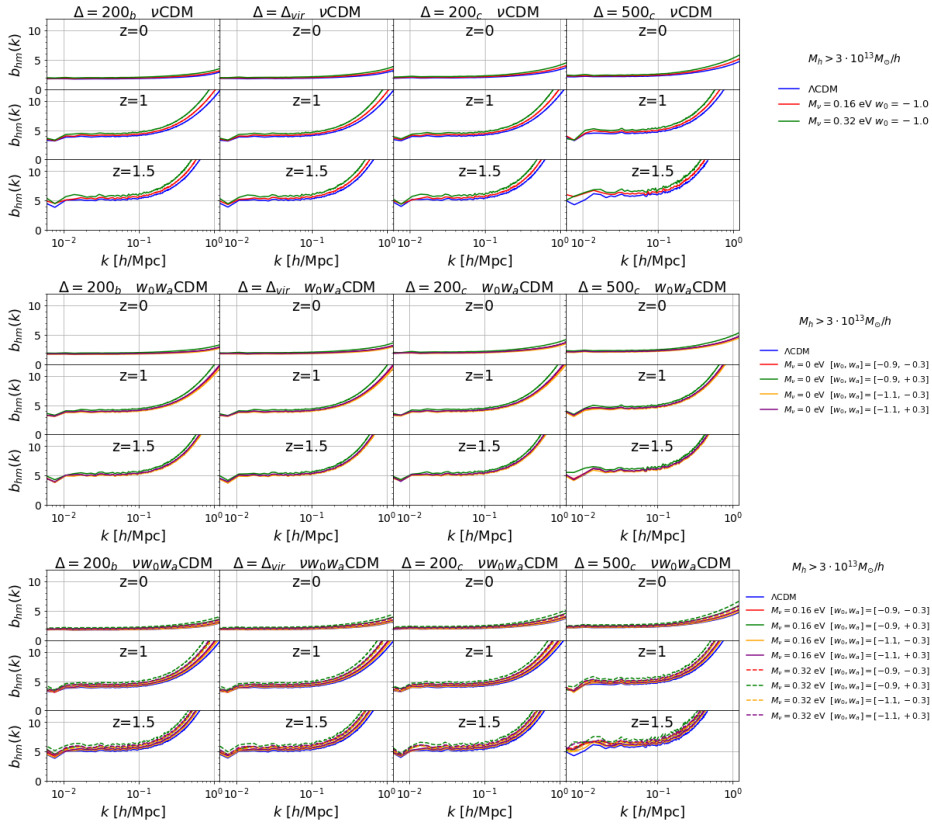

Figure 7.11: Effective halo bias from halo-matter cross-spectra in $\nu w_0 w_a$CDM cosmologies. Minimum halo mass $M_{h,min} = 3 \times 10^{13} h^{-1} M_\odot$. Upper panels: Halo Bias in the presence of massive neutrinos with two values of total mass $M_\nu = 0.16, 0.32$ eV. Middle panels: Halo Bias in the presence of dynamical dark energy. Lower panels: Halo Bias in the presence of both massive neutrinos and dynamical dark energy. The columns and the rows in each panel represent the measurements for different overdensity and redshift values respectively.

masses are more distinguishable. Indeed, at $k = 0.3$. $z = 1$ and for the $\Delta = 500_c$, b_{hm} reaches the level of 7 for neutrino of mass $M_\nu = 0.16$ eV and 8 for $M_\nu = 0.32$ eV. Also, at $z = 1.5$ b_{hm} is up to 10 for neutrino of mass $M_\nu = 0.16$ eV and 11 for $M_\nu = 0.32$ eV.

$w_0 w_a$CDM scenarios: Furthermore, as shown in the middle panels of Figure 7.11, the relevant characteristic for cosmologies with dynamical dark energy models is that only in the $[w_0, w_a] = [-0.9, +0.3]$ case (green lines) the bias b_{hm} is distinguishable from the ΛCDM one. Furthermore, the gap is more and more noticeable on small scales as k increases, starting from $k = 0.1\,h/$Mpc. For example, at $k = 0.5$ and $z = 1$, for the $\Delta = 200_b$, in the $[w_0, w_a] = [-0.9, +0.3]$ case b_{hm} is up to 8 and for the remaining cosmologies is lower at 7. Then, at the same scale and overdensity threshold, but higher redshift $z = 1.5$, b_{hm} increases up to 11.5 and 10.5 for the $[w_0, w_a] = [-0.9, +0.3]$ case and the other cosmologies respectively.

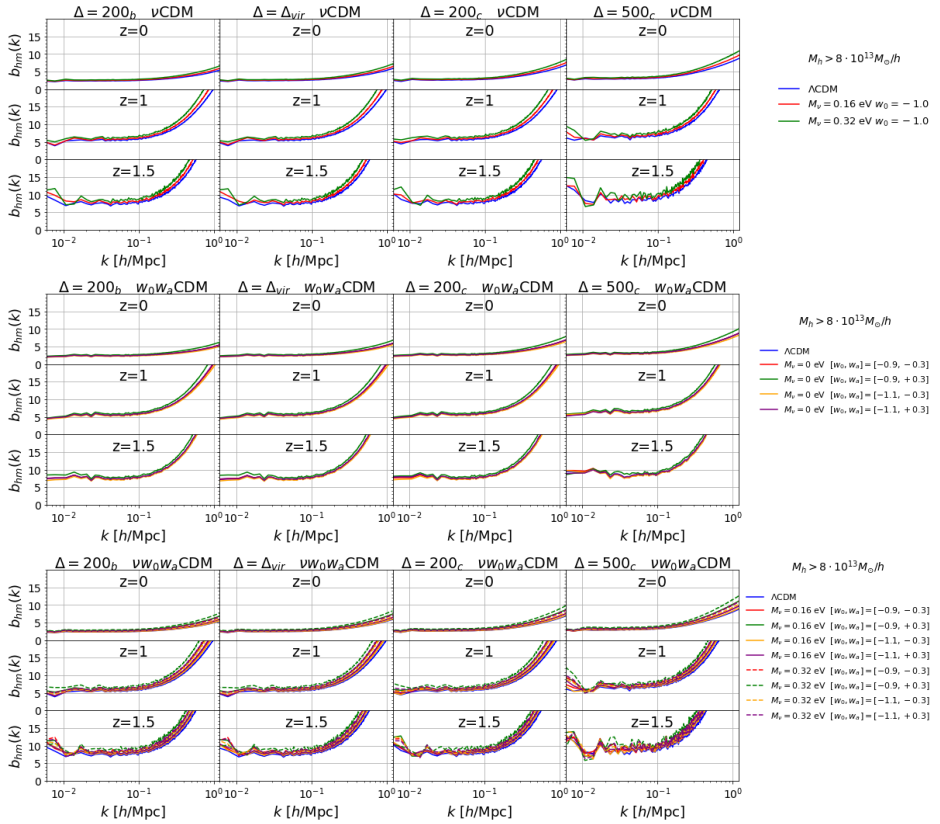

Figure 7.12: Effective halo bias from halo-matter cross-spectra in $\nu w_0 w_a$CDM cosmologies. Minimum halo mass $M_{h,min} = 8 \times 10^{13} h^{-1} M_\odot$. Upper panels: Halo Bias in the presence of massive neutrinos with two values of total mass $M_\nu = 0.16, 0.32$ eV. Middle panels: Halo Bias in the presence of dynamical dark energy. Lower panels: Halo Bias in the presence of both massive neutrinos and dynamical dark energy. The columns and the rows in each panel represent the measurements for different overdensity and redshift values respectively. Note the different scale along the y-axis with respect to Figure 7.11 due to the halo bias increase with the mass-cutoff.

$\nu w_0 w_a$CDM scenarios: Due to the combination of massive neutrinos and dynamic dark energy, the bias b_{hm} appears grouped in two different beams, one for mass $M_\nu = 0.16$ eV and the other for mass $M_\nu = 0.32$ eV, which is shifted to higher values. Finally, the case with $M_n u = 0.32$ eV and $[w_0, w_a] = [-0.9, +0.3]$ differs significantly from this bundle, which reaches the highest bias values: at $k = 0.5$ for 200_b up to 3 at z=0, 10 at z=1 and 13.5 at z=1.5.

Finally, the bias b_{hm} with the largest mass-cutoff at $M_{h,min} = 8 \times 10^{13} h^{-1} M_\odot$, shown in Figure 7.12, presents the same features as for $M_{h,min} = 3 \times 10^{13} h^{-1} M_\odot$. In this case, the bias is shifted toward larger values, due to the lack of less massive haloes.

7.4 The halo bias in $\nu w_0 w_a$CDM cosmologies: mass bin analysis

In order to study how the halo bias varies with the halo mass, I compute the halo and auto- and halo-matter cross-spectra in several mass bins (in the case of the auto-spectra

the shot-noise is sumstracted), with the same width in logarithmic scale, $\Delta M_{bin} = 0.2$, starting from a minimum mass $M_{h,min} = 3 \times 10^{13} M_{\odot}/h$. In particular, I consider the mass bins, containing at least 10000 haloes, in common between the different cosmological models, and apply Equations 7.3 and 7.4 to measure b_{hh} and b_{hm}, respectively.

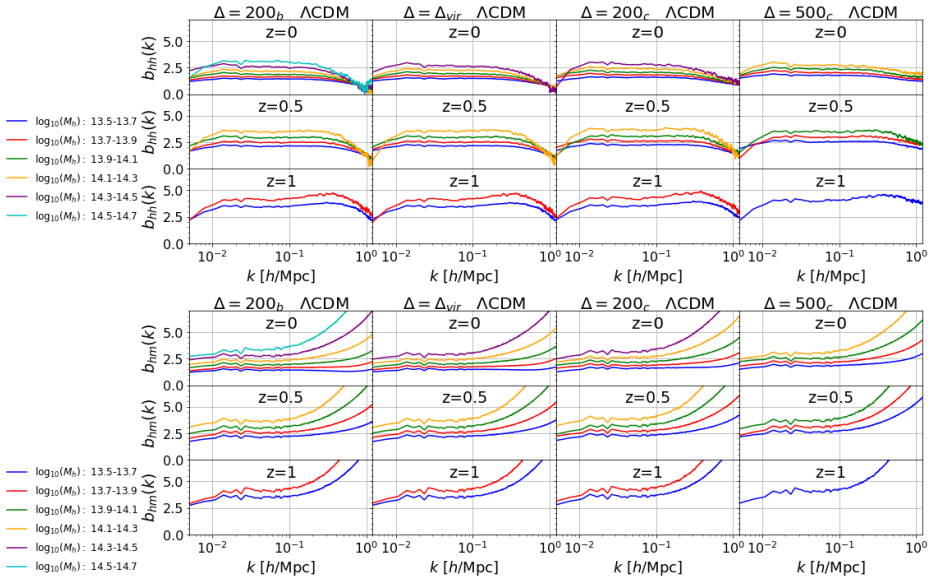

Figure 7.13: Halo bias from auto- and cross-spectra in the ΛCDM model (top and bottom panels, respectively). Mass bins starting from $M_{h,min} = 3{\times}10^{13} M_{\odot}/h$ with the amplitude of $\Delta M_{bin} = 0.2$ in logarithmic scale. The columns and the rows in each panel represent respectively the measurements for the overdensity and redshift values considered in this work. The different mass bins are indicated with different colours and each cosmological model is represented with a specific line-style.

Figure 7.13 show measurements of b_{hh} and b_{hm} for the ΛCDM case in different halo mass bins. Comparing the top and bottom panels, we observe that b_{hh} and b_{hm} are very similar and mostly scale-independent up to $k \sim 0.1h$/Mpc, i.e. in the linear regime of cosmological perturbations, but then tend to deviate from each other, and, entering the non-linear regime, acquire a scale-dependence which is much more enhanced for b_{hm}. Probably this is due to the fact that measurements of b_{hm} suffer more than b_{hh} the nonlinear evolution of matter perturbations. Moreover, the departure from the scale-independence behaviour seems to increase with the redshift, the mass bin and the overdensity threshold.

Figures 7.14, 7.15 and 7.16 show the measurements of the halo bias at different mass bins in the cosmologies with: i) massive neutrinos and cosmological constant; ii) massless neutrinos and dynamical dark energy; iii) in the presence of both components, respectively. In each figure the upper panels represent the measurements of the effective halo bias from the auto power spectra, and the lower panels the ones obtained from the halo-matter cross-spectra. Also, the columns run over different spherical overdensity thresholds, and the rows on different redshifts. The measurements at various logarithmic mass bins are represented with different colours, while the various cosmological models with different line-styles.

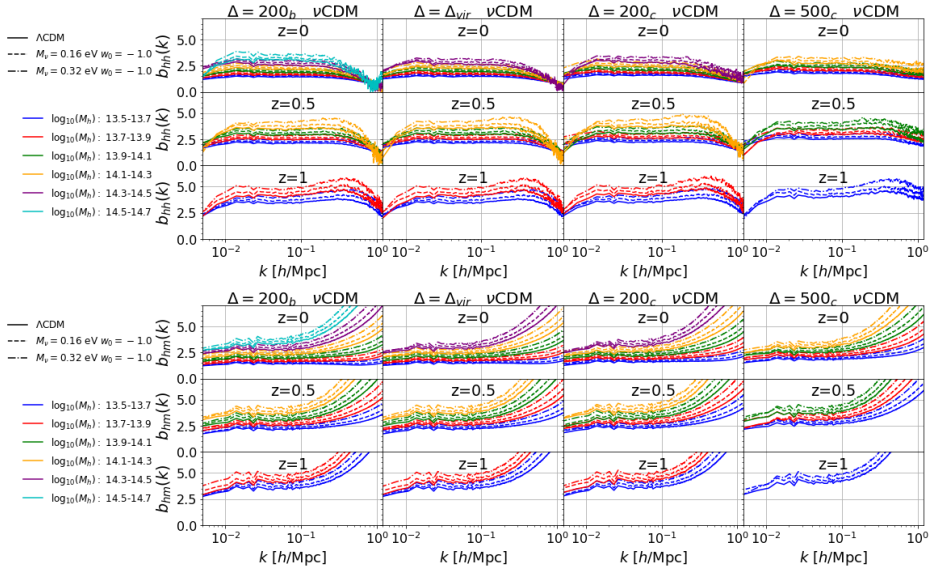

Figure 7.14: Halo bias from auto- and cross-spectra in the $\nu\Lambda$CDM cosmologies. Mass bins starting from $M_{h,min} = 3 \times 10^{13} M_{\odot}/h$ with the amplitude of $\Delta M_{bin} = 0.2$ in logarithmic scale. The columns and the rows in each panel represent respectively the measurements for the overdensity and redshift values considered in this work. The different mass bins are indicated with different colours and each cosmological model is represented with a specific line-style.

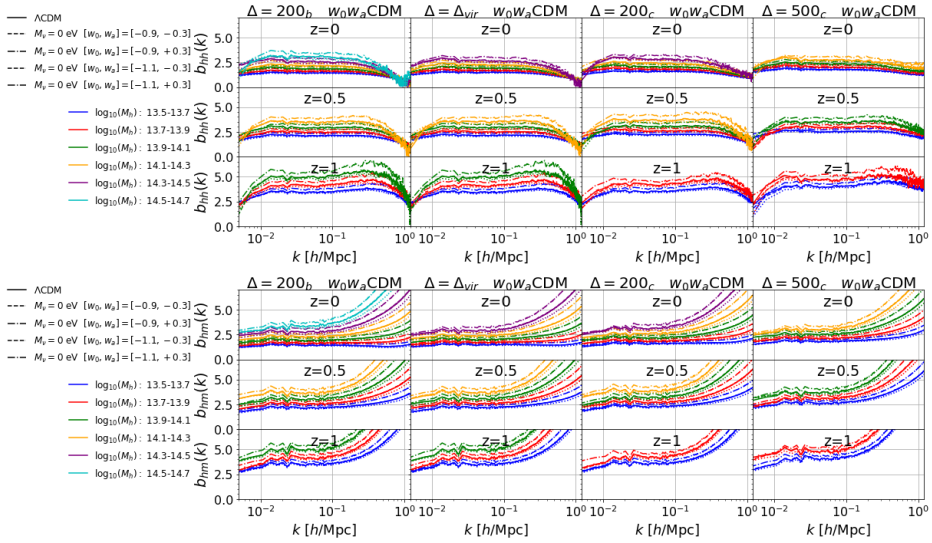

Figure 7.15: Halo bias from auto- and cross-spectra in $w_0 w_a$CDM cosmologies. Mass bins starting from $M_{h,min} = 3 \times 10^{13} M_{\odot}/h$ with the amplitude of $\Delta M_{bin} = 0.2$ in logarithmic scale. The columns and the rows in each panel represent the measurements for different overdensity and redshift values respectively. Different mass bins are indicated with different colours and each cosmological model is represented with a specific line-style.

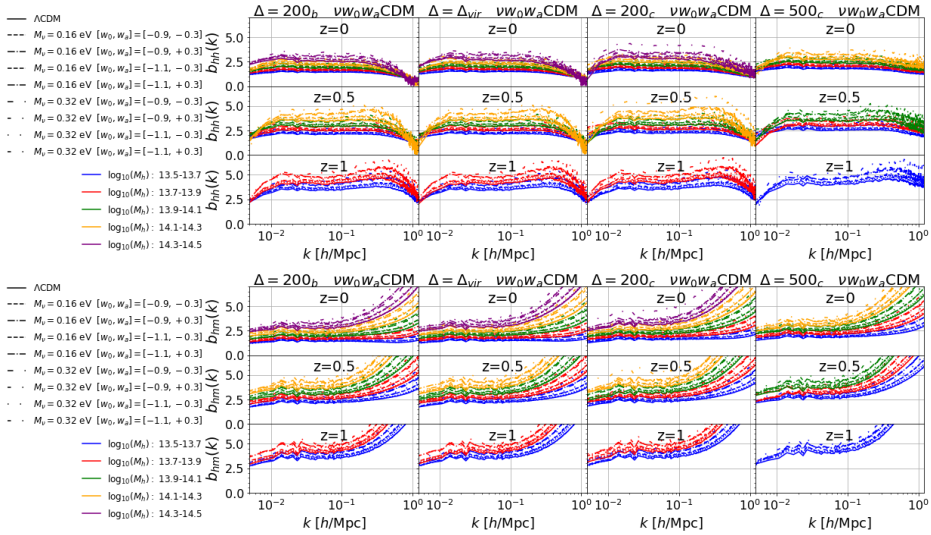

Figure 7.16: Halo bias from auto- and cross-spectra in $\nu w_0 w_a$CDM cosmologies. Mass bins starting from $M_{h,min} = 3 \times 10^{13} M_\odot/h$ with the amplitude of $\Delta M_{bin} = 0.2$ in logarithmic scale. The columns and the rows in each panel represent the measurements for different overdensity and redshift values respectively. Different mass bins are indicated with different colours and each cosmological model is represented with a specific line-style.

As shown in Figure 7.14, as expected the bias grows as the central mass of the bin increases. Indeed, at $z = 0$ and $M_\nu = 0$, for $\Delta = 200_b$, on scales for $k < 0.1\,h$/Mpc, where the two halo bias estimates, b_{hh} and b_{hm}, have similar values, the bias ranges between a minimum value of ~ 1.5, corresponding to the minimum mass bin ($\log_{10} M_h : 13.5 - 13.7$), up to ~ 4 for the maximum mass min ($\log_{10} M_h : 14.5 - 14.7$).

As the redshift and overdensity increase, there are fewer and fewer mass bins that contain at least 10,000 objects. However, as the redshift increases, the distinction between the measurements corresponding the two different neutrino masses is more evident. The halo biases are even more separated for higher mass bins. In particular, for $k = 0.1\,h$/Mpc, in the lowest mass bin $\log_{10}(M_h) : (13.5 - 13.7)$ and overdensity threshold $\Delta = 200_b$ the bias assumes the following values for $M_\nu = 0, 0.16, 0.32$, respectively:

- at $z = 0$: $b = 1.51, 1.59, 1.68$;
- at $z = 0.5$: $b = 2.24, 2.37, 2.55$;
- at $z = 1.5$: $b = 3.84, 4.21, 4.70$;

while for the mass bin $\log_{10}(M_h) : (13.7 - 13.9)$, with increasing M_ν the bias is

- at $z = 0$: $b = 1.72, 1.85, 2.01$;
- at $z = 0.5$: $b = 2.59, 2.74, 2.97$;
- at $z = 1$: $b = 4.72, 5.21, 5.81$.

The halo bias in the presence of dynamical dark energy, shown in Figure 7.15, presents the same features discussed before: an increasing amplitude for higher mass bins and

larger redshifts. It is particularly evident that the $[w_0, w_a] = [-0.9, +0.3]$ cosmology deviates from the ΛCDM measurements, unlike the remaining three combinations of parameters for which the measurements are very similar to the ΛCDM. Indeed, the case $w_0 w_a$CDM at $z = 1$ in the lowest bin of mass and at $k = 0.1\,h$/Mpc both b_{hh} and b_{hm} reach a value of ~ 5.5, while, for the remaining cosmologies, the bias is equal to ~ 5.

Finally, for scenarios with both massive neutrinos and dark energy, the halo bias, indicated in Figure7.16, is always shifted to higher values than in the ΛCDM case. Furthermore, with respect to the latter, the different alternative cosmological models are significantly distinguished. In particular, the model that stands out the most is the one with $M_\nu = 0.32$ eV and $[w_0, w_a] = [-0.9, +0.3]$, as b_{hm} and b_{hh} reach values equal to ~ 6 at $z = 1$ in the mass bin $\log_{10}(M_h) : 13.7 - 13.9$ and at $k = 0.1\,h$/Mpc.

CHAPTER 8

Halo power spectrum multipoles in redshift space

In this Chapter, I discuss the measurements of the power spectra multipoles in redshift-space extracted from the halo catalogues of DEMNUni simulations obtained with the DenHF halo-finder.

8.1 Power spectrum multipoles from the full halo catalogue

First of all, I map the positions of the halo centres of mass in the comoving snapshot of the simulation, from real space to redshift space, adding to their comoving distance in the real space the velocity of the halo centres of mass:

$$s = r + \frac{v}{aH} \,, \tag{8.1}$$

where r is the line-of-sight position in real space, s is the line-of-sight position in redshift space, v is the line-of-sight velocity, a is the scale factor, and H is the Hubble parameter at a.

I add RSD along the z-axis of a simulation box and I create the mesh of the halo catalogues with the RSD, specifying the size of the box $L_{box} = 2$ Gpc/h, the number of meshes $N_{mesh} = 2048$ and the TSC resampler method with the specifications of interlacing and compensating in order to correct the aliasing effects.

From the mesh with RSD positions, I compute the monopole, quadrupole and exadecapole of the 2D power spectrausing the FFTPower algorithm implemented in the Nbodykit libraries.

I repeat these steps to compute the monopole, quadrupole and exadecapole ($\ell = 0, 2, 4$, respectively with the line-of-sight along the other two x- and y-directions. Finally, I estimate the power spectra multipoles averaging the measurements along the three different lines-of-sight.

I use this method to estimate the power spectra multipoles of the halo catalogues, selecting the objects with mass larger than a minimum value $M_{h,min} = 10^{12.7} M_{\odot}/h$.

Figure 8.1 shows measurements of $kP_{\ell}(k)$ with $\ell = 0, 2, 4$ in the cosmological models with massive neutrinos and cosmological constant, at $z = 1$ for 6 different values of the overdensity thresholds: $\Delta = 200_b, \Delta_{vir}, 200_c, 500_c, 1000_c, 2500_c$, indicated in each panel. The various neutrino mass values $M_{\nu} = 0, 0.16, 0.32$ eV are indicated with different colours and the three distinct multipoles with different line-styles.

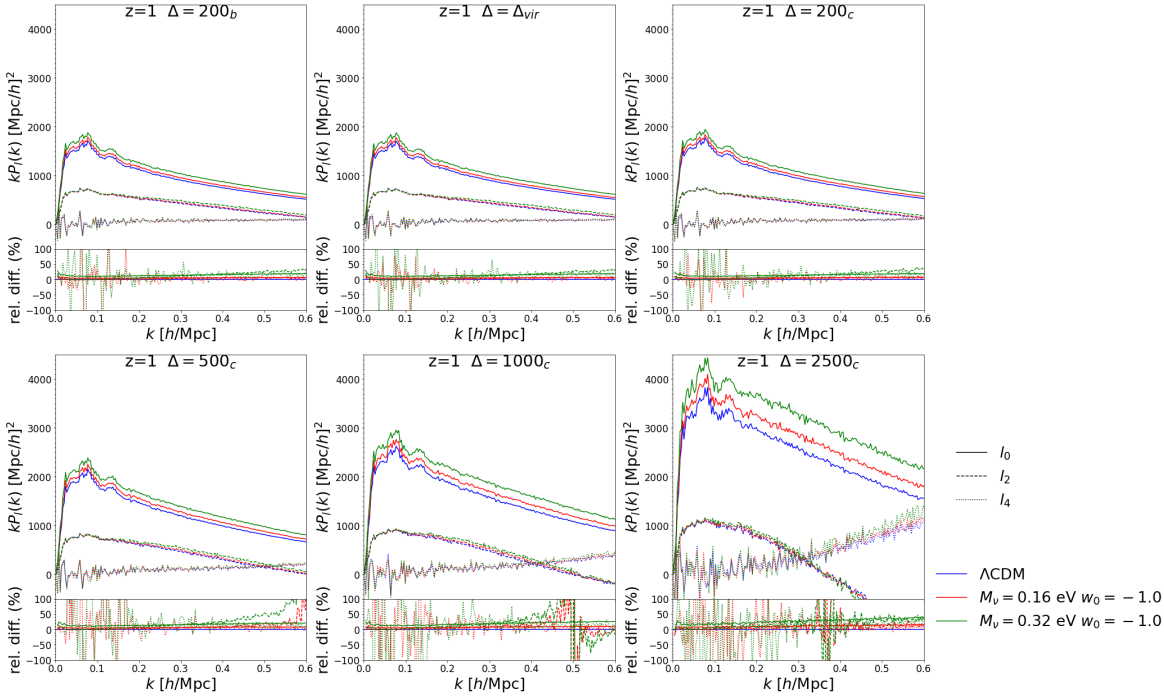

Figure 8.1: Multipole measurements in the ΛCDM and $\nu\Lambda$CDM cosmologies with $M_\nu = 0.16, 0.32$ eV $w_0 = -1.0$, from halo catalogues with minimum mass $10^{12.7} M_\odot/h$ at z=1. Relative differences to the ΛCDMmodel. Each panel shows the results at different growing values of the overdensity threshold: $\Delta = 200_b, \Delta_{vir}, 200_c, 500_c, 1000_c, 2500_c$. The various neutrino mass values $M_\nu = 0, 0.16, 0.32$ eV are indicated with different colours and the three distinct multipoles with different line-styles.

The monopole presents an increasing amplitude with the enhancement of the overdensity values. Indeed, at $z = 1$ the monopole, $kP_\ell(k)$, in the ΛCDM has a peak at $k \sim 0.07\ h/\mathrm{Mpc}$ with amplitude of $\sim 1700\ [\mathrm{Mpc}/h]^2$ for at $\Delta = 200_b$, of $\sim 2100\ [\mathrm{Mpc}/h]^2$ for $\Delta = 500_c$, and of $\sim 3800\ [\mathrm{Mpc}/h]^2$ at $\Delta = 2500_c$. The quadrupole has also an increasing trend with the spherical overdensity. Indeed, in the ΛCDM the quadrupole has a peak at $k \sim 0.07\ h/\mathrm{Mpc}$ with an amplitude of $\sim 700\ [\mathrm{Mpc}/h]^2$ at $\Delta = 200_b$, of $\sim 800\ [\mathrm{Mpc}/h]^2$ at $\Delta = 500_c$, and of $\sim 1100\ [\mathrm{Mpc}/h]^2$ at $\Delta = 2500_c$.

As shown in Figure 8.1, the monopole amplitude is shifted at larger values as the total neutrino mass increases, and the relative differences with respect to the ΛCDM case become larger as the the neutrino total mass increases. In addition, the effect becomes more and more noticeable as the overdensity threshold increases. Indeed, at $z = 1$ the amplitude of the monopole peak for $M_\nu = 0.16$ eV and $M_\nu = 0.32$ eV is, respectively, up to $\sim 1800\ [\mathrm{Mpc}/h]^2$ - $1900\ [\mathrm{Mpc}/h]^2$ for $\Delta = 200_b$, $\sim 2200\ [\mathrm{Mpc}/h]^2$ - $2400\ [\mathrm{Mpc}/h]^2$ for $\Delta = 500_c$, $\sim 4100\ [\mathrm{Mpc}/h]^2$ - $4400\ [\mathrm{Mpc}/h]^2$ for $\Delta = 2500_c$. In addition, the relative differences of the quadrupole measurements in the $\nu\Lambda$CDM cosmologies with respect to the neutrino massless ΛCDM case are amplified at smaller scales, as the residuals in the subplots show. Indeed, at $k \sim 0.5\ h/Mpc$ the percent relative difference for $M_\nu = 0.16$ eV and $M_\nu = 0.32$ eV are, respectively:

- for $\Delta 200_b$: 10% - 20% for the monopole, 10% - 30% for the quadrupole;

- for $\Delta 200_c$: 10% - 20% for the monopole, 10% - 30% for the quadrupole;
- for $\Delta 500_c$: 10% - 20% for the monopole, 15% - 50% for the quadrupole;
- for $\Delta 2500_c$: 20% - 40% for the monopole, 20% - 40% for the quadrupole.

On the other hand, the measurements of the exadecapole are very noisy at all scales in the range $0.05 < k < 0.6$.

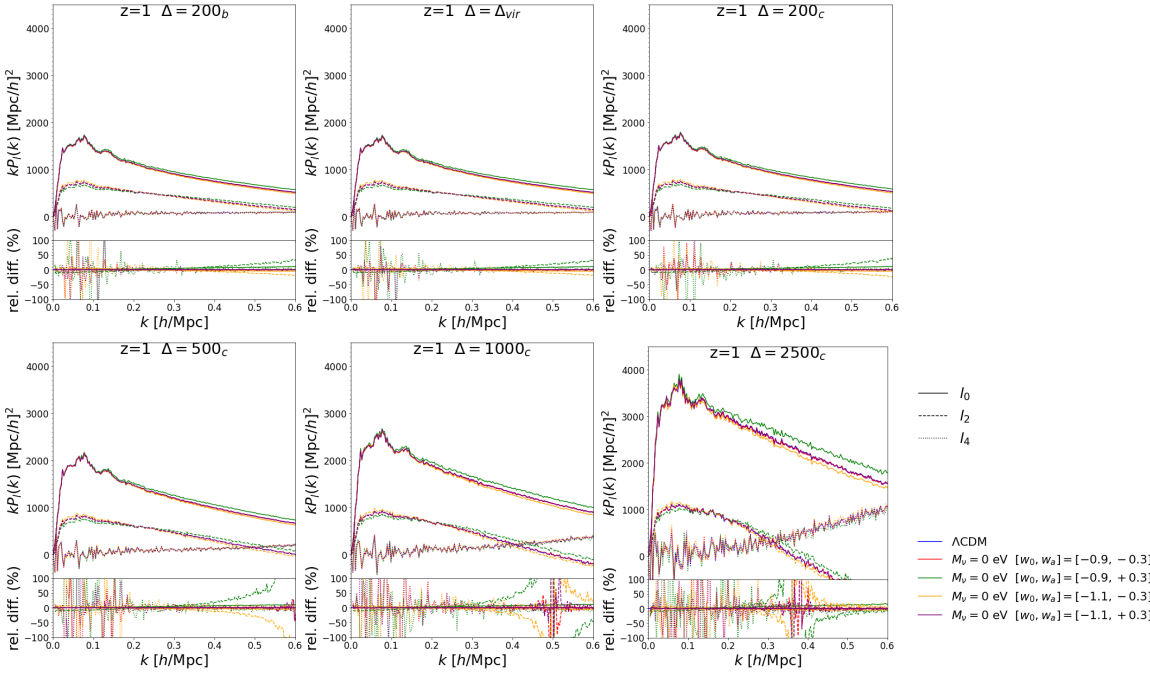

Figure 8.2: Multipole measurements in $w_0 w_a$CDM cosmologies, from halo catalogues with minimum mass $10^{12.7} M_\odot/h$ at z=1. Relative differences to the ΛCDMmodel. Each panel shows the results at different growing values of overdensity yhresholds: $\Delta = 200_b, \Delta_{vir}, 200_c, 500_c, 1000_c, 2500_c$. The four different combinations of the dynamical dark energy parameters w_0, w_a are indicated with different colours and the three distinct multipoles with different line-styles.

Figure 8.2 indicates the measurements of the multipoles of the power spectrum at $z = 1$ in the cosmologies with the presence of dynamical dark energy and massless neutrinos.

I note that there are two cosmological models which differs significantly from the standard ΛCDM both in the monopole and in the quadrupole measurements: $[w_0, w_a] = [-0.9, +0.3]$ and $[w_0, w_a] = [-1.1, -0.3]$. The former differs most from the ΛCDM, and has positive differences, while the latter has damped measurements with lower and negative differences. As for the case of the power spectra in real space, this is due to the increased halo bias as the growth factor decreases and structure formation is suppressed. Indeed, at $k = 0.5$ the percent relative difference for the models $[w_0, w_a] = [-1.1, -0.3]$ and $[w_0, w_a] = [-0.9, +0.3]$ are, respectively:

- for $\Delta 200_b$: -0.5% and 10% for the monopole, -10% and 20% for the quadrupole;

- for $\Delta 200_c$: -0.5% and 10% for the monopole, -20% and 25% for the quadrupole;
- for $\Delta 500_c$: -0.5% and 10% for the monopole, -35% and 50% for the quadrupole;
- for $\Delta 2500_c$: -0.5% and 20% for the monopole, 15% and 30% for the quadrupole.

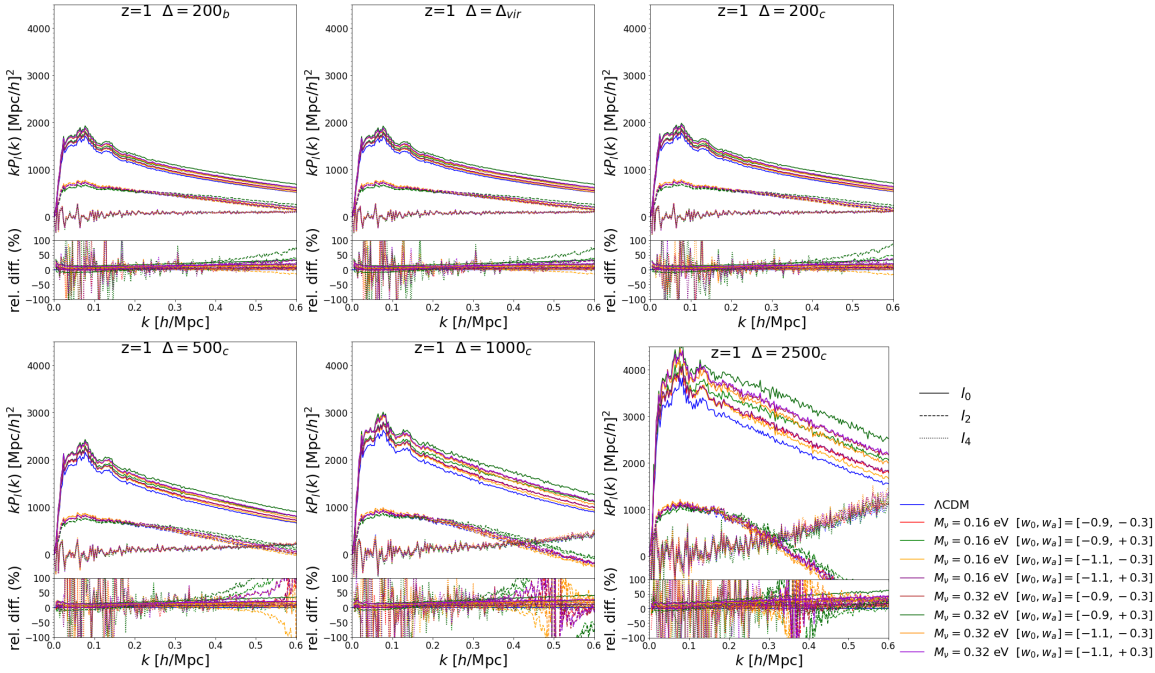

Figure 8.3: Multipole measurements in $\nu w_0 w_a$CDM cosmologies, from halo catalogues with minimum mass $10^{12.7} M_\odot/h$ at $z = 1$. Relative differences to the ΛCDMmodel. Each panel shows the results at different growing values of overdensity thresholds: $\Delta = 200_b, \Delta_{vir}, 200_c, 500_c, 1000_c, 2500_c$. The eight different combinations of the dynamical dark energy parameters w_0, w_a and massive neutrinos are indicated with different colours and the three distinct multipoles with different lines-tyles.

Figure 8.3 shows the measurements of the multipoles in the cosmological models with the combinations of massive neutrinos and dynamical dark energy. All the measurements in the eight different combinations of the w_0, w_a parameters and neutrino mass are positively shifted in amplitude relatively to the measurements in the ΛCDM. In particular, the models with $M_\nu = 0.32$ eV and $[w_0, w_a] = [-0.9, +0.3]$ differs most from the standard case and the percent relative differences are larger as the overdensity value increases. Indeed, in this model the values of the relative differences at $k = 0.5$ are the following:

- for $\Delta = 200_b$: 25% in the monopole, 45% in the quadrupole;
- for $\Delta = \Delta_{vir}$: 30% in the monopole, 50% in the quadrupole;
- for $\Delta = 200_c$: 30% in the monopole, 55% in the quadrupole;
- for $\Delta = 500_c$: 35% in the monopole, 100% in the quadrupole.

8.2 Power spectrum multipoles for a selected halo mass bin

Furthermore, using the same procedure discussed in details in the previous section, I compute the multipoles of the power spectra of the halo catalogues extracted from the DEMNUni simulations, selecting objects in a fixed halo mass bin $10^{12.7} M_\odot/h < M_h < 10^{13.2} M_\odot/h$, where the bias has an almost scale-independent trend.

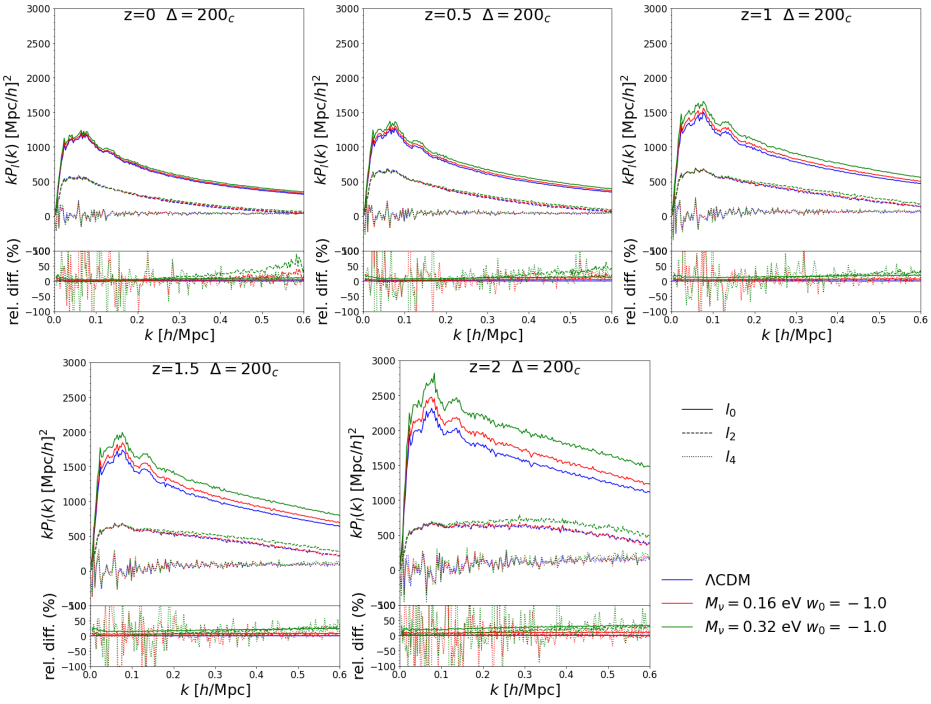

Figure 8.4: Multipole measurements in the ΛCDM and νΛCDM cosmologies with $M_\nu = 0.16 - 0.32$ eV $w_0 = -1.0$, from 200_c halo catalogue with in the mass bin $10^{12.7} M_\odot/h < M_H < 10^{13.2} M_\odot/h$ at $z = 1$. Relative differences to the ΛCDMmodel. Each panel shows the results at different growing values of redshift $z = 0, 0.5, 1, 1.5, 2$. The various neutrino mass values, $M_\nu = 0, 0.16, 0.32$, eV are indicated with different colours and the three distinct multipoles with different line-styles.

Figure 8.4 represents the multipoles measurements of $kP_\ell(k)$ with $\ell = 0, 2, 4$ in the selected mass bin for the cosmological models with massive neutrinos and cosmological constant, at the spherical overdensity $\Delta = 200_c$ at five different redshifts: $z = 0, 0.5, 1.0, 1.5, 2.0$, indicated in each panel. The various neutrino mass values $M_\nu = 0, 0.16, 0.32$ eV are indicated with different colours and the three distinct multipoles with different line-styles.

The amplitudes of the monopole and the quadrupole are shifted at higher values for increasing redshift and also increasing neutrino mass. Moreover, also the percent relative differences with respect to the ΛCDM case increase with redshift. Indeed, for $M_\nu = 0.16, 0.32$ eV at $k = 0.5$ the differences are:

- at $z = 0$: for the monopole 5% and 10%, for the quadrupole 5% and 30%;
- at $z = 1$: for the monopole 7% and 20%, for the quadrupole 5% and 30%;

- at $z = 2$: for the monopole 10% and 30%, for the quadrupole 5% and 35%.

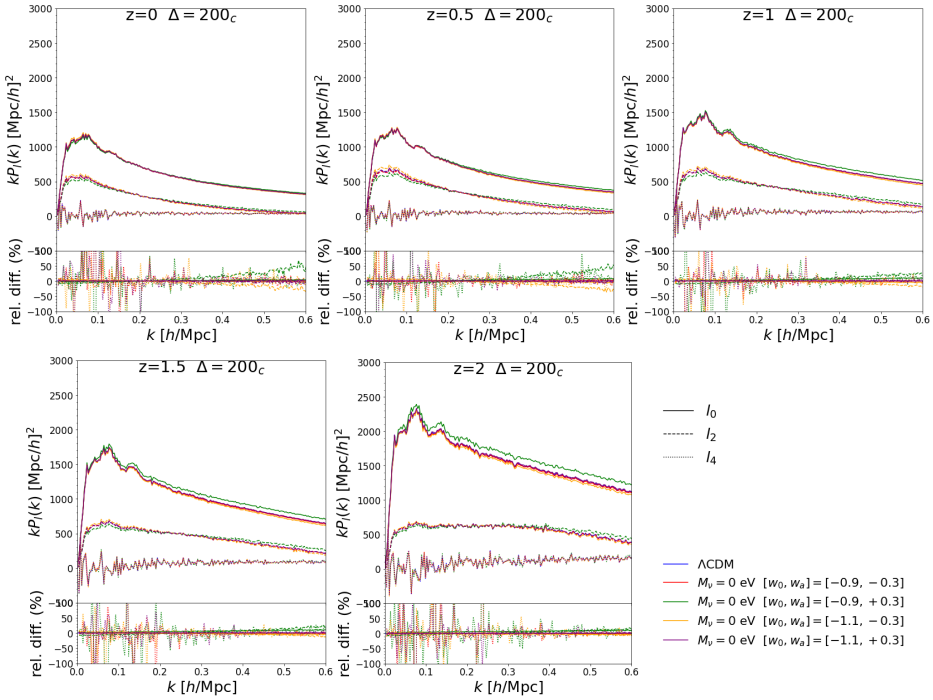

Figure 8.5: Multipole measurements in $w_0 w_a$CDM cosmologies, from 200_c halo catalogue with in the mass bin $10^{12.7} M_\odot/h < M_H < 10^{13.2} M_\odot/h$ at $z = 1$. Relative differences to the ΛCDMmodel. Each panel shows the results at different growing values of redshift $z = 0, 0.5, 1, 1.5, 2$. The four different combinations of the dynamical dark energy parameters w_0, w_a are indicated with different colours and the three distinct multipoles with different line-styles.

Figure 8.5 indicates the measurements of the monopole, quadrupole, exadecapole in the considere mass bin $10^{12.7} M_\odot/h < M_h < 10^{13.2} M_\odot/h$, at $z = 0, 0.5, 1, 1.5, 2$ for the 200_c overdensity, in the cosmologies with massless neutrinos and dynamical dark energy in four combinations of the equation of state parameters w_0, w_a.

The monopole and the quadrupole measurements in the cosmological models $[w_0, w_a] = [-0.9, +0.3]$ and $[w_0, w_a] = [-1.1, -0.3]$ differ significantly from the standard ΛCDM case. On the other hand, the remaining two models have differences of only few percents. The $[w_0, w_a] = [-0.9, +0.3]$ case differs most from the ΛCDM, and has positive differences, while the $[w_0, w_a] = [-1.1, -0.3]$ case has damped measurements with lower and negative differences, as for the case of the auto-spectra in real space, showed in the previous Chapter. Indeed, at $k = 0.5\ h/Mpc$ the percent relative difference for the models with $[w_0, w_a] = [-0.9, +0.3]$ and $[w_0, w_a] = [-1.1, -0.3]$ are, respectively:

- at $z = 0$: for the monopole 5% and -5%, for the quadrupole 20% and -15%;
- at $z = 1$: for the monopole 10% and -5%, for the quadrupole 20% and -15%;
- at $z = 2$: for the monopole 10% and -5%, for the quadrupole 10% and -5%.

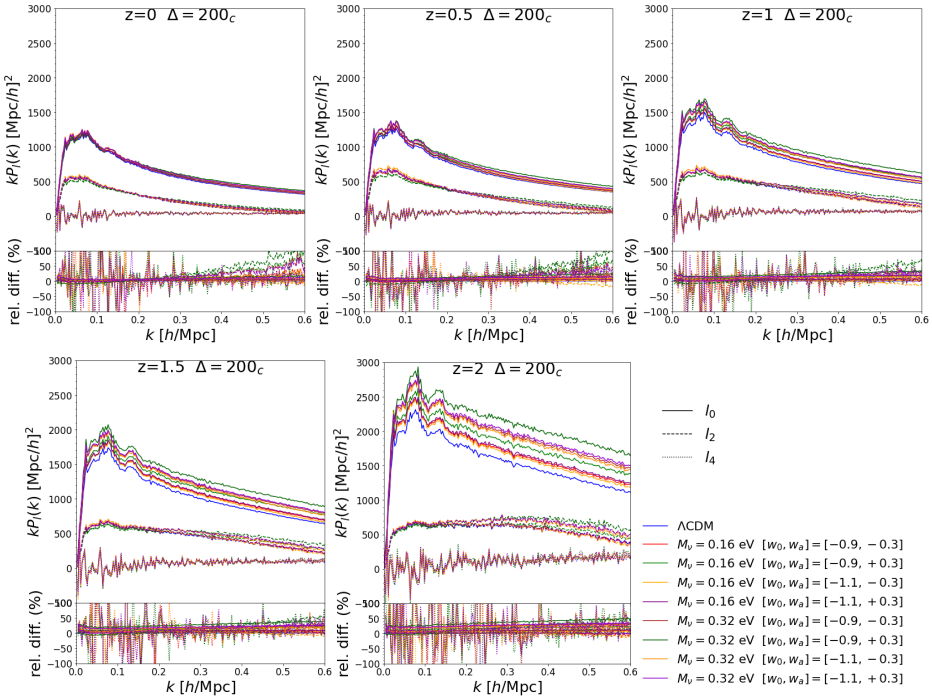

Figure 8.6: Multipole measurements in $\nu w_0 w_a$CDM cosmologies, from 200_c halo catalogue with in the mass bin $10^{12.7} M_\odot/h < M_H < 10^{13.2} M_\odot/h$ at $z = 1$. Relative differences to the ΛCDMmodel. Each panel shows the results at different growing values of redshift $z = 0, 0.5, 1, 1.5, 2$. The four different combinations of the dynamical dark energy parameters w_0, w_a are indicated with different colours and the three distinct multipoles with different line-styles.

Finally, Figure 8.6 shows the multipole measurements in the mass bin $10^{12.7} M_\odot/h < M_H < 10^{13.2} M_\odot/h$ for the overdensity threshold $\Delta = 200_c$, in eight different cosmological models with the combinations of dynamical dark energy and massive neutrinos, at $z = 0, 0.5, 1, 1.5, 2$.

All the measurements are positively shifted in amplitude compared to the results in the ΛCDM. In particular, the models with $M_\nu = 0.32$ eV and $[w_0, w_a] = [-0.9, +0.3]$ differs the most from the standard case, and the values of the percent relative differences at $k = 0.5$ are the following:

- at $z = 0$ for the monopole 15%, for the quadrupole 50%;
- at $z = 1$ for the monopole 30%, for the quadrupole 55%;
- at $z = 2$ for the monopole 45%, for the quadrupole 45%.

Conclusions

In this thesis I presented my work for the PhD project on the creation and analysis of mock galaxy and galaxy-cluster catalogues in cosmologies with the presence of massive neutrinos and dynamical dark energy.

Mock catalogues are useful to provide modelling and make predictions for future galaxy surveys, Euclid in particular, and also to test codes for the data analysis pipeline in view of upcoming cosmological datasets.

I have tackled three main topics.

First of all, I developed a code to implement a subhalo abundance matching (SHAM) technique, useful to connect galaxy observations to dark matter subhaloes in simulations, obtaining the stellar-to-halo-mass relation (SHMR) able to produce large and accurate galaxy mocks in different cosmological models.

I applied to the DEMNUni simulations, described in Chapter 4, the SHAM technique, which assumes a one-to-one relation between a physical property of a dark matter halo/subhalo and an observational property of the galaxy that it hosts.

In particular, in this work I considered the stellar mass as a galaxy property, because it is expected to be closely related to the dark matter content of the hosting dark matter halo. As a dark matter halo/subhalo property I used their mass, representing a measure of the depth of the associated potential well.

I adopted an empirical parameterisation of the SHMR from Moster et al. (2010) [50] that links the halo mass to the corresponding stellar mass of a galaxy hosted by the halo. Via a MCMC bayesian approach, described in Chapter 5, I computed the best-fit parameters of the SHMR as a function of redshift in the presence of dark energy and massive neutrinos, considering the datasets from the Sloan Digital Sky Survey (SDSS) for redshifts $z < 0.2$, and the Cosmological Evolution Survey (COSMOS) observations for $0.2 < z < 2$. In particular, the measurements of the galaxy-stellar-mass function from COSMOS 2020 (Weaver et al. 2022), described in details in Chapter 4, are considered in the SHAM procedure.

Implementing such a method, I populated with galaxies the dark matter structures in the DEMNuni simulations finding the dependence of the SHMR on the total neutrino mass and the dark energy equation of state, as described in Chapter 6. The obtained galaxy mocks account both for central and satellite galaxies, spanning the redshift range $0 < z < 2$, which covers both the photometric and spectroscopic galaxy samples of the upcoming Euclid survey.

Furthermore, I obtained fitting formulas for the SHMR parameters, which allow us to reconstruct the stellar mass as a function of the neutrino mass and the time-dependent dark energy equation of state. This procedure can be very useful for the realisation of

mock galaxy catalogues in cosmologies which span the most important cosmological parameters the Euclid mission has been conceived to measure.

Moreover, using the COSMO Bologna Libraries [83], an open source code useful to perform galaxy clustering measurements on mock and real galaxy catalogues, I studied the galaxy clustering properties of the mock galaxy catalogues. In particular, I measured the galaxy 2-pt correlation functions from the DEMNUni galaxy mocks in $\nu w_0 w_a$CDM cosmological scenarios in real and redshift space, and compared them with a simple model which accounts for the changes of the galaxy bias and growth rate in the presence of neutrinos and dynamical dark energy. Finally, I compared the results with the measurements of the correlation function from the VIPERS survey, considering a subsample of galaxies with mass $M > 10^{11} M_{\odot}$. The results of Chapter 6 will be presented in the next future in the paper "DEMNUni: The galaxy-halo connection in the presence of dynamical dark energy and massive neutrinos", of which I am the leading author.

Secondly, in Chapter 7 I extracted cluster catalogues from the DEMNUni simulations via the DenHF halo finder. In particular, I wrote a pipeline in order to automatically run the code Galileo100 at CINECA with several spherical overdensity values and redshift values. Also, I wrote scripts to measure, via the Nbodykit libraries, the matter, halo and cross power-spectra from the simulated catalogues. Finally, I analysed the different measurements and from them estimated how the effective halo bias changes in different $\nu w_0 w_a$CDM scenarios. The finding of Chapter 7 constitute the most part of the Euclid pre-launch Key Project (KP) CL-3 paper-4 "Halo mass function and bias in non-standard models", of which I am the leading author.

Third, in Chapter 8 I estimated the clustering properties in redshift-space of the DEMNUni halo catalogues, extracted with the DenHF halo finder. In particular, I measured the multipoles of the halo power spectra, i.e. the monopole, the quadrupole and the exadecapole, and compared their behaviour in the different $\nu w_0 w_a$CDM cosmologies. These measurements will contribute to the Euclid pre-launch KP-JC-6 paper-3 "Cosmological constraint on non-standard cosmologies from simulated Euclid probes", and Euclid pre-launch KP-TH-1 paper-6 "Impact of nonlinear clustering on beyond- LCDM constraints with Euclid", of which I am co-author in the first group.

As future outlook, it will be possible to apply the SHAM method implemented in this work to simulations with higher mass resolution, in order to also include galaxies lower stellar masses, such as the star-forming galaxies. Secondly, in the forthcoming months I am going to extend the DenHF pipeline to estimate the halo catalogues from simulations with modified gravity and dark matter, such as the Dustgrain and the DAKAR simulations from Marco Baldi. Moreover, I will also measure with the NbodyKit code the halo/matter/cross power-spectra and the effective halo bias from the latter simulations. These measurements will also enter the Euclid pre-launch KP CL-3 paper-4.

Bibliography

[1] C. Marinoni, J. Bel and A. Buzzi, *The scale of cosmic isotropy*, *Journal of Cosmology and Astroparticle Physics* **2012** (2012) 036 [1205.3309].

[2] Planck Collaboration, P. A. R. Ade, N. Aghanim, C. Armitage-Caplan, M. Arnaud, M. Ashdown et al., *Planck 2013 results. XVI. Cosmological parameters*, *Astron. Astrophys.* **571** (2014) A16 [1303.5076].

[3] Planck Collaboration, P. A. R. Ade, N. Aghanim, M. Arnaud, M. Ashdown, J. Aumont et al., *Planck 2015 results - xiii. cosmological parameters*, *Astron. Astrophys.* **594** (2016) A13 [1502.01589].

[4] Planck Collaboration, Y. Akrami, F. Arroja, M. Ashdown, J. Aumont, C. Baccigalupi et al., *Planck 2018 results. I. Overview and the cosmological legacy of Planck*, *Astron. Astrophys.* **641** (2020) A1 [1807.06205].

[5] A. Einstein, *Cosmological Considerations in the General Theory of Relativity*, *Sitzungsber.Preuss.Akad.Wiss.Berlin (Math.Phys.)* (1917) 142.

[6] Planck Collaboration, N. Aghanim, Y. Akrami, M. Ashdown, J. Aumont, C. Baccigalupi et al., *Planck 2018 results. vi. cosmological parameters*, *Astron. Astrophys.* **641** (2020) A6 [1807.06209v4].

[7] M. Pellejero-Ibanez, C.-H. Chuang, J. A. Rubiño-Martín, A. J. Cuesta, Y. Wang, G.-b. Zhao et al., *The clustering of galaxies in the completed sdss-iii baryon oscillation spectroscopic survey: double-probe measurements from boss galaxy clustering & planck data – towards an analysis without informative priors*, *Mon. Not. R. Astron. Soc.* **468** (2017) 4116–4133 [1607.03152v1].

[8] M. Scodeggio, L. Guzzo, B. Garilli, B. R. Granett, M. Bolzonella, S. de la Torre et al., *The VIMOS public extragalactic redshift survey (VIPERS)*, *Astron. Astrophys.* **609** (2018) A84 [1611.07048].

[9] M. Chevallier and D. Polarski, *Accelerating universes with scaling dark matter*, *International Journal of Modern Physics D* **10** (2001) 213 [gr-qc/0009008].

[10] E. V. Linder, *Exploring the Expansion History of the Universe*, *PhysRevLett.* **90** (2003) 091301 [0208512].

[11] G. Parimbelli, C. Carbone, J. Bel, B. Bose, M. Calabrese, E. Carella et al., *DEMNUni: comparing nonlinear power spectra prescriptions in the presence of massive neutrinos and dynamical dark energy*, *Journal of Cosmology and Astroparticle Physics* **2022** (2022) 041 [2207.13677].

[12] DES Collaboration, *Dark Energy Survey Year 1 Results: Constraints on Extended Cosmological Models from Galaxy Clustering and Weak Lensing* , *Phys. Rev. D* **99** (2019) [1810.02499].

[13] A. Semenaite, A. G. Sá nchez, A. Pezzotta, J. Hou, A. Eggemeier, M. Crocce et al., *Beyond – λcdm constraints from the full shape clustering measurements from BOSS and eBOSS*, *Monthly Notices of the Royal Astronomical Society* **521** (2023) 5013 [2210.07304].

[14] J. Lesgourgues and S. Pastor, *Massive neutrinos and cosmology*, *Physics Reports* **429** (2006) 307 [0603494].

[15] G. Mangano, G. Miele, S. Pastor, T. Pinto, O. Pisanti and P. D. Serpico, *Relic neutrino decoupling including flavour oscillations*, *Nuclear Physics B* **729** (2005) 221 [hep-ph/0506164].

[16] J. Lesgourgues and S. Pastor, *Neutrino cosmology and planck*, *New Journal of Physics* **16** (2014) 065002 [1404.1740].

[17] E. Castorina, C. Carbone, J. Bel, E. Sefusatti and K. Dolag, *DEMNUni: the clustering of large-scale structures in the presence of massive neutrinos*, *J. of Cosm. and Astroparticle Phys.* **7** (2015) 043 [1505.07148].

[18] C. Carbone, M. Petkova and K. Dolag, *DEMNUni: ISW, Rees-Sciama, and weak-lensing in the presence of massive neutrinos*, *J. of Cosm. and Astroparticle Phys.* **7** (2016) 034 [1605.02024].

[19] V. Springel, *The cosmological simulation code GADGET-2*, *Mon. Not. R. Astron. Soc.* **364** (2005) 1105–1134 [0505010].

[20] S. Alam, M. Aubert, S. Avila, C. Balland, J. E. Bautista, M. A. Bershady et al., *Completed SDSS-IV extended baryon oscillation spectroscopic survey: Cosmological implications from two decades of spectroscopic surveys at the apache point observatory*, *Physical Review D* **103** (2021) [2007.08991].

[21] A. G. Riess, S. Casertano, W. Yuan, L. Macri, J. Anderson, J. W. MacKenty et al., *New parallaxes of galactic cepheids from spatially scanning the hubble space telescope: Implications for the hubble constant*, *The Astrophysical Journal* **855** (2018) 136 [1801.01120].

[22] M. S. Longair, *Galaxy formation*. Springer Berlin Heidelberg New York, July, 2007.

[23] S. D. Landy and A. S. Szalay, *Bias and Variance of Angular Correlation Functions*, *Astrophys. J.* **412** (1993) 64.

[24] A. J. S. Hamilton, *Linear redshift distortions: A review*, in *Astrophysics and Space Science Library*, pp. 185–275. Springer Netherlands, 1998. astro-ph/9708102v2. DOI.

[25] R. Scoccimarro and J. Frieman, *Loop corrections in nonlinear cosmological perturbation theory*, *The Astrophysical Journal Supplement Series* **105** (1996) 37 [astro-ph/9509047].

[26] S. Alam, M. Ata, S. Bailey, F. Beutler, D. Bizyaev, J. A. Blazek et al., *The clustering of galaxies in the completed SDSS-III baryon oscillation spectroscopic survey: cosmological analysis of the DR12 galaxy sample*, *Monthly Notices of the Royal Astronomical Society* **470** (2017) 2617 [1607.03155].

[27] A. Pezzotta, S. de la Torre, J. Bel, B. R. Granett, L. Guzzo, J. A. Peacock et al., *The VIMOS public extragalactic redshift survey (VIPERS)*, *Astronomy & Astrophysics* **604** (2017) A33 [1612.05645].

[28] A. Taruya, T. Nishimichi and S. Saito, *Baryon acoustic oscillations in 2d: Modeling redshift-space power spectrum from perturbation theory*, *Physical Review D* **82** (2010) [1006.0699].

[29] S. de la Torre, E. Jullo, C. Giocoli, A. Pezzotta, J. Bel, B. R. Granett et al., *The VIMOS public extragalactic redshift survey (VIPERS)*, *Astronomy & Astrophysics* **608** (2017)

A44 [1612.05647].

[30] A. J. Hawken, B. R. Granett, A. Iovino, L. Guzzo, J. A. Peacock, S. de la Torre et al., *The VIMOS public extragalactic redshift survey*, *Astronomy & Astrophysics* **607** (2017) A54 [1611.07046].

[31] V. Springel, N. Yoshida and S. D. White, *GADGET: a code for collisionless and gasdynamical cosmological simulations*, *New Astronomy* **6** (2001) 79 [astro-ph/0003162].

[32] K. Dolag, S. Borgani, G. Murante and V. Springel, *Substructures in hydrodynamical cluster simulations*, *Monthly Notices of the Royal Astronomical Society* **399** (2009) 497 [0808.3401].

[33] P. S. Behroozi, R. H. Wechsler and H.-Y. Wu, *THE ROCKSTAR PHASE-SPACE TEMPORAL HALO FINDER AND THE VELOCITY OFFSETS OF CLUSTER CORES*, *The Astrophysical Journal* **762** (2012) 109 [1110.4372].

[34] J. F. Navarro, C. S. Frenk and S. D. M. White, *The structure of cold dark matter halos*, *The Astrophysical Journal* **462** (1996) 563 [astro-ph/9508025].

[35] R. H. Wechsler and J. L. Tinker, *The connection between galaxies and their dark matter halos*, *Annual Review of Astronomy and Astrophysics* **56** (2018) 435.

[36] D. Nelson, A. Pillepich, S. Genel, M. Vogelsberger, V. Springel, P. Torrey et al., *The illustris simulation: Public data release*, *Astronomy and Computing* **13** (2015) 12 [1504.00362].

[37] S. McAlpine, J. Helly, M. Schaller, J. Trayford, Y. Qu, M. Furlong et al., *The eagle simulations of galaxy formation: Public release of halo and galaxy catalogues*, *Astronomy and Computing* **15** (2016) 72 [1510.01320].

[38] D. J. Croton, A. R. H. Stevens, C. Tonini, T. Garel, M. Bernyk, A. Bibiano et al., *Semi-analytic galaxy evolution (sage): Model calibration and basic results*, *The Astrophysical Journal Supplement Series* **222** (2016) 22 [1601.04709].

[39] B. M. B. Henriques, S. D. M. White, P. A. Thomas, R. E. Angulo, Q. Guo, G. Lemson et al., *Galaxy formation in the planck cosmology – IV. mass and environmental quenching, conformity and clustering*, *Monthly Notices of the Royal Astronomical Society* **469** (2017) 2626 [1611.02286].

[40] V. Gonzalez-Perez, C. G. Lacey, C. M. Baugh, C. D. P. Lagos, J. Helly, D. J. R. Campbell et al., *How sensitive are predicted galaxy luminosities to the choice of stellar population synthesis model?*, *Monthly Notices of the Royal Astronomical Society* **439** (2014) 264 [1309.7057].

[41] A. V. Kravtsov, A. A. Berlind, R. H. Wechsler, A. A. Klypin, S. Gottlober, B. Allgood et al., *The dark side of the halo occupation distribution*, *The Astrophysical Journal* **609** (2004) 35 [astro-ph/0308519].

[42] A. Tasitsiomi, A. V. Kravtsov, R. H. Wechsler and J. R. Primack, *Modeling galaxy-mass correlations in dissipationless simulations*, *The Astrophysical Journal* **614** (2004) 533 [astro-ph/0404168].

[43] A. Vale and J. P. Ostriker, *Linking halo mass to galaxy luminosity*, *Monthly Notices of the Royal Astronomical Society* **353** (2004) 189 [astro-ph/0402500].

[44] C. Conroy, R. H. Wechsler and A. V. Kravtsov, *Modeling luminosity-dependent galaxy clustering through cosmic time*, *The Astrophysical Journal* **647** (2006) 201 [astro-ph/0512234].

[45] P. S. Behroozi, C. Conroy and R. H. Wechsler, *A comprehensive analysis of uncertainties affecting the stellar mass - halo mass relation for* $0 < z < 4$, *The Astrophysical Journal* **717** (2010) 379 [1001.0015v2].

[46] S. Trujillo-Gomez, A. Klypin, J. Primack and A. J. Romanowsky, *Galaxies in ΛCDM with Halo Abundance Matching: Luminosity-Velocity Relation, Baryonic Mass-Velocity Relation, Velocity Function, and Clustering*, *Astrophys. J.* **742** (2011) 16 [1005.1289].

[47] S. E. Nuza, A. G. Sánchez, F. Prada, A. Klypin, D. J. Schlegel, S. Gottlöber et al., *The clustering of galaxies at $z \approx 0.5$ in the SDSS-III data release 9 BOSS-CMASS sample: a test for the λCDM cosmology*, *Monthly Notices of the Royal Astronomical Society* **432** (2013) 743 [1202.6057].

[48] S. A. Rodrí guez-Torres, C.-H. Chuang, F. Prada, H. Guo, A. Klypin, P. Behroozi et al., *The clustering of galaxies in the SDSS-III baryon oscillation spectroscopic survey: modelling the clustering and halo occupation distribution of BOSS CMASS galaxies in the final data release*, *Monthly Notices of the Royal Astronomical Society* **460** (2016) 1173 [1509.06404].

[49] G. Favole, J. Comparat, F. Prada, G. Yepes, E. Jullo, A. Niemiec et al., *Clustering properties of g-selected galaxies at $z \sim 0.8$*, *Monthly Notices of the Royal Astronomical Society* **461** (2016) 3421 [1507.04356].

[50] B. P. Moster, R. S. Somerville, C. Maulbetsch, F. C. Van den Bosch, A. V. Macciò, T. Naab et al., *Constraints on the relationship between stellar mass and halo mass at low and high redshift*, *Astrophys. J.* **710** (2010) 903 [0903.4682].

[51] B. P. Moster, T. Naab and S. D. M. White, *Galactic star formation and accretion histories from matching galaxies to dark matter haloes*, *Mon. Not. R. Astron. Soc.* **428** (2013) 3121–3138 [1205.5807].

[52] R. M. Reddick, R. H. Wechsler, J. L. Tinker and P. S. Behroozi, *THE CONNECTION BETWEEN GALAXIES AND DARK MATTER STRUCTURES IN THE LOCAL UNIVERSE*, *The Astrophysical Journal* **771** (2013) 30 [1207.2160].

[53] J. Chaves-Montero, R. E. Angulo, J. Schaye, M. Schaller, R. A. Crain, M. Furlong et al., *Subhalo abundance matching and assembly bias in the EAGLE simulation*, *Monthly Notices of the Royal Astronomical Society* **460** (2016) 3100 [1507.01948].

[54] S. Contreras, R. E. Angulo and M. Zennaro, *A flexible subhalo abundance matching model for galaxy clustering in redshift space*, *Monthly Notices of the Royal Astronomical Society* **508** (2021) 175 [2012.06596].

[55] S. Contreras, R. E. Angulo, V. Springel, S. D. M. White, B. Hadzhiyska, L. Hernquist et al., *The millenniumtng project: Inferring cosmology from galaxy clustering with accelerated n-body scaling and subhalo abundance matching*, 2022. 10.48550/ARXIV.2210.10075.

[56] A. P. Hearin and D. F. Watson, *The dark side of galaxy colour*, *Mon. Not. R. Astron. Soc.* **435** (2013) 1313 [1304.5557].

[57] L. Gao and S. D. M. White, *Assembly bias in the clustering of dark matter haloes*, *Monthly Notices of the Royal Astronomical Society: Letters* **377** (2007) L5 [0611921].

[58] I. Zehavi, S. Contreras, N. Padilla, N. J. Smith, C. M. Baugh and P. Norberg, *The impact of assembly bias on the galaxy content of dark matter halos*, *The Astrophysical Journal* **853** (2018) 84 [1706.07871v1].

[59] R. S. Somerville and J. R. Primack, *Semi-analytic modelling of galaxy formation: the local universe*, *Monthly Notices of the Royal Astronomical Society* **310** (1999) 1087 [astro-ph/9802268].

[60] S. Cole, C. G. Lacey, C. M. Baugh and C. S. Frenk, *Hierarchical galaxy formation*, *Monthly Notices of the Royal Astronomical Society* **319** (2002) 168 [astro-ph/0007281].

[61] R. G. Bower, I. G. McCarthy and A. J. Benson, *The flip side of galaxy formation: a*

combined model of galaxy formation and cluster heating, *Monthly Notices of the Royal Astronomical Society* (2008) [0808.2994].

[62] B. M. B. Henriques, S. D. M. White, P. A. Thomas, R. Angulo, Q. Guo, G. Lemson et al., *Galaxy formation in the planck cosmology – i. matching the observed evolution of star formation rates, colours and stellar masses*, *Monthly Notices of the Royal Astronomical Society* **451** (2015) 2663 [1410.0365].

[63] Z. Zheng, A. A. Berlind, D. H. Weinberg, A. J. Benson, C. M. Baugh, S. Cole et al., *Theoretical models of the halo occupation distribution: Separating central and satellite galaxies*, *The Astrophysical Journal* **633** (2005) 791 [astro-ph/0408564].

[64] J. A. Peacock and R. E. Smith, *Halo occupation numbers and galaxy bias*, *Monthly Notices of the Royal Astronomical Society* **318** (2000) 1144 [0005010].

[65] R. H. Wechsler, R. S. Somerville, J. S. Bullock, T. S. Kolatt, J. R. Primack, G. R. Blumenthal et al., *Galaxy formation at $z \sim 3$: Constraints from spatial clustering*, *The Astrophysical Journal* **554** (2001) 85 [astro-ph/0011261].

[66] A. A. Berlind and D. H. Weinberg, *The halo occupation distribution: Toward an empirical determination of the relation between galaxies and mass*, *The Astrophysical Journal* **575** (2002) 587 [astro-ph/0109001].

[67] Z. Zheng, A. L. Coil and I. Zehavi, *Galaxy evolution from halo occupation distribution modeling of DEEP2 and SDSS galaxy clustering*, *The Astrophysical Journal* **667** (2007) 760 [astro-ph/0703457].

[68] Y.-T. Lin, J. J. Mohr and S. A. Stanford, *K-band properties of galaxy clusters and groups: Luminosity function, radial distribution, and halo occupation number*, *The Astrophysical Journal* **610** (2004) 745 [astro-ph/0402308v3].

[69] X. Yang, H. J. Mo and F. C. van den Bosch, *Galaxy groups in the sdss dr4: Iii. the luminosity and stellar mass functions*, *The Astrophysical Journal* **695** (2009) 900 [0808.0539v2].

[70] S. M. Hansen, E. S. Sheldon, R. H. Wechsler and B. P. Koester, *The galaxy content of sdss clusters and groups*, *The Astrophysical Journal* **699** (2009) 1333 [0710.3780].

[71] P. S. Behroozi, R. H. Wechsler and C. Conroy, *The average star formation histories of galaxies in dark matter halos from $z = 0 - 8$*, *The Astrophysical Journal* **770** (2013) 57 [1207.6105].

[72] Q. Guo, S. White, C. Li and M. Boylan-Kolchin, *How do galaxies populate dark matter haloes?*, *Monthly Notices of the Royal Astronomical Society* (2010) [0909.4305].

[73] B. P. Moster, T. Naab and S. D. M. White, *emerge – an empirical model for the formation of galaxies since z ∼ 10*, *Monthly Notices of the Royal Astronomical Society* **477** (2018) 1822 [1705.05373].

[74] L. Wang and Y. P. Jing, *Modelling galaxy stellar mass evolution from $z \sim 0.8$ to today*, *Monthly Notices of the Royal Astronomical Society* **402** (2010) 1796 [0911.1864].

[75] X. Yang, H. J. Mo, F. C. van den Bosch, Y. Zhang and J. Han, *Evolution of the galaxy - dark matter connection and the assembly of galaxies in dark matter halos*, *The Astrophysical Journal* **752** (2012) 41 [1110.1420v3].

[76] A. V. Kravtsov, A. A. Vikhlinin and A. V. Meshcheryakov, *Stellar mass – halo mass relation and star formation efficiency in high-mass halos*, *Astronomy Letters* **44** (2018) 8 [1401.7329].

[77] P. Behroozi, R. H. Wechsler, A. P. Hearin and C. Conroy, *UniverseMachine: The correlation between galaxy growth and dark matter halo assembly from z = 0-10*, *Monthly Notices of the Royal Astronomical Society* **488** (2019) 3143 [1806.07893].

[78] V. Springel, N. Naoki Yoshida and S. White, *GADGET: A code for collisionless*

andgasdynamical cosmological simulations, *New Astron.* **6** (2001) 79 [0003162].

[79] I. K. Baldry, K. Glazebrook and S. P. Driver, *On the galaxy stellar mass function, the mass-metallicity relation, and the implied baryonic mass function*, *Mon. Not. R. Astron. Soc.* **388** (2008) 945 [0804.2892].

[80] J. R. Weaver, I. Davidzon, S. Toft, O. Ilbert, H. J. McCracken, K. M. L. Gould et al., *Cosmos2020: The galaxy stellar mass function: On the assembly and star formation cessation of galaxies at* $0.2 < z \leq 7.5$, 2022. 10.48550/ARXIV.2212.02512.

[81] H. J. McCracken, B. Milvang-Jensen, J. Dunlop, M. Franx, J. P. U. Fynbo, O. L. Fè vre et al., *UltraVISTA: a new ultra-deep near-infrared survey in COSMOS*, *Astronomy & Astrophysics* **544** (2012) A156 [1204.6586].

[82] B. P. Moster, R. S. Somerville, J. A. Newman and H.-W. Rix, *A cosmic variance cookbook*, *The Astrophysical Journal* **731** (2011) 113 [1001.1737].

[83] F. Marulli, A. Veropalumbo and M. Moresco, *Cosmobolognalib: C++ libraries for cosmological calculations*, *Astronomy and Computing* **14** (2016) 35 [1511.00012v2].

[84] G. Despali, C. Giocoli, R. E. Angulo, G. Tormen, R. K. Sheth, G. Baso et al., *The universality of the virial halo mass function and models for non-universality of other halo definitions*, *Monthly Notices of the Royal Astronomical Society* **456** (2015) 2486 [1507.05627].

[85] J. Tinker, A. V. Kravtsov, A. Klypin, K. Abazajian, M. Warren, G. Yepes et al., *Toward a halo mass function for precision cosmology: The limits of universality*, *The Astrophysical Journal* **688** (2008) 709 [0803.2706].

[86] D. Foreman-Mackey, D. W. Hogg, D. Lang and J. Goodman, *emcee: The MCMC Hammer*, *Astronomical Society of the Pacific* **125** (2013) [1202.3665].

[87] A. Gelman and D. B. Rubin, *Inference from iterative simulation using multiple sequences*, *Statist. Sci.* **7** (1992) 457.

[88] G. Girelli, L. Pozzetti, M. Bolzonella, C. Giocoli, F. Marulli and M. Baldi, *The stellar-to-halo mass relation over the last 12 Gyr*, *Astron. Astrophys.* **634** (2020) 23 [2001.02230].

[89] P. S. Behroozi, C. Conroy and R. H. Wechsler, *A comprehensive analysis of uncertainties affecting the Stellar-to-halo-mass relation for* $0 < z < 4$, *Astrophys.J.* **717** (2010) 379 [1001.0015].

[90] P. S. Behroozi, R. H. Wechsler and C. Conroy, *The average star formation histories of galaxies in dark matter halos from* $z = 0 - 8$, *ApJ* **770:57** (2013) [1207.6105].

[91] P. S. Behroozi, R. H. Wechsler, A. Hearing and C. Conroy, *UNIVERSE MACHINE: The Correlation between Galaxy Growth and Dark Matter Halo Assembly from* $z = 0 - 10$, *Mon. Not. R. Astron. Soc.* **488** (2018) 3143 [1806.07893].

[92] Q. Guo, S. White, C. Li and M. Boylan-Kolchin, *How do galaxies populate Dark Matter halos?*, *Mon. Not. R. Astron. Soc.* **404** (2010) 1111–1120 [0909.4305].

[93] A. Rodriguez-Puebla, J. R. Primack, V. Avila-Reese and S. M. Faber, *The galaxy-halo connection over the last* 13.3 *Gyrs*, *Mon. Not. R. Astron. Soc.* **470** (2017) 651–687 [1703.04542].

[94] A. Knebe and S. R. e. a. Knollmann, *Haloes gone MAD: The Halo-Finder Comparison Project*, *Mon. Not. R. Astron. Soc.* **415** (August) 2293–2318 [1104.0949].

[95] R. E. Angulo, V. Springel, S. D. M. White, A. Jenkins, C. M. Baugh and C. S. Frenk, *Scaling relations for galaxy clusters in the Millennium-XXL simulation*, *Mon. Not. R. Astron. Soc.* **426** (Sept) 2046–2062 [1203.3216v2].

[96] G. Verza, C. Carbone, A. Pisani and A. Renzi, *Demnuni: disentangling dark energy from massive neutrinos with the void size function*, 2022.

[97] A. Kiakotou, O. Elgarøy and O. Lahav, *Neutrino Mass, Dark Energy, and the Linear Growth Factor*, *Phys. Rev. D* **77** (2008) [0709.0253].

[98] S. Satpathy, S. Alam, S. Ho and M. e. a. White, *The clustering of galaxies in the completed SDSS-III Baryon Oscillation Spectroscopic Survey: On the measurement of growth rate using galaxy correlation functions*, *Mon. Not. R. Astron. Soc.* **469** (2017) 1369–1382 [1607.03148v2].